MULTIFLUID NONEQUILIBRIUM SIMULATION OF ARCJET THRUSTERS

by

Scott Alan Miller

S.B. Aeronautics and Astronautics, Massachusetts Institute of Technology, 1988
S.M. Aeronautics and Astronautics, Massachusetts Institute of Technology, 1990

SUBMITTED TO THE DEPARTMENT OF
AERONAUTICS AND ASTRONAUTICS IN PARTIAL FULFILLMENT OF THE
REQUIREMENTS FOR THE DEGREE OF

Doctor of Science
in Aeronautics and Astronautics
at the
Massachusetts Institute of Technology
February 1994

Signature of Author ______________________________
Department of Aeronautics and Astronautics
October 15, 1993

Certified by ______________________________
Professor Manuel Martinez-Sanchez, Thesis Supervisor
Department of Aeronautics and Astronautics

Certified by ______________________________
Professor Daniel E. Hastings, Thesis Committee Member
Department of Aeronautics and Astronautics

Certified by ______________________________
Professor Mark Drela, Thesis Committee Member
Department of Aeronautics and Astronautics

Accepted by ______________________________
Professor Harold Y. Wachman, Chairman
Department Graduate Committee

Multifluid Nonequilibrium Simulation of Arcjet Thrusters

by

Scott Alan Miller

Submitted to the Department of Aeronautics and Astronautics
on October 15, 1993, in partial fulfillment of the
requirements for the degree of
Doctor of Science

A detailed numerical model has been developed to study the gasdynamic flow in an electrothermal arcjet thruster. This two-temperature, Navier-Stokes model consistently incorporates viscosity, heat conduction, ohmic dissipation, collisional energy transfer between electrons and heavy species, ambipolar diffusion, nonequilibrium dissociation and ionization, and radiation. The fluid equations are solved by MacCormack's method while an iterative procedure is used to relax an electric potential equation, from which the current distribution in the thruster is obtained. Using hydrogen propellant, solutions are achieved for a range of input parameters and the underlying physics and internal structures of these arcjet flows are revealed. In particular, a mechanism for self-sustaining anodic arc attachment is identified. It is found that ambipolar diffusion from the arc core coupled with enhanced nonequilibrium dissociation and ionization in the outer flow provide enough charge carriers for the current to pass self-consistently between the arc core and the anode wall.

Numerical solutions are compared with experimental results from the German TT1 radiatively-cooled arcjet thruster. Calculated discharge voltage is within 1-2% to 10% of experimental measurements, and predicted specific impulse is within 5-10% agreement over a range of applied currents and mass flow rates. In addition, flow solutions are used to explain observed trends in performance as quantities such as the specific power and mass flow rate are varied. An anode thermal model is constructed which yields more accurate predictions of the inlet gas and electrode wall temperatures, and this model is coupled to the arcjet flow solver in order to obtain a more self-consistent solution. Finally, a simplified stability analysis of the near-anode arc attachment region is performed. It is found that a localized ionization instability may be initiated in this region, but that the system is stable under the flow conditions predicted by the arcjet simulation of this research.

Thesis Supervisor: Manuel Martinez-Sanchez
Title: Professor of Aeronautics and Astronautics

Acknowledgements

I would first like to thank my advisor, Professor Manuel Martinez-Sanchez, for his direction and guidance over the course of this project. Professor Martinez-Sanchez is a brilliant man and a dedicated scientist, and I feel lucky to have worked with him. He has the ability to see through the complexities of a system to discern the important physical processes, and was always able to help me work out problems with my research. The zeal with which he attacks research and his structured problem-solving approach pushed me to work harder and think more effectively. Professor Daniel Hastings was a valuable source of scientific insight and his help in establishing contacts in the space power and propulsion community was much appreciated. I am also indebted to Professor Hastings for constantly providing our lab with the latest, fastest computers and visualization software. In addition, I would like to thank Professors Mark Drela, John Dugundji, and Miklos Porkolab for serving on my thesis committee and giving me advice along the way.

I have been fortunate to have been surrounded by many outstanding students and research staff members during my graduate tenure at M.I.T. I owe a particularly large debt of gratitude to Eli Niewood, upon whom I could always call when I had difficulties with my computer code or with understanding electric propulsion physics. I was able to draw on his experience in MPD thruster numerical simulation to foresee and avoid potential problems as my own research progressed, undoubtably saving myself many extra hours of debugging and derivation. Eric Sheppard was a source of needed information on nonequilibrium rate processes, radiative transfer, nondimensionalization, and bowling. Rodger Biasca served as my answer man for computer questions and taught me everything I needed to know about managing the SPPL's computer systems. I also received much valuable computer support from Bob Haimes and Steve Ellis. I enjoyed having long conversations with Damon Wells about everything from ancient history to politics to winning strategies for Magic Sword, and with Jackie Auzias de Turenne about sports, star trek, and card collecting. My thanks also goes out to Knox Millsaps, Todd Barber, John Conger, Chris Lentz, David Oh, Mohanjit Jolly, Jim Kalamas, Ray Sedwick, Pamela Barry, Robie Samanta-Roy, David Rivas, Nick Gatsonis, and Jean-Marc Chanty for their help, friendship, and camaraderie. In a broader sense I would like to thank Steve Knowles and William (W^2) Smith at Rocket Research Company, whose engineering professionalism I greatly admire and whose enthusiasm for electric propulsion helped set the course of my academic career.

No acknowledgement section would be complete without paying tribute to the Incorrigible Hulk Man, whose keen wit and superheroism filled my otherwise uneventful

first three years as a graduate student with meaning. I'll never forget the great times we had then (The List!), and I'll always value our friendship. Eliot Sobel was always there to keep my spirits up and to get me away from M.I.T. when I needed a break. I also valued the friendships of Richard Carreiro, Sharad Joshi, and John Schoen while I was at school and Joe Darby, Bruce Miller, John Lloyd, and Doug Snyder when I was home in Ohio for vacation.

My parents, Arlen and Gwen Miller, and my brother Jeff have supported me all these years, and I knew I could always turn to them if I needed anything. I wish to thank them for all the ways they have guided and enriched my life. I also want to thank Renee's parents, Doug and LeAnn Mong, and her sister Michelle, who made me feel like a part of their family from the very beginning.

Finally, I wish to thank Renee, the most important person in my life. I don't know what I would have done without her the past two and a half years. Before I met her I was but half of a whole person, and I was amazed by the magnitude of happiness and fulfillment she brought into my life. Her love and confidence in me kept me going when sometimes I thought I'd never solve a particular problem, and I could always talk about my research with her or let her take my mind off arcjets for a while depending on which I needed to do. She also helped proofread and edit this thesis, no small task in itself.

This thesis is dedicated to my wife, Renee.

The material herein is based upon work supported in part by a National Science Foundation Graduate Fellowship. Any opinions, findings, conclusions, or recommendations expressed in this publication are those of the author and do not necessarily reflect the views of the National Science Foundation. Additional funding was received under a National Defense Science and Engineering Graduate Fellowship administered by the U.S. Army Research Office. Computer time was funded by a grant from the Air Force Office of Scientific Research, and the NASA Lewis Research Center provided free supercomputer access for a period of time.

Contents

List of Figures

List of Tables

List of Symbols

a	Speed of sound $[m/s]$
$\vec{B}$	Magnetic field $[T]$
c	Exit velocity $[m/s]$
$\bar{c}$	Random thermal velocity $[m/s]$
$\hat{c}_p$	Specific heat at constant pressure $[J/mole/^oK]$
$\hat{c}_v$	Specific heat at constant volume $[J/mole/^oK]$
D_a	Ambipolar diffusion coefficient $[m^2/s]$
D_H	Heat diffusion coefficient $[m^2/s]$
d_{er}	Ambipolar flux of ions and electrons $[1/m^2/s]$
e	Electric proton charge $[C]$, internal energy per unit mass $[J/kg]$
E	Total energy per unit mass $[J/kg]$
$\vec{E}$	Electric field $[V/m]$
E_i	Ionization energy $[J]$
E_{int}	Internal energy $[J]$
E_d	Dissociation energy $[J]$
E_l	Elastic collisional energy transfer $[W/m^3]$
E_{vib}	Vibrational excitation energy $[J]$
f	Distribution function
$\mathbf{F}$	Axial flux vector
$\vec{F}$	External force $[N]$
$\mathbf{G}$	Radial flux vector
h	Planck's constant $[Js]$, enthalpy per unit mass $[J/kg]$
$\hat{h}$	Enthalpy per mole $[J/mole]$
H	Total enthalpy per unit mass $[J/kg]$
I	Total current $[A]$
I_{sp}	Specific impulse $[s]$
$\vec{j}$	Electric current density $[A/m^2]$
J	Jacobian of coordinate transformation

k	Boltzman's constant $[J/^oK]$
K	Equilibrium constant
m	Particle mass $[kg]$
M	Molecular weight, Mach number
n	Number density $[1/m^3]$
$\dot{n}_e$	Net electron production rate $[1/m^3/s]$
$\dot{n}_S$	Net atomic species production rate $[1/m^3/s]$
$\hat{N}$	Avogadro's number $[1/mole]$
p	Scalar pressure $[Pa]$
P_r	Prandtl number
$\vec{q}$	Heat flux vector $[W/m^2]$
q	Partition function
Q	Collision cross section $[m^2]$
R	Real gas constant $[J/kg/^oK]$
$\hat{R}$	Universal gas constant $[J/mole/^oK]$
$\dot{R}$	Radiative energy transfer per unit volume $[W/m^3]$
T	Temperature $[^oK]$, thrust $[N]$
u	Degeneracy function
$\mathbf{U}$	State vector for fluid equations
$\vec{u}$	Mean flow velocity $[m/s]$
v_B	Bohm velocity $[m/s]$
$\vec{V}$	Slip velocity $[m/s]$
x	Mole fraction
x^M	Mass fraction
α	Ionization fraction, heat diffusivity $[m^2/s]$
β	Hall parameter
$\triangle$	Dissociation fraction
$\triangle v$	Velocity increment $[m/s]$
γ	Ratio of specific heats
ϵ	Emissivity

κ	Coefficient of thermal conductivity $[W/m/^oK]$
μ	Coefficient of viscosity $[kg/ms]$
μ_0	Permeability of vacuum $[H/m]$
$\hat{\mu}_0$	Chemical potential $[J/mole]$
ν	Collision frequency $[1/s]$, stoichiometric coefficient
ϕ	Electric potential $[V]$
Φ	Viscous dissipation function $[W/m^3]$
ψ	Electron mobility $[m^2/\Omega/C]$
ρ	Mass density $[kg/m^3]$
σ	Electrical conductivity $[mho/m]$, molar concentration $[moles/m^3]$
σ_{SB}	Stefan-Boltzmann constant $[W/m^2/^oK^4]$
τ	Viscous stress tensor component $[N/m^2]$
θ	Ratio of electron temperature to heavy species temperature
θ_d	Dissociation characteristic temperature $[^oK]$
θ_r	Rotational excitation characteristic temperature $[^oK]$
θ_v	Vibrational excitation characteristic temperature $[^oK]$
Ω	Average effective collision integral $[m^2]$
$< >$	Average value of a quantity

Chapter 1

Introduction

The basic function of any rocket engine is to produce thrust by expelling mass in a given direction, thereby producing acceleration in the opposite direction. The magnitude of this thrust is given by the product of the propellant mass flow rate and its effective, or vacuum, exit velocity:

$$T = \dot{m}c. \tag{1.1}$$

Nearly all space propulsion needs are currently filled by chemical propulsion systems. Examples include the liquid hydrogen - liquid oxygen space shuttle main engines, the solid rocket boosters of the Titan IV, and the monopropellant hydrazine stationkeeping thrusters of communications satellites. Chemical rockets are relatively simple in design and can produce unlimited thrust, but their performance is limited by the chemical energy stored within the propellants. In practice, this restricts their attainable exit velocity to a maximum of approximately 4500m/s. In terms of specific impulse, a more common measure of rocket performance ($I_{sp} = \frac{c}{g}$), the maximum for a chemical propulsion system is about 450 seconds.

A propulsion device which could produce a higher specific impulse than that of a chemical rocket would be more desirable, since the same thrust could be produced with less propellant. This would provide the spacecraft designer the luxury of adding additional scientific experiments or other useful payload in place of the propellant mass saved. Alternatively, if no change were made in the vehicle design then a more efficient propulsion system would allow the spacecraft to travel farther or perform more attitude adjustments than one with a less efficient system. Considering the monetary cost of launching payloads into space (currently on the order of $10,000 per kilogram), the amount of fuel saved by a more efficient propulsion device could also translate into a substantial launch cost savings, especially for missions requiring a large total velocity increment, or Δv, and therefore a large propellant mass fraction.

A number of different propulsion system types are shown in Figure 1.1, arranged based on performance in terms of I_{sp} and thrust-to-weight ratio. Clearly the most desirable system would lie in the upper right-hand corner of this diagram, providing both a large acceleration and a high specific impulse. Unfortunately, as with any engineering problem there are tradeoffs involved. With the propulsion systems developed thus far, specific impulse can be increased substantially beyond that available with chemical rockets, but only at the cost of significantly decreased acceleration due to the increased mass of the propulsion system itself. In practical terms, this means that none of these advanced propulsion devices can be used for earth launches with the exception of nuclear rockets, which face major environmental obstacles to their development. Once an object is in earth orbit or in free space, however, gravitational forces are greatly diminished and a rocket can still be effective even if its thrust-to-weight ratio is much less than one. Any space propulsion system with a higher I_{sp} than a given system could then provide a savings in required propellant mass at the expense of a longer burn time to complete the same maneuver. Applicable missions for these advanced propulsion devices include satellite stationkeeping, orbital maneuvering, and interplanetary travel.

1.1 Electric Propulsion

Electric propulsion devices are one family of advanced propulsion systems which can achieve high specific impulse at low levels of thrust. These devices include resistojets, arcjets, magnetoplasmadynamic thrusters, stationary plasma thrusters, and ion engines. Each of these uses power supplied by an external source to increase the exit velocity of the propellant. Three main types of electric propulsion can be identified in Figure 1.1: electrothermal, electromagnetic, and electrostatic.

Electrothermal thrusters include resistojets, arcjets, and all other devices in which electric power is used to increase the temperature of the propellant, which is then expanded in a nozzle to convert the thermal energy into kinetic thrust. In a resistojet the propellant gas is heated by contact with a hot electrically-heated surface, somewhat like placing an incandescent light bulb in the thruster plenum chamber. Arcjets achieve very high gas temperatures in certain regions of the thruster by passing an electric arc discharge between a central cathode and concentric anode. Other heating methods, such as laser-induced, microwave, and radio frequency heating have been tested. The maximum gas temperature inside an electrothermal thruster is limited by the melting

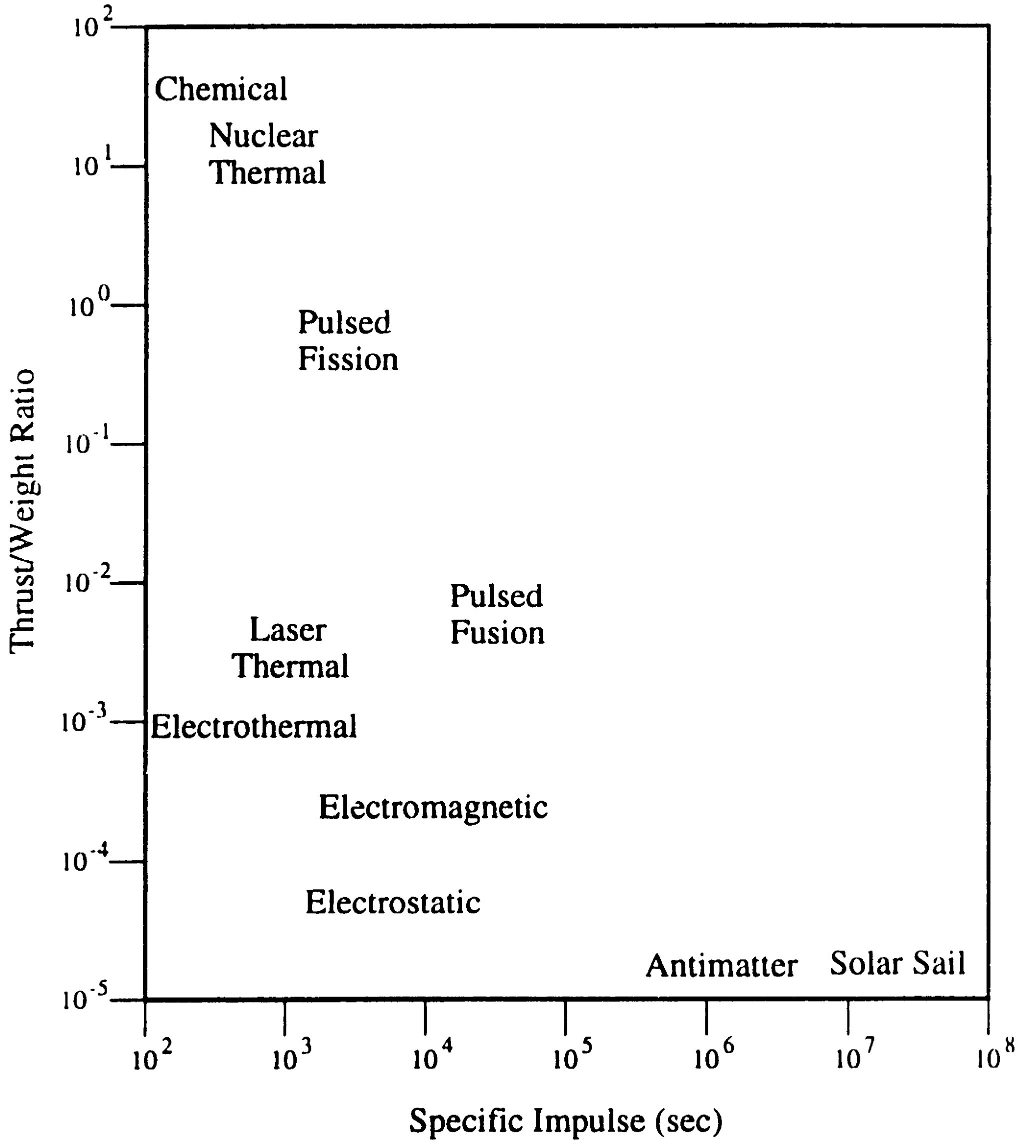

Figure 1.1: Acceleration and Specific Impulse of Various Propulsion System Types

points of the thruster materials, however, and this sets an upper limit on the attainable specific impulse. The typical I_{sp} for these devices ranges from 300 to 1600 seconds.

Electromagnetic propulsion devices overcome the specific impulse limitation of electrothermal thrusters by accelerating ionized propellants with induced or applied magnetic fields. As a result, much higher exit velocities can be reached, with specific impulses ranging from 1000 to 5000 seconds. The magnetoplasmadynamic, or MPD, thruster is probably the most well known electromagnetic propulsion device. It is essentially an arcjet operated at much higher power and lower pressure than its electrothermal counterpart. In this case, however, the radial current between the anode and cathode is strong enough to induce a substantial magnetic field in the azimuthal direction. The Lorentz force between the current and this self-magnetic field accelerates the ionized propellant in the axial direction toward the nozzle exit plane. Collisions between ions and neutral gas particles then produce a bulk axial acceleration of the entire flow. MPD thrusters may be operated in either a steady or pulsed mode, and applied magnetic fields may be used to further control the acceleration of the propellant. Other types of electromagnetic thrusters include pulsed inductive thrusters, pulsed plasma thrusters, electromagnetic rail guns, and stationary plasma or Hall thrusters, which combine aspects of both MPD thrusters and low thrust ion engines.

The development of electrostatic thrusters, or ion engines, has progressed further than any of the electric propulsion devices previously mentioned. After many years of analysis and testing, most of the physical and technological issues of ion engine design have been solved. The remaining questions primarily involve lifetime and system integration concerns. Electrostatic thrusters operate by first ionizing the propellant by electron bombardment, contact ionization, or radiofrequency heating and then accelerating the ions through a large potential difference between two perforated grids. The resulting high velocity ion beam is then neutralized by an electron emitting device downstream of the accelerating grids. In this manner specific impulses of 2000-10,000 seconds can be achieved, but at the price of very low thrust density due to space charge limitations.

Since all electric propulsion systems by definition require electrical power, a practical limitation on their use is the available power in space. Communications satellites can currently spare only a few kilowatts of power for possible use by electric propulsion. Future space applications such as orbital transfer vehicles or the space station could make available 10-100kW of power, particularly if nuclear reactors such as the SP-100 are employed for power generation. Unfortunately, even at these high power levels electric propulsion thrusters produce a relatively low thrust, and certain electromagnetic devices such as the MPD thruster are not practical.

The two highest performance electric propulsion devices at currently available space power levels are the electrothermal arcjet and the ion engine. Of these two the arcjet is most worthy of additional study by analytical and numerical modeling. The internal physics of arcjets are less well understood than those of ion engines, and due to thrust density and system integration concerns arcjets may be superior to ion engines for current applications such as the stationkeeping of geosynchronous satellites. In addition, advances in the understanding of electrothermal arcjets could translate into increased understanding of similar devices such as the higher power MPD thruster. For these reasons and others, the numerical modeling of electrothermal arcjet thrusters was selected as the focus of this research.

1.2 Principles of Arcjet Thruster Operation

1.2.1 Basic Principles

A basic diagram of an arcjet thruster is shown in Figure 1.2. The device is coaxial in design and consists primarily of a central cathode rod surrounded by a contoured anode block. Propellant is injected through an insulating backplate and an arc discharge is struck between the two electrodes. High energy arc electrons heat the propellant gas through collisions to temperatures as high as 30,000°K in the core of the arc. This thermal energy is then converted to thrust in the nozzle expansion. The bulk of an arcjet propulsion system consists of the power processing unit, propellant feed system, and electrode holder/casing, some of which is illustrated in the schematic of Figure 1.3. The main flow region depicted in Figure 1.2, typically 1-10cm in length, is but one small piece of the total arcjet thruster assembly.

The cathode is typically made of tungsten due to its high melting point (3680°K) and impregnated with 2% thorium to decrease the work function of the surface. The conical tip of the cathode creates a localized "hot spot" which enhances the thermionic emission of electrons needed to carry the arc current. Arcjet anodes are generally passive blocks of pure tungsten which serve two purposes: to collect and carry the arriving electron current and to serve as the outer wall boundary that defines the thruster constrictor and nozzle. The anode may be water-cooled or radiatively-cooled, the latter being the more efficient method since the resulting higher temperature electrodes can then be used to heat the incoming propellant and the cooler outer gas flow by conduction from the electrode walls. A high temperature dielectric such as boron nitride

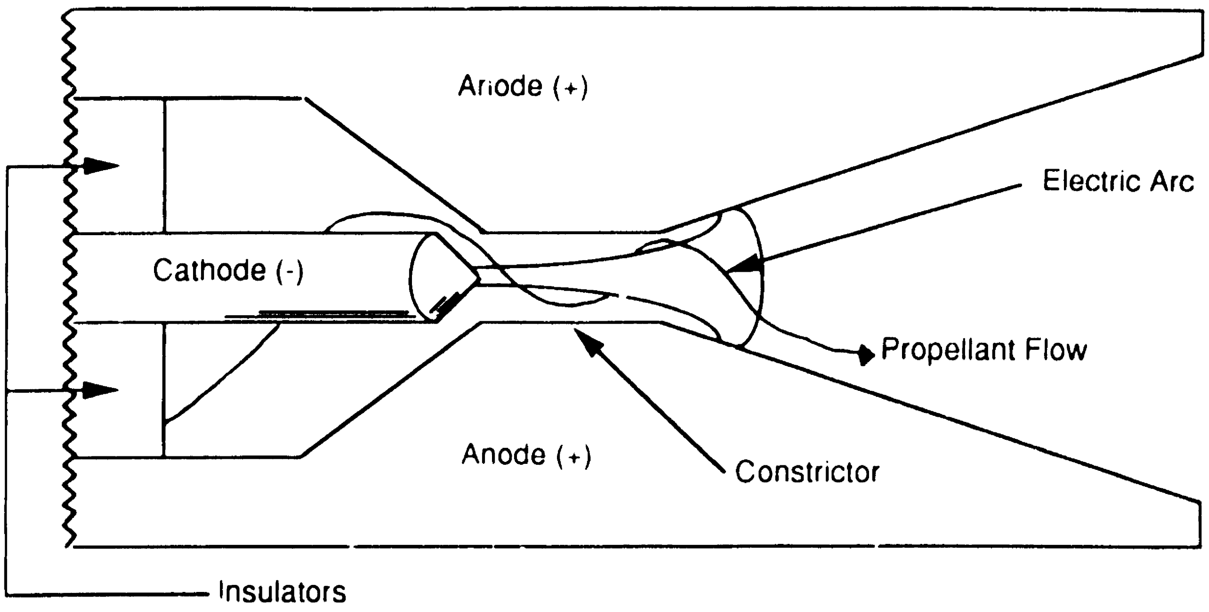

Figure 1.2: Diagram of Axisymmetric Arcjet Flow

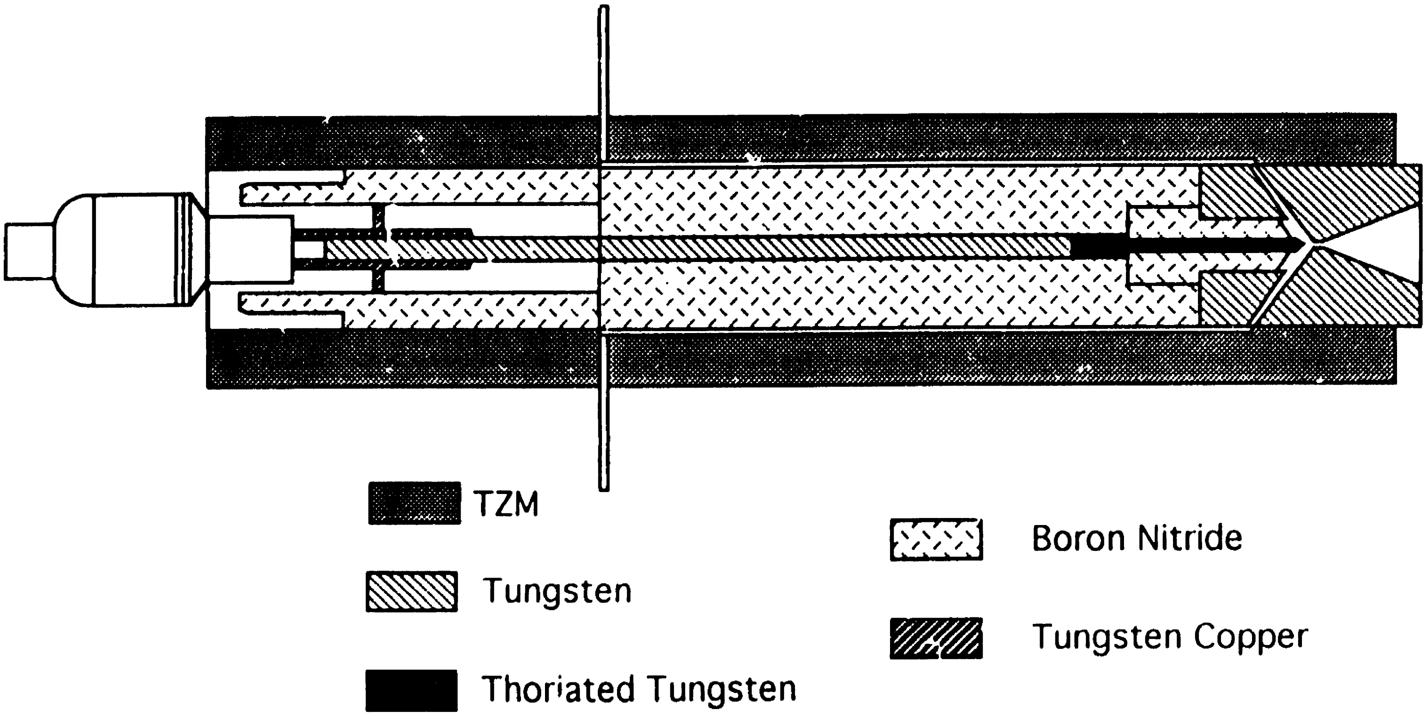

Figure 1.3: Arcjet Thruster Schematic Diagram

separates the two electrodes upstream of the propellant inlet, and the entire thruster assembly is often encased in a tungsten or molybdenum housing. The role of the constrictor region is to stabilize the arc in a fixed position along the thruster centerline and to maintain a high temperature in the core of the arc. Typically the arc is further stabilized by injecting the propellant with an azimuthal "swirl" velocity component, which centrifugates the cooler gas outside of the arc towards the anode wall. The use of injected swirl is not necessary for arc stability and is continued primarily for historical reasons, although it may slightly improve heat transfer and mixing in the nozzle expansion.

Operational characteristics of electrothermal arcjets are listed in Table 1.1. The attainable I_{sp} can be two to three times that of the most advanced chemical rockets at up to 50% overall efficiency. In general, as the applied current is increased the voltage decreases due to increased conductivity within the arc. The efficiency of the arcjet decreases with increasing current due to increased frozen losses, and increases with increasing mass flow rate (or pressure) due to recovery of those frozen losses. The attainable specific impulse for a given propellant and thruster geometry is essentially a function of the specific power, or the input power divided by the mass flow rate. As expected from basic fluid dynamics, propellants with a low molecular weight such as hydrogen yield the highest overall performance.

Low power arcjet systems, on the order of 1-3kW, will soon be used by geosynchronous satellites for north-south orbital stationkeeping. A higher power class of arcjets in the 15-30kW range can be utilized for orbital transfers, space platform or space station orbital maintenance, and spacecraft attitude control or course correction. In principle any gas may be used as propellant. Ammonia and hydrazine (N_2H_4) are favorites because these gases are currently being used as blowdown propellants on satellite propulsion systems. Pure hydrogen yields better performance because of its lower atomic weight and dissociation energy, but also suffers from frozen flow losses inherent in the dissociation process, a characteristic shared by ammonia and hydrazine as well.

1.2.2 Gas Dynamics

Electrothermal arcjets are typically operated at pressures near one atmosphere. This pressure is high enough to maintain strong collisional coupling between electrons and the propellant gas in the arc core, and low enough that thruster design is not adversely impacted by structural requirements. Referring to Figure 1.2, the flow inside an arcjet thruster can be divided into three regions: the high temperature arc core, the transition

Table 1.1: Typical Range of Electrothermal Arcjet Thruster Parameters

Input Power	1-30 kW
Voltage	30-200 V
Efficiency	20-50%
Specific Impulse	400-1600 sec
Thrust	0.1-3 N
Mass Flow Rate	0.001-0.6 g/s
Propellant	H_2,NH_3,N_2H_4

region, and the cooler outer flow. Within the core of the arc, the gas is likely both fully dissociated and fully ionized. Temperatures range from 3000°K to upwards of 30,000°K, but since the pressure is nearly constant in a given cross-sectional plane, the fraction of propellant within this core region is small compared to that in the cooler outer flow. The core gas is effectively a highly collisional quasineutral plasma, probably near equilibrium conditions.

In the transition region, steep gradients in the radial direction lead to radial broadening of the arc through heat conduction and diffusion of species. The gas in this region may be considerably away from thermal and chemical equilibrium. Broadening of the arc continues through the constrictor until attachment to the anode occurs over some portion of the nozzle wall. Depending on the propellant used, the thruster geometry, and operating conditions, some or all of the attachment zone may fall upstream of the constrictor exit. In a well designed arcjet, however, the current should attach entirely downstream of the constrictor. Most of the propellant actually flows in the outer region where little or no dissociation or ionization occurs. The temperature of this outer flow is essentially that of the anode wall.

There are a number of processes which lead to inefficiencies in an arcjet thruster. In the constrictor, high temperatures cause dissociation and ionization of the propellant gas. High speeds in the nozzle expansion (5,000-20,000m/s), however, prevent recombination processes from returning the gas to its equilibrium state, likely to be neutral if not molecular at the nozzle exit. A "frozen flow" inefficiency then results because the energy of dissociation and/or ionization has been retained in the flow and not converted to useful thrust. A second source of inefficiency is the nonuniformity of the velocity and other gas properties in the radial direction. In addition, since the Reynolds number is usually not large ($10^2 - 10^4$), friction losses may be considerable.

Finally, the physics of the near-electrode regions is such that local voltage drops $\triangle V_c$ and $\triangle V_a$ are associated with the cathode and anode, respectively. Multiplied by the arc current, these near-electrode power losses may represent a significant fraction of the input power. The surplus power, particularly at the anode, is mostly dumped into the electrodes through heating.

1.2.3 Electrode Regions

Since the electrodes are intimately tied to the creation and behavior of the electric arc and the near-electrode regions may be responsible for large power losses, further discussion of these regions is warranted. In general, the electric arc in a plasma torch, arc gas heater, or arcjet thruster can be divided into five physical regions, as shown in Figure 1.4. The main body of the arc is denoted by region III, the arc column. This quasi-neutral region is characterized by minimal longitudinal gradients in the plasma properties, such as temperature, mass density, current density, and electric potential. A near-electrode region (I and V) is defined as that portion of the arc adjacent to an electrode in which there is a net space charge present. Otherwise known as a plasma sheath or fall zone, the width of this region is on the order of the local electron mean free path. Plasma properties may vary greatly within the sheath, and in particular the net space charge may create an electric field which is orders of magnitude greater than that in the arc column. As a result, even though the sheath is very thin, an appreciable voltage drop may be produced. In extreme cases this potential drop may equal or even exceed that of the main arc column, leading to large inefficiencies in the application device. The arc column and plasma sheath are joined by a transition region (II and IV) in which gradients in the plasma properties may be large but charge neutrality is maintained. For an atmospheric pressure high intensity arc such as that of a typical arcjet thruster, the transition regions are on the order of 10^{-3}m in width, and the near-electrode regions are approximately 10^{-5}-10^{-6}m in width.

As previously mentioned, the governing mechanism for electron production at the cathode is thermionic emission. The electron current generated by thermionic emission is a function of the cathode surface temperature and the work function of the cathode material, as expressed by the Richardson-Dushman equation[87]:

$$j_e = AT_c^2 e^{\frac{-e\phi_c}{kT_c}} \tag{1.2}$$

where $A \approx 6 \times 10^5 A/m^2/^o K^2$ is a constant. The work function for tungsten is approximately 4.5V. Cathodes are often impregnated with thorium ($\phi_{Th} = 3.35$V) or thorium oxide ($\phi_{ThO_2} = 2.94$V) in order to enhance thermionic emission by lowering the net

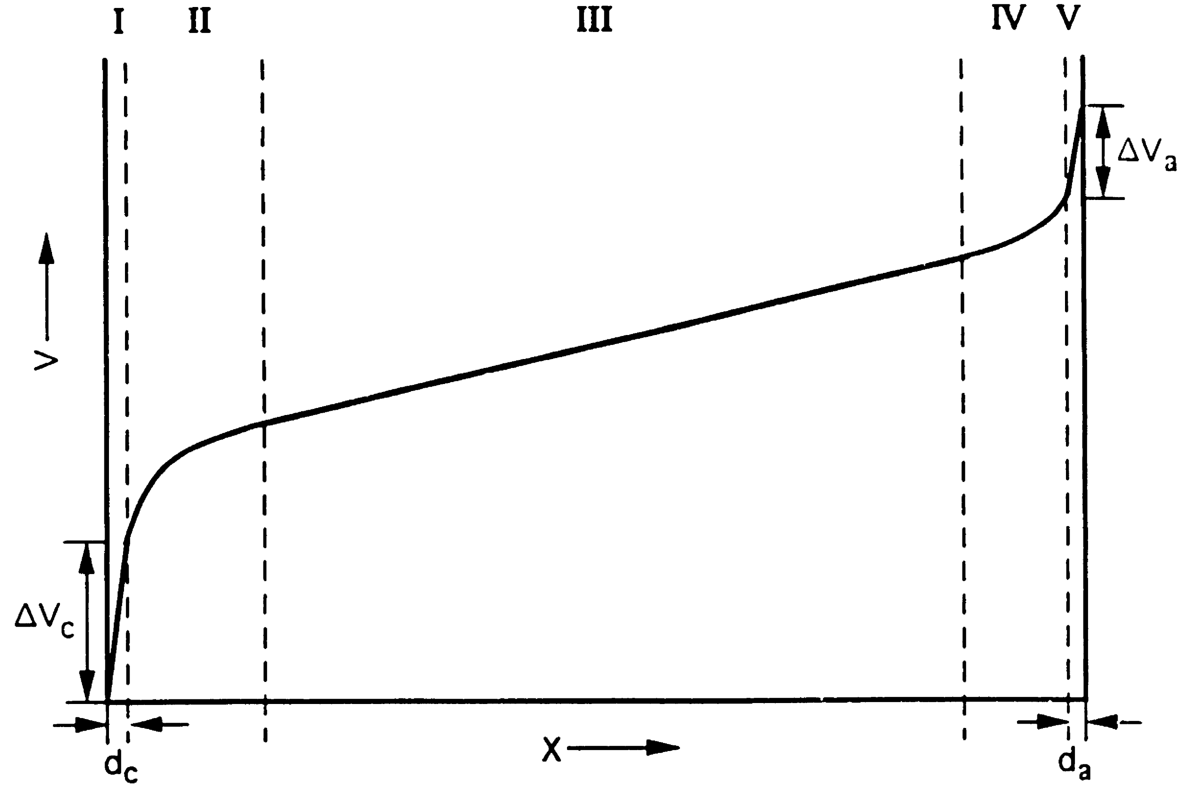

Figure 1.4: Physical Regions of a Stable Arc

work function of the surface. Recent work, however, has shown that once a stable arc is achieved most of the thorium is boiled off the tip attachment region, so there is some uncertainty as to whether the desired effect is being achieved[22]. Using the melting point of tungsten as the cathode temperature and 4.5V as the work function in Eqn. 1.2, an electron current density of $5.3 \times 10^6 A/m^2$ is obtained. Experimental measurements of arcjet cathode phenomena, however, indicate that cathode tip current densities of the order of $10^9 A/m^2$ are present for total currents of the order of 100A[22]. In reality, this discrepancy is resolved by current contributions from electric field enhanced electron emission from the tip and also from the ion current which impinges on the cathode, both of which together typically comprise 10-20% of the total current.

The Richardson-Dushman equation was modified by Schottky to account for electric field enhanced electron emission[87]:

$$j_t = j_e e^{\frac{4.389\sqrt{E}}{T_c}} . \tag{1.3}$$

To produce a current density of $10^9 A/m^2$, this equation requires an electric field of $2 \times 10^7 V/m$. Measurements of the near-cathode voltage drop in arc discharges by numerous researchers show that $\triangle V_c$ is generally on the order of the ionization potential of the breakdown gas. For hydrogen and nitrogen, this would indicate a sheath size of $0.5 - 1.0 \times 10^{-6}$m, which is roughly the same as that predicted by electron mean free path arguments. Given the high current densities involved in this application, there may also be some direct autoelectronic or field emission current drawn from the cathode surface by the action of the electric field alone. By accounting for a portion of the total current, this process of direct field emission would reduce by some degree the electric field required to produce the total cathode current. The magnitude of this emission current is given by the Fowler-Nordheim equation

$$j = 1.54 \times 10^{-6} \frac{E^2}{e\phi_c} exp \left[\frac{-6.83 \times 10^9 (e\phi_c)^{\frac{3}{2}}}{E} f \left(\frac{3.79 E^{\frac{1}{2}}}{e\phi_c} \times 10^{-5} \right) \right] (A/m^2), \qquad (1.4)$$

where the function f decreases from $f(0) = 1$ to $f(1) = 0$[87].

An important design concern for the arcjet cathode is the minimization of electrode erosion, which is caused primarily by evaporation of the cathode material in the high temperature arc attachment region. Satellite stationkeeping missions for low power arcjets dictate a minimum life of 600 hours of operation, and the required operational lifetime of higher power arcjets may be 1000 hours or more. It is therefore necessary to ensure that electrode erosion over many thruster firings and many hours of use does not degrade system performance or result in failure of the arcjet itself. Experiments performed by Curran and Haag[22], Deininger et al.[27], and Mankins et al.[72] indicate that cathode mass loss rates are on the order of 0.05-0.15mg/hr for 1-2kW arcjets and 1-3mg/hr for 30kW arcjets. The loss rate increases with current and decreases with continuous firing time, and it is also a function of the propellant gas, cathode material, and cathode geometry (which determines the local heat transfer characteristics). Based on tests of a wide range of refractory metals and impregnated cathodes, 2% thoriated tungsten is at this point the cathode material which shows the lowest erosion rate while providing good thermionic performance. Long duration (1000 hour) life tests of low power arcjets have shown that cathode erosion is low enough to meet mission requirements, but further testing is necessary to determine whether the same is true at high power levels.

Arcjet anodes are designed to be passive collectors of both the arc current and the recombination energy of the current-carrying electrons. Experimental data for arcjet thrusters indicate that anode current attachment is effectively diffuse in nature, a result of either a diffuse attachment mode or a time-averaged effect of multiple moving arc feet or a single rapidly moving constricted arc. Macroscopic and microscopic examinations of anode blocks after testing as well as data taken during thruster operation indicate that for at least some arcjet geometries, power levels, and propellants the mode of anode attachment is diffuse[106]. Spot attachment during startup can cause significant localized anode erosion and deposition of molten cathode material on the relatively cool nozzle wall, but generally once steady behavior is achieved the diffuse attachment mode prevails. Some anode materials such as TZM show susceptibility to chemical erosion with hydrazine propellant, and the most robust anode material at this time appears to be pure tungsten. While some erosion of the anode surface does occur under normal operating conditions, the mass loss rate is typically much lower than at the cathode tip. The voltage drop in the near-anode region ($\triangle V_a$) is composed of a voltage drop due to anode energy deposition from heat conduction and electron impact plus an anode sheath voltage drop, which may be positive or negative depending on the magnitude of the collected current density. a few volts for radiation-cooled thrusters, while a near-anode voltage drop consistent with the recombination length of electrons is associated with the electron energy transmitted to the anode surface.

1.3 Thesis Overview

Electrothermal arcjets will soon be tested in space for the stationkeeping of geosynchronous satellites. Although a large body of experimental data has been compiled for these thrusters, questions remain concerning the details of their operation. The effect of physical processes such as viscosity, diffusion, nonequilibrium dissociation and ionization, and thermal nonequilibrium on the behavior of the electric arc and on overall performance must be better understood in order to continue thruster design improvements. Due to the difficulty in obtaining experimental measurements of these quantities in the confined, high temperature regions of arcjet constrictors, this task has fallen to numerical simulation. Unfortunately, simulations have yet to produce a consistent two-dimensional description of the internal flow of an arcjet along with sufficiently accurate comparisons to experiment. The physics of arc attachment at the anode are particularly problematic and at the same time very important since they dictate the discharge voltage and hence the efficiency of an arcjet thruster. No simulation has yet managed to self-consistently model this process. The goal of this thesis is to develop a detailed model of the gasdynamic flow in an electrothermal arcjet which includes all the relevant physical processes. Finite difference techniques are used to discretize and numerically solve the resulting multifluid, nonequilibrium set of Navier-Stokes equations for realistic arcjet thruster geometries. Comparison of the model results to experimental data for hydrogen propellant shows that thrust, voltage, and efficiency are accurately predicted, and an examination of the interior flow distributions reveals the underlying mechanism of anode current attachment. Ultimately, this model will be used as a tool to identify methods by which to improve arcjet thruster performance.

The current status of arcjet research is described in Chapter 2 of this thesis. Experimental measurements of global performance, electrode erosion, and temperature, density, and velocity distributions in thruster plumes are detailed as well as recent attempts to determine current and heat flux distributions on the anode surfaces and temperatures in arcjet constrictors. Next the analytical and numerical models developed thus far to simulate arcjet flows are summarized and critiqued. Based on the known shortcomings of these models and a knowledge of what the dominant effects in each region of an arcjet thruster should be, the governing equations of the model of this research are derived in Chapter 3. In addition, models of important physical effects such as nonequilibrium dissociation and ionization, ambipolar diffusion, collisional energy transfer, and the forms of the transport coefficients are described. Chapter 4 presents the numerical methods used to solve the governing equations of the model. Relevant details such as boundary conditions, stability, numerical smoothing, and convergence behavior are also discussed. Verification of the model and an in-depth discussion of results for one baseline case are presented in Chapter 5. Chapter 6 extends experimental comparisons to a range of operating conditions and identifies trends in the simulation results. A model of the heat balance in the anode and thruster assembly is derived in Chapter 7 for a particular radiation-cooled arcjet design. This model is then combined with the flow model of Chapter 3 to provide a better estimate of inlet gas and anode wall temperatures. These new temperatures are then used as new boundary conditions in the flow simulation in order to produce a more self-consistent results with respect to anode thermal losses. Chapter 8 contains a linearized stability analysis of the near-anode attachment region to investigate whether instabilities are present there. Finally, conclusions and recommendations for further work are presented in Chapter 9. A number of appendices are included which summarize physical data, experimental measurements, and numerical results. The structure of the computer code and instructions for compiling and running the program are also described in an appendix.

Chapter 2

Previous Research

Research on arcjet thrusters began in the late 1950's and early 1960's, progressing from simple analytical models and unconstricted arc experiments to fully designed arcjet thruster prototypes which were extensively tested at many operating points for relatively long firing durations. By 1966, however, nearly all work on arcjets had been discontinued due to lack of an appropriate mission. At that time insufficient power was available in space to make arcjet thrusters a viable propulsion option for satellite stationkeeping or orbital maneuvering. Some low-level analytical and numerical work continued, especially as a derivative of ongoing arc heater research. It wasn't until the mid-1980's, however, that arcjet research began again in earnest. By that time the communications satellite and defense/intelligence satellite industries had grown to the point where electric propulsion devices such as arcjets could be used to obtain much greater performance than current monopropellant stationkeeping thrusters. The growth in size of the newer satellites and their demand for greater power eventually made it possible for 1-2kW of electric power to become available for periodic firings of electric thrusters. In the last ten years many different experimental programs have been started around the world, and numerical simulations of arcjets have become increasingly more complex and accurate. With the coming of Space Station Freedom, or at least a smaller periodically-tended derivative, and renewed interest in space nuclear power sources such as the SP-100 and Topaz 100kW class reactors, potential uses for arcjet thrusters will increase even more substantially in the next few decades. The first flight test of a low power arcjet thruster is scheduled to take place this year on a GE communications satellite.

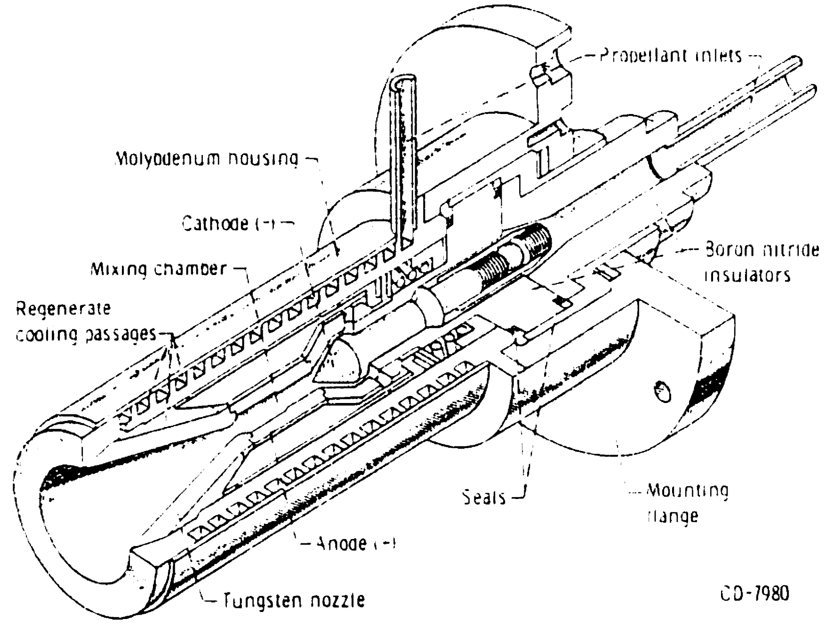

Figure 2.1: Cutaway View of 30kW Regeneratively-Cooled Giannini Arcjet Thruster (from Todd and Sheets)

2.1 Experimental Work

During the 1960's, experimental arcjet thruster research was undertaken primarily by three companies in the U.S.: Giannini Scientific/Plasmadyne, General Electric, and Avco. Efforts at Giannini focused on the development of 2kW and 30kW radiation-cooled and regeneratively-cooled arcjets using hydrogen as propellant[31, 116]. Figure 2.1 shows a cutaway view of the 30kW regeneratively-cooled Giannini design. Measurements of thrust, specific impulse, efficiency, arc chamber pressure, and power radiated were taken while the 30kW arcjet was life tested to a duration of 500 hours. At General Electric a 30kW radiation cooled AC arcjet was constructed and tested with hydrogen and ammonia propellants[96]. Work at Avco produced water-cooled and radiation-cooled 30kW arcjet thrusters which were also tested with hydrogen and ammonia[56, 58]. In addition to thrust, specific impulse, and efficiency data, electrode erosion measurements were made. Also, spectroscopic measurements taken through a quartz window in the constrictor indicated that the core temperature was greater than 20,000°K. Basic trends in performance data were verified by these early experiments. For example, the negative slope of the voltage-current characteristic, seen in earlier DC arc discharge columns, was also found in arcjet thrusters up to a certain current level, beyond which the voltage remained nearly constant. This occurs primarily because the conductivity of the breakdown gas increases as the current is increased.

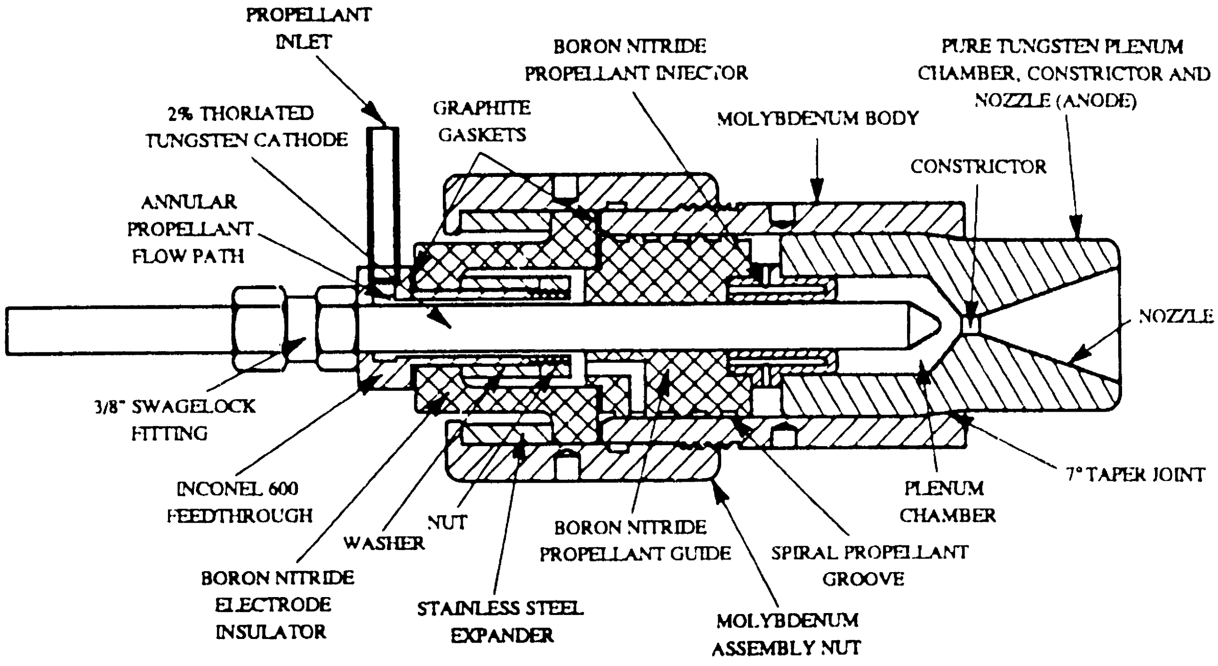

Figure 2.2: JPL 30kW Class Ammonia Arcjet Design (from Polk and Goodfellow)

In the mid-1980's, the Jet Propulsion Laboratory began testing a 30kW radiation-cooled ammonia arcjet. The design of this thruster, pictured in Figure 2.2, is typical of most radiation-cooled arcjets in use today. Initial studies focused on optimizing the design with respect to cathode placement, cathode tip geometry, and nozzle contour[26]. Test data from this thruster illustrates some important characteristics of arcjet operation[41]. The voltage-current curves in Figure 2.3 display the characteristic negative slope, and the voltage is seen to increase with increasing mass flow rate. This is due to the increased difficulty of the arc in penetrating the cooler outer layer of gas flow as the flow rate in that region increases, since the heat diffusivity ($\alpha = \frac{\kappa}{\rho c_p}$) is inversely proportional to density. The plots of specific impulse versus input power not surprisingly show a positive slope, and it can be seen that increasing the mass flow rate decreases the I_{sp} of the device. When the specific impulse is graphed against the specific power ($P/\dot{m}$), however, the data tends to collapse onto one curve for a given thruster geometry and propellant. Long duration endurance tests of 600 to 1500 hours showed that the primary failure mechanism is cathode tip erosion and damage to the anode surface between the constrictor midpoint and a point one constrictor length into the nozzle[89, 90]. Anode damage due to deposition of molten cathode material and tracking of the arc foot was discovered, and the boron nitride injector eventually experienced erosion and fracture. Effective thruster lifetime was observed to decrease roughly linearly with increasing current.

Experimental arcjet investigations at the NASA Lewis Research Center began in

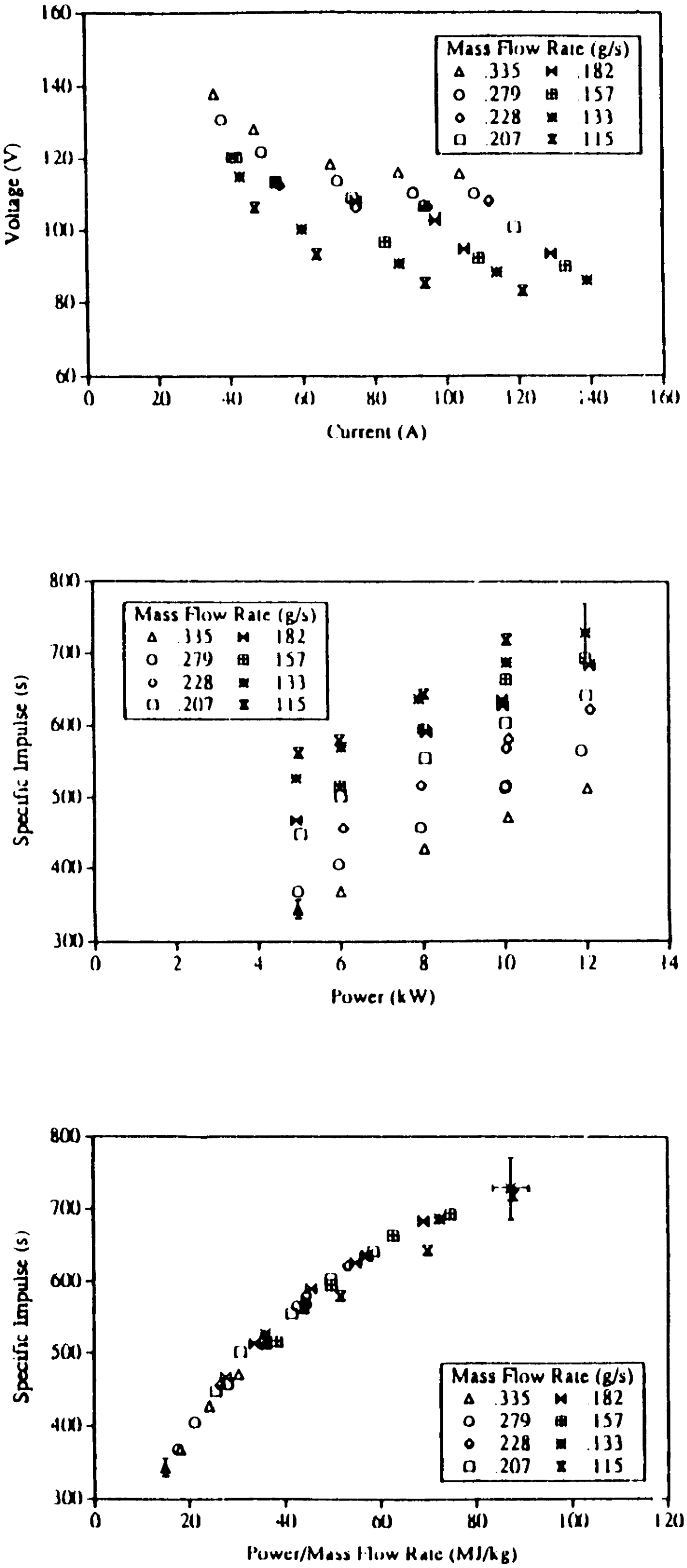

Figure 2.3: Voltage and Specific Impulse Data From 30kW Class Ammonia Arcjet (from Goodfellow and Polk)

1984 with the resurrection of the Giannini 1kW class radiation-cooled thruster[19, 83]. An intact arcjet from the Giannini laboratory was tested with hydrogen, nitrogen, ammonia, and hydrazine propellants. Voltage, thrust, and efficiency were measured over a range of currents and mass flow rates. Based on the experienced gained with this initial testing, a new low power arcjet was designed and evaluated with ammonia and hydrazine propellants[20, 45]. Results of a 1000-hour life test showed some cathode degradation and microcracks and molten material on the anode surface, but to no greater extent than seen in short-duration tests. Electrode degradation was therefore determined not to be life-limiting over realistic mission lifetimes for this arcjet thruster. A number of design evaluation experiments have been performed on the NASA Lewis low power arcjet. Five different nozzle configurations were tested to determine their effect on thrust and propulsive efficiency[21]. Sharply contoured bell-shaped nozzles were found to produce the lowest performance of the configurations tested, while a short trumpet-shaped nozzle generated the same thrust as the baseline nozzle but at a 25% higher discharge voltage and hence lower efficiency. A test of three different constrictor diameters showed that smaller constrictors could produce a modest 1-2% increase in efficiency[23]. Comparisons between similar radiation-cooled and water-cooled arcjets showed that a significant 10-15% increase in specific impulse could be achieved through regenerative heating with the radiation-cooled design[102]. Since higher voltages were produced by the water-cooled arcjet, the superiority of the radiation-cooled design was even greater in terms of overall efficiency. Finally, a thruster with five electrically insulated anode segments was tested to determine the current distribution on the anode[24]. Measured discharge voltage was about 35V higher than with the solid anode baseline low power arcjet, but trends versus current were similar. The current was observed to attach fairly evenly over the anode; as the mass flow rate was increased, the bulk of the current attached further downstream in the nozzle. More recently, NASA Lewis researchers have developed a higher power 30kW class radiation-cooled arcjet very similar in design to the TT1 arcjet built previously at the University of Stuttgart[44]. Performance data was recorded for hydrogen using a nozzle similar to that used at Stuttgart and also for two additional conical nozzles - one longer than and one shorter than the baseline configuration. Results of the three nozzle configurations were somewhat mixed because each also used different constrictor geometries, but it appeared that narrower constrictors and shorter nozzles improved performance.

Rocket Research Company has been working toward a flight-qualified, low power, radiation-cooled hydrazine arcjet for stationkeeping use on geosynchronous satellites. Initially, a design optimization program was begun with a research and technology grant from NASA Lewis[60]. Parametric performance studies were undertaken with respect to cathode and constrictor geometry, applied current, mass flow rate, and electrode materials in the 1-3kW power range. Subsequent funding from General Electric was used for flight qualification of an arcjet thruster system to be used on the new GE 7000 Telstar 4 series of communications satellites[61, 107]. Qualification involved thermal and vibrational tests, an 800-hour life test, an 800-firing startup test, power conditioning unit (PCU) efficiency tests, leakage tests, and a system mass minimization requirement. Launch of the system is scheduled for 1993.

An extensive electric propulsion laboratory has been built at the University of Stuttgart in Germany, and arcjet thrusters with various propellants have been tested at power levels from 1-80kW. The first design to be implemented was that of the TT1 water-cooled 15kW class arcjet[33]. The anode of this thruster is segmented, with three segments upstream of the constrictor, one segment in the constrictor, and four segments in the nozzle. Both the current and heat flux into each segment can be measured. Performance data such as voltage, thrust, efficiency, and chamber pressure has been recorded over a range of currents and mass flow rates for argon, nitrogen, hydrogen, and hydrazine propellants. In general, arc attachment was observed to occur upstream of the constrictor for argon, in the constrictor and the first portion of the nozzle for nitrogen and hydrazine, and in the first 20-30% of the nozzle for hydrogen. Experiments were also conducted with a quartz window in the constrictor, which allowed for measurements of the arc diameter and estimations of the arc temperature by spectral analysis[37]. Core temperatures of $12,000 - 28,000^{o}$K and arc edge temperatures of $5,000 - 10,000^{o}$K were calculated depending on the propellant, operating point, and axial location. A similar radiation-cooled 15kW class TT1 arcjet has been constructed and fired with hydrogen and hydrazine propellants[35]. In addition to performance measurements, temperatures at three different points on the outer casing of the radiation-cooled arcjet were measured during thruster operation[36]. A 1kW radiation-cooled hydrazine arcjet named ARTUS and a 50kW water-cooled hydrogen arcjet named HIPARC have also been constructed and tested[39, 63]. The high power arcjet has a four-segment nozzle like the water-cooled TT1 thruster, allowing for measurement of the current and heat flux to each segment. At a mass flow rate of 0.1g/s, 50% of the current attached in the first nozzle segment and 80% in the first two segments. As the mass flow rate was increased, the current was observed to spread out over the entire nozzle, as would be expected.

Two research groups in Japan have developed experimental arcjet programs, one at the Institute for Space and Astronautical Science (ISAS) and a joint venture between

Osaka University and Ishikawajima-Harima Heavy Industries. At ISAS a low power (1-3kW) radiation-cooled hydrazine arcjet was designed and tested with voltage, specific impulse, and thermal efficiency measurements taken[122]. At Osaka/IHI, both a low power radiation-cooled and a high power water-cooled have been tested[111, 112, 123]. The low power thruster was run through a 50-hour life test and a 600 shot multiple startup test with hydrazine propellant in order to assess electrode erosion rates and identify possible failure modes. A variety of propellants (argon, helium, nitrogen, and hydrazine) were tested with the high power arcjet and voltage, specific impulse, and efficiency were measured for each. Anode arc attachment was observed to occur upstream of the constrictor for argon, and in or beyond the constrictor for the other propellants. One design incorporated a quartz window upstream of or inside the constrictor through which transmission spectra were used to estimate excitation temperatures. Temperatures of 10,000°K were measured in the plenum chamber and 7000 - 13,000°K in the constrictor for argon and nitrogen.

In the last few years an experimental arcjet program has been undertaken jointly by the University of Pisa and BPD in Italy[17, 18]. Both low power (1kW) and medium power (3-10kW) radiatively-cooled arcjet prototypes have been constructed and tested. The medium power thruster was run with argon and nitrogen propellants. Voltage-current characteristics were recorded and anode temperatures were measured, ranging from $1000^{o}K$ at 3kW to $1500^{o}K$ at 10kW. The low power arcjet thruster was tested with ammonia and hydrazine, and bulk performance parameters such as voltage, thrust, and efficiency were measured over a range of currents and mass flow rates. A 300-hour endurance test was also completed, after which cathode and anode erosion measurements were taken and the electrode surfaces were characterized.

Over the past six years a number of studies have been undertaken to measure the number density, temperature, and velocity distributions in arcjet thruster plumes. Several techniques, including plasma probes, emission spectroscopy, and laser induced flourescence (LIF), have been demonstrated. Manzella and Capelli used atomic absorption spectroscopy to measure the ground state atomic hydrogen number density in a 1kW hydrogen arcjet[74]. A peak number density greater than $3 \times 10^{19} m^{-3}$ was indicated in the core of the plume. Velocity measurements in a low power hydrogen arcjet plume were made by Liebeskind et al. using LIF[68]. They calculated an axial velocity profile which peaked at 13,000m/s on the axis 0.13 diameters from the exit plane. Electron temperature and number density profiles over the exit plane of a 10kW hydrogen arcjet were obtained by Hoskins et al. with emission spectroscopy[51]. Calculated electron temperature varied only from 0.2eV at the nozzle wall to 0.35eV at the centerline, while electron number peaked at approximately $4 \times 10^{20} m^{-3}$ on the centerline. Plume characterization of a 1kW ammonia arcjet was performed by Lichtin, Janson, et al. using emission spectroscopy and a time-of-flight mass spectrometer[55, 67]. Peak N_2 velocities of 6000m/s, N_2 translational temperatures of 3000 – 4000°K, and NH rotational and vibrational temperatures of 3000 – 7000°K were measured. Velocity measurements in a 30kW ammonia arcjet by Pivirotto and Deininger indicated a peak axial velocity of 21,000m/s at a specific impulse of 800 seconds[88]. The plume of a low power hydrazine arcjet was investigated by Manzella, Sankovic, et al. at NASA Lewis Research Center[73, 101]. Electron temperatures of 0.2-0.3eV and electron number densities of $10^{16} - 10^{17} m^{-3}$ were calculated 3-15cm downstream of the exit plane. An electron number density of $2 \times 10^{19} m^{-3}$ and rotational temperatures of 750°K, 1750°K, and 2500°K for N_2, N_2^+, and NH respectively were measured at the thruster exit plane.

2.2 Analytical and Numerical Models

The theoretical and numerical analysis of electrothermal arcjet thrusters has lagged behind experimental work ever since the inception of the field some thirty years ago. This is due primarily to the complexity of the physical processes involved, which makes analytic insight difficult and numerical simulation time-inefficient and costly depending on the available computing power and the complexity of the code. The widespread availability of computers in the late 1960's and 1970's allowed significant progress to be made using semi-analytic and simplified numerical methods. Recent advances in detailed numerical modeling including the results of this research have been made possible by the introduction of successively faster, smaller, and less expensive computer workstations over the last 5-10 years.

2.2.1 Semi-Analytic Techniques

Much of the early analytical work on arcjets was performed by R.R. John et al. at Avco Research and Advanced Development[57]. Using one-dimensional modeling in which the flow was divided into three regions (arc core, transition, and outer flow) and drawing upon experimental data from 30kW arcjet testing, the basic principles of thermal energy addition were identified and examined. In addition, the importance of loss mechanisms such as frozen flow losses, nozzle wall drag, flow nonuniformities, finite area ratio effects, angular momentum losses, and power radiated from the anode were estimated.

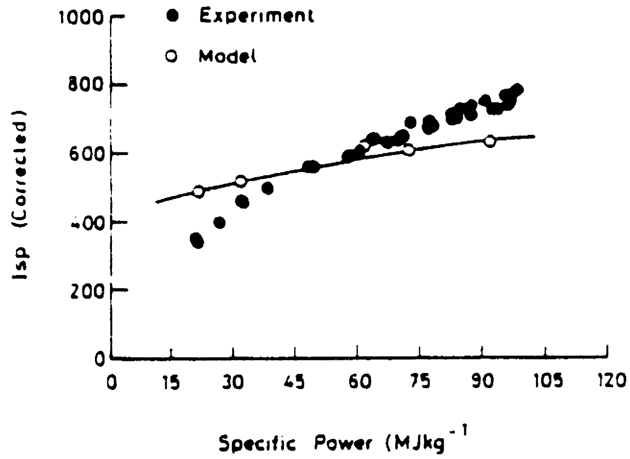

Figure 2.4: Comparison of Predicted and Experimental Specific Impulse for a 30kW Class Ammonia Arcjet (from Spurrett and Bond)

More recently, Spurrett and Bond have derived a one-dimensional arcjet thruster model at Culham Laboratory in England[109]. This model is composed of axial mass, momentum, and energy conservations equations, a dissociation reaction rate equation, and the thermodynamic relationships for the propellant. Hydrogen, nitrogen, and hydrogen-nitrogen mixtures such as hydrazine are simulated, but since the model predicts peak gas temperatures of only 6000°K nitrogen dissociation is ignored. Wall friction and conductive heat loss are estimated based on the assumption of fully developed flow, and radiation losses are also calculated. The model can be reduced to two ordinary differential equations, one for the flow velocity and one for the degree of dissociation. These equations are simultaneously integrated downstream with heat addition based on the run parameters until the flow becomes choked, signaling the sonic point and the end of the constant-area constrictor. No heat addition is included beyond the sonic point, as the arc is assumed to have attached to the anode wall at that point. Once a solution is obtained by space marching from a set of initial conditions, the initial total pressure is varied until the choked mass flow rate matches that of the experimental data for comparison. The program was first validated by comparing to analytic results for heat addition in a constant area channel with and without friction. Arcjet results were then obtained for ammonia at 5-30kW and for hydrogen and hydrazine at 1-3kW. Figure 2.4 shows that predicted specific impulse increases with specific power for the ammonia propellant case, but at a lower slope than that presented by the experimental data. For each of the propellants, predicted specific impulse and efficiency are in error by as much as 25-50%, and the model is probably too simplistic to expect closer agreement with experimental results.

At the University of Stuttgart, Glocker, Schrade, and Sleziona have constructed a dual channel model of an arcjet thruster in which the solution is space-marched from the constrictor inlet to the nozzle exit with radial profiles determined at each axial station from integral relations[34]. Separate but coupled calculations are made in the inner arc core and in the outer cold gas flow in the constrictor. Within the constrictor, the core velocity is assumed to be sonic and the cold gas velocity is calculated by assuming the outer flow is adiabatic. Calculations are made with hydrogen, ammonia, hydrazine, and argon as propellants. Only equilibrium ionization is modeled, however, so that in the first three cases the molecular components are assumed to be completely dissociated. Temperatures in the arc core are determined by an energy equation which includes ohmic heating, radial heat conduction, and radiation. In the outer cold gas flow the temperature is calculated by balancing the energy conducted outward from the arc with the enthalpy convected downstream. The pressure is assumed to be constant radially over both regions, and the mass flow rate at each axial station is enforced in an integral manner in order to determine the remaining flow properties at each point. The arc is assumed to attach at the constrictor exit, so that there is no additional heating in the nozzle. In the nozzle the flow is considered frozen and the inner and outer axial velocities are determined by performing an analytic quasi-1D expansion. Example calculations for hydrogen in the TT1 arcjet thruster are shown in Figure 2.5. As was the case with the model of Spurrett and Bond, predicted performance trends are in the right direction, but the predicted slope is incorrect. The accuracy of the model ranges from 0-50%, but that is predicated on fitting one point of each curve in Figure 2.5 with the experimental data. Thus the predictive accuracy is even worse. Discharge voltage is calculated by way of a power balance between the enthalpies of the inner and outer flows and the electrical power input. Compared to experiment, the predicted voltage is high by 10-20%. This model predicts trends in experimental data with curve fitting to some degree. The neglect of too many physical processes, however, such as dissociation, current attachment, and convection in the core to name a few, severely limits its applicability.

Martinez-Sanchez has also developed a two stream type of quasi-1D model at M.I.T.[77]. The inner arc core and the outer gas flow regions are analyzed separately, but they are connected by the assumption that the enthalpy flux of the arc is the difference between the enthalpy at the outer edge of the arc and the enthalpy in the colder gas flow multiplied by the rate of increase of the mass flow rate in the arc region. That is, the arc expands radially as heat conducted outward is absorbed by gas in the outer flow region flowing into the arc. Integral relations are established in the radial direction to obtain averaged values of the flow variables, and the pressure is assumed

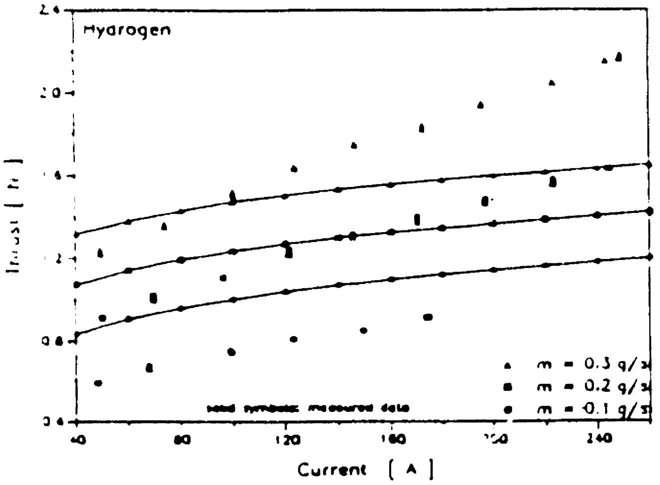

Figure 2.5: Comparison of Predicted and Experimental Thrust for TT1 Hydrogen Arcjet (from Glocker et al.)

to be constant over the cross-section. In the arc core ohmic dissipation and radial heat conduction are considered, while outside the arc the flow is assumed to behave isentropically. The gas is assumed to be in equilibrium with linear relationships between the enthalpy, internal energy, heat flux potential, and electrical conductivity. The solution is integrated axially by a fourth order Runge-Kutta scheme until the sonic point is reached. By varying the total pressure at the inlet, the location of the calculated sonic point is varied until it matches the position of the constrictor exit for the thruster being simulated. In the nozzle, arc heating is turned off and the flow is assumed to be frozen. Comparisons are made to arcjet thrusters over a wide range of power, for hydrogen and hydrazine propellants, and for both water-cooled and radiation-cooled designs. The current attachment point, temperature of the anode wall, and voltage drop at the anode are all specified by the user to best match experimental data for a given thruster and propellant. Specific impulse is accurate to within 1-25% and voltage to within 1-40% of experimental data, erring high or low depending on the operating point and the thruster being modeled. Considering the wide range of applicability and the simplicity of this model, it does well in predicting trends in data and for some cases in accurately predicting performance.

2.2.2 Simplified Axisymmetric Numerical Schemes

The first significant numerical arcjet model was that developed by Watson and Pegot at NASA Ames Research Center in 1967[120]. This program calculates the characteristics of a gas flowing axially through a constricted arc, so it is applicable to the constrictor region of an arcjet thruster. The flow is assumed to be axisymmetric and the electric potential is assumed to be constant perpendicular to the axis of symmetry. Convection, radial heat conduction, ohmic heating, radiation, and viscous shear are incorporated in the model, and the transport coefficients and enthalpy are determined by equilibrium tabulations as a function of temperature and pressure. The governing equations are an energy equation and an axial momentum equation, and continuity is ensured by iteration at each axial location until the proper mass flow rate is attained. The computational domain is divided into a number of concentric cells in the radial direction, and the solution is space-marched from an initial set of conditions to the constrictor exit, which is defined as the point at which the flow becomes aerodynamically choked. The arc is carried only by those cells with temperatures above a threshold required for electrical conduction. Results are presented for large diameter (1cm) constrictors at pressures between one and two atmospheres for hydrogen and nitrogen propellants. Simulated axial arc voltage gradients and mass-averaged enthalpies follow parametric trends in experimental data, even though accuracy varies considerably. This model delivers good insight on the constrictor physics for its relative simplicity, but it suffers substantially in terms of predictive accuracy. Most importantly, no details of the arc attachment at either electrode are incorporated, and global performance cannot be predicted since no nozzle calculations are made.

Andrenucci et al. have recently applied the model of Watson and Pegot to 1kW class hydrogen arcjets through the development of a computer program at the University of Pisa and Centrospazio[3]. No comparisons to experiment have been made, but future work is expected to include the addition of a gas dynamics code to calculate the flow in the diverging nozzle. The authors note that the solutions obtained are strongly dependent on the starting conditions given at the inlet of the constrictor. This leads one to question the reliability of future results unless some model is included which describes the initiation of the arc at the cathode tip.

An axisymmetric model of the flow in an argon plasma torch has been developed by Kovitya, Scott, and Haddad at the CSIRO Division of Applied Physics in New South Wales[62]. While the operating point of the plasma torch is different from that of most arcjet thrusters (1 atm ambient pressure, subsonic flow, argon or air as a plasma source), the model developed by these authors can be applied with modifications to both. Governing equations are derived for the global density; radial, axial, and azimuthal global momentum; energy; and electric potential. The gas is assumed to be in local thermodynamic equilibrium and ohmic dissipation, viscous shear, heat conduction, and radiative transfer are incorporated. The equations are discretized using a control volume approach and solved by a line iterative method. The electric arc is assumed to initiate at a cathode spot and attach at a prescribed anode spot. Artificially high gas temperatures are specified at each attachment point in order to allow stable and fixed arc behavior. Results are obtained for laminar and turbulent flow and compared to experiment for a range of currents and mass flow rates. Discharge voltage is found to underpredict experimental results by about 40%. Efficiency is predicted but no corresponding experimental data are provided.

2.2.3 Advanced Numerical Simulations with Complex Physics

Pawlas and Keith have begun work on a viscous, equilibrium, swirling, axisymmetric arcjet flow model at the University of Toledo[86]. The governing Navier-Stokes equations with viscosity and heat conduction are modified to include ohmic heating and radiation, and a magnetic field equation is incorporated. The equations are nondimensionalized and transformed to natural coordinates, whence they are solved by MacCormack's flux-split, implicit, line Gauss-Seidel algorithm. At present only cold flow (arc off) solutions have been obtained, but the results are sufficiently detailed to show the oblique shock which is generated by the anode wall discontinuity at the constrictor exit. Centerline Mach number predictions compare very well with experimental data, and Reynolds number and swirl effects are described. It remains to be seen, however, whether the numerical model can successfully handle the electric effects, which so drastically alter the flow behavior.

Okamoto, Nishida, and Tanaka have begun work on a viscous, nonequilibrium, axisymmetric arcjet flow model at Kyushu University based on earlier experience modeling MPD thrusters[84]. The model includes equations for the global density, radial and axial global momentum, energy, and electron density. Viscosity, heat conduction, and ohmic dissipation are incorporated. The governing equations are transformed into natural coordinates and then integrated via a hybrid TVD-MacCormack scheme. A potential equation is concurrently solved based on the updated flow properties at each time level. In this model, the potential is fixed at both electrodes and the current distribution is allowed to evolve according to the governing equations. Results are obtained with argon, but thus far only at power levels below 140W, that is with little or no current. Numerical instabilities occurred at higher power levels. The maximum ionization fraction in the thruster was 5×10^{-5}, while a maximum gas temperature of 3000^oK was reported. Clearly this model suffers from numerous numerical and problems, and thus far it is capable of predicting the interior flow only under arc-off conditions.

At Rocket Research Company, Butler and King have developed an inviscid axisymmetric arcjet flow model with finite rate chemistry and have used the computer program to simulate low power nitrogen and hydrogen arcjet thrusters[14, 15, 59].

Governing equations of the model include a global continuity equation, two species continuity equations, radial and axial momentum equations, an energy equation, and a magnetic field equation. Physical effects such as ohmic heating, viscous dissipation, Bremsstrahlung radiation, thermal conduction, and finite rate chemistry are incorporated, and realistic geometries are simulated. The governing equations are solved by a semi-implicit, total variation diminishing (TVD), finite volume scheme which includes both Eulerian and Lagrangian integration phases. This numerical solver was originally developed at Los Alamos National Laboratory to solve magnetohydrodynamic (MHD) flow problems. Simulation results have been compared to experiment for both hydrogen and nitrogen. Figure 2.6 shows velocity and Mach number distributions for a typical nitrogen simulation. For nitrogen, the model was found to overpredict discharge voltage by a factor of two. Thrust and efficiency were not compared to experiment beyond the fact that they seem to follow similar trends with respect to specific power ($\frac{P}{\dot{m}}$). For hydrogen, similar problems were found with respect to voltage overprediction. The problems were overcome by a heuristic "fix" in which a minimum electrical conductivity was imposed in order to alter the anode current attachment pattern. Figure 2.7 shows the effect of the specified conductivity floor on the simulation results. Although this fix allowed the predicted voltage to become more in line with the experimentally determined value, specific impulse was still being overpredicted by as much as 20% and the current was observed to attach throughout the constrictor and nozzle walls (Figure 2.8), which does not correlate with experimental measurements of arc-induced heat transfer to the anode surface for hydrogen. This model produces good qualitative results for a range of arcjet operating parameters, but it suffers quantitatively from the neglect of several important physical processes. A second energy equation for the electrons could eliminate the need for an electrical conductivity "floor" by allowing increased electrical conduction and ionization in the arc attachment region. This would also promote a more concentrated anode attachment and therefore a lower discharge voltage. Performance predictions could be significantly improved by including viscous shear and ambipolar diffusion in the governing equations and also by the separation of the electron and heavy species temperatures.

Rhodes and Keefer have constructed a viscous, equilibrium, axisymmetric arcjet flow solver at the University of Tennessee Space Institute[93, 94, 95]. Governing equations include the global continuity, global momentum (radial, axial, and azimuthal), energy, and magnetic field equations. Ohmic dissipation, viscosity, heat conduction, and radiation are included and the equations are solved by a semi-implicit procedure. The assumption of equilibrium composition presents a serious problem in the outer

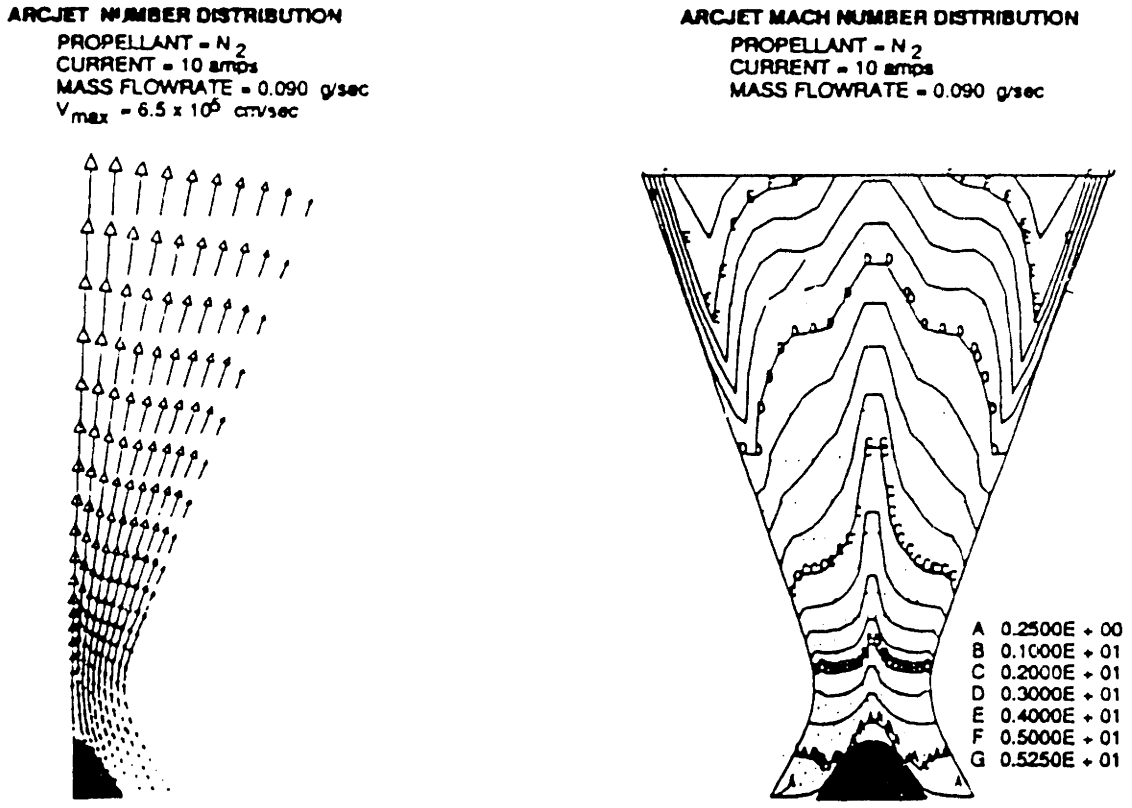

Figure 2.6: Predicted Velocity and Mach Number Distributions for Nitrogen Propellant (from Butler and King)

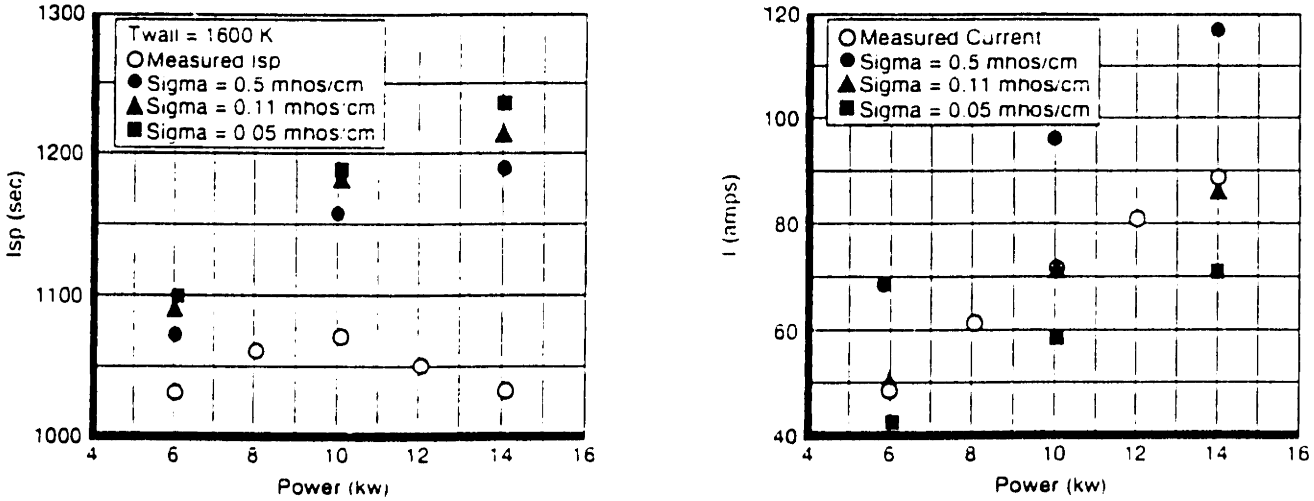

Figure 2.7: Effect of Electrical Conductivity Floor on Hydrogen Arcjet Performance Predictions (from Butler and King)

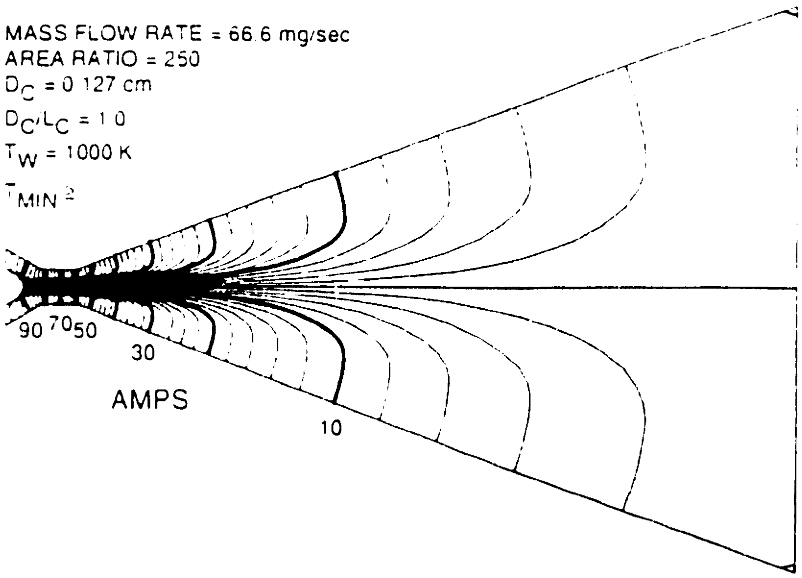

Figure 2.8: Predicted Current Distribution in a 10kW Hydrogen Arcjet (from Butler and King)

cooler gas flow because the temperature is too low to provide the necessary charge carriers for electrical conduction. This model therefore requires several fixes in order to allow current penetration of the outer layer and attachment at the anode wall. First, the electrical conductivity is modified so that an artificially high value (many orders of magnitude higher than the equilibrium value) is used by the program for temperatures less than 10,000°K. Second, a shape factor is prescribed which specifies the distributional form of the current flow. Current attachment is specified to occur evenly over the nozzle wall surface only. Finally, the local input power from ohmic dissipation is multiplied by 0.75 in order to better match experimental total power measurements. The omission of nonequilibrium effects and a separate electron energy equation to control the finite rate dissociation and ionization processes leads to severe arc modeling difficulties unless a number of arbitrary matching fixes are made. Results have been achieved for ammonia and hydrogen as propellants at power levels on the order of 20-30kW. For ammonia, discharge voltage is overpredicted by about 35% and specific impulse as a function of specific power is overpredicted by 10-15%. For hydrogen, specific impulse is overpredicted by up to 12% and efficiency is overpredicted by up to 25%, but agreement is close in some operating regions and predicted trends seem to follow experimentally observed results as a function of specific power. Figure 2.9 shows calculated axial and radial distributions of temperature and velocity for both ammonia and hydrogen at 30kW input power, while Figure 2.10 compares predicted specific impulse and efficiency to experimental data for hydrogen at a particular mass

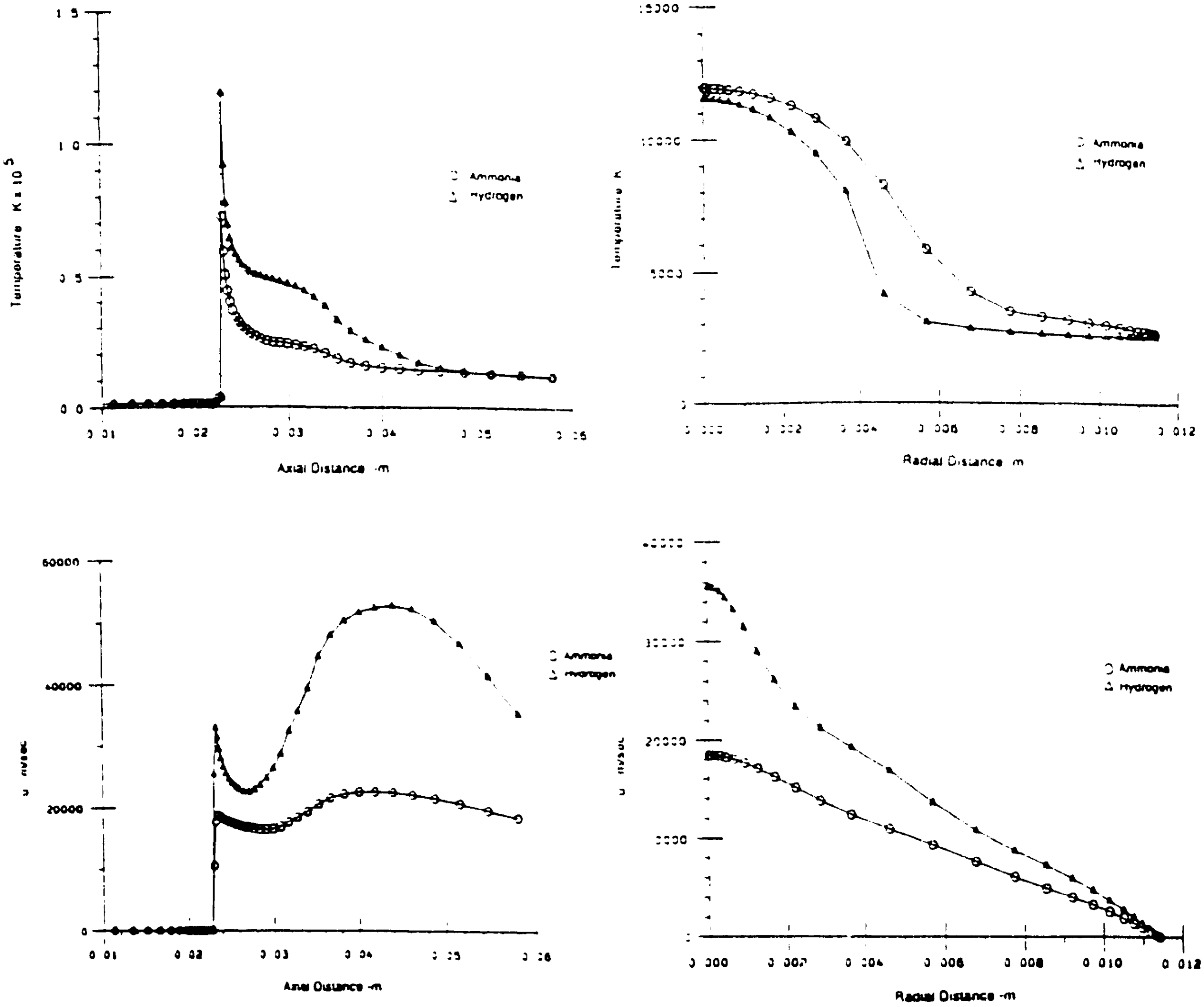

Figure 2.9: Predicted Temperature and Velocity Distributions for Ammonia and Hydrogen at 30kW (from Rhodes and Keefer)

flow rate. The results of this model could probably be brought into closer agreement with experimental data by including nonequilibrium effects, ambipolar diffusion, and more realistic current attachment boundary conditions.

2.3 Outline of This Research

As detailed in the preceding sections, a large number of experiments have been performed during the past eight years in order to document the performance of electrothermal arcjets and to try to measure flow quantities in the thruster interior and plume. Most of the impetus for arcjet design improvements has come from the empirical results

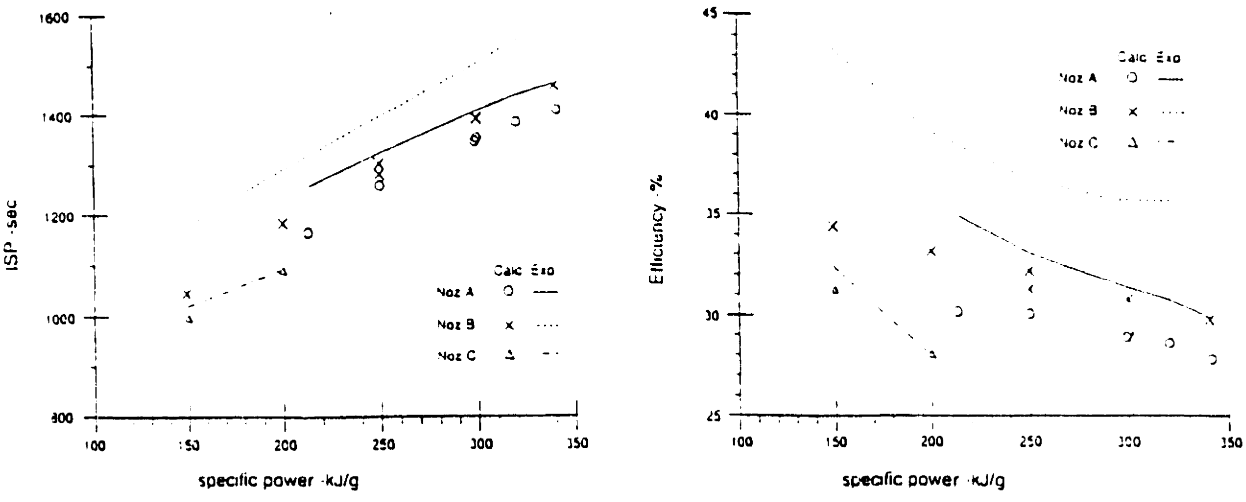

Figure 2.10: Comparison of Predicted Specific Impulse and Efficiency for Hydrogen to Experimental Data (from Rhodes and Keefer)

of these experiments. A need remains, however, to better understand the underlying physics, detailed energy balances, and transport mechanisms of these devices if we are to further optimize performance and achieve developmental maturity of the field. Unfortunately, most of the important processes occur in the high temperature region of the constrictor and nozzle inlet, which is relatively inaccessible by current diagnostic means. As a result, analytic and numerical methods have been utilized to attempt to model the gasdynamics of arcjet flows. Because many complex interacting phenomena are involved, however, analytic techniques are limited to simplified cases, from which one may obtain useful insights but inadequate predictions of thruster performance. Numerical simulations have advanced from simplified models of the constricted arc to viscous, axisymmetric models which incorporate many of the important physical phenomena. Even these detailed codes, though, fail to consistently model anode current attachment or predict performance with better than 10-30% accuracy. The focus of this research is the development of an arcjet model which overcomes these two problems in order to provide a detailed picture of the interior flow of an arcjet from which a better physical understanding of arcjet operation can be drawn.

Due to its high performance and simplicity, a radiation-cooled hydrogen arcjet is modeled by this thesis. The most significant improvement of this model over previous simulations is the use of two separate energy equations, one for the electrons and one for the other heavy species. It is postulated that ohmic dissipation in the flow outside the arc causes the electron temperature to be much higher than the gas temperature in the current attachment region, thereby providing an increased level of charge-carrying electrons through nonequilibrium dissociation and ionization. This, combined with the ambipolar diffusion of electrons from the central arc, creates a physical path for the current to pass through the cooler outer gas layer and to reach the anode wall. Incorporation of a separate electron energy equation, nonequilibrium rate terms, and ambipolar diffusion allows the model of this research to consistently simulate anode current attachment and therefore to accurately predict discharge voltage. Other physical effects such as viscous shear and heating, collisional energy transfer between species, continuum radiation, and an azimuthal "swirl" component to the flow velocity are included in the model and contribute to its excellent performance predictions with respect to experimental data. The governing equations include equations for the electron, atomic hydrogen, and global densities; the radial, axial, and azimuthal momentum; the electron and heavy species energy; the electric potential; and the temperature distribution in the anode thruster assembly. These equations are solved by MacCormack's method and successive overrelaxation, combined with the implementation of the proper boundary conditions.

In order to obtain more accurate estimates of the the inlet gas and anode wall temperatures, a thermal model of the anode and thruster assembly is constructed. Using the heat flux input to the anode wall as predicted by the arcjet flow model, the resulting temperature distribution in the thruster assembly is found. Improved estimates of the inlet gas and anode wall temperatures are then used as new boundary conditions for the flow solver in order to produce more self-consistent solutions with respect to anode thermal losses. A linearized stability analysis of the anode current attachment region is also performed. Although the mechanism for an ionization instability is identified, the arc appears to be stable for the near-anode conditions predicted by the arcjet numerical simulation.

Chapter 3

Governing Equations

3.1 Basic Equations

In general, the equations governing the gasdynamic flow in an arcjet thruster are Maxwell's Equations, the electron, ion, and neutral species conservation equations, and the equation of state.

3.1.1 Maxwell's Equations

Maxwell's equations can be written in vector form as

$$\nabla \times \vec{E} = -\frac{\partial \vec{B}}{\partial t} \tag{3.1}$$

$$\nabla \times \vec{B} = \mu_0 \left(\vec{j} + \epsilon_0 \frac{\partial \vec{E}}{\partial t} \right) \tag{3.2}$$

$$\nabla \cdot \vec{E} = \frac{e(n_i - n_e)}{\epsilon_0} \tag{3.3}$$

$$\nabla \cdot \vec{B} = 0. \tag{3.4}$$

3.1.2 Species Conservation Equations

The species conservation equations can be derived from Boltzmann's Equation, which describes the rate of change of the distribution function of a species s with respect to time and position in six-dimensional phase space ($d^3 r d^3 v$). Boltzmann's Equation can be written in vector form as in Bittencourt[9]:

$$\frac{\partial f_s}{\partial t} + \vec{v} \cdot \nabla f_s + \frac{\vec{F}_s}{m_s} \cdot \nabla_v f_s = \left(\frac{\partial f_s}{\partial t} \right)_{coll}, \tag{3.5}$$

where $\vec{F}_s$ is an externally applied force vector and the term on the right-hand side indicates the net time rate of change of the distribution function of species s due to collisions.

The first step in deriving the species conservation equations is to multiply Equation 3.5 by some function $\phi(\vec{x}, \vec{v}, t)$ which may vary with respect to position, velocity, and time. Integrating over all phase space, the general transport equation is obtained

$$\frac{\partial}{\partial t}(n_s < \phi >_s) - n_s < \frac{\partial \phi}{\partial t} >_s + \nabla \cdot (n_s < \phi \vec{v} >_s) - n_s < \vec{v} \cdot \nabla \phi >_s$$

$$- n_s < \frac{F_s}{m_s} \cdot \nabla_v \phi >_s = \int \phi \left(\frac{\partial f_s}{\partial t} \right)_{coll} d^3 v, \tag{3.6}$$

where the definition of the average value of a quantity ($<\ >$) has been used. Substituting appropriate values for the function ϕ, produces the three species conservation equations, which are closed by Maxwell's equations, the equation of state

$$p = \sum_s n_s k T_s = \sum_s \rho_s R_s T_s, \tag{3.7}$$

and phenomenological laws for the viscous stress tensor and heat flux.

Taking $\phi = m_s$ in Equation 3.6 results in the species continuity equation, which is a statement of the conservation of mass of species s:

$$\frac{\partial \rho_s}{\partial t} + \nabla \cdot (\rho_s \vec{u}_s) = S_s = m_s \int \left(\frac{\partial f_s}{\partial t} \right)_{coll} d^3 v. \tag{3.8}$$

Here the source term on the right-hand side of the equation, S_s, represents the rate per unit volume that particles of species s are created or destroyed as a result of collisional events, such as ionization or recombination.

Using $\phi = m_s \vec{v}$, the species momentum equation is obtained:

$$\rho_s \left[\frac{\partial \vec{u}_s}{\partial t} + (\vec{u}_s \cdot \nabla) \vec{u}_s \right] + \nabla \cdot \bar{\bar{p}}_s - n_s < \vec{F} >_s = \vec{A}_s - \vec{u}_s S_s. \tag{3.9}$$

The quantity $\bar{\bar{p}}_s$ is the kinetic pressure dyad, representing the scalar pressure and tangential shear forces. The source term $\vec{A}_s$ denotes the collisional rate of change of mean momentum for species s, while the term S_s is the same as that employed in Equation 3.8. Since the effect of the Lorentz force is of concern in this research, the following substitution may be made:

$$< \vec{F} >_s = q_s \left(\vec{E} + \vec{u}_s \times \vec{B} \right). \tag{3.10}$$

In addition, the collisional momentum term may be written as

$$\vec{A}_s = \rho_s \sum_s \nu_{sr} \left(\vec{u}_r - \vec{u}_s \right). \qquad (s \neq r) \tag{3.11}$$

This leads to the statement of species momentum conservation in the following form:

$$\rho_s \left[\frac{\partial \vec{u}_s}{\partial t} + (\vec{u}_s \cdot \nabla) \vec{u}_s \right] + \nabla \cdot \bar{\bar{p}}_s = n_s q_s \left(\vec{E} + \vec{u}_s \times \vec{B} \right) + \rho_s \sum_s \nu_{sr} \left(\vec{u}_r - \vec{s}_r \right) - \vec{u}_s S_s. \tag{3.12}$$

Multiplying the species continuity equation by $\vec{u}_s$ and substituting into Equation 3.12 results in the following conservative form of the species momentum equation:

$$\frac{\partial \rho_s \vec{u}_s}{\partial t} + \nabla \cdot (\rho_s \vec{u}_s \vec{u}_s) + \nabla \cdot \bar{\bar{p}}_s = n_s q_s \left(\vec{E} + \vec{u}_s \times \vec{B} \right) + \rho_s \sum_s \nu_{sr} \left(\vec{u}_r - \vec{u}_s \right). \tag{3.13}$$

Finally, the species energy equation may be obtained by substituting $\phi = \frac{1}{2} m_s v^2$ in the general transport equation. Again after some manipulation the following form is achieved:

$$\begin{aligned} \frac{D_s}{D_s t} \left(\frac{3}{2} p_s + \rho_s \frac{E_{int}}{m_s} \right) + \left(\frac{3}{2} p_s + \rho_s \frac{E_{int}}{m_s} \right) \nabla \cdot \vec{u}_s + \frac{\partial}{\partial t} \left(\frac{1}{2} \rho_s u_s^2 \right) + \nabla \cdot \left(\frac{1}{2} \rho_s u_s^2 \vec{u}_s \right) \\ + \nabla \cdot (\bar{\bar{p}}_s \cdot \vec{u}_s) + \nabla \cdot \vec{q}_s - n_s < \vec{F} \cdot \vec{v} >_s = M_s, \end{aligned} \tag{3.14}$$

where $\frac{D_s}{D_s t}$ is the substantial derivative for species s, $\vec{q}_s = -k_s \nabla T_s$ is the heat flux vector, and M_s, which represents the rate of change of energy per unit volume due to collisions, given by

$$M_s = \frac{1}{2} m_s \int v^2 \left(\frac{\partial f_s}{\partial t} \right)_{coll} d^3 v = \sum_r \frac{\rho_s \nu_{sr}}{m_s + m_r} \left[3k(T_r - T_s) + m_r (\vec{u}_r - \vec{u}_s)^2 \right]. \tag{3.15}$$

Equation 3.14 also contains terms representing additional forms of internal energy (E_{int}), such as the energy of dissociation, ionization, and vibrational excitation. This equation, however, is specific to monatomic gases. For diatomic gases, the extra degree of freedom (rotational excitation) results in an internal energy of $\frac{5}{2} p_s$ rather than $\frac{3}{2} p_s$. Substituting for the electromagnetic forces and heat flux vector and rearranging, it is found that for monatomic gases

$$\begin{aligned} \frac{D_s}{D_s t} \left(\frac{3}{2} p_s + \rho_s \frac{E_{int}}{m_s} \right) + \left(\frac{3}{2} p_s + \rho_s \frac{E_{int}}{m_s} \right) \nabla \cdot \vec{u}_s + \frac{\partial}{\partial t} \left(\frac{1}{2} \rho_s u_s^2 \right) + \nabla \cdot \left(\frac{1}{2} \rho_s u_s^2 \vec{u}_s \right) \\ + \nabla \cdot (\bar{\bar{p}}_s \cdot \vec{u}_s) - \nabla \cdot (k_s \nabla T_s) = \vec{j}_s \cdot \vec{E} + M_s, \end{aligned} \tag{3.16}$$

and for diatomic gases

$$\begin{aligned} \frac{D_s}{D_s t} \left(\frac{5}{2} p_s + \rho_s \frac{E_{int}}{m_s} \right) + \left(\frac{5}{2} p_s + \rho_s \frac{E_{int}}{m_s} \right) \nabla \cdot \vec{u}_s + \frac{\partial}{\partial t} \left(\frac{1}{2} \rho_s u_s^2 \right) + \nabla \cdot \left(\frac{1}{2} \rho_s u_s^2 \vec{u}_s \right) \\ + \nabla \cdot (\bar{\bar{p}}_s \cdot \vec{u}_s) - \nabla \cdot (k_s \nabla T_s) = \vec{j}_s \cdot \vec{E} + M_s. \end{aligned} \tag{3.17}$$

These equations may be simplified and written in a more familiar form by using the definitions of internal and total energy per unit mass:

$$E_s = e_s + \frac{1}{2}u_s^2, \tag{3.18}$$

where e_s represents the internal energy calculated by an appropriate statistical mechanical model of the molecule in question, including as necessary the translational, rotational, vibrational, excitation, dissociation, and/or ionization energies of the molecule. Then the species energy equation becomes

$$\frac{\partial}{\partial t}(\rho_s E_s) + \nabla \cdot (\rho_s \vec{u}_s E_s) + \nabla \cdot (\bar{\bar{p}}_s \cdot \vec{u}_s) - \nabla \cdot (k_s \nabla T_s) = \vec{j}_s \cdot \vec{E} + M_s. \tag{3.19}$$

3.1.3 Equation of State

The equation of state for an ideal multicomponent gas is given by

$$p = \sum_s \rho_s R_s T_s, \tag{3.20}$$

where $R_s = \frac{k}{m_s}$ is the real gas constant specific to each component gas.

3.2 Axisymmetric Arcjet Flow Model

Using the equations of Section 3.1 for the case of axisymmetric flow of a multicomponent partially ionized gas, a model of the flow in an arcjet thruster can be developed. Figure 1.2 shows a diagram of this flow. Variations in flow quantities in the θ-direction are neglected because of the axial symmetry of the model. A component of the flow velocity in the θ-direction, however, is incorporated to account for the "swirl" injection of most experimental arcjets. This injected vortex has been shown to stabilize arc attachment and to help maintain a concentrated arc along the centerline of the thruster. Although the azimuthal velocity is assumed constant in the θ-direction, it is allowed to develop in the axial and radial directions through the conservation of global angular momentum.

The model has been developed in a general enough sense so that any monatomic or diatomic propellant may be simulated. For the purpose of this research hydrogen was selected as the propellant of choice due to its low molecular weight (and therefore high performance) and simple molecular structure, which allows for analytical evaluation of the necessary transport coefficients. The use of these polyatomic gases as propellants and the extreme range of temperatures produced within arcjet devices, however, introduce two important complications of the model which extend beyond the scope of most ordinary fluid codes. First, as the gas temperature increases a dissociation process will take place, whereby the composition of the gas will change from diatomic to monatomic neutrals. This requires a chemical kinetic description of the dissociation reaction to be developed and implemented. Second, at sufficiently high temperatures the gas will ionize, requiring an equation to reflect the net effect of electron impact ionization and three-body recombination. As a result, there are four species of particles to be accounted for by the model: diatomic molecules, monatomic neutrals and ions, and electrons. Effects of the possible presence of diatomic hydrogen ions (H_2^+) are neglected. The gas is not assumed to be in dissociative or ionizational equilibrium. Instead, the net ionization and dissociation rates are computed and included as source terms in the relevant conservation equations.

The following assumptions are made regarding the state of the flow in the thruster and the physical processes involved. The plasma produced by ionizing electron collisions is assumed to be macroscopically neutral, so that $n_e = n_i$. Strong coupling is assumed between the ions and neutrals, designated together as the heavy species. This implies that $\vec{u}_i \cong \vec{u}_n \cong \vec{u}$ (except for ambipolar diffusion), and $T_i \cong T_n \cong T_g \neq T_e$. This then is a two fluid model that separately tracks electron and heavy species quantities, although transport properties can be calculated for the ions and neutrals separately and their individual velocities may be extracted in an approximate sense. Effects which are consistently incorporated include ambipolar diffusion, heat conduction, viscous shear and dissipation, ohmic heating, radiation, and collisional energy transfer between electrons and heavy species. In addition, the individual species are assumed to obey the ideal gas law.

A final assumption is that the self-induced magnetic field of the ionized gas is neglected. The main effect of the magnetic field, which delineates electrothermal arcjets from MPD thrusters, is the Lorentz acceleration of the ionized propellant. This is evidenced by a magnetic pressure term, $\frac{B^2}{2\mu_0}$, in the global momentum equations. The degree to which a thruster can be considered magnetically dominated is given by the ratio of the magnetic pressure to the fluid pressure

$$\eta_0 = \frac{B_0^2}{2\mu_0 P_0}, \tag{3.21}$$

where the zero subscript denotes the inlet values of the quantities for reference purposes. Using the fact that $B_0 = \frac{\mu_0 I}{2\pi R_c}$ (R_c=cathode radius) for a coaxial device, it is found that

$$\eta_0 = \frac{\mu_0 I^2}{8\pi^2 R_c^2 P_0}. \tag{3.22}$$

Table 3.1: Magnetic Parameter for Electrothermal Arcjets and MPD Thrusters

	TT1 Arcjet	MPD Thruster
Current	200A	30kA
P_0	1.5atm	0.01atm
R_c	2mm	5.2cm
η_0	0.001	5

Clearly the characterization of a given thruster depends not only on the power applied but also on the plenum pressure and the geometry. Table 3.1 compares η_0 for typical operating points of the German TT1 arcjet thruster[33] and the MPD thruster of Heimerdinger[47]. The effect of the magnetic field is essentially negligible for the TT1 arcjet, which is the primary thruster modeled in this research. The same can be said of other low and medium power electrothermal arcjet thrusters currently being tested. The magnetic field could be introduced into an electrothermal arcjet model as a way of incorporating a consistent set of boundary conditions for the arc current distribution, but at the cost of additional memory usage and computational time. For an arcjet, in fact, the arc boundary conditions are more easily applied through a potential formulation.

Given the aforementioned assumptions, the model can be summarized by a set of nine partial differential equations which must be solved locally in order to generate a viable simulation of the flow in an arcjet thruster. These governing equations include equations for the ion, neutral atom, and global density; the axial, radial, and azimuthal momentum; the electron and heavy species energy; and the electric potential, from which the current distribution is extracted.

3.2.1 Electric Potential Equation

The electric potential equation is derived from the electron momentum equation and Maxwell's Equations. Using the definitions of current density, $\vec{j} = en_e(\vec{u}_i - \vec{u}_e)$, and electrical conductivity (cf. Section 3.4.4), the well known generalized Ohm's Law may be obtained:

$$\sigma(\vec{E} + \vec{u} \times \vec{B}) = \vec{j} + \vec{j} \times \vec{\beta} - \frac{e}{m_e \sum_r \nu_{er}} \nabla p_e, \tag{3.23}$$

where β is the Hall parameter, given by

$$\beta = \frac{eB}{m_e \sum_r \nu_{er}}. \tag{3.24}$$

Neglecting the self-consistent magnetic field, this may be simplified to

$$\vec{j} = \sigma \vec{E} + \psi \nabla p_e, \tag{3.25}$$

where

$$\psi = \frac{e}{m_e \sum_r \nu_{er}} \tag{3.26}$$

is the electron mobility and $\sum_r \nu_{er}$ is the collision frequency of electrons with the other species present. Since the plasma is macroscopically neutral and $\vec{B} = 0$, Maxwell's equations reduce to $\nabla \times \vec{E} = 0$, $\nabla \cdot \vec{j} = 0$, and $\nabla \cdot \vec{E} = 0$. Therefore, the electric field may be written as the gradient of a scalar potential:

$$\vec{E} = -\nabla \phi. \tag{3.27}$$

With Equation 3.25 it is found that

$$\nabla \cdot (\sigma \nabla \phi - \psi \nabla p_e) = 0. \tag{3.28}$$

Written in terms of axisymmetric coordinates, the electric potential equation is then

$$\frac{\partial}{\partial r}(\phi_r) + \frac{\partial}{\partial z}(\phi_z) + \frac{\phi_r}{r} = \psi \left(\frac{\partial^2 p_e}{\partial r^2} + \frac{1}{r}\frac{\partial p_e}{\partial r} + \frac{\partial^2 p_e}{\partial z^2} \right) + \frac{\partial p_e}{\partial r}\frac{\partial \psi}{\partial r} + \frac{\partial p_e}{\partial z}\frac{\partial \psi}{\partial z}, \tag{3.29}$$

where

$$\phi_r = \sigma \frac{\partial \phi}{\partial r} \qquad \phi_z = \sigma \frac{\partial \phi}{\partial z}. \tag{3.30}$$

3.2.2 Mass Conservation Equations

From Equation 3.8, the four species continuity equations which govern the flow can be written as

$$\frac{\partial \rho_{S_2}}{\partial t} + \nabla \cdot (\rho_{S_2} \vec{u}_{S_2}) = -m_S (\dot{n}_S + < \sigma v > n_e n_{S_2}) \tag{3.31}$$

$$\frac{\partial \rho_S}{\partial t} + \nabla \cdot (\rho_S \vec{u}_S) = m_S (\dot{n}_S + < \sigma v > n_e n_{S_2} - \dot{n}_e) \tag{3.32}$$

$$\frac{\partial \rho_{S^+}}{\partial t} + \nabla \cdot (\rho_{S^+} \vec{u}_{S^+}) = m_S \dot{n}_e \tag{3.33}$$

$$\frac{\partial \rho_e}{\partial t} + \nabla \cdot (\rho_e \vec{u}_e) = m_e \dot{n}_e, \tag{3.34}$$

where the subscript S represents the propellant species (hydrogen in the case of this research), $\dot{n}_S$ represents the net rate of production of atomic species per unit volume

where D_a is the ambipolar diffusion coefficient, given by

$$D_a = \sqrt{\frac{\pi k T_g}{4 m_S}} \frac{\left(1 + \frac{T_e}{T_g}\right)}{Q_{in}(n_e + n_n)}. \tag{3.41}$$

A derivation of this particular form of the coefficient of ambipolar diffusion is presented for reference in Appendix C. Physically the process of ambipolar diffusion may be described in the following manner. In the presence of ions and electrons, this diffusion originates from the combined action of pressure gradients and electrostatic coupling between the two species. Electron pressure gradients cause diffusion of electrons and ion pressure gradients cause diffusion of ions. In order to maintain charge neutrality, however, the less mobile ions are pulled with the electrons so that both species diffuse together at a rate which lies somewhere between their respective free diffusion rates. The incorporation of an electron/ion diffusion term controlled by the coefficient D_a represents an approximation to the actual behavior of these species. This diffusion turns out to be very important in terms of mass and energy transport in the ionized regions of the arcjet thruster. In an axisymmetric coordinate system the ion continuity equation then becomes

$$\frac{\partial \rho_e}{\partial t} + \frac{\partial \rho_e u_r}{\partial r} - \frac{\partial}{\partial r}\left(D_a \frac{\partial \rho_e}{\partial r}\right) + \frac{\partial \rho_e u_z}{\partial z} - \frac{\partial}{\partial z}\left(D_a \frac{\partial \rho_e}{\partial z}\right) + \frac{\rho_e}{r}\left(u_r - D_a \frac{\partial \rho_e}{\partial r}\right) = m_e \dot{n}_e. \tag{3.42}$$

Including terms for an axial and radial slip velocity, the monatomic continuity equation is given by

$$\frac{\partial \rho_S}{\partial t} + \frac{\partial \rho_S u_r}{\partial r} + \frac{\partial \rho_S V_{S_r}}{\partial r} + \frac{\partial \rho_S u_z}{\partial z} + \frac{\partial \rho_S V_{S_z}}{\partial z} + \frac{\rho_S (u_r + V_{S_r})}{r}$$

$$= m_S \left(\dot{n}_S + < \sigma v > n_e n_{S_2} - \dot{n}_e\right). \tag{3.43}$$

The neutral atom slip velocity, defined by the relation $\vec{u}_S = \vec{u} + \vec{V}_S$, is in general calculated by solving a set of diffusion equations for each of the species present. The existence of gradients in the atomic and diatomic species densities would generally lead to diffusion of these species away from regions of higher concentration in a process analogous to the ambipolar diffusion of ions and electrons. In this case, however, only the neutral velocity slip produced solely by ambipolar diffusion is considered. Using the definition of the mean flow velocity and assuming that both neutral species travel at the same velocity implies that

$$V_{S_2} = V_S = -\frac{\rho_{S^+}}{\rho_{S_2} + \rho_S} V_{S^+}, \tag{3.44}$$

or

$$\rho_S \vec{V}_S = \frac{\rho_S}{\rho_{S_2} + \rho_S} D_a \frac{m_S}{m_e} \nabla \rho_e. \tag{3.45}$$

Inserting this expression into Equation 3.43, the final form of the neutral atom mass conservation equation becomes

$$\frac{\partial \rho_S}{\partial t} + \frac{\partial \rho_S u_r}{\partial r} + \frac{\partial}{\partial r}\left(\frac{\rho_S}{(\rho_{S_2} + \rho_S)} D_a \frac{m_S}{m_e}\frac{\partial \rho_e}{\partial r}\right) + \frac{\partial \rho_S u_z}{\partial z} + \frac{\partial}{\partial z}\left(\frac{\rho_S}{(\rho_{S_2} + \rho_S)} D_a \frac{m_S}{m_e}\frac{\partial \rho_e}{\partial z}\right)$$

$$+ \frac{\rho_S}{r}\left(u_r + \frac{\rho_S}{(\rho_{S_2} + \rho_S)} D_a \frac{m_S}{m_e}\frac{\partial \rho_e}{\partial r}\right) = m_S\left(\dot{n}_S + < \sigma v > n_e n_{S_2} - \dot{n}_e\right). \tag{3.46}$$

The net production rate source terms in the above equations are determined by dissociation and ionization nonequilibrium relations, described in Sections 3.3.1 and 3.3.2 of this document.

3.2.3 Momentum Conservation Equations

Summing the four species momentum equations defined by Equation 3.13 and substituting the definitions of global density, mean flow velocity, and pressure ($p = \sum_j p_j$) results in a statement of global momentum conservation. In this process the collisional momentum terms and the electric field terms cancel, and the Lorentz force terms are neglected, so that the global momentum equation is given by

$$\frac{\partial \rho \vec{u}}{\partial t} + \nabla \cdot \rho \vec{u}\vec{u} + \nabla \cdot \overline{\overline{p}} = 0. \tag{3.47}$$

Separating out the shear and stress components of the pressure tensor, the component equations of the global conservation of momentum are given by

$$\frac{\partial \rho u_r}{\partial t} + \frac{\partial(\rho u_r^2 + p - \tau_{rr})}{\partial r} + \frac{\partial(\rho u_r u_z - \tau_{rz})}{\partial z} + \frac{\rho u_r^2 - \rho u_\theta^2 - \tau_{rr} + \tau_{\theta\theta}}{r} = 0 \tag{3.48}$$

$$\frac{\partial \rho u_\theta}{\partial t} + \frac{\partial(\rho u_r u_\theta - \tau_{r\theta})}{\partial r} + \frac{\partial(\rho u_\theta u_z - \tau_{\theta z})}{\partial z} + 2\frac{\rho u_r u_\theta - \tau_{r\theta}}{r} = 0 \tag{3.49}$$

$$\frac{\partial \rho u_z}{\partial t} + \frac{\partial(\rho u_r u_z - \tau_{rz})}{\partial r} + \frac{\partial(\rho u_z^2 + p - \tau_{zz})}{\partial z} + \frac{\rho u_r u_z - \tau_{rz}}{r} = 0, \tag{3.50}$$

where

$$\tau_{rr} = \frac{2}{3}\mu_g\left(2\frac{\partial u_r}{\partial r} - \frac{\partial u_z}{\partial z} - \frac{u_r}{r}\right) \tag{3.51}$$

$$\tau_{\theta\theta} = \frac{2}{3}\mu_g\left(2\frac{u_r}{r} - \frac{\partial u_r}{\partial r} - \frac{\partial u_z}{\partial z}\right) \tag{3.52}$$

$$\tau_{zz} = \frac{2}{3}\mu_g \left(2\frac{\partial u_z}{\partial z} - \frac{\partial u_r}{\partial r} - \frac{u_r}{r}\right) \tag{3.53}$$

$$\tau_{r\theta} = \mu_g \left(\frac{\partial u_\theta}{\partial r} - \frac{u_\theta}{r}\right) \tag{3.54}$$

$$\tau_{rz} = \mu_g \left(\frac{\partial u_r}{\partial z} + \frac{\partial u_z}{\partial r}\right) \tag{3.55}$$

$$\tau_{\theta z} = \mu_g \frac{\partial u_\theta}{\partial z}, \tag{3.56}$$

and μ_g is the heavy species viscosity, to be derived as a function of the species viscosities in Section 3.4.1. Three momentum equations are required, but due to the assumed azimuthal symmetry all derivatives in this direction are neglected. Additionally, the contributions of the electrons have been neglected in the above expressions for the shear stress.

3.2.4 Energy Conservation Equations

3.2.4.1 Heavy Species

The energy conservation equations for the three heavy species (diatomic molecules, atoms, and ions) are found from Equation 3.19:

$$\frac{\partial}{\partial t}(\rho_{S_2} E_{S_2}) + \nabla\cdot(\rho_{S_2}\vec{u}_{S_2}E_{S_2}) + \nabla\cdot\left(\bar{\bar{p}}_{S_2}\cdot\vec{u}_{S_2}\right) - \nabla\cdot(k_{S_2}\nabla T_g) = M_{S_2} \tag{3.57}$$

$$\frac{\partial}{\partial t}(\rho_S E_S) + \nabla\cdot(\rho_S\vec{u}_S E_S) + \nabla\cdot(\bar{\bar{p}}_S\cdot\vec{u}_S) - \nabla\cdot(k_S\nabla T_g) = M_S \tag{3.58}$$

$$\frac{\partial}{\partial t}(\rho_{S^+} E_{S^+}) + \nabla\cdot(\rho_{S^+}\vec{u}_{S^+}E_{S^+}) + \nabla\cdot(\bar{\bar{p}}_{S^+}\cdot\vec{u}_{S^+}) - \nabla\cdot(k_{S^+}\nabla T_g) = \vec{j}_{S^+}\cdot\vec{E} + M_{S^+}, \tag{3.59}$$

where T_g is the heavy species temperature.

The enthalpy, and consequently the energy E_s, of each species is obtained by considering both the internal energy based on molecular degrees of freedom and the energies associated with dissociation and ionization. In this case the energy of dissociation is bound to the neutral atoms, while the ionization energy is arbitrarily bound to the electrons. Therefore the enthalpy per molecule for the heavy species may be written as

$$h_{S_2} = \frac{7}{2}kT_g - E_d + \frac{E_{vib}}{e^{\frac{E_{vib}}{kT_g}} - 1} + \triangle \tag{3.60}$$

and

$$h_S = h_{S^+} = \frac{5}{2}kT_g + \frac{\triangle}{2}, \tag{3.61}$$

where E_d is the dissociation energy, E_{vib} is the vibrational excitation energy of the diatomic molecule, and $\triangle$ is a constant chosen to make the enthalpy of the S_2 molecule zero at the common reference temperature $T_f = 298.16^o$K. For gases of interest in this application such as hydrogen and nitrogen, the vibrational excitation is negligible at the reference temperature, so $\triangle = E_d - \frac{7}{2}T_f$. Therefore

$$h_{S_2} = \frac{7}{2}k(T_g - T_f) + \frac{E_{vib}}{e^{\frac{E_{vib}}{kT_g}} - 1} \tag{3.62}$$

and

$$h_S = h_{S^+} = \frac{5}{2}kT_g + \frac{1}{2}E_d - \frac{7}{4}kT_f. \tag{3.63}$$

The total enthalpy and energy per unit volume are then given by

$$\begin{aligned}\rho H &= \sum_j n_j h_j + \sum_j \frac{1}{2}\rho_j u_j^2 \\ &= \frac{5}{2}(\rho_S + \rho_{S^+})R_S T_g + \frac{7}{2}\rho_{S_2} R_{S_2} T_g + \frac{1}{2}(\rho_S + \rho_{S^+})R_S \theta_d + \frac{\rho_{S_2} R_{S_2} \theta_v}{e^{\frac{\theta_v}{T_g}} - 1} \\ &- \frac{7}{2}\rho_{S_2} R_{S_2} T_f - \frac{7}{4}(\rho_S + \rho_{S^+})R_S T_f + \frac{1}{2}\rho_{S_2} u_{S_2}^2 + \frac{1}{2}\rho_S u_S^2 + \frac{1}{2}\rho_{S^+} u_{S^+}^2\end{aligned} \tag{3.64}$$

and

$$\rho E = \rho H - \rho_{S_2} R_{S_2} T_g - (\rho_S + \rho_{S^+})R_S T_g, \tag{3.65}$$

where $\theta_d = \frac{E_d}{k}$ and $\theta_v = \frac{E_{vib}}{k}$ are the characteristic dissociation and vibrational excitation temperatures, respectively.

Taking advantage of their common temperature the three heavy species energy equations may be combined into a single energy equation by summation and simplification. Summing Equations 3.57-3.59 implies that

$$\begin{aligned}&\frac{\partial}{\partial t}(\rho_{S_2} E_{S_2} + \rho_S E_S + \rho_{S^+} E_{S^+}) + \nabla \cdot (\rho_{S_2} \vec{u}_{S_2} E_{S_2} + \rho_S \vec{u}_S E_S + \rho_{S^+} \vec{u}_{S^+} E_{S^+}) \\ &+\nabla \cdot \left(\bar{\bar{p}}_{S_2} \cdot \vec{u}_{S_2}\right) + \nabla \cdot (\bar{\bar{p}}_S \cdot \vec{u}_S) + \nabla \cdot (\bar{\bar{p}}_{S^+} \cdot \vec{u}_{S^+}) - \nabla \cdot (k_g \nabla T_g) \\ &= \vec{j}_{S^+} \cdot \vec{E} + M_{S_2} + M_S + M_{S^+},\end{aligned} \tag{3.66}$$

where the individual thermal conductivities have been combined into an overall heavy species conductivity, k_g, to be derived in Section 3.4.3. In order to write this heavy species energy equation in terms of the mean flow velocity $\vec{u}$, the slip velocities for each of the species are defined by the relation

$$\vec{u}_j = \vec{u} + \vec{V}_j. \tag{3.67}$$

The slip velocity in the axial direction is assumed to be negligible in terms of the transport of energy, while the radial slip velocity, though small, can be an important transport mechanism because of the steep radial density and temperature gradients at the edge of the arc. Therefore the slip velocities will be retained in the radial divergence term of the heavy species energy equation but neglected everywhere else. As a result, Equation 3.66 may be recast in the following form in axisymmetric coordinates:

$$\begin{aligned}\frac{\partial \rho E}{\partial t} &+ \frac{\partial(\rho u_r H + q_{gr} - u_r\tau_{rr} - u_\theta\tau_{r\theta} - u_z\tau_{rz})}{\partial r} + \frac{\partial(\rho u_z H + q_{gz} - u_r\tau_{rz} - u_\theta\tau_{\theta z} - u_z\tau_{zz})}{\partial z} \\ &+ \frac{\rho u_r H + q_{gr} - u_r\tau_{rr} - u_\theta\tau_{r\theta} - u_z\tau_{rz}}{r} + \frac{\partial(\rho_{S_2} V_{S_2 r} H_{S_2} + \rho_S V_{S r} H_S + \rho_{S^+} V_{S^+ r} H_{S^+})}{\partial r} \\ &+ \frac{\rho_{S_2} V_{S_2 r} H_{S_2}}{r} + \frac{\rho_S V_{S r} H_S}{r} + \frac{\rho_{S^+} V_{S^+ r} H_{S^+}}{r} = E_l,\end{aligned} \tag{3.68}$$

where

$$q_{gr} = -k_g \frac{\partial T_g}{\partial r} \quad and \quad q_{gz} = -k_g \frac{\partial T_g}{\partial z} \tag{3.69}$$

and

$$E_l = 3\frac{\rho_e}{m_S}(\nu_{eS^+} + \nu_{eS} + \delta_s \nu_{eS_2})k(T_e - T_g). \tag{3.70}$$

The collisional energy transfer from the electrons to the heavy species, represented by E_l, is the only term which remains from the summation of the M_j. The δ_s factor preceding the electron - diatomic molecule collision frequency is needed to correct for the fact that electron collisions with polyatomic molecules are not elastic since some of the electron energy can be absorbed by rotational or vibrational excitation of the molecule. Figure 3.1 shows the value of this correction factor for hydrogen, as taken from Sutton and Sherman[110]. In addition, $\vec{q}_g$ is the heavy species heat flux vector, and the total enthalpy and energy are given by Equations 3.64 and 3.65 respectively. The ohmic term $\vec{j}_{S^+} \cdot \vec{E}$ was neglected as the arc current is carried primarily by electrons rather than by ions.

Equation 3.68 is considered the strong conservative form of the energy equation for the heavy species. Computationally, it was found that this form was not appropriate for the arcjet simulation. Because the flow in the core of the arc can attain such high velocities in the nozzle expansion region (greater than 20,000m/s), the kinetic energy portion of the total energy can become very large. Similarly, in certain regimes the dissociation energy term can become the dominant part of the total energy, since the

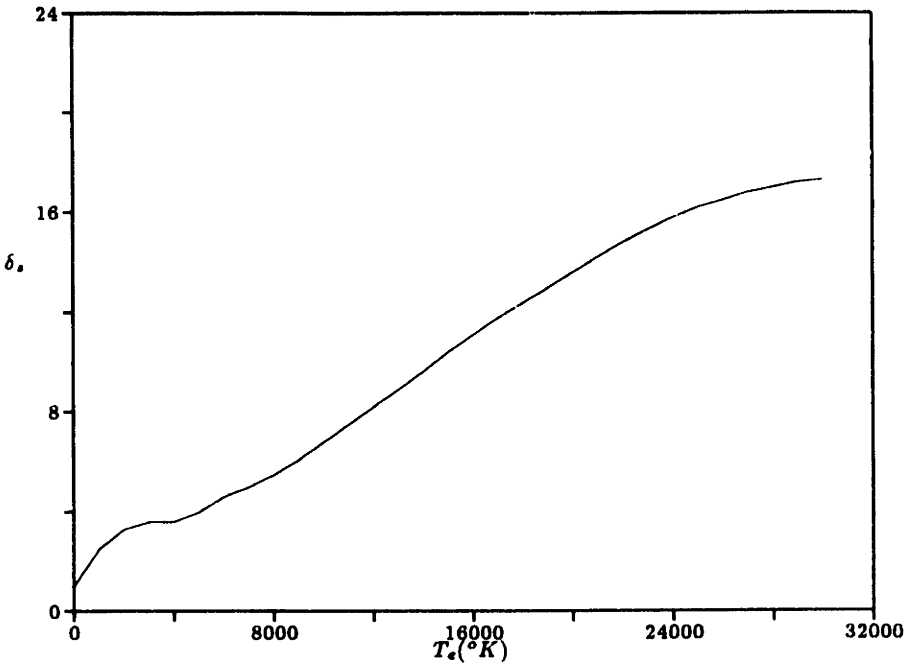

Figure 3.1: Inelastic Correction Factor for Energy Transfer Between Electrons and H_2 Molecules

characteristic dissociation temperature is so high. Numerically, these two effects can lead to a situation where the thermal energy is orders of magnitude less than the kinetic or dissociation energy, resulting in a loss of information or indeterminate temperature when the gas temperature is extracted from the total energy after each integration step. Furthermore, these large total energy terms can lead to enthalpy fluxes which are the dominant terms in the numerical integration. This situation could cause unusually large changes in the total energy through the unsteady term in order to balance the discrete equation. If the changes are too large in the negative direction a negative gas temperature may result, which is clearly non-physical. Consequently, in order to prevent non-physical results and numerical difficulties, a modified internal energy form of the heavy species energy equation is utilized. By using the species continuity and momentum equations together with Equation 3.68, the following statement of heavy species energy conservation results:

$$\frac{\partial \rho e_g}{\partial t} + \frac{\partial(\rho e_g u_r + q_{gr})}{\partial r} + \frac{\partial(\rho e_g u_z + q_{gz})}{\partial z} + p_g \frac{\partial u_r}{\partial r} + p_g \frac{\partial u_z}{\partial z} + \frac{\rho h_g u_r + q_{gr}}{r}$$

$$+ \frac{\partial}{\partial r}\left(\rho_{S_2} e_{S_2} V_{S_2 r} + \rho_S e_S V_{S r} + \rho_{S^+} e_{S^+} V_{S^+ r}\right) + p_{S_2} \frac{\partial V_{S_2 r}}{\partial r} + p_S \frac{\partial V_{S r}}{\partial r} + p_{S^+} \frac{\partial V_{S^+ r}}{\partial r}$$

$$+ \frac{\rho_{S_2} h_{S_2} V_{S_2 r} + \rho_S h_S V_{S r} + \rho_{S^+} h_{S^+} V_{S^+ r}}{r} = \Phi + E_l - \frac{1}{2} E_d \dot{n}_S, \qquad (3.71)$$

where

$$\Phi = \mu_g \left[2\left(\frac{\partial u_r}{\partial r}\right)^2 + 2\left(\frac{\partial u_z}{\partial z}\right)^2 + 2\left(\frac{u_r}{r}\right)^2 + \left(\frac{\partial u_r}{\partial z} + \frac{\partial u_z}{\partial r}\right)^2 \right.$$

$$\left. + \left(\frac{\partial u_\theta}{\partial r} - \frac{u_\theta}{r}\right)^2 + \left(\frac{\partial u_\theta}{\partial z}\right)^2 - \frac{2}{3}\left(\frac{\partial u_r}{\partial r} + \frac{\partial u_z}{\partial z} + \frac{u_r}{r}\right)^2 \right] \tag{3.72}$$

$$\rho e_g = \frac{3}{2}\left(\rho_S + \rho_{S^+}\right) R_S T_g + \frac{5}{2}\rho_{S_2} R_{S_2} T_g + \frac{\rho_{S_2} R_{S_2} \theta_v}{e^{\frac{\theta_v}{T_g}} - 1} - \frac{7}{4}\rho R_S T_f \tag{3.73}$$

$$\rho h_g = \rho e_g + \rho_{S_2} R_{S_2} T_g + \left(\rho_S + \rho_{S^+}\right) R_S T_g \tag{3.74}$$

$$e_{S_2} = \frac{5}{2} R_{S_2} T_g - \frac{7}{2} R_{S_2} T_f + \frac{R_{S_2}\theta_v}{e^{\frac{\theta_v}{T_g}} - 1} \tag{3.75}$$

$$e_S = e_{S^+} = \frac{3}{2} R_S T_g - \frac{7}{4} R_S T_f \tag{3.76}$$

and

$$h_j = e_j + R_j T_g. \tag{3.77}$$

Although this internal energy form of the equation is not conservative, it is accurate as long as the flow is free of strong shocks or other discontinuities.

3.2.4.2 Electrons

The energy conservation equation for electrons is given directly by Equation 3.19:

$$\frac{\partial}{\partial t}\left(\frac{3}{2}p_e + \frac{1}{2}\rho_e u_e^2 + \rho_e \frac{E_i}{m_e}\right) + \nabla \cdot \left[\left(\frac{3}{2}p_e + \frac{1}{2}\rho_e u_e^2 + \rho_e \frac{E_i}{m_e}\right)\vec{u}_e\right] + \nabla \cdot \left(\bar{\bar{p}}_e \cdot \vec{u}_e\right)$$

$$- \nabla \cdot \left(k_e \nabla T_e\right) = \vec{j}_e \cdot \vec{E} + M_e, \tag{3.78}$$

where E_i is the ionization energy. Neglecting the electron shear terms, substituting for M_e, and rearranging, the electron energy equation may be written as

$$\frac{\partial}{\partial t}\left(\frac{3}{2}p_e + \frac{1}{2}\rho_e u_e^2 + \rho_e \frac{E_i}{m_e}\right) + \nabla \cdot \left(\frac{5}{2}p_e \vec{u}_e + \frac{1}{2}\rho_e u_e^2 \vec{u}_e + \rho_e \frac{E_i}{m_e}\vec{u}_e\right) - \nabla \cdot \left(\kappa_e \nabla T_e\right)$$

$$= \frac{j^2}{\sigma} - E_l - E_d < \sigma v > n_e n_{S_2} - \dot{R}, \tag{3.79}$$

where terms proportional to the square of the electron velocity slip have been neglected, E_l is the collisional energy transfer given by Equation 3.70, $E_d < \sigma v > n_e n_{S_2}$ is the energy lost per unit volume due to electron impact ionization, and $\dot{R}$ is the energy lost per unit volume due to radiation. As with the heavy species energy equation, it is desirable for numerical reasons to eliminate the ionization energy from the total energy, and instead to rely on a finite rate source term on the right hand side of the equation. Using the electron continuity equation and the definitions of total energy and enthalpy, Equation 3.79 in axisymmetric coordinates becomes

$$\frac{\partial(\rho_e E_e)}{\partial t}+\frac{\partial(\rho_e u_{er} H_e+q_{er})}{\partial r}+\frac{\partial(\rho_e u_{ez} H_e+q_{ez})}{\partial z}+\frac{\rho_e u_{er} H_e+q_{er}}{r}$$

$$=\frac{j^2}{\sigma}-E_l-E_d<\sigma v>n_e n_{S_2}-E_i\dot{n}_e-\dot{R}, \tag{3.80}$$

where

$$E_e=\frac{3}{2}R_e T_e+\frac{1}{2}u_e^2 \tag{3.81}$$

$$H_e=E_e+R_e T_e \tag{3.82}$$

$$q_{er}=-k_e\frac{\partial T_e}{\partial r} \qquad q_{ez}=-k_e\frac{\partial T_e}{\partial z}. \tag{3.83}$$

The formulation of the radiative transfer term $\dot{R}$ follows the model of Morris, Rudis, and Yos[82] as simplified by Watson and Pegot[120]. Watson and Pegot neglected line radiation by hydrogen because the absorption coefficients were found to be sufficiently large to preclude radiative energy transfer. Continuum radiation from electron-ion recombination and free electron transitions (bremsstrahlung), however, were included in the Watson and Pegot model and calculated by a quantum defect method. Since these continuum processes involve the electrons, in the model of this thesis the radiated energy is considered to have been lost in the electron energy balance rather than the heavy species energy balance. The energy radiated is assumed to escape to the thruster walls rather than to be captured in the gas flow. Calculation of the radiation transfer term is accomplished by interpolation from a data set as a function of temperature and pressure. For illustration, the radiated power in hydrogen as a function of temperature is plotted in Figure 3.2 for a pressure of 1 atm.

A simple calculation can be made to estimate the maximum possible size of the line radiation loss term for hydrogen. The highest radiation loss for hydrogen will come from the first excited state, which is separated from the ground state energy level by 10.2eV. The radiative power loss per unit volume for this transition is given by

$$\dot{R}_{21}=n_2 A_{21} E_{21}\beta, \tag{3.84}$$

where n_2 is the number density of the excited state, given by Boltzmann's relation

$$\frac{n_2}{n_1}=\frac{g_2}{g_1}e^{-E_{21}/kT_g}=3.14\times10^{-8}n_1 e^{-118{,}300/T_g}, \tag{3.85}$$

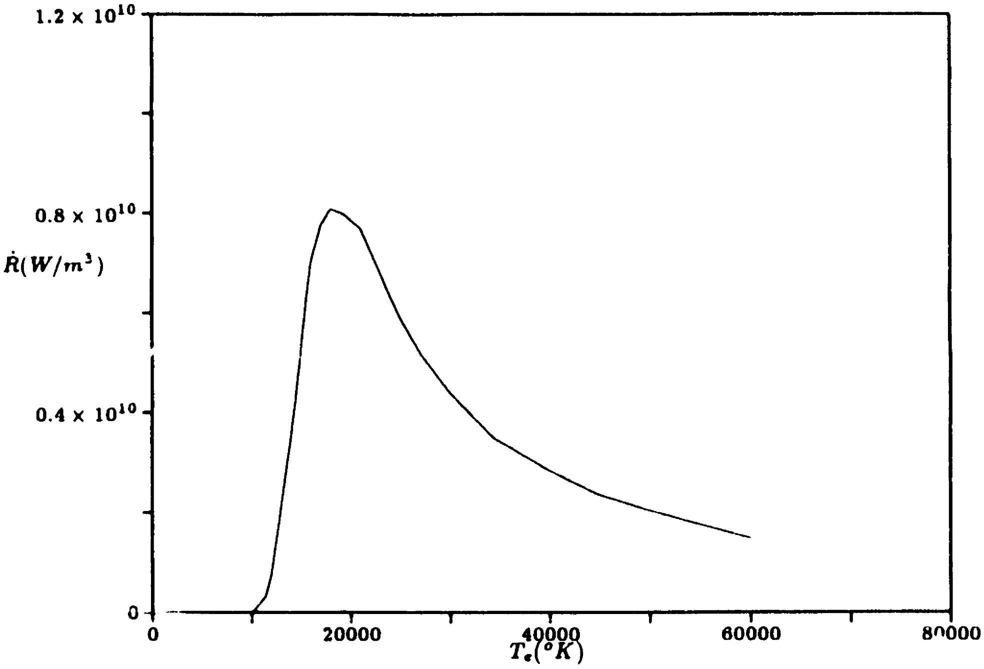

Figure 3.2: Ionization Recombination and Bremsstrahlung Continuum Radiation in Hydrogen at 1atm

A_{21}^{-1} is the lifetime of the first excited state, E_{21} is the energy difference between the first excited state and the ground state, β is the escape factor, and n_1 is the number density of the ground state. By assuming that the escape factor β is unity, the worst case value of the radiation loss rate is obtained. Comparison of the magnitude of $\dot{R}_{21}$ to other terms in the heavy species energy equation shows that the worst case radiation loss is negligible everywhere except in a narrow band 0.1-0.2mm wide in the constrictor region which lies along the boundary between the central arc and the outer flow. Within this band the number density of atomic hydrogen is a maximum, and the gas temperature is still relatively high (10,000 – 20,000°K). The dominant term in the heavy species energy equation in this region is radial heat conduction, and line radiation can be of the same order as this term within this narrow band. Since the absorption coefficients for hydrogen are very large under these conditions, however, the escape factor is therefore very small, and the line radiation loss term can be neglected. Although little or no radiated energy is lost, there may be a net radial transport of energy since the radiation may be absorbed in a different place from where it was emitted. This effect, however, is not modeled by this thesis.

3.2.5 Additional Equations

Additional equations required to complete the model are the equation of state and the definition of the electron velocity in terms of the current density and the mean flow velocity:

$$p = p_g + p_e = \sum_j \rho_j R_{gj} T_g + \rho_e R_e T_e \tag{3.86}$$

$$u_{er} = u_{S^+r} - \frac{j_r}{en_e} \qquad u_{ez} = u_{S^+z} - \frac{j_z}{en_e} \tag{3.87}$$

The electron velocity appears and is utilized solely in the electron energy equation.

It is also of interest to derive a formula for the ratio of specific heats (γ) for the gas as a whole, as it is required in calculating the Mach number and in obtaining stability criteria for a numerical integration method. For monatomic species $\gamma_S = \frac{5}{3}$, while for diatomic species at low temperature $\gamma_{S_2} = \frac{7}{5}$. At higher temperatures of several thousand degrees Kelvin, the vibrational excitation of diatomic molecules decreases γ through the factor δ by

$$\gamma_{S_2} = 1 + \frac{1}{\frac{5}{2} + \delta} \tag{3.88}$$

where

$$\delta = \frac{\theta_v / T_g}{e^{\theta_v/T_g} - 1}. \tag{3.89}$$

The factor delta goes to zero as T_g approaches zero, and it goes to one as T_g becomes much larger than θ_v, meaning $\gamma_{H_2}(T_g \gg \theta_v) = 1.286$. The "frozen" ratio of specific heats for the gas is then given by the ratio of the mass-averaged specific heats of each of its constituents:

$$\gamma = \frac{c_p}{c_v} = \frac{\left(1 - \frac{\rho_{S_2}}{\rho}\right)\frac{5}{2} + \frac{\rho_{S_2}}{\rho}\left[\frac{7}{2} + \left(\frac{\theta_v}{T_g}\right)^2 \frac{e^{\frac{\theta_v}{T_g}}}{\left(e^{\frac{\theta_v}{T_g}} - 1\right)^2}\right]}{\left(1 - \frac{\rho_{S_2}}{\rho}\right)\frac{3}{2} + \frac{\rho_{S_2}}{\rho}\left[\frac{5}{2} + \left(\frac{\theta_v}{T_g}\right)^2 \frac{e^{\frac{\theta_v}{T_g}}}{\left(e^{\frac{\theta_v}{T_g}} - 1\right)^2}\right]} = \frac{\frac{5}{2} + \frac{\rho_{S_2}}{\rho}\left[1 + \left(\frac{\theta_v/2T_g}{\sinh(\theta_v/2T_g)}\right)^2\right]}{\frac{3}{2} + \frac{\rho_{S_2}}{\rho}\left[1 + \left(\frac{\theta_v/2T_g}{\sinh(\theta_v/2T_g)}\right)^2\right]} \tag{3.90}$$

3.3 Dissociation and Ionization Processes

3.3.1 Dissociation

Since a diatomic gas is utilized as the propellant in this research, modeling of the dissociation process is required. The reaction

$$S_2 \rightleftharpoons 2S \tag{3.91}$$

governs this process, and for hydrogen it occurs within the temperature range 1500 – 7000°K for pressures between 10^{-4} and 10^{0} atm. The corresponding dissociation energy is 4.478eV ($7.174 \times 10^{-19} J$).

3.3.1.1 Equilibrium Flow

In the equilibrium case, the law of mass action written in terms of the partial pressures is

$$\frac{p_S^2}{p_{S_2}} = K_p(T_g) = \exp\left[-\frac{1}{\hat{R}T_g}\left(2\hat{\mu}_S^0 - \hat{\mu}_{S_2}^0\right)\right], \tag{3.92}$$

where $\hat{R}$ is the universal gas constant, K_p is the equilibrium constant, and $\hat{\mu}_s^0$ is the chemical potential, or Gibbs free energy per unit mole, of the pure species at unit pressure, given by

$$\hat{\mu}_s^0 = \int_{T_{g0}}^{T_g} \hat{c_{p_s}} dT_g - T_g \int_{T_{g0}}^{T_g} \hat{c_{p_s}} \frac{dT_g}{T_g} + \hat{h}_{s0} - T_g \hat{s}_{s0} - \hat{R}T_g \ln p_0. \tag{3.93}$$

Alternatively, by writing the law of mass action in terms of number density, the equilibrium constant $K = kT_g K_p$ may be written in terms of the partition functions of the reactants and products as

$$\frac{n_S^2}{n_{S_2}} = K = \frac{q_S^2}{q_{S_2}}. \tag{3.94}$$

For hydrogen, for example,

$$q_H = 2q_H^{tr} e^{-\frac{\Delta}{2T_g}} \tag{3.95}$$

and

$$q_{H_2} = 2^{\frac{3}{2}} q_H^{tr} \frac{T_g}{2\theta_r} \frac{e^{\frac{\theta_d - \Delta}{T_g}}}{1 - e^{-\frac{\theta_v}{T_g}}}, \tag{3.96}$$

where

$$q_H^{tr} = \left(\frac{2\pi m_H k T_g}{h^2}\right)^{\frac{3}{2}}, \tag{3.97}$$

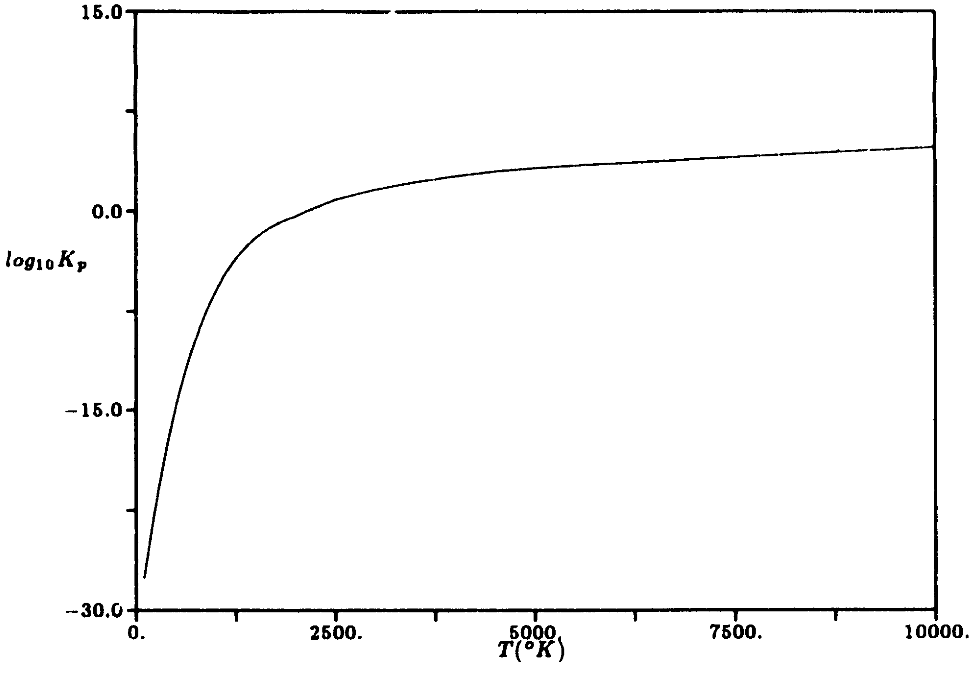

Figure 3.3: $Log_{10}K_p$ versus Temperature for Dissociating Hydrogen

$$\triangle = \theta_d - \frac{7}{2}T_f - \frac{\theta_v}{e^{\frac{\theta_v}{T_f}} - 1}, \tag{3.98}$$

θ_r is the rotational excitation temperature, θ_v is the vibrational excitation temperature, θ_d is the characteristic temperature of dissociation, and T_f is the reference temperature 298.16°K.

Since the equilibrium constant is a function of temperature only, it is convenient to use tabulated values of K_p when solving Equation 3.92 for a specific thermodynamic state. For hydrogen, a plot of $\log_{10} K_p$ versus temperature from Martinez and Elverum[75] is shown in Figure 3.3. Equation 3.92 can be solved for the partial pressures, mole fractions, or mass fractions of the two species, given information about the total pressure, number of moles, or density of the gas at the point of interest. In practice this information is available from the global fluid equations which are solved simultaneously. The above method compares favorably with the independently calculated data of Grier[42]. Figure 3.4 shows the equilibrium mole fraction of atomic hydrogen as a function of temperature at 1atm pressure calculated by both Grier and this research. The effect of pressure on hydrogen dissociation is portrayed in Figure 3.5. Increasing the pressure essentially delays the onset of and increases the width of the dissociating region in terms of temperature.

The equilibrium amounts of molecular and atomic hydrogen can be calculated from the solution of a quadratic equation which is well defined over the dissociating regime.

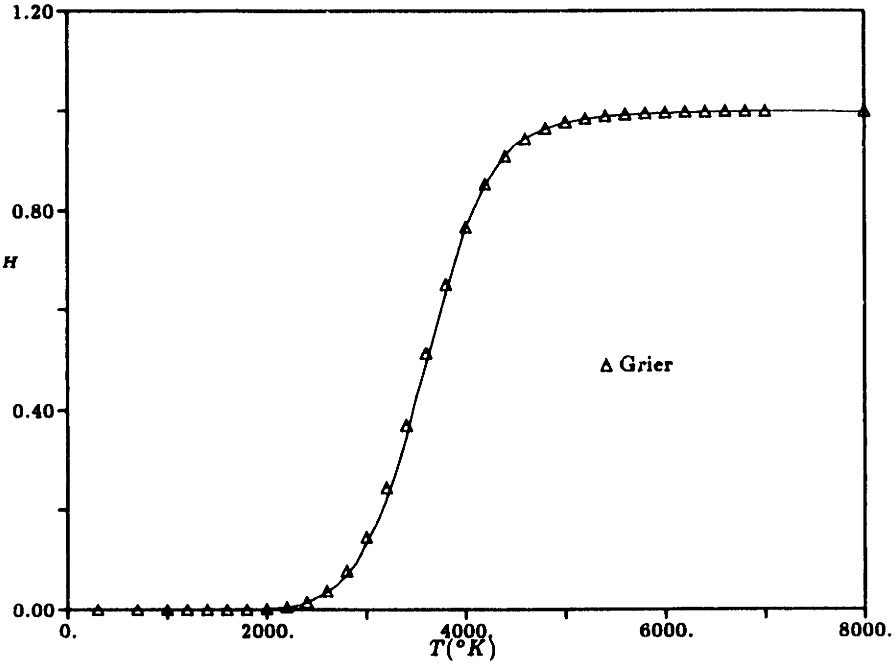

Figure 3.4: Equilibrium Dissociation of Hydrogen at 1 atm by This Research and Grier

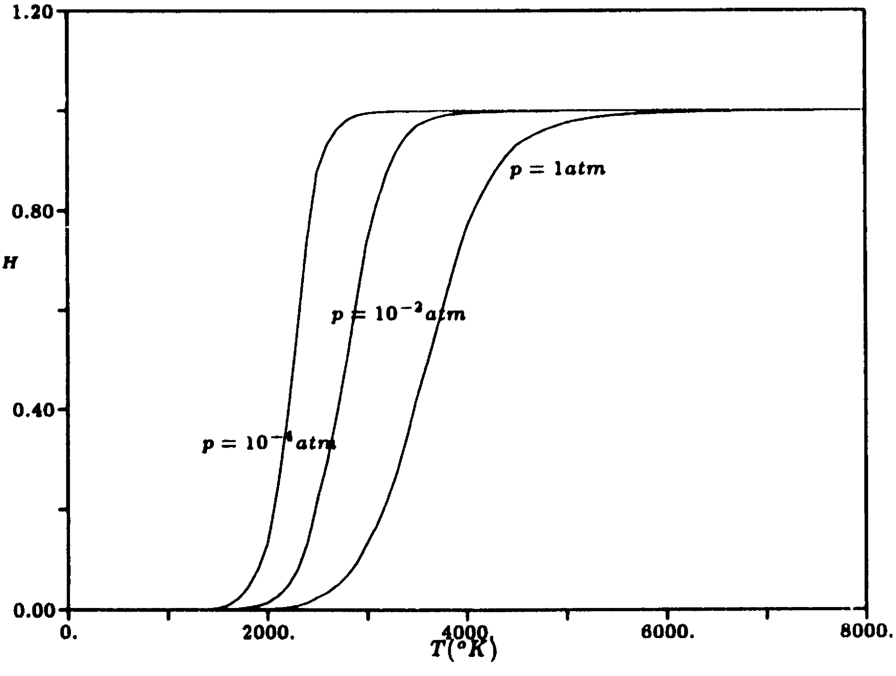

Figure 3.5: Equilibrium Dissociation of Hydrogen versus Temperature and Pressure

When the degree of ionization becomes significant and the ionization process overlaps the dissociation process in the pressure-temperature plane, or when the gas and electron temperatures are not equal, simultaneous solution of the Saha equation (which determines the equilibrium level of ionization) is necessary.

3.3.1.2 Nonequilibrium Flow

In this research nonequilibrium dissociation is considered so that a finite rate of production of atomic species exists. Dissociation by both heavy species collisions and electron impact is modeled. For the heavy species collisions the procedure and nomenclature of Biasca[8] and Mitchner and Kruger[81] is followed. Consider the gas to be a mixture of N_s species governed by N_r chemical reactions. Let the i^{th} chemical reaction be written as

$$\sum_{j=1}^{N_s} \nu_{ij} s_j = \sum_{j=1}^{N_s} \nu'_{ij} s_j, \tag{3.99}$$

where s_j refers to the j^{th} molecular species and ν_{ij} is the stoichiometric coefficient of species j in the i^{th} reaction. The prime notation denotes the products of the reaction. The rate of production for the i^{th} forward reaction is given by

$$R_{f,i} = k_{f,i} \prod_{j=1}^{N_s} (\sigma_j)^{\nu_{ij}}, \tag{3.100}$$

where σ_j is the molar concentration of species j, and the forward rate constant $k_{f,i}$ is given by the Arrhenius formula

$$k_{f,i} = A_i T_g^{n_i} \exp\left(-\frac{B_i}{\hat{R} T_g}\right), \tag{3.101}$$

where $\hat{R}$ is the universal gas constant. Similarly, the backward production rate for the i^{th} reaction is given by

$$R_{b,i} = k_{b,i} \prod_{j=1}^{N_s} (\sigma_j)^{\nu'_{ij}}. \tag{3.102}$$

The backward rate constant can be related to the forward rate constant through the relation

$$k_{b,i} = \frac{k_{f,i}}{K_{c,i}}, \tag{3.103}$$

where $K_{c,i}$ is the equilibrium constant in terms of concentration for the i^{th} reaction, related to the $K_{p,i}$ in Equation 3.92 by

$$K_{c,i} = K_{p,i} (\hat{R} T_g)^{\sum_{j=1}^{N_s} (\nu_{ij} - \nu'_{ij})}. \tag{3.104}$$

Table 3.2: Constants for the Hydrogen and Nitrogen Dissociation Rate Equations

Constant	Hydrogen	Nitrogen
A ($m^3/mole - s$)	5.5×10^{12}	2.1×10^{15}
B (J/mole)	435,600	943,800
n	-1	-1.5
$\hat{m}_S$	5	3
$\hat{m}_{S_2}$	2	5

The net production rate of species j is then the difference between the forward and backward production rates, or using Eqns. 3.99-3.104:

$$\frac{d\sigma_j}{dt} = \sum_{i=1}^{N_r} \left(\nu'_{ij} - \nu_{ij}\right) k_{f,i} \left[\prod_{j=1}^{N_s} (\sigma_j)^{\nu_{ij}} - \frac{1}{K_{c,i}} \prod_{j=1}^{N_s} (\sigma_j)^{\nu'_{ij}}\right] . \tag{3.105}$$

For chemical reactions such as the hydrogen dissociation of Equation 3.91 where a third body M is required, the molar concentration of the third body in reaction i is given by

$$\sigma_{M,i} = \sum_{j=1}^{N_s} \hat{m}_{ij}\sigma_j, \tag{3.106}$$

where $\hat{m}_{ij}$ is the efficiency factor of the j^{th} species in reaction i. Thus the reaction governing the dissociation process is more precisely

$$M + S_2 \rightleftharpoons 2S + M. \tag{3.107}$$

Writing Equation 3.105 for the above reaction yields the following expression for the atomic production rate in terms of molar concentration:

$$\frac{d\sigma_S}{dt} = k_f\sigma_M \left[\sigma_{S_2} - \frac{1}{K_c}\sigma_S^2\right] = AT_g^n \exp\left(-\frac{B}{\hat{R}T_g}\right) \left(\hat{m}_S\sigma_S + \hat{m}_{S_2}\sigma_{S_2}\right) \left[\sigma_{S_2} - \frac{\hat{R}T_g}{K_p}\sigma_S^2\right] . \tag{3.108}$$

In terms of the net atomic production rate this expression becomes

$$\dot{n}_S = A\hat{N}T_g^n \exp\left(-\frac{B}{\hat{R}T_g}\right) \left(\hat{m}_S\sigma_S + \hat{m}_{S_2}\sigma_{S_2}\right) \left[\sigma_{S_2} - \frac{\hat{R}T_g}{K_p}\sigma_S^2\right] , \tag{3.109}$$

where $\hat{N}$ is Avogadro's number. Table 3.2 lists some of the constants required in Equation 3.109, from Rogers and Schexnayder[98] for hydrogen and Langan et al.[66] for nitrogen.

To account for dissociation by electron impact, a term of the form

$$\dot{n}_{S,e} = < \sigma v > n_e n_{S_2} \tag{3.110}$$

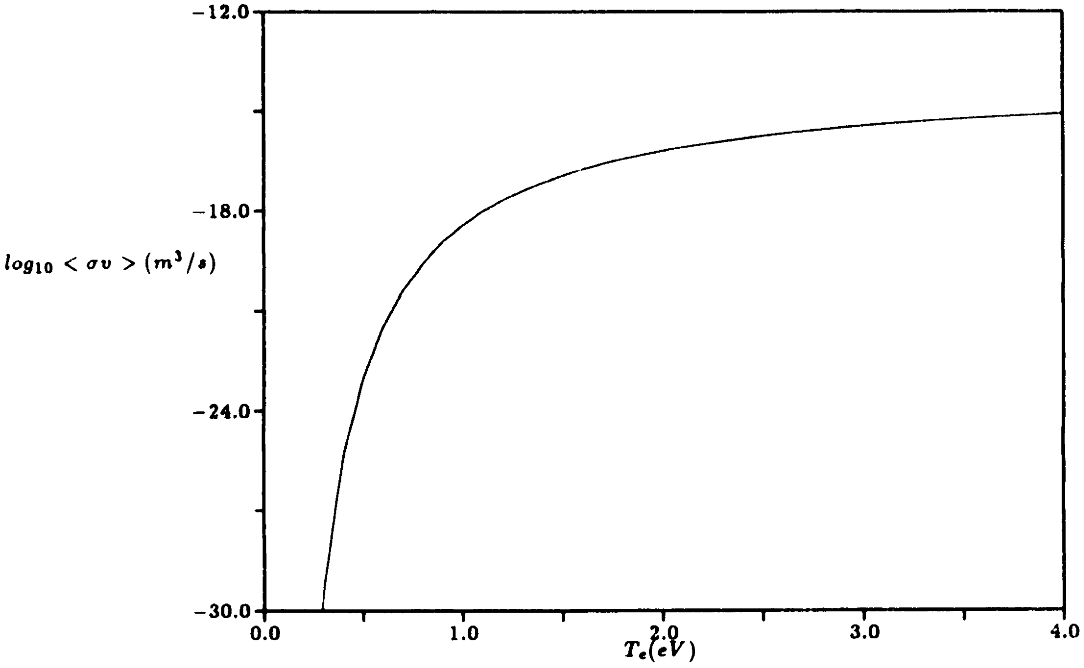

Figure 3.6: Reaction Rate Coefficient for $e - H_2$ Dissociating Collisions

is added to Equation 3.109. The reaction rate coefficient $< \sigma v >$ is taken from Janev et al.[54] and plotted versus electron temperature in Figure 3.6 for hydrogen. Comparisons of the collision cross-sections and number densities between electron impact dissociation and the reverse reaction ($S + S + e \rightarrow S_2 + e$) show that the forward reaction dominates in the relevant arcjet flow regions[54]. The total dissociation rate is thus given by

$$\dot{n}'_S = \dot{n}_S + \dot{n}_{S,e}$$

$$= A\hat{N}T_g^n \exp\left(-\frac{B}{\hat{R}T_g}\right)(\hat{m}_S\sigma_S + \hat{m}_{S_2}\sigma_{S_2})\left[\sigma_{S_2} - \frac{\hat{R}T_g}{K_p}\sigma_S^2\right] + < \sigma v > n_e n_{S_2}. \quad (3.111)$$

A recent investigation by Zube and Myers[124] has shown that for nitrogen propellant the rotational, vibrational, and electron excitation temperatures of the gas in an arcjet nozzle may be considerably out of equilibrium. The data, a sample of which is shown in Figure 3.7, was obtained by spectroscopic methods from a 1kW class arcjet thruster. Thermal nonequilibrium between the various internal states could have a significant effect on the net dissociation rate in the nozzle since T_g in the expression for $\dot{n}_S$ could be very different from the temperature calculated by the heavy species energy equation. The dissociation rate would then be indeterminate without the incorporation of energy conservation equations for the respective internal modes. A number of models have been suggested to deal with this complication, including those of Gnoffo et al.[38],

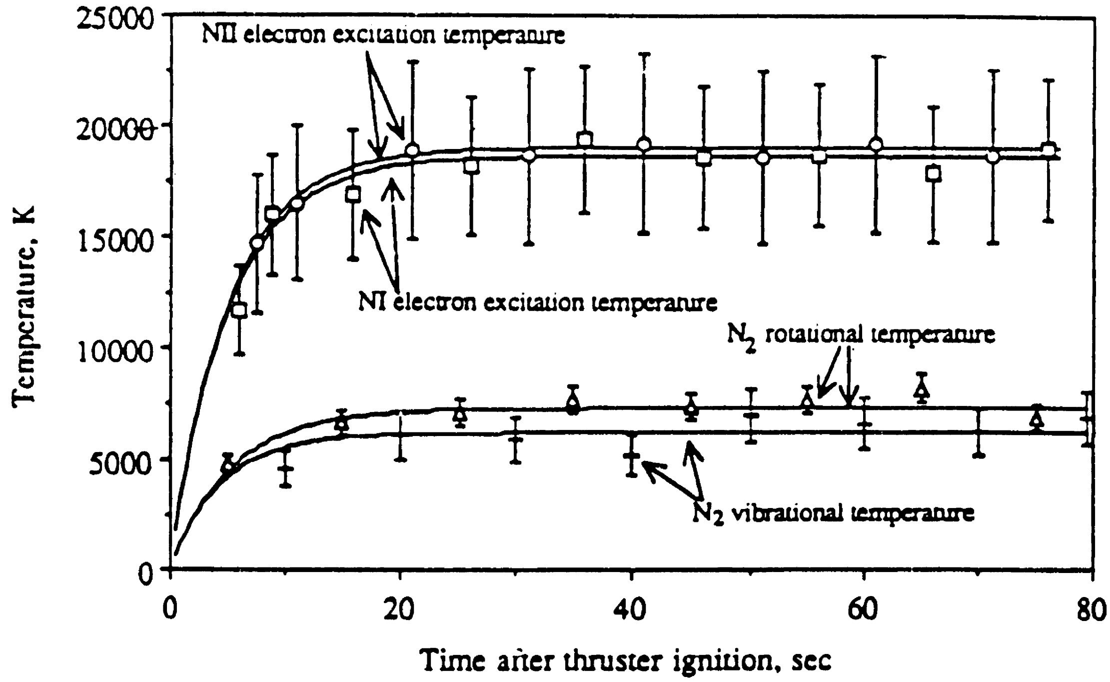

Figure 3.7: Temperature Nonequilibrium in an Arcjet Nozzle with Nitrogen Propellant

Gonzales and Varghese[40], Landrum and Candler[65], and Park[85]. In the simplest formulation, it is assumed that the translational and rotational temperatures are in equilibrium, while an additional energy equation is used to solve for the vibrational excitation temperature of the gas. The temperature used in the determination of the dissociation rate is then given by the geometric mean of these two gas temperatures.

Close inspection of Zube and Myers' results, however, shows that it is the electron excitation temperature, not the vibrational temperature, which has a significantly longer relaxation time and thus remains elevated in the nozzle expansion. The difference in temperature between the rotational and vibrational states varies from 2-15% in the nozzle with corresponding error bars of 13-22%. This would result in a modification of T_g in the dissociation rate equation by no more than about 5%. Given the already complex nature of the flow equations to be solved, it was decided not to add an additional vibrational temperature equation for this purpose; the extra computation would not be worth the minimal gain in accuracy. If future experiments show a large and definite temperature difference for hydrogen arcjet nozzles, however, a coupled vibrational temperature equation would be necessary to achieve accurate simulation results.

3.3.2 Ionization

3.3.2.1 Equilibrium Flow

The equilibrium level of ionization can be calculated from the Saha equation. Since macroscopic neutrality is also assumed and only ionizing collisions of electrons with atomic species are considered, the Saha equation may be written as

$$\frac{n_e^2}{n_S} = \frac{2u_{S^+}}{u_S}\left(\frac{2\pi m_e k T_e}{h^2}\right)^{\frac{3}{2}} e^{-\frac{E_i}{kT_e}}, \tag{3.112}$$

where u_j are the appropriate degeneracy functions and E_i is the ionization energy. The electron temperature has been specified in the above equation since for a multi-temperature plasma it is this temperature which is relevant to the ionization process. This is because the electrons carry the energy of ionization with them and it is their translational motion which is dominant in ionizing collisions with neutral atoms. For hydrogen $E_i = 2.178 \times 10^{-18}$J, or 13.598eV, while for nitrogen $E_i = 2.328 \times 10^{-18}$J, or 14.534eV. Over the range of temperatures encountered in arcjet thrusters, the degeneracies of hydrogen can be approximated as $u_{H^+} \approx 1$ and $u_H \approx 2$ [30], so that

$$\frac{n_e^2}{n_H} = 2.415 \times 10^{21} T_e^{\frac{3}{2}} e^{-\frac{E_i}{kT_e}}. \tag{3.113}$$

The degeneracies of nitrogen vary appreciably for temperatures up to 30,000°K, but they may be approximated by the linear curve fits[30]

$$u_N = 2.25 + 2.5 \times 10^{-4} T_g \quad and \quad u_{N^+} = 7.95 + 1.5 \times 10^{-4} T_g. \tag{3.114}$$

Thus the Saha equation for equilibrium ionization of nitrogen may be written as

$$\frac{n_e^2}{n_N} = 4.83 \times 10^{21} \frac{u_{N^+}}{u_N} T_e^{\frac{3}{2}} e^{-\frac{E_i}{kT_e}}. \tag{3.115}$$

The equilibrium ionization fraction for hydrogen is plotted as a function of temperature for several pressures in Figure 3.8. The effect of pressure is essentially the same as that observed for the dissociation process.

3.3.2.2 Nonequilibrium Flow

For the case of nonequilibrium flow, the net electron production rate is given by the generalized model of ionization and three-body recombination[81] as modified by Sheppard[104]:

$$\dot{n}_e = R n_e \left(S n_S - n_e^2\right), \tag{3.116}$$

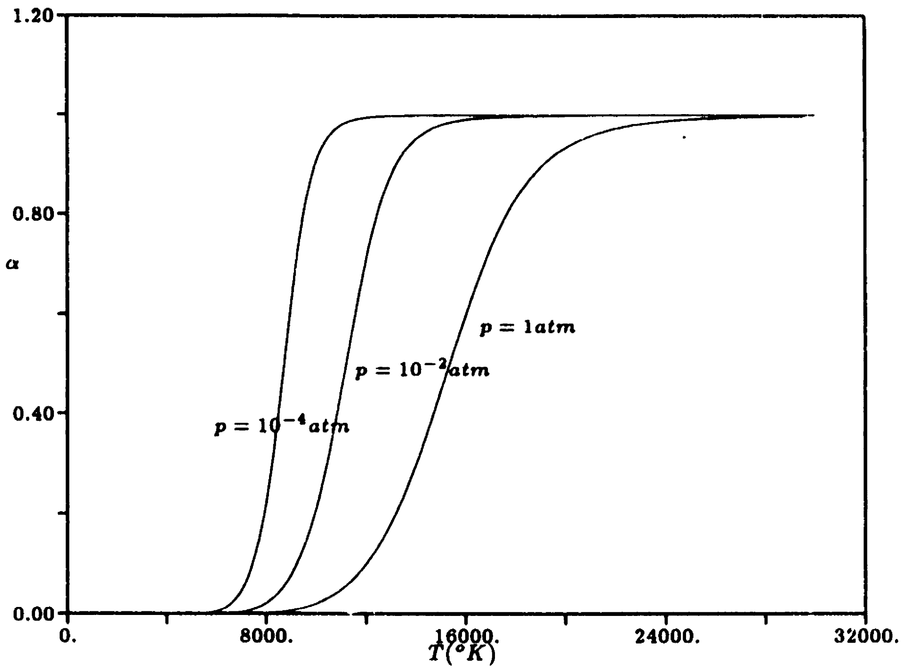

Figure 3.8: Equilibrium Ionization of Hydrogen versus Temperature and Pressure

where

$$S = \frac{2u_{S+}}{u_S}\left(\frac{2\pi m_e kT_e}{h^2}\right)^{\frac{3}{2}} e^{-\frac{B_i}{kT_e}} \qquad (3.117)$$

and

$$R = 6.985 \times 10^{-42} exp\left(\frac{(ln\frac{T_e}{1000} - 4.0833)^2}{0.8179}\right) \qquad (Sheppard) \qquad (3.118)$$

as opposed to

$$R = \frac{1.09 \times 10^{-20}}{T_e^{\frac{9}{2}}}. \qquad (Hinnov - Hirschberg) \qquad (3.119)$$

The Hinnov-Hirschberg recombination rate coefficient (Eqn. 3.119) had been used in a number of arcjet models at MIT until it was shown by Sheppard to overpredict experimental determinations of R by up to two orders of magnitude over the expected range of electron temperatures. Figure 3.9 compares both the Hinnov-Hirschberg and Sheppard models of the recombination coefficient for the hydrogen atom, the latter of which is incorporated into the model of this research.

3.3.3 Dissociation and Ionization with Thermal Nonequilibrium

An example of the effect of combined dissociation and ionization processes on the equilibrium mole fractions of hydrogen species is shown in Figure 3.10 for a pressure

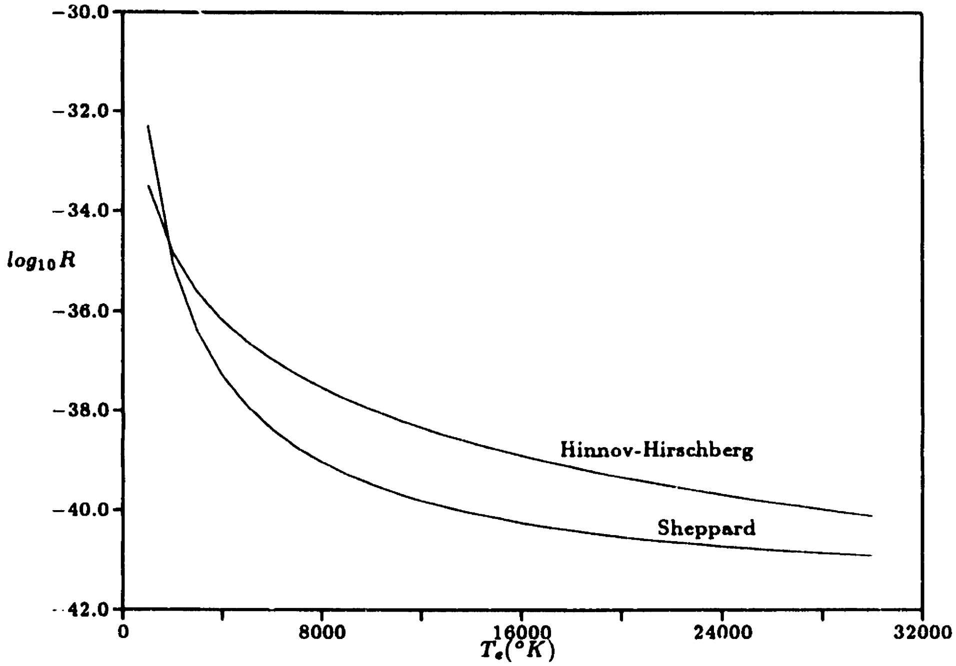

Figure 3.9: Comparison of Sheppard and Hinnov-Hirshberg Recombination Coefficient Models for Hydrogen

of 1atm; essentially a maximum in the mole fraction of atomic hydrogen is created, lying between the dissociation and ionization regimes. The calculation of the hydrogen constituent mole fractions in this case is accomplished by simultaneous solution of Equations 3.92 and 3.113 with atom conservation and enthalpy conservation as constraints. In terms of the ion mole fraction the equation to be solved is of the form

$$\frac{2c^3}{ab^2} x_{H^+}^4 + \frac{c}{b} x_{H^+}^2 + x_{H^+} - 1 = 0, \tag{3.120}$$

where

$$a = \frac{K_p}{kT_g} \tag{3.121}$$

$$b = 2.415 \times 10^{21} T_e^{\frac{3}{2}} e^{-\frac{E_i}{kT_e}} \tag{3.122}$$

$$c = \frac{\rho}{m_H}. \tag{3.123}$$

For simple plots such as that in Figure 3.10, Equation 3.120 may be solved by a hybrid Newton-Raphson/bisection root-finding scheme in the interval between 0 and 1, after which the atomic and diatomic hydrogen mole fractions are found by simple substitution. When applied as a subroutine within an overall fluid code, however, it is not the gas temperature but rather the enthalpy which is known at every point, and which also depends on the mole fractions. Therefore the mole fraction equations must

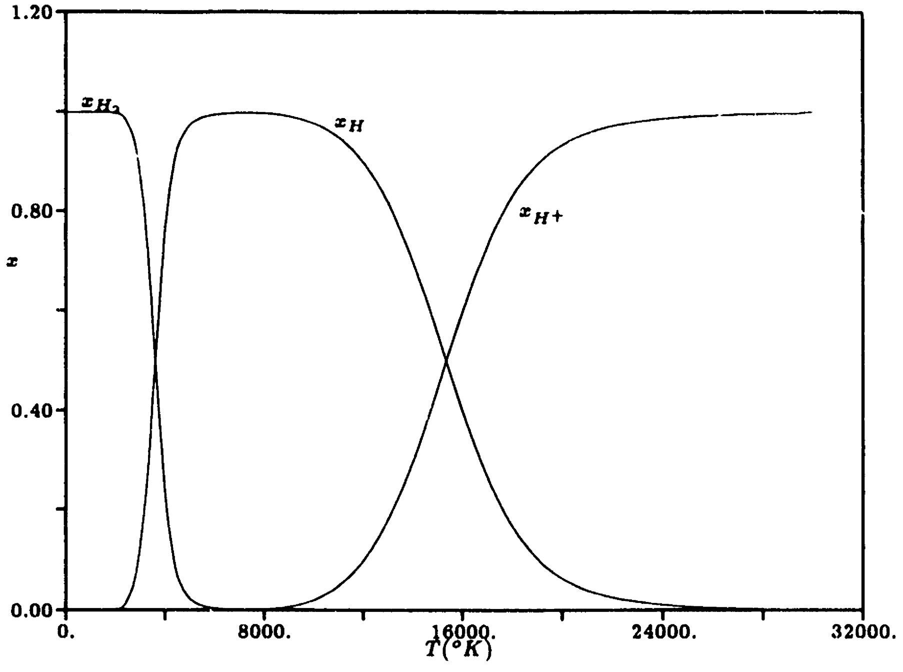

Figure 3.10: Equilibrium Dissociation and Ionization of Hydrogen at 1 atm

be solved simultaneously with the constant enthalpy condition in order to obtain a consistent solution. Since the enthalpy contains an exponential term of the form $e^{\frac{\theta_v}{T_g}}$, the solution of this system of nonlinear equations is relatively difficult. In practice an alternative solution technique would be used such as the element potential method, which minimizes the Gibbs free energy while applying atom conservation restraints through Lagrange multipliers.

Figure 3.10 illustrates a special case, however, because the gas and electron temperatures were taken to be equal, which in general is not a valid assumption. At low densities the electron and heavy species temperatures are effectively uncoupled, and while T_g is a function of the gas dynamics of the application and the spatial location, the electron conservation equations are generally balanced such that T_e is on the order of 1eV everywhere in the flow. At higher densities and pressures greater than 1atm, the two temperatures are more closely coupled. The low power electrothermal arcjet falls somewhere between these two extremes but closer to one-temperature equilibrium than the MPD thruster. As an illustration, Figures 3.11 and 3.12 contain plots of the equilibrium mole fractions of hydrogen with a fixed electron temperature and varying gas temperature up to 24,000°K. Note that even at low gas temperatures on the order of 3,000°K, significant ionization occurs for an electron temperature greater than 1eV. In addition, for the $T_e = 18,000°K$ case the ionization process dominates over the dissociation process at all gas temperatures. So for unequal gas and electron tem-

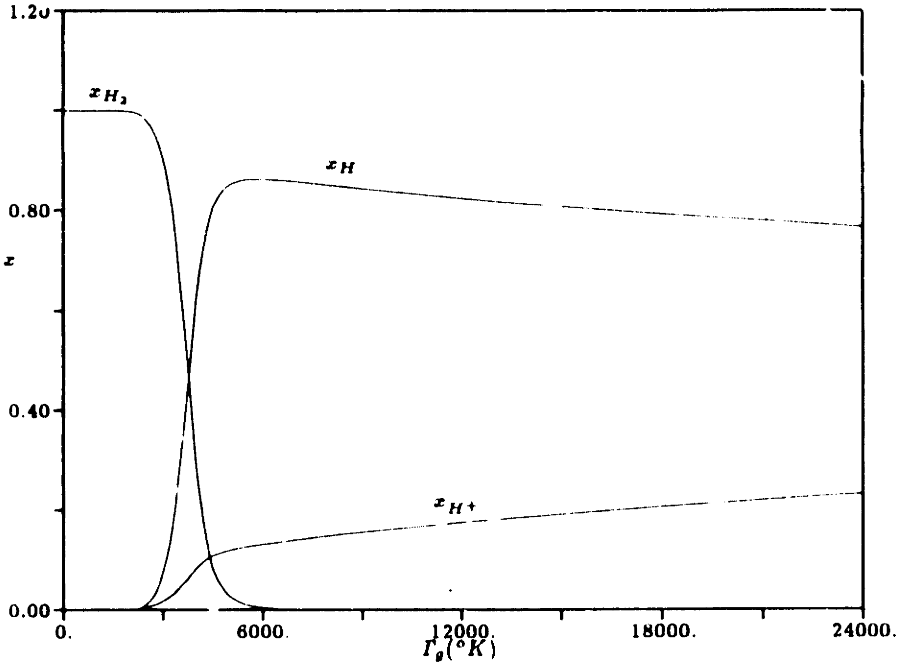

Figure 3.11: Equilibrium Dissociation and Ionization of Hydrogen at 1 atm, $T_e = 13,000°K$

peratures, the equilibrium composition of a gas can be much different from that when $T_g = T_e$, thereby significantly altering the values of the transport coefficients and the overall flow characteristics.

For the case of nonequilibrium dissociation and ionization, the ion and atomic species continuity equations are integrated independently. Thus the two-temperature condition is implicit, creating no added complexity in the model.

3.4 Transport Properties

In general, for a plasma in the presence of magnetic and electric fields, the transport properties are functions of the direction of transport with respect to these fields. The transport equations thus become tensor equations. For example, the generalized Ohm's Law of Equation 3.23, neglecting ion currents, pressure gradients, and the Hall term, can be written in tensor notation as $\vec{j}_e = \bar{\bar{\sigma}} \cdot \vec{E}'$ Here $\bar{\bar{\sigma}}$ is the electrical conductivity tensor, or dyad. For the case of a magnetic field in the $\hat{z}$ direction only, the equivalent expression in terms of matrices is

$$\begin{bmatrix} j_{ex} \\ j_{ey} \\ j_{ez} \end{bmatrix} = \begin{bmatrix} \sigma_\perp & -\sigma_H & 0 \\ \sigma_H & \sigma_\perp & 0 \\ 0 & 0 & \sigma_\parallel \end{bmatrix} \begin{bmatrix} E'_x \\ E'_y \\ E'_z \end{bmatrix}, \qquad (3.124)$$

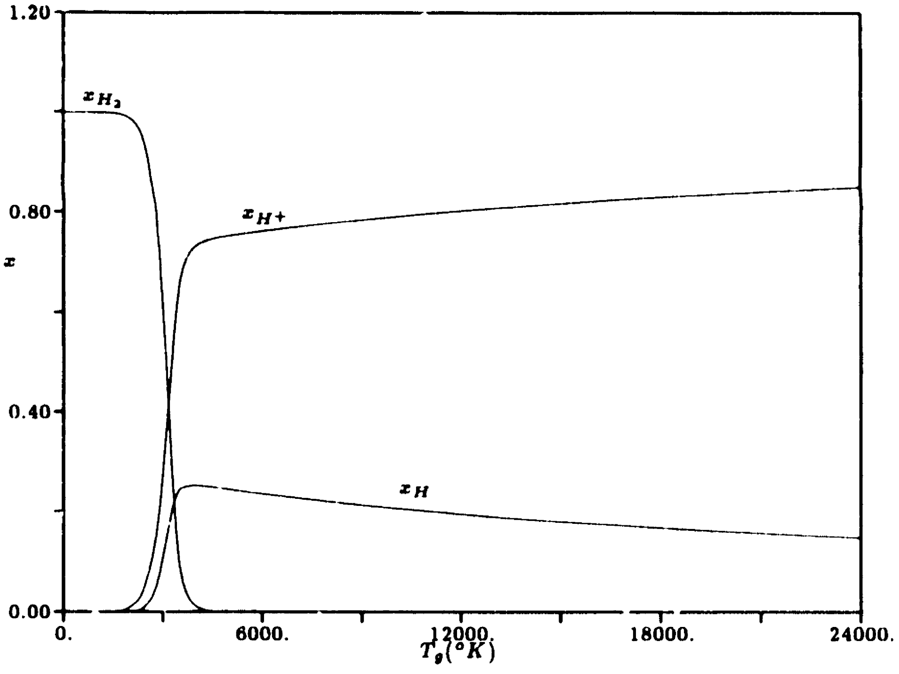

Figure 3.12: Equilibrium Dissociation and Ionization of Hydrogen at 1atm, $T_e = 18,000^oK$

where

$$\sigma_{\|} \sim \frac{e^2 n_e}{m_e \sum_r \nu_{er}} \qquad \sigma_{\perp} = \frac{\sigma_{\|}}{1+\beta^2} \qquad \sigma_H = \frac{\beta\sigma_{\|}}{1+\beta^2} \tag{3.125}$$

and β is the Hall Parameter. The quantity $\sigma_{\|}$ is called the longitudinal conductivity, as it governs the flow of current in the direction parallel to the magnetic field. The quantity $\sigma_{\perp}$ is the perpendicular or transverse conductivity, which controls electrical current in the direction perpendicular to the magnetic field and parallel to the electric field component. Finally, σ_H, denoted as the Hall conductivity, governs current flow in the direction perpendicular to both the magnetic field and the electric field component. Since the self-magnetic field is neglected in this model, the plasma is assumed to be isotropic, with $\sigma_{\perp} = \sigma_{\|}$ and $\sigma_H = 0$. The electron and heavy species thermal conductivities can be similarly formulated in tensor notation and are also considered to be isotropic functions. Thermal diffusion is not included in this model.

3.4.1 Viscosity

An equation for the viscosity coefficient of a single component gas may be obtained by examining the form of the pressure tensor in terms of a perturbed velocity distribution function. Although a closed form solution of this equation is not possible, an approximate solution yielding an expression for the coefficient of viscosity can be obtained to any order with the use of Sonine polynomial expansions. To lowest order the viscosity of a pure gas is given by[50]

$$\mu = \frac{5}{16}\left(\frac{\sqrt{\pi m k T_g}}{\pi \sigma^2 \Omega^{(2,2)}}\right) = 2.6693 \times 10^{-26}\frac{(M T_g)^{\frac{1}{2}}}{\overline{\Omega}^{(2,2)}}\,, \tag{3.126}$$

where σ is the collision diameter, $\Omega^{(2,2)}$ is the viscosity collision integral, M is the molecular weight, and $\overline{\Omega}^{(2,2)}$ is the average effective viscosity collision integral. Higher order corrections are not considered in this research because the marginal gains in accuracy do not outweigh the substantial increase in computational complexity.

The kinetic theory of multicomponent gases has been rigorously applied to the calculation of the viscosity coefficient by Curtiss and Hirschfelder[25]. For a gas composed of n different species, the lowest order approximation to the coefficient of viscosity can be written as the ratio of two determinants:

$$\mu_{tot} = -\frac{\begin{vmatrix} H_{11} & H_{12} & \cdots & H_{1n} & x_1 \\ H_{12} & H_{22} & \cdots & H_{2n} & x_2 \\ \vdots & \vdots & & \vdots & \vdots \\ H_{1n} & H_{2n} & \cdots & H_{nn} & x_n \\ x_1 & x_2 & \cdots & x_n & 0 \end{vmatrix}}{\begin{vmatrix} H_{11} & H_{12} & \cdots & H_{1n} \\ H_{12} & H_{22} & \cdots & H_{2n} \\ \vdots & \vdots & & \vdots \\ H_{1n} & H_{2n} & \cdots & H_{nn} \end{vmatrix}} \tag{3.127}$$

where

$$H_{ii} = \frac{x_i^2}{\mu_i} + \sum_{k=1,k\neq i}^{n} \frac{2x_i x_k}{(M_i + M_k)}\frac{\hat{R}T_g}{pD_{ik}}\left[1 + \frac{3}{5}\frac{M_k}{M_i}\frac{\Omega_{ik}^{(2,2)}}{\Omega_{ik}^{(1,1)}}\right] \tag{3.128}$$

and

$$H_{ij} = -\frac{2x_i x_k}{(M_i + M_j)}\frac{\hat{R}T_g}{pD_{ij}}\left[1 - \frac{3}{5}\frac{\Omega_{ij}^{(2,2)}}{\Omega_{ij}^{(1,1)}}\right] \qquad (i \neq j). \tag{3.129}$$

Here x_i is the mole fraction, M_i is the molecular weight, and μ_i is the pure viscosity of component i. A first approximation to the coefficient of binary diffusion for species i and j (D_{ij}) is given by

$$D_{ij} = \frac{3}{16}\frac{\sqrt{2\pi k^3 T_g^3/\mu_{ij}}}{p_g \pi \sigma^2 \Omega^{(1,1)}} = 2.6628 \times 10^{-22}\frac{T_g^{\frac{3}{2}}}{p_g \overline{\Omega}_{ij}^{(1,1)}}\left(\frac{M_i + M_j}{2M_i M_j}\right)^{\frac{1}{2}}, \tag{3.130}$$

where μ_{ij} is the reduced mass of species i and j and $\overline{\Omega}_{ij}^{(1,1)}$ is the average effective collision integral for diffusion. Equation 3.127 can be expanded as

$$\mu_{tot} = \sum_{i=1}^{n} \frac{x_i^2}{H_{ii}} - \sum_{i=1}^{n} \sum_{j=1,j\neq i}^{n} \frac{x_i x_j H_{ij}}{H_{ii} H_{jj}} + \sum_{i=1}^{n} \sum_{j=1,j\neq i}^{n} \sum_{k=1,k\neq i}^{n} \frac{x_j x_k H_{ij} H_{ik}}{H_{ii} H_{jj} H_{kk}} \cdots \tag{3.131}$$

Buddenberg and Wilke[12] took advantage of the fact that the off-diagonal elements H_{ij} are small compared to the diagonal elements H_{ii} in order to derive the following approximate formula for the viscosity coefficient of a multicomponent gas:

$$\mu_{tot} \approx \sum_{i=1}^{n} \frac{\mu_i}{1 + 1.385 \frac{\mu_i}{x_i} \sum_{j=1,j\neq i}^{n} \frac{x_j}{\rho_i D_{ij}}}. \tag{3.132}$$

The empirical factor 1.385 was introduced to more closely correlate the results with experimental data. In order to further simplify the calculation of μ_{tot}, Wilke[121] eliminated the diffusion coefficients in Equation 3.132 to obtain the following approximation:

$$\mu_{tot} \approx \sum_{i=1}^{n} \frac{\mu_i}{1 + \frac{1}{x_i} \sum_{j=1,j\neq i}^{n} x_j \psi_{ij}}, \tag{3.133}$$

where

$$\psi_{ij} = \frac{\left[1 + (\mu_i/\mu_j)^{\frac{1}{2}} (M_j/M_i)^{\frac{1}{4}}\right]^2}{(4/\sqrt{2}) \left[1 + (M_i/M_j)\right]^{\frac{1}{2}}}. \tag{3.134}$$

Each of the two previous approximations yield similar, yet somewhat unsatisfactory results, especially in the regime of partial ionization. This results from the rough approximation to the mixture viscosity formula used and from the uncertainty in the diffusion and unlike-particle collision integrals required. Computational complexity precludes the use of more accurate approximations within the framework of a fluid dynamic code, so the solution in this case is to employ an even simpler mixture rule derived by Mitchner and Kruger[81] from mean free path arguments, with empirical modifications to better correlate the results with accurate theoretical and experimental data. This final approximation is given by

$$\mu_{tot} \approx \sum_{i=1}^{n} \frac{n_i \mu_i}{\sum_{j=1}^{n} n_j \chi_{ij}}, \tag{3.135}$$

where

$$\chi_{ij} = \sqrt{\frac{2\mu_{ij}}{m_i} \frac{\bar{\Omega}_{ij}^{(2,2)}}{\bar{\Omega}_{ii}^{(2,2)}}}. \tag{3.136}$$

For the purposes of this research, one empirical constant for the ionization region is incorporated into Equation 3.135, and interactions between hydrogen molecules and hydrogen ions are neglected. The final result for the gas viscosity can then be written

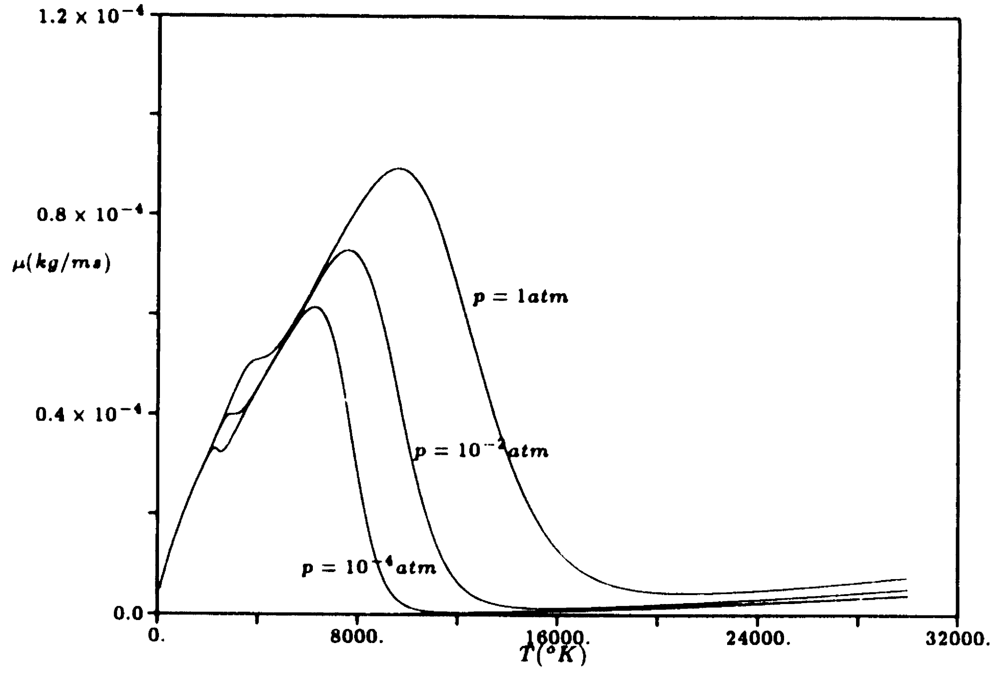

Figure 3.13: Equilibrium Coefficient of Viscosity for Hydrogen versus Temperature and Pressure

explicitly as

$$\mu_g \approx \frac{n_{H_2}\mu_{H_2}}{n_{H_2} + n_H\sqrt{\frac{2}{3}}\frac{\bar{\Omega}^{(2,2)}_{H_2-H}}{\bar{\Omega}^{(2,2)}_{H_2-H_2}}} + \frac{n_H\mu_H}{n_H + n_{H_2}\sqrt{\frac{4}{3}}\frac{\bar{\Omega}^{(2,2)}_{H_2-H}}{\bar{\Omega}^{(2,2)}_{H-H}} + 2n_{H^+}\frac{\bar{\Omega}^{(2,2)}_{H-H^+}}{\bar{\Omega}^{(2,2)}_{H-H}}}$$

$$+ \frac{n_{H^+}\mu_{H^+}}{n_{H^+} + 2n_H\frac{\bar{\Omega}^{(2,2)}_{H-H^+}}{\bar{\Omega}^{(2,2)}_{H^+-H^+}}}. \qquad (3.137)$$

The viscosity of electrons is considered negligible and is thus neglected in the above expression.

For hydrogen in chemical kinetic and ionizational equilibrium, the coefficient of viscosity has been calculated by various authors using multiple order approximations (Belov[7], Brezing[10], Devoto[29], Grier[42, 43], and Vanderslice et al.[117]). Figure 3.13 shows the equilibrium hydrogen viscosity coefficient obtained with Equation 3.137 as a function of pressure and temperature, while Figure 3.14 compares μ_g calculated from this research with the results of some of the aforementioned studies for a pressure of 1atm. Excellent agreement is achieved over the entire temperature range, including the dissociation and ionization regions. A pure viscosity coefficient that increases monotonically with temperature is exhibited by all three components of the hydrogen gas (molecules, atoms, and ions). The value of the atomic viscosity is somewhat less than that of the molecular viscosity, however, and in addition the ionic viscosity is

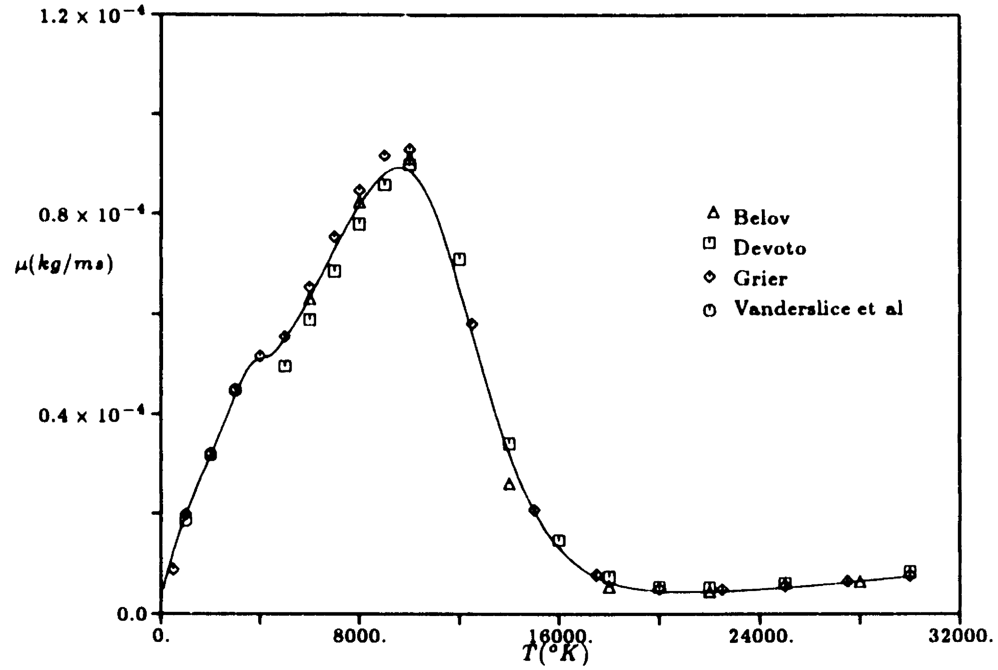

Figure 3.14: Comparison of Equilibrium Hydrogen Viscosity Coefficient at 1 atm with Previous Work

more than an order of magnitude smaller than the neutral viscosities. This fact is directly related to differences in the pure average effective collision integrals for the three components (*cf.* Tables B.2 and B.3), and is responsible for the local maxima in the mixture viscosity (μ_g) located in the dissociation and ionization regions. The dominant pressure effects on the mixture viscosity are due to the displacement versus temperature of the dissociating and ionizing regions themselves, although the ionic viscosity also increases slightly with increasing pressure.

3.4.2 Thermal Conductivity

Analogous to the coefficient of viscosity, the thermal conductivity coefficient for a gas may be calculated to any order accuracy with the use of Sonine polynomial expansions. For pure monatomic gases, the first approximation to the coefficient of thermal conductivity is given by

$$\kappa_{monatomic} = \frac{15}{4}\frac{\hat{R}}{M}\mu. \qquad (3.138)$$

For polyatomic gases, the effect of internal degrees of freedom on the thermal conductivity must be taken into account. This is accomplished by means of the Eucken correction, which approximates the transfer of energy between internal and translational degrees of freedom:

$$\kappa_{polyatomic} = \frac{15}{4}\frac{\hat{R}}{M}\mu\left(\frac{4}{15}\frac{\hat{c}_v}{\hat{R}} + \frac{3}{5}\right). \tag{3.139}$$

For monatomic gases, for which $\hat{c}_v = \frac{3}{2}\hat{R}$, the Eucken formula reduces to Equation 3.138. For diatomic molecules such as H_2, $\hat{c}_v = \frac{5}{2}\hat{R}$ and the appropriate expression is

$$\kappa_{diatomic} = \frac{19}{4}\frac{\hat{R}}{M}\mu. \tag{3.140}$$

The first approximation to the thermal conductivity of a multicomponent gas consists of a sum of terms similar in form to the ratio of determinants given in the multicomponent viscosity formula and is too cumbersome to state explicitly here. The full expression depends on the pure component thermal conductivities, the binary diffusion coefficients, the thermal diffusion coefficients, the species molecular weights, and the other thermodynamic variables and collision integrals present in the H_{ii} and H_{ij} terms of Equations 3.127 - 3.129. For chemically reacting flows, the thermal conductivity can be thought of as the sum of a contribution from the heat of reaction, κ_r, and the normal "frozen" thermal conductivity, κ_f [117]. In this research, however, the transport of the hydrogen energy of dissociation is incorporated by carrying the dissociation energy with the internal energy of hydrogen atoms, and the reactive effect on the multicomponent thermal conductivity is neglected. Again various approximations to the mixture thermal conductivity are available in the literature (Brokaw[11], Vanderslice et al.[117]); however all are more complicated than those mentioned for the mixture viscosity, and the agreement with rigorous theory is less than adequate. Therefore the mean free path mixture formula of Mitchner and Kruger is again utilized, given in this case by

$$\kappa_{tot} \approx \sum_{i=1}^{n} \frac{n_i \kappa_i}{\sum_{j=1}^{n} n_j \chi_{ij}}, \tag{3.141}$$

where χ_{ij} is given by Equation 3.136. For the case of dissociating and ionizing hydrogen gas, neglecting interactions between molecules and ions, the resulting formula again includes one empirical factor in the ionization regime and is given by

$$\kappa_g \approx \frac{n_{H_2}\kappa_{H_2}}{n_{H_2} + n_H\sqrt{\frac{2}{3}}\frac{\overline{\Omega}^{(2,2)}_{H_2-H}}{\overline{\Omega}^{(2,2)}_{H_2-H_2}}} + \frac{n_H\kappa_H}{n_H + n_{H_2}\sqrt{\frac{4}{3}}\frac{\overline{\Omega}^{(2,2)}_{H_2-H}}{\overline{\Omega}^{(2,2)}_{H-H}} + \frac{3}{2}n_{H^+}\frac{\overline{\Omega}^{(2,2)}_{H-H^+}}{\overline{\Omega}^{(2,2)}_{H-H}}}$$

$$+ \frac{n_{H^+}\kappa_{H^+}}{n_{H^+} + \frac{3}{2}n_H\frac{\overline{\Omega}^{(2,2)}_{H-H^+}}{\overline{\Omega}^{(2,2)}_{H^+-H^+}}}. \tag{3.142}$$

The above equations are sufficient to calculate the coefficient of thermal conductiv-

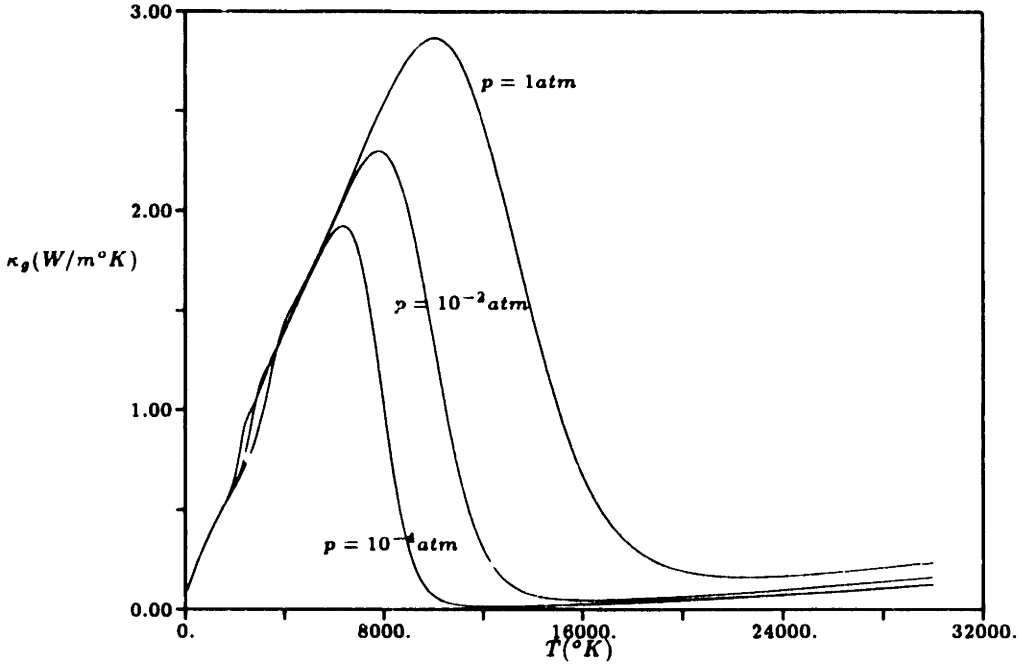

Figure 3.15: Equilibrium Heavy Species Coefficient of Thermal Conductivity for Hydrogen versus Temperature and Pressure

ity for each heavy species and the resulting thermal conductivity of the hydrogen gas (κ_g). In this model, however, since the electrons and heavy species are treated as two separate fluids, the electron coefficient of thermal conductivity must be individually known. In order to determine κ_e, a separate calculation is performed using Equation 3.141 for the electrons only:

$$\kappa_e = \frac{n_{H^+}\kappa_e}{(1+\sqrt{2})n_{H^+} + \sqrt{2}n_H \frac{\overline{\Omega}^{(2,2)}_{e-H}}{\overline{\Omega}^{(2,2)}_{e-e}} + \sqrt{2}n_{H_2} \frac{\overline{\Omega}^{(2,2)}_{e-H_2}}{\overline{\Omega}^{(2,2)}_{e-e}}}, \tag{3.143}$$

where use has been made of the fact that $\overline{\Omega}^{(2,2)}_{e-H^+} = \overline{\Omega}^{(2,2)}_{e-e}$.

Figures 3.15 and 3.16 show the variation of κ_g and κ_e with respect to temperature and pressure for hydrogen. Since the gas thermal conductivity is proportional to the viscosity, κ_g exhibits behavior similar to that of μ_g as a function of temperature. The electron coefficient of thermal conductivity increases monotonically with temperature and dominates over the ionic thermal conductivity once the gas becomes ionized due to the much smaller mass of the electrons. The total (electron plus heavy species) thermal conductivity coefficient at 1atm is compared in Figure 3.17 with the results of more rigorous calculations by Grier[42, 43] and Devoto[29]. The comparison shows good agreement over the range of temperatures shown.

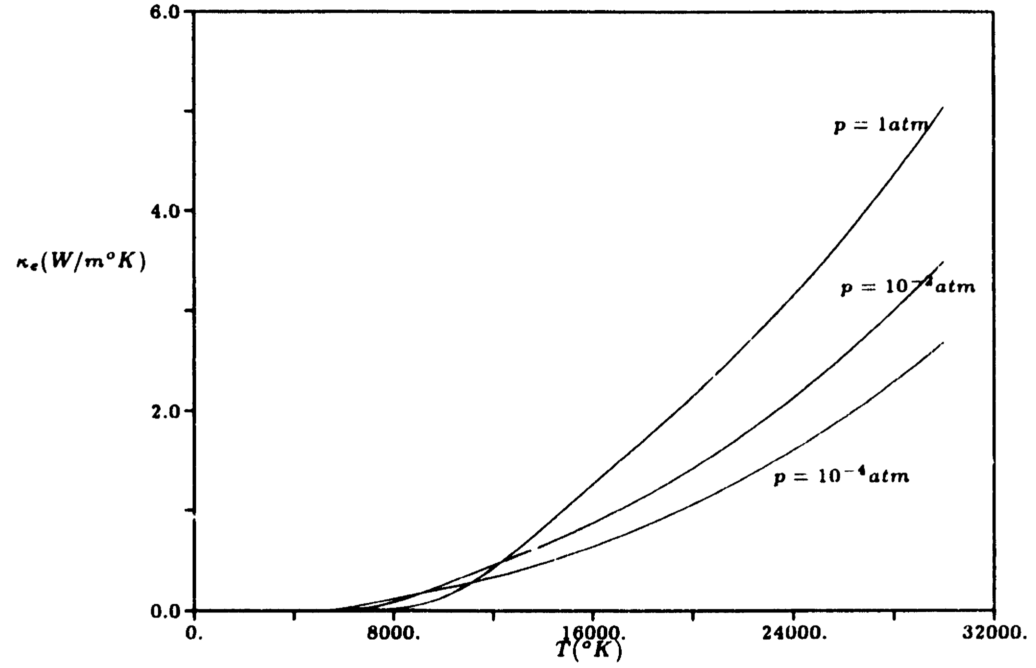

Figure 3.16: Equilibrium Electron Coefficient of Thermal Conductivity in Hydrogen versus Temperature and Pressure

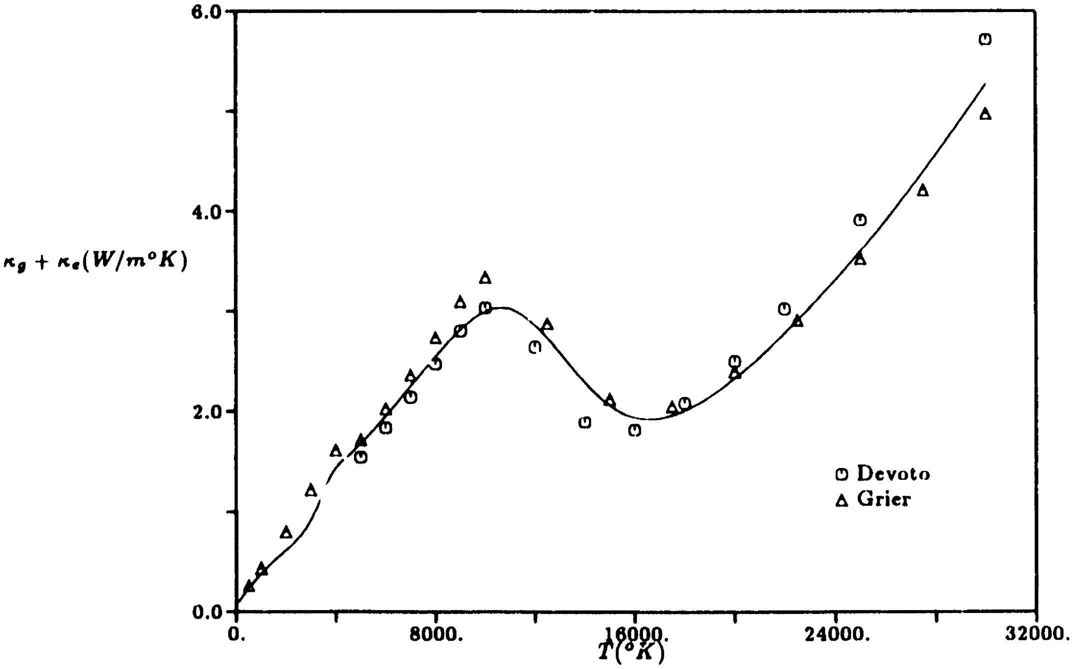

Figure 3.17: Comparison of Equilibrium Thermal Conductivity of Hydrogen with Previous Work

3.4.3 Electrical Conductivity

Within a factor of two or three, the electrical conductivity of a conducting gas is given in general by the simple formula

$$\sigma = \sigma_e + \sigma_i, \tag{3.144}$$

where

$$\sigma_e = \frac{e^2 n_e}{m_e \sum_g \bar{\nu}_{eg}} \quad and \quad \sigma_i = \frac{e^2 n_i}{m_i \sum_g \bar{\nu}_{eg}} \frac{\rho_i}{\rho} \left[1 + \frac{\rho_n}{\rho_i} \frac{\bar{\nu}_{en}}{\bar{\nu}_{in}} \right]. \tag{3.145}$$

In the above expressions, $\sum_g \bar{\nu}_{eg}$ represents the collision frequency of electrons with all heavy species, $\bar{\nu}_{en}$ is the electron-neutral collision frequency, and $\bar{\nu}_{in}$ is the ion-neutral collision frequency. Assuming that $n_e = n_i$ and noting that $m_e/m_i \ll 1$ implies that

$$\sigma \approx \sigma_e = \frac{e^2 n_e}{m_e \sum_g \bar{\nu}_{eg}}. \tag{3.146}$$

In general, asymptotic or Sonine polynomial expansions must be used in order to obtain an accurate value of the electrical conductivity. Exact analytic values are known only in the limiting cases of weak or full ionization, given respectively by the Lorentzian conductivity

$$\sigma = \frac{4\pi}{3} \frac{e^2 n_e}{kT_e} \int_0^\infty \frac{v^4 f_e^M(v)}{\sum_n \bar{\nu}_{en}(v)} dv \tag{3.147}$$

and the Spitzer-Härm conductivity

$$\sigma = 1.975 \frac{e^2 n_e}{m_e \bar{\nu}_{ei}}. \tag{3.148}$$

To calculate the electrical conductivity at an arbitrary level of ionization without performing complex expansion procedures, two approximations of note have been suggested. Devoto proposed an approximate formula based on the binary diffusion coefficients[28] which is given by

$$\sigma \approx \frac{e^2 n}{\rho k T_e} \sum_j n_j m_j D_{ej}, \tag{3.149}$$

while Grier derived a formula that modifies the first approximation by a second approximation correction factor[43]. For hydrogen this formulation can be expressed as follows:

$$\sigma_0 = \frac{3}{16} \sqrt{\frac{2}{\pi m_e k T_e}} \frac{x_{H^+} e^2}{x_{H^+} \bar{\Omega}^{(1,1)}_{e-H^+} + (1 - x_{H^+}) \bar{\Omega}^{(1,1)}_{e-H}} \tag{3.150}$$

and

$$\sigma = \frac{\sigma_0}{1 - \Delta_c}, \tag{3.151}$$

where

$$\triangle_c = \frac{5A_1^2}{2A_0A_2}$$

$$A_0 = x_{H^+}4\sqrt{\pi}\overline{\Omega}^{(1,1)}_{e-H^+} + x_H 4\sqrt{\pi}\overline{\Omega}^{(1,1)}_{e-H}$$

$$A_1 = x_{H^+}Z_{e-H^+}4\sqrt{\pi}\overline{\Omega}^{(1,1)}_{e-H^+} + x_H Z_{e-H}4\sqrt{\pi}\overline{\Omega}^{(1,1)}_{e-H}$$

$$A_2 = x_{H^+}\left[Y_{e-H}4\sqrt{\pi}\overline{\Omega}^{(1,1)}_{e-H^+} + 0.2\sqrt{2}Z^*_{e-e}4\sqrt{\pi}\overline{\Omega}^{(1,1)}_{e-e}\right] + x_H Y_{e-H}4\sqrt{\pi}\overline{\Omega}^{(1,1)}_{e-H}$$

$$Z_{ij} = 1 - \frac{6}{5}C^*_{ij} \qquad Z^*_{ii} = 2A^*_{ii} \qquad Y_{ij} = \frac{5}{2} - \frac{6}{5}B^*_{ij}$$

$$A^*_{ij} = \frac{\overline{\Omega}^{(2,2)}_{ij}}{\overline{\Omega}^{(1,1)}_{ij}} \qquad B^*_{ij} = \frac{5\overline{\Omega}^{(1,2)}_{ij} - 4\overline{\Omega}^{(1,3)}_{ij}}{\overline{\Omega}^{(1,1)}_{ij}} \qquad C^*_{ij} = \frac{\overline{\Omega}^{(1,2)}_{ij}}{\overline{\Omega}^{(1,1)}_{ij}}.$$

Grier's method (Equations 3.150 and 3.151) was chosen as the basis for the electrical conductivity model of this research. Instead of performing the additional computations necessary to determine $\triangle_c$, however, the second approximation correction factor is calculated by interpolation of Grier's previously determined data as a function of temperature and pressure. The resulting value of the thermal conductivity is therefore accurate near chemical and ionizational equilibrium, but not necessarily accurate to the same order in nonequilibrium regimes. This is in contrast to the more general mixture rules previously described for the viscosity and thermal conductivity coefficients. Note that the average effective collision integrals in Equation 3.150 are the diffusion cross-sections, which are tabulated as a function of temperature in Tables B.2 and B.3.

For a hydrogen gas, the electrical conductivity calculated with Equations 3.150 and 3.151 is plotted as a function of temperature and pressure in Figure 3.18. It is apparent that σ increases monotonically with increasing temperature and also with increasing pressure with one qualification. That is, as the pressure is increased, the ionization region is displaced further to the right in Figure 3.18, reducing the number of charged particles and thus lowering the electrical conductivity at a given temperature. Thus below a certain temperature- and pressure-dependent critical parameter, σ decreases with increasing pressure, while above it σ increases with pressure. Equilibrium results using this approximation are compared with detailed calculations by Devoto[29] and Grier[43] for a pressure of 1atm in Figure 3.19. The agreement is satisfactory except perhaps at high temperatures (> 30,000°K), but this is of little concern since these temperatures are not expected to occur within arcjet thrusters. In general, it can be stated that the simplified models of transport coefficients derived in this section

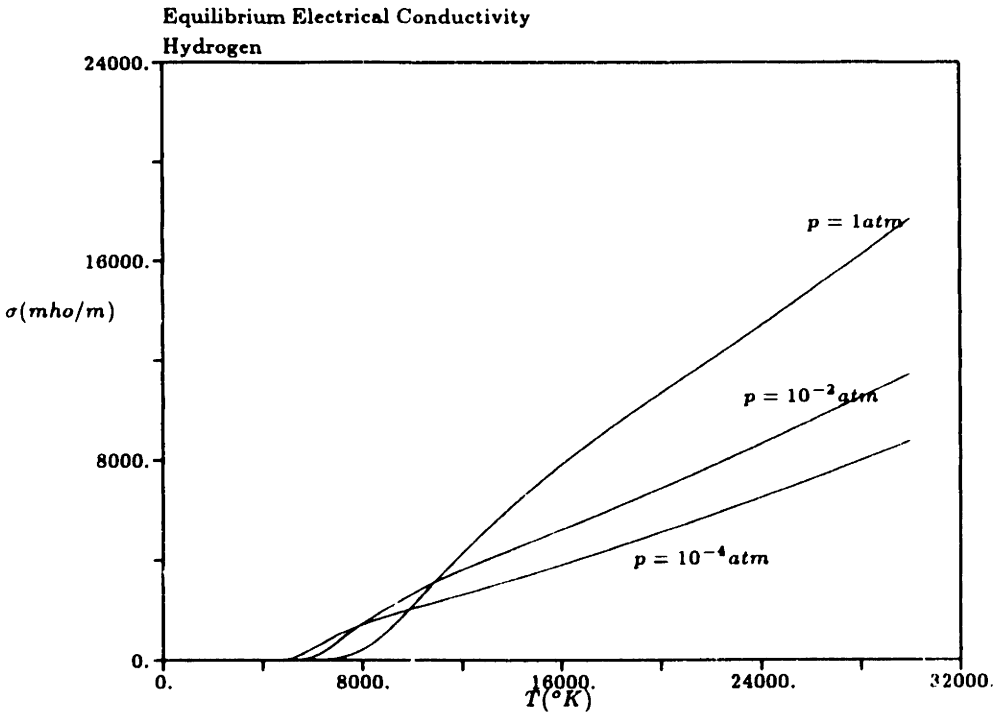

Figure 3.18: Equilibrium Hydrogen Electrical Conductivity versus Temperature and Pressure

are sufficiently accurate for numerical calculations over a wide range of temperatures and pressures, particularly in the temperature range 0 – 30,000°K and pressure range 10^{-3} – 10^{0}atm) expected in low power arcjet simulations.

3.4.4 Collision Frequencies

In order to solve the two energy conservation equations, it is necessary to know the collision frequency between electrons and heavy species, $\sum_g \nu_{eg} = \nu_{eS_2} + \nu_{eS} + \nu_{eS^+}$. These collision frequencies are given by

$$\nu_{eS_2} = n_{S_2}\bar{c}_e\overline{Q}_{eS_2}, \tag{3.152}$$

$$\nu_{eS} = n_S\bar{c}_e\overline{Q}_{eS}, \tag{3.153}$$

and

$$\nu_{eS^+} = n_e\bar{c}_e\overline{Q}_{eS^+}, \tag{3.154}$$

where the $\overline{Q}_{er}$ are average electron momentum transfer cross-sections with species r. For hydrogen, $\overline{Q}_{eH}$ is taken from DeVoto[29] and $\overline{Q}_{eH_2}$ is taken from Itikawa[52], both tabulated for electron temperatures up to 25,000°K in Appendix B. The coulombic cross-section $\overline{Q}_{eH^+}$ is given by

$$\overline{Q}_{eH^+} = 6\pi\bar{b}_0^2 \ln\Lambda = \frac{e^4}{24\pi(\epsilon_0 kT_e)^2}\ln\Lambda, \tag{3.155}$$

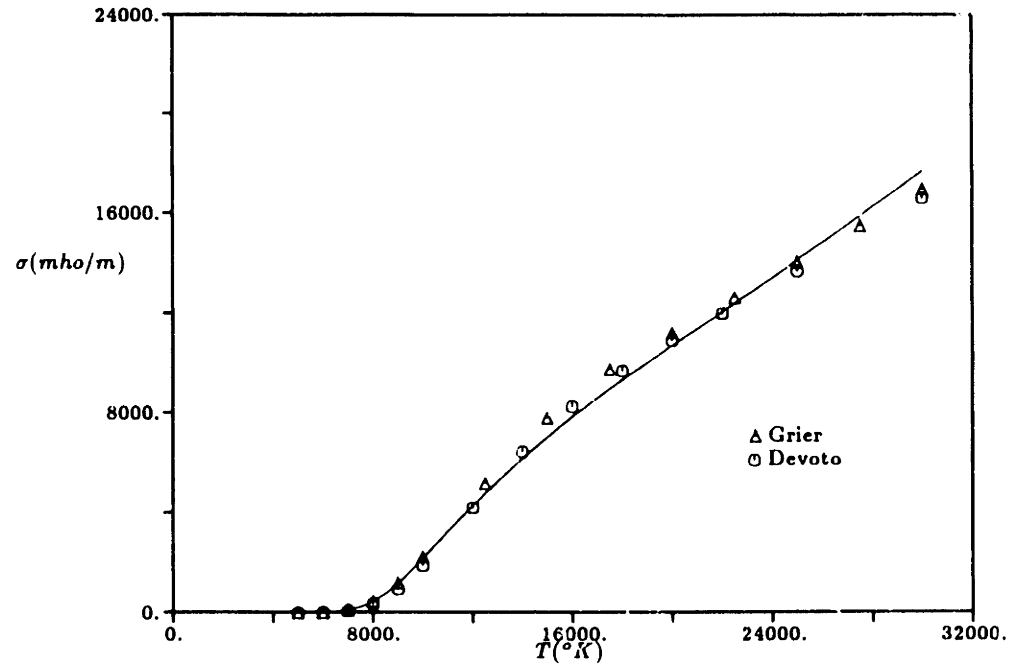

Figure 3.19: Comparison of Equilibrium Hydrogen Electrical Conductivity with Previous Work at 1 atm

where

$$\Lambda = \frac{12\pi(\epsilon_0 k T_e)^{\frac{3}{2}}}{e^3 n_e^{\frac{1}{2}}} = 1.239 \times 10^7 \left(\frac{T_e^3}{n_e}\right)^{\frac{1}{2}}. \qquad (3.156)$$

3.4.5 Collision Integrals

A number of collision integrals are required by this research in order to calculate transport coefficients. The relevant integrals for this purpose are average effective collision integrals, denoted by $\overline{\Omega}^{(2,2)}_{ij}$ for momentum transfer and $\overline{\Omega}^{(1,1)}_{ij}$ for diffusion processes. For the components of hydrogen, collision integrals have been evaluated analytically by several authors for the temperature range $0-30,000^o$K. Tables B.2 and B.3 list values for the average effective collision integrals used in this research Values of the non-Coulombic integrals are a function of temperature only, while values of the Coulombic integrals are also a function of pressure and thus specific to a pressure of 1atm in this table. In addition, only the values of $\overline{\Omega}^{(i,i)}_{H^+-H^+}$ are presented here since for a gas in thermal equilibrium the electron temperature is equal to the ion temperature, implying that $\overline{\Omega}^{(i,i)}_{H^+-H^+} = \overline{\Omega}^{(i,i)}_{e-H^+} = \overline{\Omega}^{(i,i)}_{e-e}$. In the nonequilibrium case where $T \neq T_i$, the relation $\frac{T_e^2}{T_i^2}\overline{\Omega}^{(i,i)}_{H^+-H^+} = \overline{\Omega}^{(i,i)}_{e-H^+} = \overline{\Omega}^{(i,i)}_{e-e}$ would hold true. Data were taken from Vanderslice et al.[117] for $\overline{\Omega}^{(2,2)}_{H_2-H_2}$, $\overline{\Omega}^{(2,2)}_{H_2-H}$, $\overline{\Omega}^{(2,2)}_{H-H}$, $\overline{\Omega}^{(1,1)}_{H_2-H_2}$, and $\overline{\Omega}^{(1,1)}_{H-H}$ up to $15,000^oK$. Additional data were taken from Belov[7] for $\overline{\Omega}^{(2,2)}_{H-H}$ and from Grier[43] for $\overline{\Omega}^{(2,2)}_{H-H^+}$,

$\overline{\Omega}^{(1,1)}_{e-H}$, and $\overline{\Omega}^{(2,2)}_{e-H}$ for temperatures in the range 5,000 – 30,000°K. Coulombic average effective collision integrals ($\overline{\Omega}^{(1,1)}_{H^+-H^+}$ and $\overline{\Omega}^{(2,2)}_{H^+-H^+}$) were calculated by consideration of Coulomb interactions with the Debye potential.

3.5 Summary of Axisymmetric Arcjet Equations

Equations 3.25, 3.29-3.30, 3.38-3.40, 3.45, 3.48-3.56, 3.64-3.65, 3.69-3.74, 3.80-3.87, 3.111, and 3.116 comprise an axisymmetric model of the nonequilibrium flow of a diatomic gas through an arcjet thruster. These equations are summarized below for completeness, with the axisymmetric source terms written as conservative fluxes.

$$\frac{1}{r}\frac{\partial}{\partial r}(r\phi_r) + \frac{\partial}{\partial z}(\phi_z) = \psi\left(\frac{\partial^2 p_e}{\partial r^2} + \frac{1}{r}\frac{\partial p_e}{\partial r} + \frac{\partial^2 p_e}{\partial z^2}\right) + \frac{\partial p_e}{\partial r}\frac{\partial \psi}{\partial r} + \frac{\partial p_e}{\partial z}\frac{\partial \psi}{\partial z} \tag{3.157}$$

$$\phi_r = \sigma\frac{\partial \phi}{\partial r} \qquad \phi_z = \sigma\frac{\partial \phi}{\partial z} \tag{3.158}$$

$$j_r = \psi\frac{\partial p_e}{\partial r} - \sigma\frac{\partial \phi}{\partial r} \qquad j_z = \psi\frac{\partial p_e}{\partial z} - \sigma\frac{\partial \phi}{\partial z} \tag{3.159}$$

$$p = \sum_j p_j = \sum_j n_{gj}kT_g + n_e kT_e \tag{3.160}$$

$$\frac{\partial \rho r}{\partial t} + \frac{\partial \rho u_r r}{\partial r} + \frac{\partial \rho u_z r}{\partial z} = 0 \tag{3.161}$$

$$\frac{\partial \rho_S r}{\partial t} + \frac{\partial \rho_S u_r r}{\partial r} - \frac{\partial}{\partial r}\left(\frac{\rho_S}{(\rho_{S_2} + \rho_S)}\frac{m_S}{m_e}d_{er}r\right) + \frac{\partial \rho_S u_z r}{\partial z} - \frac{\partial}{\partial z}\left(\frac{\rho_S}{(\rho_{S_2} + \rho_S)}\frac{m_S}{m_e}d_{ez}r\right)$$

$$= m_S\left(\dot{n}_S + <\sigma v> n_e n_{S_2} - \dot{n}_e\right) r \tag{3.162}$$

$$\frac{\partial \rho_e r}{\partial t} + \frac{\partial(\rho_e u_r + d_{er})r}{\partial r} + \frac{\partial(\rho_e u_z + d_{ez})r}{\partial z} = m_e \dot{n}_e r \tag{3.163}$$

$$d_{er} = -D_a\frac{\partial \rho_e}{\partial r} \qquad d_{ez} = -D_a\frac{\partial \rho_e}{\partial z} \tag{3.164}$$

$$\dot{n}_S = A\hat{N}T_g^n \exp\left(-\frac{B}{\hat{R}T_g}\right)\left(\hat{m}_S\sigma_S + \hat{m}_{S_2}\sigma_{S_2}\right)\left[\sigma_{S_2} - \frac{\hat{R}T_g}{K_p}\sigma_S^2\right] + <\sigma v> n_e n_{S_2} \tag{3.165}$$

$$\dot{n}_e = Rn_e \left(Sn_S - n_e^2 \right) \tag{3.166}$$

$$\frac{\partial \rho u_r r}{\partial t} + \frac{\partial(\rho u_r^2 + p - \tau_{rr})r}{\partial r} + \frac{\partial(\rho u_r u_z - \tau_{rz})r}{\partial z} + \tau_{\theta\theta} - \rho u_\theta^2 - p = 0 \tag{3.167}$$

$$\frac{\partial \rho u_\theta r}{\partial t} + \frac{\partial(\rho u_r u_\theta - \tau_{r\theta})r}{\partial r} + \frac{\partial(\rho u_\theta u_z - \tau_{\theta z})r}{\partial z} + \rho u_r u_\theta = 0 \tag{3.168}$$

$$\frac{\partial \rho u_z r}{\partial t} + \frac{\partial(\rho u_r u_z - \tau_{rz})r}{\partial r} + \frac{\partial(\rho u_z^2 + p - \tau_{zz})r}{\partial z} = 0 \tag{3.169}$$

$$\tau_{rr} = \frac{2}{3}\mu_g \left(2\frac{\partial u_r}{\partial r} - \frac{\partial u_z}{\partial z} - \frac{u_r}{r} \right) \tag{3.170}$$

$$\tau_{\theta\theta} = \frac{2}{3}\mu_g \left(2\frac{u_r}{r} - \frac{\partial u_r}{\partial r} - \frac{\partial u_z}{\partial z} \right) \tag{3.171}$$

$$\tau_{zz} = \frac{2}{3}\mu_g \left(2\frac{\partial u_z}{\partial z} - \frac{\partial u_r}{\partial r} - \frac{u_r}{r} \right) \tag{3.172}$$

$$\tau_{r\theta} = \mu_g \left(\frac{\partial u_\theta}{\partial r} - \frac{u_\theta}{r} \right) \tag{3.173}$$

$$\tau_{rz} = \mu_g \left(\frac{\partial u_r}{\partial z} + \frac{\partial u_z}{\partial r} \right) \tag{3.174}$$

$$\tau_{\theta z} = \mu_g \frac{\partial u_\theta}{\partial z} \tag{3.175}$$

$$\begin{aligned} &\frac{\partial \rho e_g r}{\partial t} + \frac{\partial \left(\rho e_g u_r + q_{gr} \right) r}{\partial r} + \frac{\partial \left(\rho e_g u_z + q_{gz} \right) r}{\partial z} + p_g \left(\frac{\partial u_r r}{\partial r} + \frac{\partial u_z r}{\partial z} \right) \\ &\quad + \frac{\partial \left(\rho_{S_2} e_{S_2} V_{S_2 r} + \rho_S e_S V_{S r} + \rho_{S^+} e_{S^+} V_{S^+ r} \right) r}{\partial r} \\ &+ p_{S_2} \frac{\partial V_{S_2 r} r}{\partial r} + p_S \frac{\partial V_{S r} r}{\partial r} + p_{S^+} \frac{\partial V_{S^+ r} r}{\partial r} = \left(\Phi + E_l - \frac{1}{2} E_d \dot{n}_S \right) r \end{aligned} \tag{3.176}$$

$$\rho e_g = \frac{3}{2} \left(\rho_S + \rho_{S^+} \right) R_S T_g + \frac{5}{2} \rho_{S_2} R_{S_2} T_g + \frac{\rho_{S_2} R_{S_2} \theta_v}{e^{\frac{\theta_v}{T_g}} - 1} - \frac{7}{4} \rho R_S T_f \tag{3.177}$$

$$\rho h_g = \rho e_g + \rho_{S_2} R_{S_2} T_g + \left(\rho_S + \rho_{S^+} \right) R_S T_g \tag{3.178}$$

$$V_{S+} = -\frac{D_a}{n_e}\frac{\partial n_e}{\partial r} \qquad V_{S_2} = V_S = -\frac{x^M_{S+}}{1 - x^M_{S+}} V_{S+} \tag{3.179}$$

$$q_{gr} = -k_g \frac{\partial T_g}{\partial r} \qquad q_{gz} = -k_g \frac{\partial T_g}{\partial z} \tag{3.180}$$

$$\begin{aligned} \Phi = \mu_g \Bigg[& 2\left(\frac{\partial u_r}{\partial r}\right)^2 + 2\left(\frac{\partial u_z}{\partial z}\right)^2 + 2\left(\frac{u_r}{r}\right)^2 + \left(\frac{\partial u_r}{\partial z} + \frac{\partial u_z}{\partial r}\right)^2 \\ & + \left(\frac{\partial u_\theta}{\partial r} - \frac{u_\theta}{r}\right)^2 + \left(\frac{\partial u_\theta}{\partial z}\right)^2 - \frac{2}{3}\left(\frac{\partial u_r}{\partial r} + \frac{\partial u_z}{\partial z} + \frac{u_r}{r}\right)^2 \Bigg] \end{aligned} \tag{3.181}$$

$$E_l = 3\frac{\rho_e}{m_S}(\nu_{eS+} + \nu_{eS} + \delta_s \nu_{eS_2}) k (T_e - T_g) \tag{3.182}$$

$$\begin{aligned} & \frac{\partial \rho_e E_e r}{\partial t} + \frac{\partial \left(\rho_e u_{er} H_e + q_{er}\right) r}{\partial r} + \frac{\partial \left(\rho_e u_{ez} H_e + q_{ez}\right) r}{\partial z} \\ & = \left(\frac{j^2}{\sigma} - E_l - E_d < \sigma v > n_e n_{S_2} - E_i \dot{n}_e - \dot{R}\right) r \end{aligned} \tag{3.183}$$

$$E_e = \frac{3}{2} R_e T_e + \frac{1}{2} u_e^2 \tag{3.184}$$

$$H_e = E_e + R_e T_e \tag{3.185}$$

$$q_{er} = -k_e \frac{\partial T_e}{\partial r} \qquad q_{ez} = -k_e \frac{\partial T_e}{\partial z} \tag{3.186}$$

$$u_{er} = u_{S+r} - \frac{j_r}{e n_e} \qquad u_{ez} = u_{S+z} - \frac{j_z}{e n_e} \tag{3.187}$$

Chapter 4

Numerical Method

The set of equations governing arcjet flow is essentially a modified form of the compressible Navier-Stokes equations. In an axisymmetric coordinate system, the Navier-Stokes equations can be expressed in the following simplified form, neglecting body forces and external source terms:

$$\frac{\partial \mathbf{U}}{\partial t} + \frac{\partial \mathbf{F}}{\partial z} + \frac{\partial \mathbf{G}}{\partial r} = \mathbf{S}. \tag{4.1}$$

In this conservative form **U** is a state vector, **F** and **G** are flux vectors, and **S** is a vector of source terms.

It was decided to utilize an explicit, second-order accurate numerical algorithm in solving the arcjet flow equations. Because of the complexity of the equations, which include additional diffusive and internal energy flux terms and collisional source terms not present in the compressible Navier-Stokes equations, and due to the complex nature of the boundary conditions, the simpler application of an explicit scheme is more desirable than that of an implicit method. In addition, since startup behavior and arc instabilities are currently important areas of arcjet research, it is advantageous to retain a capability for performing time-dependent calculations with the computer code. In order to calculate an accurate time evolution of the flow, however, a numerical method should be at least second-order accurate in time. Because it satisfies the conditions above and has been proved an excellent means of solving the compressible Navier-Stokes equations for a variety of conditions, MacCormack's Method was chosen as the numerical scheme for this research.

Application of MacCormack's explicit method to the potential equation, however, would result in prohibitively small time steps in order to guarantee numerical stability. Consequently, the electric potential is solved using successive overrelaxation (SOR), an iterative semi-implicit method which can accommodate a time step of the same order as the fluid time step while maintaining stability.

4.1 MacCormack's Method

4.1.1 Description

MacCormack's method, developed in 1969 by MacCormack[69], is a two step predictor-corrector scheme based on the Lax-Wendroff method. The scheme has since been modified to include time-splitting[70], which allows the solution to be advanced in each coordinate direction at the maximum possible time step. Time-splitting, while consistent in formulation, can nevertheless lead to inaccuracies in the steady-state solution depending on the geometry, integration timestep, and complexity of the equations [32], so it was not implemented in this research. The basic algorithm applied to the conservative vector form of the Navier-Stokes equations (Eqn. 4.1) yields:

Predictor

$$\mathbf{U}_{ij}^{P} = \mathbf{U}_{ij}^{n} - \frac{\Delta t}{\Delta z}\left(\mathbf{F}_{i+1,j}^{n} - \mathbf{F}_{ij}^{n}\right) - \frac{\Delta t}{\Delta r}\left(\mathbf{G}_{i,j+1}^{n} - \mathbf{G}_{ij}^{n}\right) + \Delta t \mathbf{S}_{ij}^{n} \tag{4.2}$$

Corrector

$$\mathbf{U}_{ij}^{n+1} = \frac{1}{2}\left[\mathbf{U}_{ij}^{n} + \mathbf{U}_{ij}^{P} - \frac{\Delta t}{\Delta z}\left(\mathbf{F}_{ij}^{P} - \mathbf{F}_{i-1,j}^{P}\right) - \frac{\Delta t}{\Delta r}\left(\mathbf{G}_{ij}^{P} - \mathbf{G}_{i,j-1}^{P}\right) + \Delta t \mathbf{S}_{ij}^{n}\right] \tag{4.3}$$

The superscripts n and $n+1$ represent the state vector values before and after the current integration step, respectively, while the superscript ^{P} denotes the predicted value of the state vector and associated fluxes at the (i,j)th discrete point. Terms arising from the source vector **S** are incorporated into the formulation in both the predictor and corrector fluxes in order to minimize their effect on numerical stability.

In order to maintain overall second order accuracy with MacCormack's method, the viscous and diffusive flux terms must be differenced correctly. Note that Equations 4.2 and 4.3 give explicit instructions for differencing the first derivative terms only. For second derivative terms, the differencing is accomplished in the following manner. The z-derivative terms of the **F** flux vector are differenced in the opposite direction to that used for $\frac{\partial \mathbf{F}}{\partial z}$, while the r-derivatives are approximated by central differences. Similarly in the r-direction, the r-derivative terms of **G** are differenced in the direction opposite that used for $\frac{\partial \mathbf{G}}{\partial r}$, while the z-derivative terms are approximated with central differences. For example, the $\mathbf{G}_{i,j}^{P}$ predictor term for the axial momentum equation is given by

$$\mathbf{G}^P_{i,j} = (\rho u_r u_z r)^n_{i,j} - \mu^n_{i,j} r_{i,j} \left[\frac{(u_z)^n_{i,j} - (u_z)^n_{i,j-1}}{\Delta r} + \frac{(u_r)^n_{i+1,j} - (u_r)^n_{i-1,j}}{2\Delta z} \right]. \tag{4.4}$$

4.1.2 Stability

Because of the complex nature of the compressible Navier-Stokes equations, an analytic stability expression for MacCormack's method is unattainable. Approximate stability criteria, however, have been estimated by MacCormack and Baldwin[71] based on stability analyses of the convective, diffusive, and viscous terms of the full equations. This results in the following time step limits in each coordinate direction:

$$\Delta t_z \leq \frac{\sigma \Delta z}{|u| + a + \frac{1}{\rho}\left[\frac{2\gamma\mu}{Pr\Delta z} + \frac{(-\lambda\mu)^{\frac{1}{2}}}{\Delta r}\right]} \tag{4.5}$$

and

$$\Delta t_r \leq \frac{\sigma \Delta r}{|v| + a + \frac{1}{\rho}\left[\frac{(-\lambda\mu)^{\frac{1}{2}}}{\Delta z} + \frac{2\gamma\mu}{Pr\Delta r}\right]}, \tag{4.6}$$

where

$$a = \sqrt{\frac{\gamma p}{\rho}} \tag{4.7}$$

$$Pr = \frac{\mu c_p}{k} \tag{4.8}$$

$$\lambda = -\frac{2}{3}\mu. \tag{4.9}$$

The coefficient σ represents a safety factor to account for the nonlinearity of the equations. Because these stability criteria were developed for a single component gas assuming constant transport coefficients and neglecting the presence of source terms, however, the value of σ used in this research is considerably smaller than that used for typical compressible flow applications. This became apparent from the outset since source terms such as net dissociation and ionization, collisional energy transfer, ohmic dissipation, and ambipolar diffusion were known to be important or even dominant in certain regions of the arcjet flow. In order to maintain time accuracy and consistency, the solution must be advanced in each coordinate direction for the same interval of time during each integration step. Since in general the maximum allowable time step for stability in each direction is different, the most restrictive timestep calculated in either coordinate direction at any point of the computational grid is applied to all points of the grid during the integration procedure.

The above stability criteria are consistent and functional, but they are more ideally suited for time-split calculations. A simpler and more intuitive criterion is available for the basic MacCormack scheme from Tannehill et al.[113]. This empirical formula is essentially a modification of the inviscid CFL condition for viscous compressible flow:

$$\Delta t \leq \frac{\sigma \Delta t_{CFL}}{1+\frac{2}{Re_{\Delta}}}, \tag{4.10}$$

where σ is again a safety factor, Δt_{CFL} is the CFL time step restriction given by

$$\Delta t_{CFL} = \left[\frac{|u_r|}{\Delta r} + \frac{|u_z|}{\Delta z} + a\sqrt{\frac{1}{\Delta r^2} + \frac{1}{\Delta z^2}}\right]^{-1}, \tag{4.11}$$

and Re_{Δ} is the minimum mesh Reynolds number, given by

$$Re_{\Delta} = min(Re_{\Delta r}, Re_{\Delta z}); \tag{4.12}$$

$$Re_{\Delta r} = \frac{\rho |u_r| \Delta r}{\mu_g} \quad and \quad Re_{\Delta z} = \frac{\rho |u_z| \Delta z}{\mu_g}. \tag{4.13}$$

4.1.3 Numerical Smoothing

Although the MacCormack scheme contains some inherent smoothing, it is necessary to provide additional dissipative terms to damp numerical oscillations which may arise in regions of steep gradients where the mesh is insufficiently refined. MacCormack and Baldwin[71] have developed a fourth-order product type of smoothing based on a pressure switch, which becomes significant in magnitude only where numerical truncation error creates pressure oscillations in the solution. The smoothing terms are applied as additional flux terms in the numerical scheme and are of the following form:

$$\mathbf{SZ}_{ij} = \epsilon \Delta z^4 \frac{\partial}{\partial z}\left[\frac{|u_z| + a}{4p}\left|\frac{\partial^2 p}{\partial z^2}\right|\frac{\partial \mathbf{U}}{\partial z}\right] \tag{4.14}$$

$$\mathbf{SR}_{ij} = \epsilon \Delta r^4 \frac{\partial}{\partial r}\left[\frac{|u_r| + a}{4p}\left|\frac{\partial^2 p}{\partial r^2}\right|\frac{\partial \mathbf{U}}{\partial r}\right], \tag{4.15}$$

where $0 \leq \epsilon \leq 0.5$ for stability. This smoothing scheme is conservative and provides adequate damping for simple flow problems, but it is not appropriate for more complex problems. In arcjet flows, for example, the existence of two or more distinct fluids contributing to an overall pressure and the presence of an azimuthal swirl velocity which can produce a significant centrifugal term in the radial momentum equation basically negate the effectiveness of using a pressure switch in the damping term.

Alternatively, a second order damping scheme without the pressure switch could be formulated, such as the following:

$$\mathbf{SZ}_{ij} = \epsilon \Delta z^2 \frac{\partial}{\partial z}\left[\left(|u_z| + a\right)\frac{\partial \mathbf{U}}{\partial z}\right] \tag{4.16}$$

$$\mathbf{SR}_{ij} = \epsilon \Delta r^2 \frac{\partial}{\partial r}\left[\left(|u_r| + a\right)\frac{\partial \mathbf{U}}{\partial r}\right]. \tag{4.17}$$

It was found, however, that this too was inadequate for the arcjet case considered because of the metric terms which are included in the fluxes, particularly near sharp corners and walls. The use of a predictor-corrector damping term in these regions was insufficient to control oscillations while simultaneously maintaining conservation. Consequently, a simple one step smoothing term was applied to the corrector step only, based on the method of Kutler, Sakell, and Aiello[64]:

$$\mathbf{U}^{n+1}_{ij} = \frac{1}{2}\left[\mathbf{U}^n_{ij} + \mathbf{U}^P_{ij} - \frac{\Delta t}{\Delta z}\left(\mathbf{F}^P_{ij} - \mathbf{F}^P_{i-1,j}\right) - \frac{\Delta t}{\Delta r}\left(\mathbf{G}^P_{ij} - \mathbf{G}^P_{i,j-1}\right) + \Delta t \mathbf{S}^n_{ij} + D^n_{ij}\right], \tag{4.18}$$

where

$$\begin{aligned} D^n_{ij} = {} & -d_{4\xi}\left[U^n_{i+2,j} + U^n_{i-2,j} - 4\left(U^n_{i+1,j} + U^n_{i-1,j}\right) + 6U^n_{i,j}\right] \\ & -d_{4\eta}\left[U^n_{i,j+2} + U^n_{i,j-2} - 4\left(U^n_{i,j+1} + U^n_{i,j-1}\right) + 6U^n_{i,j}\right] \\ & +d_{2\xi}\left[U^n_{i+1,j} - 2U^n_{i,j} + U^n_{i-1,j}\right] \\ & +d_{2\eta}\left[U^n_{i,j+1} - 2U^n_{i,j} + U^n_{i,j-1}\right]. \end{aligned} \tag{4.19}$$

The first two terms represent fourth order smoothing, necessary to damp out sawtooth oscillation modes. The last two terms are second order damping terms, required to prevent the growth of spontaneous singularities in the solution. The coefficients d, varying from 10^{-5} to 10^{-3} in each case, were adjusted to the lowest value necessary to insure stability.

4.1.4 Application to Arcjet Flow

MacCormack's method is applied to the model problem of this research in a straightforward manner. When the simplified arcjet flow equations (Eqn. 3.157 to Eqn. 3.187) are written in the conservative vector form of Eqn. 4.1 with a source term vector, the following representation results.

$$\frac{\partial \mathbf{U}}{\partial t} + \frac{\partial \mathbf{F}}{\partial z} + \frac{\partial \mathbf{G}}{\partial r} = \mathbf{S} \tag{4.20}$$

$$\mathbf{U} = \begin{bmatrix} \rho r \\ \rho s r \\ \rho_e r \\ \rho u_r r \\ \rho u_\theta r \\ \rho u_z r \\ \rho e_g r \\ \rho_e E_e r \end{bmatrix}$$

$$\mathbf{F} = \begin{bmatrix} \rho u_z r \\ (\rho s u_z - \frac{\rho s}{(\rho s_2 + \rho s)} \frac{m s}{m_e} d_{ez})r \\ (\rho_e u_z + d_{er})r \\ (\rho u_r u_z - \tau_{rz})r \\ (\rho u_\theta u_z - \tau_{\theta z})r \\ (\rho u_z^2 + p - \tau_{zz})r \\ (\rho u_z e_g + q_{gz})r \\ (\rho_e u_{ez} H_e + q_{ez})r \end{bmatrix}$$

$$\mathbf{G} = \begin{bmatrix} \rho u_r r \\ (\rho s u_r - \frac{\rho s}{(\rho s_2 + \rho s)} \frac{m s}{m_e} d_{er})r \\ (\rho_e u_r + d_{er})r \\ (\rho u_r^2 + p - \tau_{rr})r \\ (\rho u_r u_\theta - \tau_{r\theta})r \\ (\rho u_r u_z - \tau_{rz})r \\ (\rho u_r e_g + q_{gr} + g(\mathbf{V}))r \\ (\rho_e u_{er} H_e + q_{er})r \end{bmatrix} \qquad (4.21)$$

$$
\mathbf{S} = \begin{bmatrix} 0 \\ m_S\,(\dot{n}_S + < \sigma v > n_e n_{S_2} - \dot{n}_e)\,r \\ m_e \dot{n}_e r \\ \rho u_\theta^2 - \tau_{\theta\theta} + p \\ -\rho u_r u_\theta \\ 0 \\ -p_g(\frac{\partial u_r r}{\partial r} + \frac{\partial u_z r}{\partial z}) + s(\mathbf{V}) + (\Phi + E_l - \frac{1}{2} E_d \dot{n}_S) r \\ (\frac{j^2}{\sigma} - E_l - E_d < \sigma v > n_e n_{S_2} - E_i \dot{n}_e - \dot{R}) r \end{bmatrix}
$$

In this case $g(\mathbf{V})$ and $s(\mathbf{V})$ represent the contribution of the species slip velocities to the radial flux and source terms, respectively, in the heavy species energy equation.

4.2 Successive Overrelaxation

4.2.1 Description

The SOR method is a technique used to solve Poisson's equation, which is of the form

$$
\frac{\partial u}{\partial t} = \nabla^2 u - R, \tag{4.22}
$$

where R is a source term which may be a function of u. Once steady state is reached, this is the form of the electric potential equation, Equation 3.29. If the model equation (Eqn. 4.22) is discretized using forward time centered space (FTCS) differencing, the equation becomes

$$
u_{i,j}^{n+1} = u_{i,j}^{n} + \frac{\Delta t}{\Delta z_{min}} (u_{i+1,j}^{n} + u_{i-1,j}^{n} + u_{i,j+1}^{n} + u_{i,j-1}^{n} - 4u_{i,j}^{n}) - \Delta t R_{i,j}, \tag{4.23}
$$

where Δz_{min} is the smallest spatial step in any coordinate direction. In two dimensions the stability condition for this differencing scheme is that $\Delta t / \Delta z_{min}^2 \leq \frac{1}{4}$. Taking the largest possible time step from the stability condition gives the equation for Jacobi's Method:

$$
u_{i,j}^{n+1} = \frac{1}{4}(u_{i+1,j}^{n} + u_{i-1,j}^{n} + u_{i,j+1}^{n} + u_{i,j-1}^{n}) - \frac{\Delta z_{min}}{4} R_{i,j}. \tag{4.24}
$$

Jacobi's Method converges too slowly for practical considerations, however. By using information already available from the $n + 1$ time level, the Gauss-Seidel Method is achieved:

$$
u_{i,j}^{n+1} = \frac{1}{4}(u_{i+1,j}^{n} + u_{i-1,j}^{n+1} + u_{i,j+1}^{n} + u_{i,j-1}^{n+1}) - \frac{\Delta z_{min}}{4} R_{i,j}. \tag{4.25}
$$

The SOR procedure is obtained by making an overcorrection to the value of each $u_{i,j}^{n+1}$ at the $n+1$ time level of the Gauss-Seidel iteration, thus anticipating future corrections. The $n+1$ result from the Gauss-Seidel Method then becomes a predicted value, $u_{i,j}^{p}$, with the updated value of the function given by

$$u_{i,j}^{n+1} = \omega u_{i,j}^{p} + (1-\omega) u_{i,j}^{n}. \tag{4.26}$$

An approximate formula for the ω which results in the fastest rate of convergence is given by

$$\omega = \frac{2}{1+\sqrt{1-\rho_{Jacobi}^2}}, \tag{4.27}$$

where ρ_{Jacobi} is the spectral radius of the Jacobi Method:

$$\rho_{Jacobi} = \frac{\cos\frac{\pi}{I} + \cos\frac{\pi}{J}}{2}. \tag{4.28}$$

Here also I is the number of grid points in the z-direction, and J is the number of points in the r-direction. For the 165 × 30 mesh used in this research, the optimal ω is approximately 1.86.

4.2.2 Application to Arcjet Flow

Since the form of the electric potential equation is not exactly that of the SOR model equation, Equation 4.22, a specific description of the formulation of the finite differenced potential equation is warranted. Once the potential equation is transformed into natural coordinates for computational purposes (cf. Section 4.3.1), Equation D.1 of Appendix D results. This equation is seen to be of the form

$$a\frac{\partial^2\phi}{\partial\xi^2} + b\frac{\partial^2\phi}{\partial\eta^2} + c\frac{\partial^2\phi}{\partial\xi\partial\eta} + d\frac{\partial\phi}{\partial\xi} + e\frac{\partial\phi}{\partial\eta} = f(p_e, \psi, r), \tag{4.29}$$

where

$$a = \sigma\left(\xi_r^2 + \xi_z^2\right) \tag{4.30}$$

$$b = \sigma\left(\eta_r^2 + \eta_z^2\right) \tag{4.31}$$

$$c = 2\sigma\left(\xi_r\eta_r + \xi_z\eta_z\right) \tag{4.32}$$

$$d = \sigma\left(\xi_{rr} + \xi_{zz} + \frac{\xi_r}{r}\right) + \frac{\partial\sigma}{\partial\xi}\left(\xi_r^2 + \xi_z^2\right) + \frac{\partial\sigma}{\partial\eta}\left(\xi_r\eta_r + \xi_z\eta_z\right) \tag{4.33}$$

$$e = \sigma\left(\eta_{rr} + \eta_{zz} + \frac{\eta_r}{r}\right) + \frac{\partial\sigma}{\partial\xi}\left(\xi_r\eta_r + \xi_z\eta_z\right) + \frac{\partial\sigma}{\partial\eta}\left(\eta_r^2 + \eta_z^2\right). \tag{4.34}$$

Discretizing the terms in Equation 4.29 with forward time and centered space differences and recognizing that the grid size in computational space is unity, the following difference equation is obtained:

$$a(\phi^n_{i+1,j} - 2\phi^n_{i,j} + \phi^n_{i-1,j}) + b(\phi^n_{i,j+1} - 2\phi^n_{i,j} + \phi^n_{i,j-1})$$

$$+\frac{c}{4}(\phi^n_{i+1,j+1} - \phi^n_{i+1,j-1} - \phi^n_{i-1,j+1} + \phi^n_{i-1,j-1}) + \frac{d}{2}(\phi^n_{i+1,j} - \phi^n_{i-1,j}) + \frac{e}{2}(\phi^n_{i,j+1} - \phi^n_{i,j-1}) = f. \tag{4.35}$$

Solving for $\phi^n_{i,j}$,

$$\phi^n_{i,j} = \frac{1}{2(a+b)}\Big[a(\phi^n_{i+1,j} + \phi^n_{i-1,j}) + b(\phi^n_{i,j+1} + \phi^n_{i,j-1})$$

$$+\frac{c}{4}(\phi^n_{i+1,j+1} - \phi^n_{i+1,j-1} - \phi^n_{i-1,j+1} + \phi^n_{i-1,j-1})$$

$$+\frac{d}{2}(\phi^n_{i+1,j} - \phi^n_{i-1,j}) + \frac{e}{2}(\phi^n_{i,j+1} - \phi^n_{i,j-1}) - f\Big]. \tag{4.36}$$

This equation is solved by a relaxation process, achieved by traversing the mesh row by row and solving the (i,j)th difference equation at each grid point. In addition, the equation can be rendered more implicit by using values of ϕ at the new $n+1$ time level if they have already been calculated. Assuming the calculation proceeds over the mesh from left to right and row by row from bottom to top, this results in the following difference equation for $\phi^{n+1}_{i,j}$ at each point in the mesh:

$$\phi^{n+1}_{i,j} = \frac{1}{2(a+b)}\Big[a(\phi^n_{i+1,j} + \phi^{n+1}_{i-1,j}) + b(\phi^n_{i,j+1} + \phi^{n+1}_{i,j-1})$$

$$+\frac{c}{4}(\phi^n_{i+1,j+1} - \phi^n_{i+1,j-1} - \phi^n_{i-1,j+1} + \phi^{n+1}_{i-1,j-1})$$

$$+\frac{d}{2}(\phi^n_{i+1,j} - \phi^{n+1}_{i-1,j}) + \frac{e}{2}(\phi^n_{i,j+1} - \phi^{n+1}_{i,j-1}) - f\Big]. \tag{4.37}$$

For successive overrelaxation, the result of Equation 4.37 is inserted as the predicted value of Equation 4.27 in order to obtain the value of ϕ at the new time level.

4.3 Mesh

4.3.1 Coordinate Transformation

Due to the somewhat complicated geometry of the typical arcjet thruster, an arbitrary mesh defined in $\xi - \eta$ natural coordinates is utilized for computations. The transformation from cylindrical to natural coordinates is governed by the differential chain rule:

$$\frac{\partial}{\partial r} = \frac{\partial \xi}{\partial r}\frac{\partial}{\partial \xi} + \frac{\partial \eta}{\partial r}\frac{\partial}{\partial \eta} = \xi_r \frac{\partial}{\partial \xi} + \eta_r \frac{\partial}{\partial \eta} \tag{4.38}$$

$$\frac{\partial}{\partial z} = \frac{\partial \xi}{\partial z}\frac{\partial}{\partial \xi} + \frac{\partial \eta}{\partial z}\frac{\partial}{\partial \eta} = \xi_z \frac{\partial}{\partial \xi} + \eta_z \frac{\partial}{\partial \eta}, \tag{4.39}$$

where η_r, η_z, ξ_r, and ξ_z are the metrics of the transformation. From Anderson et al.[2], these metrics are given by

$$\eta_r = \frac{z_\xi}{J} \qquad \eta_z = -\frac{r_\xi}{J}$$

$$\xi_r = -\frac{z_\eta}{J} \qquad \xi_z = \frac{r_\eta}{J}, \tag{4.40}$$

where J is the Jacobian of the transformation, defined as

$$J = r_\eta z_\xi - r_\xi z_\eta. \tag{4.41}$$

Thus the second derivatives in transformed space may be written as

$$\frac{\partial^2}{\partial r^2} = \frac{\partial}{\partial r}\left(\frac{\partial}{\partial r}\right) = \eta_r^2 \frac{\partial^2}{\partial \eta^2} + 2\xi_r \eta_r \frac{\partial^2}{\partial \xi \partial \eta} + \xi_r^2 \frac{\partial^2}{\partial \xi^2} + \eta_{rr}\frac{\partial}{\partial \eta} + \xi_{rr}\frac{\partial}{\partial \xi} \tag{4.42}$$

$$\frac{\partial^2}{\partial z^2} = \frac{\partial}{\partial z}\left(\frac{\partial}{\partial z}\right) = \eta_z^2 \frac{\partial^2}{\partial \eta^2} + 2\xi_z \eta_z \frac{\partial^2}{\partial \xi \partial \eta} + \xi_z^2 \frac{\partial^2}{\partial \xi^2} + \eta_{zz}\frac{\partial}{\partial \eta} + \xi_{zz}\frac{\partial}{\partial \xi}, \tag{4.43}$$

where

$$\eta_{rr} = \xi_r(\eta_r)_\xi + \eta_r(\eta_r)_\eta = \frac{1}{J}\left[\xi_r\left(z_{\xi\xi} - \eta_r J_\xi\right) + \eta_r\left(z_{\xi\eta} - \eta_r J_\eta\right)\right] \tag{4.44}$$

$$\eta_{zz} = \xi_z(\eta_z)_\xi + \eta_z(\eta_z)_\eta = \frac{1}{J}\left[-\xi_z\left(r_{\xi\xi} + \eta_z J_\xi\right) - \eta_z\left(r_{\xi\eta} + \eta_z J_\eta\right)\right] \tag{4.45}$$

$$\xi_{rr} = \xi_r(\xi_r)_\xi + \eta_r(\xi_r)_\eta = \frac{1}{J}\left[-\xi_r\left(z_{\xi\eta} + \xi_r J_\xi\right) - \eta_r\left(z_{\eta\eta} + \xi_r J_\eta\right)\right] \tag{4.46}$$

$$\xi_{zz} = \xi_z(\xi_z)_\xi + \eta_z(\xi_z)_\eta = \frac{1}{J}\left[\xi_z\left(r_{\xi\eta} - \xi_z J_\xi\right) + \eta_z\left(r_{\eta\eta} - \xi_z J_\eta\right)\right]. \tag{4.47}$$

Since the electric potential equation is solved by an iterative relaxation method, the metrics of the transformed equations may be calculated by centered differences at all points in the flow. For the fluid equations, which are solved by an alternating direction predictor-corrector numerical method, care must be taken to insure that the metrics are consistently calculated. In a forward (predictor) step, the relevant metrics are obtained by first order differences over the $j|j+1$ mesh interval. For a backward (corrector) step, the metrics are calculated by first order approximations between the j and $j-1$ mesh points. For viscous terms, the metric calculation may require a centered or one-sided difference to maintain consistency, depending on the integration step being performed. Leaving the transformed flow equations with $[\xi,\eta]_{r,z}$ metrics outside the derivatives, as in Eqns. 4.38-4.43, results in a set of equations which appear to be less conservative. A more conservative approach in which the metrics are moved inside the derivatives was tried, as described in Appendix F, but inferior results were generated. As a result of the coordinate transformation the partial differential equations governing arcjet flow become quite complicated. They are listed in Appendix D for reference.

4.3.2 Grid Generation

The transformed governing equations are solved on a Cartesian computational mesh but yield solutions to the state vector which are valid at grid points in either the computational or the arbitrary physical domain. The grid spacing in the computational mesh is set to unity, thereby reducing the computational time since no operations involving $d\xi$ or $d\eta$ need be performed in the numerical integration. At present 30 grid points are used in the radial direction and 140 in the axial direction, with the thruster being modeled symmetrically about the centerline. The grid is clustered near the walls of the thruster in order to resolve viscous boundary effects and also in the constrictor region in order to resolve the gradients associated with the electric arc present there. Additional mesh refinement is necessary near the cathode tip and the end of the constrictor, where arc attachment leads to steep gradients in the electric potential and current distributions.

The boundaries of the mesh are chosen to accurately model the geometry of an arcjet thruster. In order to prevent physical boundary discontinuities from propagating into the mesh, an elliptic partial differential equation method based on the work of Thompson et al.[114, 115] is employed to determine the locations of the interior grid points. First the boundary grid points are specified, and then the interior points are found by solving the coupled Poisson equations

$$\xi_{zz} + \xi_{rr} = P(\xi,\eta) \tag{4.48}$$

and

$$\eta_{zz} + \eta_{rr} = Q(\xi,\eta), \tag{4.49}$$

where the source terms P and Q are responsible for the control of grid spacing within the interior of the physical domain. In practice, Equations 4.48 and 4.49 are transformed to computational space to yield the following coupled elliptic partial differential equations to be solved:

$$\alpha z_{\xi\xi} - 2\beta z_{\xi\eta} + \gamma z_{\eta\eta} = -J^2(P z_\xi + Q z_\eta) \tag{4 50}$$

$$\alpha r_{\xi\xi} - 2\beta r_{\xi\eta} + \gamma r_{\eta\eta} = -J^2(P r_\xi + Q r_\eta), \tag{4.51}$$

where

$$\alpha = z_\eta^2 + r_\eta^2 \tag{4.52}$$

$$\beta = z_\xi z_\eta + r_\xi r_\eta \tag{4.53}$$

$$\gamma = z_\xi^2 + r_\xi^2 \tag{4.54}$$

and

$$J = \frac{\partial(z,r)}{\partial(\xi,\eta)} = z_\xi r_\eta - z_\eta r_\xi. \tag{4.55}$$

A typical grid in the physical domain is illustrated in Figures 4.1 and 4.2, while the computational grid is shown in Figure 4.3. Figure 4.2 shows that the cathode is blunted, with a flat vertical tip to aid in the modeling of the cathode boundary conditions on the electric potential and current density. Physically, the cathode produces electrons by thermionic emission, and arc attachment occurs within a very small region of the cathode tip. During startup the arc is observed to ablate the cathode tip through microinstabilities until a blunted rather than pointed cathode tip is presented to the arc, after which time operation appears to be steady. Since the process of thermionic emission is not addressed by the model of this research, a number of adjustments are made in the cathode geometry and mesh spacing in order to best overcome this simplification. The cathode tip is assumed to possess a small flat tip, and the arc is constrained to attach at the tip only. In addition, the mesh is concentrated near the cathode tip to resolve steep gradients in the near attachment zone and also near the projected arc attachment at the anode just beyond the constrictor. Finally, the computational domain of the electric potential calculation is restricted to the region downstream of the cathode tip, so that the potential boundary equations may be used effectively to limit current attachment to the cathode tip only.

4.4 Boundary Conditions

4.4.1 Inlet

The conditions at the inlet of the computational domain are postulated to be essentially those of a flow which has just been injected into the thruster plenum by a large number of evenly spaced jets. The flow is therefore assumed to be subsonic and parallel to the thruster walls ($u_r = 0$). For the inlet condition on the swirl velocity, u_θ, a fraction

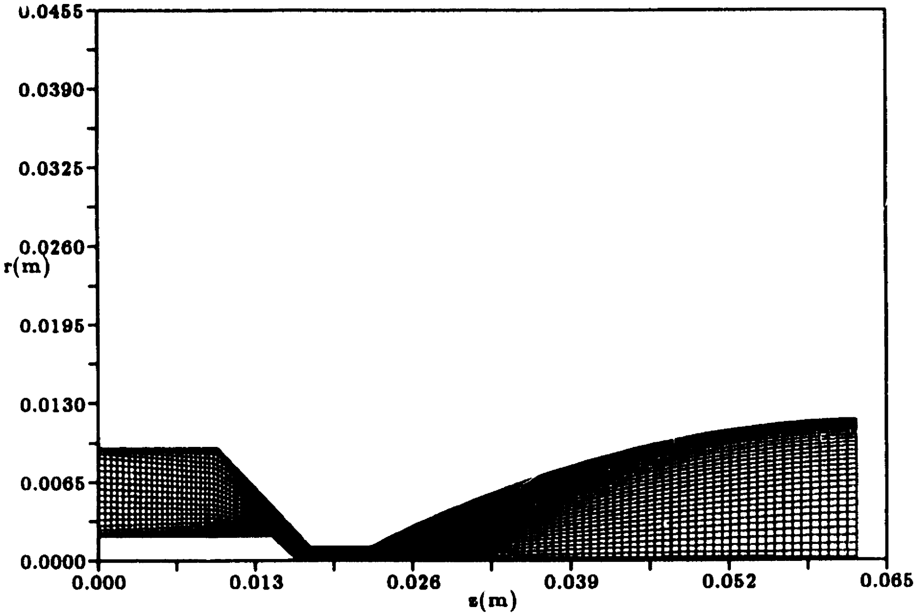

Figure 4.1: Physical Grid for Axisymmetric Arcjet Flow ($z - r$)

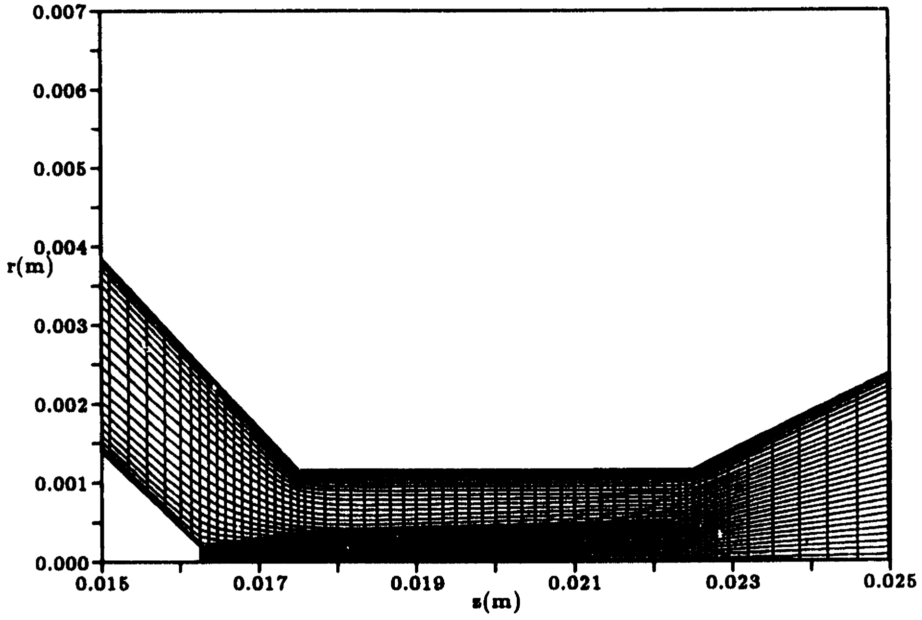

Figure 4.2: Constrictor Region of Arcjet Grid ($z - r$)

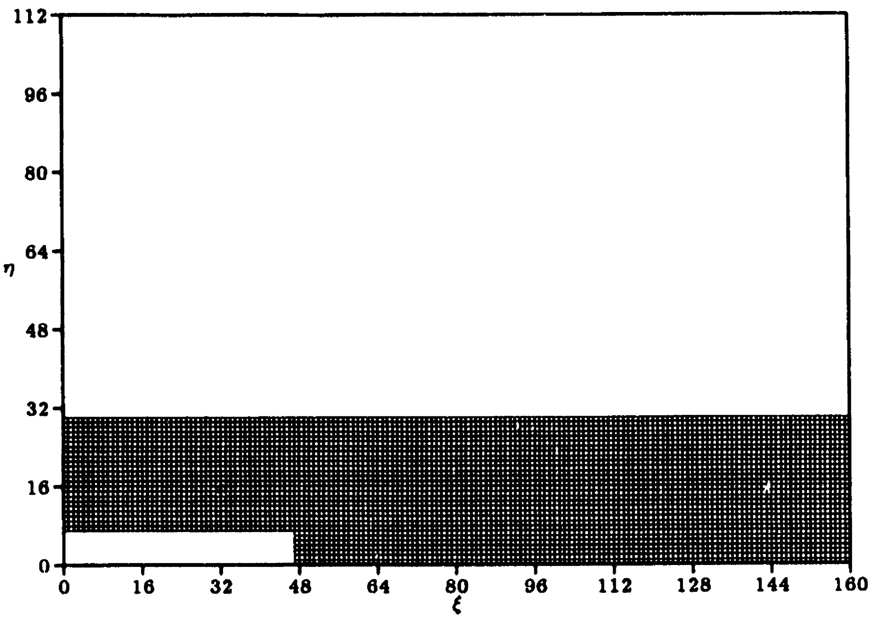

Figure 4.3: Computational Grid for Flow Calculations ($\xi - \eta$)

of the total inlet velocity is specified as being in the azimuthal direction, typically on the order of 30-50%. The mass flow rate, total enthalpy, and ionization fraction are specified. The ionization fraction is set to a small value, typically 1×10^{-6}, and is assumed to be constant over the cross-section of the inlet. This value is low enough that it does not affect the state of the heavy species and high enough that the electron equations may be solved without numerical difficulties. Finally, the inlet atomic mass fraction is also required, and it is set equal to 1×10^{-4}. The reasoning behind these initial minimum values is described in more detail in Appendix F.

Given the above parameters and information from the next inside grid point, all conditions at the inlet may be calculated. By assuming that the electron thermal conductivity is sufficiently large, the inlet electron temperature may be set equal to that of the next inside point. The heavy species temperature is either specified or calculated from the conservation of total enthalpy at each inlet point:

$$H_{t0} = \frac{\gamma p_g}{(\gamma - 1)\rho} + \frac{5}{2}\frac{p_e}{\rho} + \frac{1}{2}\left(u_z^2 + u_\theta^2\right), \tag{4.56}$$

where γ is a function of the degree of dissociation ($\gamma = \frac{5}{3}$ for a monatomic gas, and $\gamma = 1+1/(\frac{5}{2}+\frac{\theta_v/T_g}{e^{\theta_v/T_g}-1})$ for a diatomic gas). Using a downwind difference approximation to the overall continuity equation and given the specified mass flow rate, the inlet density and axial velocity may be determined. The species pressures are then given by the specified ionization and dissociation fractions, and the electron velocities are calculated from the equation for current density (Eqn. 3.187). Since no current may pass upstream of the inlet, or alternatively upstream of the imposed vertical boundary for the potential calculation region, the condition on the electric potential is that $j_z = \psi \frac{\partial p_e}{\partial z} - \sigma \frac{\partial \phi}{\partial z} = 0$.

4.4.2 Outlet

The boundary conditions at the outlet of the channel depend on whether the exit flow is subsonic or supersonic. In both cases the electron temperature is set equal to that of the next inside point and no current is allowed to pass outside the exit plane of the thruster ($j_z = \psi \frac{\partial p_e}{\partial z} - \sigma \frac{\partial \phi}{\partial z} = 0$). If the flow is supersonic at a point on the exit plane, then the remaining quantities are extrapolated from their values at the previous two grid points. In this case, the pressure at the outlet is given by

$$p_I = p_{I-1} \tag{4.57}$$

and the gas temperature is then determined from the other known quantities.

If the flow is subsonic, then the exit pressure is set equal to some small value representing near-vacuum conditions and the density and axial velocity are given by the Riemann invariants

$$\rho_I = \left(\frac{p_I}{p_{I-1}}\right)^{\frac{1}{\gamma}} \rho_{I-1} \tag{4.58}$$

and

$$u_I = u_{I-1} + \frac{2}{\gamma - 1}(a_{I-1} - a_I). \tag{4.59}$$

In general, the presence of a magnetic field or electric field potential and the associated distribution of current renders simple invariant theory inapplicable, and it is not utilized at the inlet. At the outlet, however, most of the current will have been attached to the anode, so the use of Riemann invariants at the exit boundary introduces minimal additional error to the solution. The remaining quantities at a subsonic outlet point are then calculated as in the supersonic case.

4.4.3 Thruster Walls

Wall boundary conditions are applied to all remaining boundary points of the electrothermal arcjet model, except those beyond the end of the cathode on the symmetry line ($r = 0$) of the mesh. On these points the radial and azimuthal flow velocities are set equal to zero and a zero radial gradient is imposed on the remaining quantities.

At the thruster walls viscous no-slip conditions are imposed on the axial and radial fluid velocities ($u_z = 0$, $u_r = 0$). The electron temperature is set equal to that of the next inside grid point, and the heavy species temperature is held constant at 1000°K upstream of the constrictor, increasing linearly to 1100°K at the constrictor exit. This profile was chosen based on experimental and numerical calculations of the wall temperature distribution for a reasonable operating range of the German TT1 radiatively-cooled arcjet thruster[36]. It is assumed that the gas temperature at the walls is substantially lower than the melting point of the electrode material and nearly constant along the length of the channel due to good conduction within the metallic electrodes. This temperature is compatible with electrodes composed of high-temperature metals such as tungsten or lower-temperature metals such as copper alloyed with nickel, titanium, molybdenum, or similar materials. On the cathode, however, a wall temperature profile linearly increasing in the axial direction is assumed. Here the wall gas temperature increases as the cathode narrows, reaching a value of 2000°K at the cathode tip.

Recent experimental and analytical work has shown that for the electrothermal arcjet the gas temperature at the anode depends heavily on the heat balance within the anode material and on whether regenerative or radiative cooling is employed. In addition, the value of the wall temperature has a strong effect on the development and composition of the arc column and surrounding cooler gas flow. Fixing a value of the wall temperature therefore constitutes an arbitrary simplification of the real physical situation, but it is probably a reasonable one for a radiatively-cooled arcjet. The model described in Chapter 7 shows the effect of incorporating a consistent heat balance model of the anode for the radiatively-cooled case.

For the boundary condition on electron density at each electrode, a balance is postulated between the flux of ions arriving at the sheath edge by ambipolar diffusion and the flux of ions arriving at the wall by virtue of their thermal energy at the Bohm velocity (v_B)[119]:

$$D_a \frac{dn_e}{d\hat{n}} = 0.61 n_e v_B, \tag{4.60}$$

where

$$v_B = \sqrt{\frac{k\left(T_e + T_g\right)}{m_i}}. \tag{4.61}$$

The Bohm velocity is derived by assuming that at the edge of the plasma sheath located on each electrode, the ion velocity is limited by an electrostatically choked flow condition beyond which the ions free-fall collisionlessly through the sheath to the wall[46]. This boundary condition neglects the voltage drops present in the non-neutral plasma sheath, which are typically on the order of 10V. Also omitted is the dependence of the thermionic emission of electrons at the cathode on the cathode wall temperature. Introducing additional modeling to account for these phenomena would add another iterative level to the already complex and time-consuming set of governing equations for these models.

The radial global momentum equation applied at the interior thruster walls provides the approximate condition

$$\frac{dp}{dr}\Big|_{wall} = 0, \tag{4.62}$$

where inertial and viscous terms have been neglected. This approximation, however, is consistent only along wall surfaces that are oriented parallel to the axis of the thruster. For thruster sections of varying cross-sectional area a modified criterion must be derived which can be applied on the convergent anode section upstream of the constrictor, on the tip of the cathode, and on the divergent nozzle section of the anode. For these sections, a local curvilinear coordinate system $(\hat{s}, \hat{n})$ is defined as shown in Figure 4.4. In terms of the localized coordinates, Equation 4.62 then becomes

$$\frac{dp}{dr}\Big|_{wall} = \frac{dp}{d\hat{n}}\frac{d\hat{n}}{dr}\Big|_{wall} + \frac{dp}{d\hat{s}}\frac{d\hat{s}}{dr}\Big|_{wall} = \frac{dp}{d\hat{s}}\frac{d\hat{s}}{dr}\Big|_{wall} \tag{4.63}$$

since $\frac{dp}{d\hat{n}} = 0$ by assumption. Thus the pressure at the wall point may be obtained by a time-lagged approximation to Equation 4.63. For the lower wall boundary, this implies that

$$p_{i,0}^{n+1} = p_{i,1}^{n+1} \pm \frac{\Delta s'}{2\Delta s}\left(p_{i+1,0}^{n} - p_{i-1,0}^{n}\right), \tag{4.64}$$

where the positive sign is appropriate for a negatively sloped wall and the negative sign is appropriate for a positively sloped wall. For the upper wall boundary, of course, the opposite is true.

The condition on the wall electric potential is that there is no current perpendicular to an insulating section and that ϕ on the anode is set equal to a fixed but arbitrary voltage. For numerical reasons, the electric arc is restricted to attach downstream of the constrictor exit in this model. Therefore the outer walls upstream of the nozzle entrance are assumed to be insulating, while the nozzle itself is assumed to be electrically conducting. When this restriction is removed, the arc attaches upstream in the constrictor and the simulation incorrectly predicts voltage and performance. More discussion concerning this requirement can be found in the succeeding chapters. On the cathode tip, a uniform axial current density is prescribed which sums to the specified total current. The potential at the cathode is then chosen so as to maintain this current density distribution. During post-processing, a cathode voltage drop equal to the ionization potential plus one half the dissociation potential of the gas (15.8V for

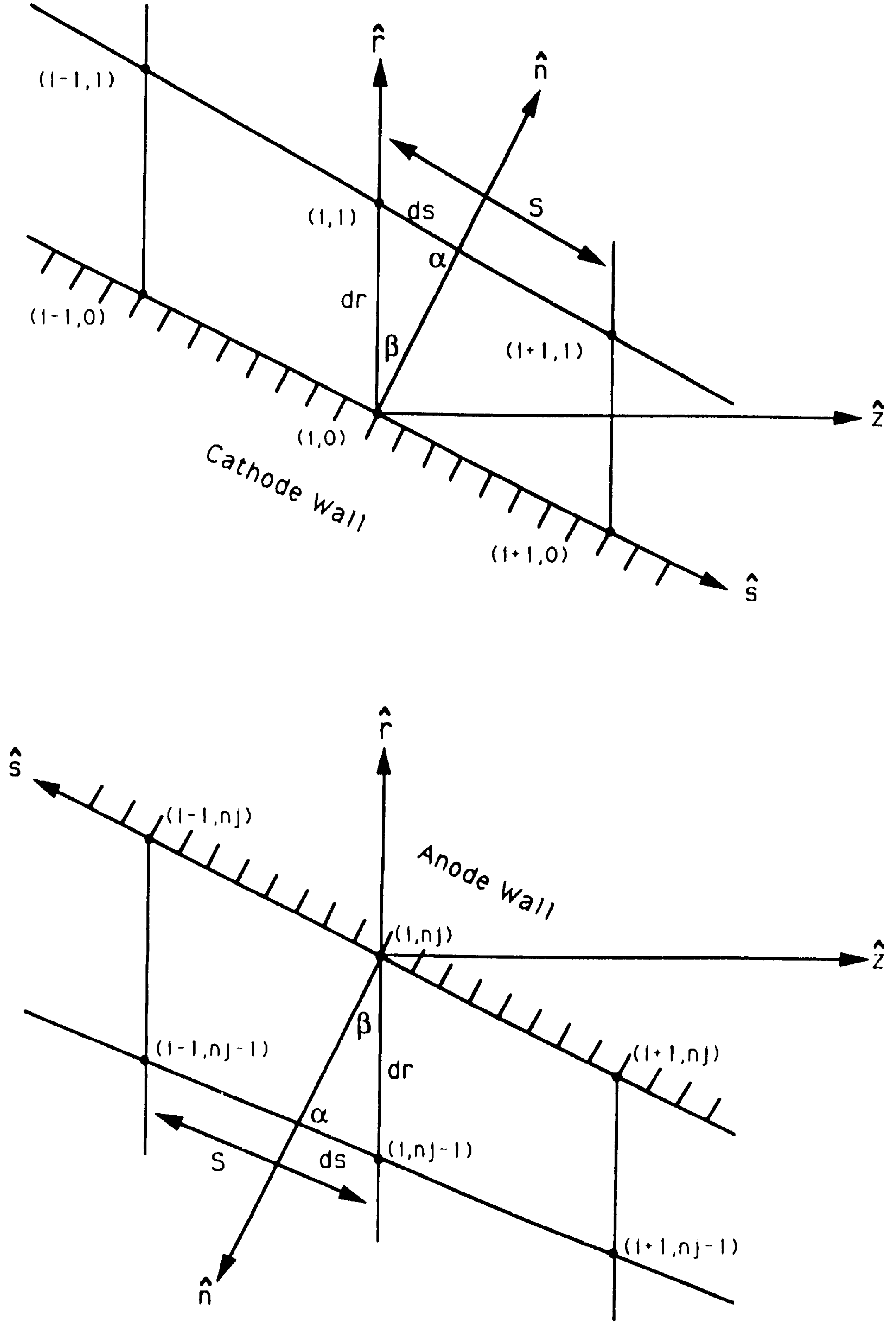

Figure 4.4: Local Curvilinear Coordinate System for a Nonparallel Wall Boundary

hydrogen) is added to the total voltage in order to account for the model's neglect of this region. At the anode, in all cases simulated the extracted current density does not exceed the random thermal flux of electrons to the wall ($j_{anode} \ll \frac{en_e\bar{c}}{4}$). Consequently, a potential well must exist in the non-neutral anode sheath which repels excess electrons in the random thermal flux. The current balance is then given by

$$j = \frac{en_e}{4}\sqrt{\frac{8kT_e}{\pi m_e}}e^{-\frac{e\triangle V_a}{kT_e}} - 0.61en_e\sqrt{\frac{kT_e}{m_i}}. \tag{4.65}$$

This yields an anode voltage drop of

$$\triangle V_a = \frac{kT_e}{e}\left[ln\left(\frac{\sqrt{m_i/m_e}}{0.61\sqrt{2\pi}}\right) - ln\left(1 + \frac{j}{0.61en_e\sqrt{\frac{kT_e}{m_i}}}\right)\right]. \tag{4.66}$$

For typical conditions at the anode attachment as predicted by the model of this thesis ($T_e = 2eV$, $n_e = 2 \times 10^{20}m^{-3}$, $j = 10^6A/m^2$), this yields a voltage drop of about 7V, which must be subtracted from the voltage calculated in the simulation to produce a final total voltage prediction. Given the above conditions, the remaining flow quantities can be determined at each wall boundary.

4.5 Initial Conditions

The initial conditions are chosen as a first approximation to the steady-state solution of the problem. When possible, the computed solution to a similar case, such as a simulation with the same thruster geometry but at a different operating point, is used. Otherwise the following initialization of variables is used. The electron temperature is set to a constant value over the mesh, while the radial fluid velocity is everywhere set equal to zero. The gas temperature and ionization fraction are defined as linearly increasing functions in the axial direction with parabolic radial distributions. Distributions of the current density and electron velocity are given by the specified electric potential distribution. The initial conditions on the density and axial velocity are determined by the constraint that the pressure is uniform in the radial direction and by enforcing a constant mass flow rate at each axial location between the thruster inlet and exit. The initial level of hydrogen dissociation is specified as a linearly increasing function of z.

4.6 Procedure

Once the initial conditions of the flow have been specified, the solution is calculated numerically as follows. First, the time steps are calculated for the overall and heavy species equations at all grid points in each direction from the stability criteria. The most restrictive time step is chosen as the time interval for the current integration step, and these equations are integrated according to MacCormack's method. During each predictor and corrector step, the fluxes and damping terms are calculated and the boundary conditions are updated. Next, the electron density and energy equations are integrated based on their individual stability restrictions and maintaining consistency with the previously determined time interval. The electron equations are integrated separately because the stability criterion can be up to 100 times more restrictive than for the overall flow equations. Performing the electron integrations separately while holding the other variables constant allows the overall time restriction on the governing equations to be relaxed, thus saving computational time. The potential equation is also integrated separately for the same reason.

Once the time step integration has been completed, the time counter is updated and the error is estimated by calculating the root mean square changes in heavy species pressure, electron pressure, and electric potential over the mesh. The system of equations is repeatedly integrated until either a specified number of iterations has been reached or the solution is considered converged. Convergence is achieved when the RMS pressure changes over the entire mesh are negligible and the mass flow errors at each axial station are within a few percent of the input mass flow rate. Computations were performed on a DECStation 5000/200 microcomputer using the Ultrix operating system, on a DEC 3000-500 Alpha AXP workstation using the OS/1 operating system, on a Silicon Graphics Iris Indigo workstation with the Irix operating system, on an IBM RS6000 workstation with the AIX operating system, and on a Cray X-MP supercomputer under Unicos.

A number of logical flowcharts are provided here as a further aid in revealing the structure of the actual arcjet code. Figure 4.5 shows a top level flowchart which highlights the most basic program operations. The following three flowcharts describe the integration procedures used for the heavy species, electron, and potential equations. The code is described in more detail in Appendix E, wherein the main variables and subroutines are listed, program input and output is described, and instructions are provided for compiling, linking, and running the program. In addition, Appendix F describes some of the numerical problems encountered in the development of this code and the steps that were taken to overcome them.

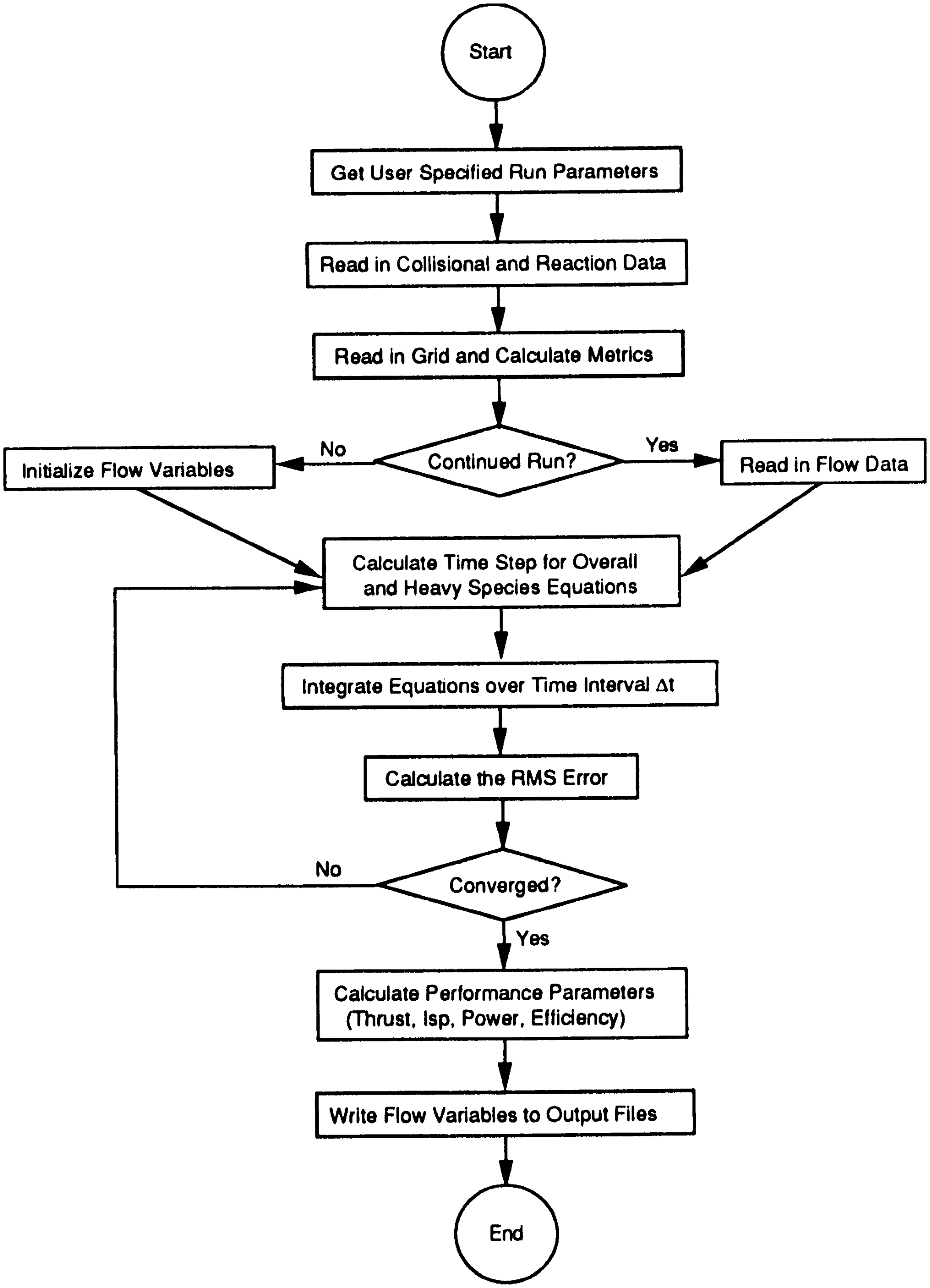

Figure 4.5: Top Level Flowchart for the Arcjet Program

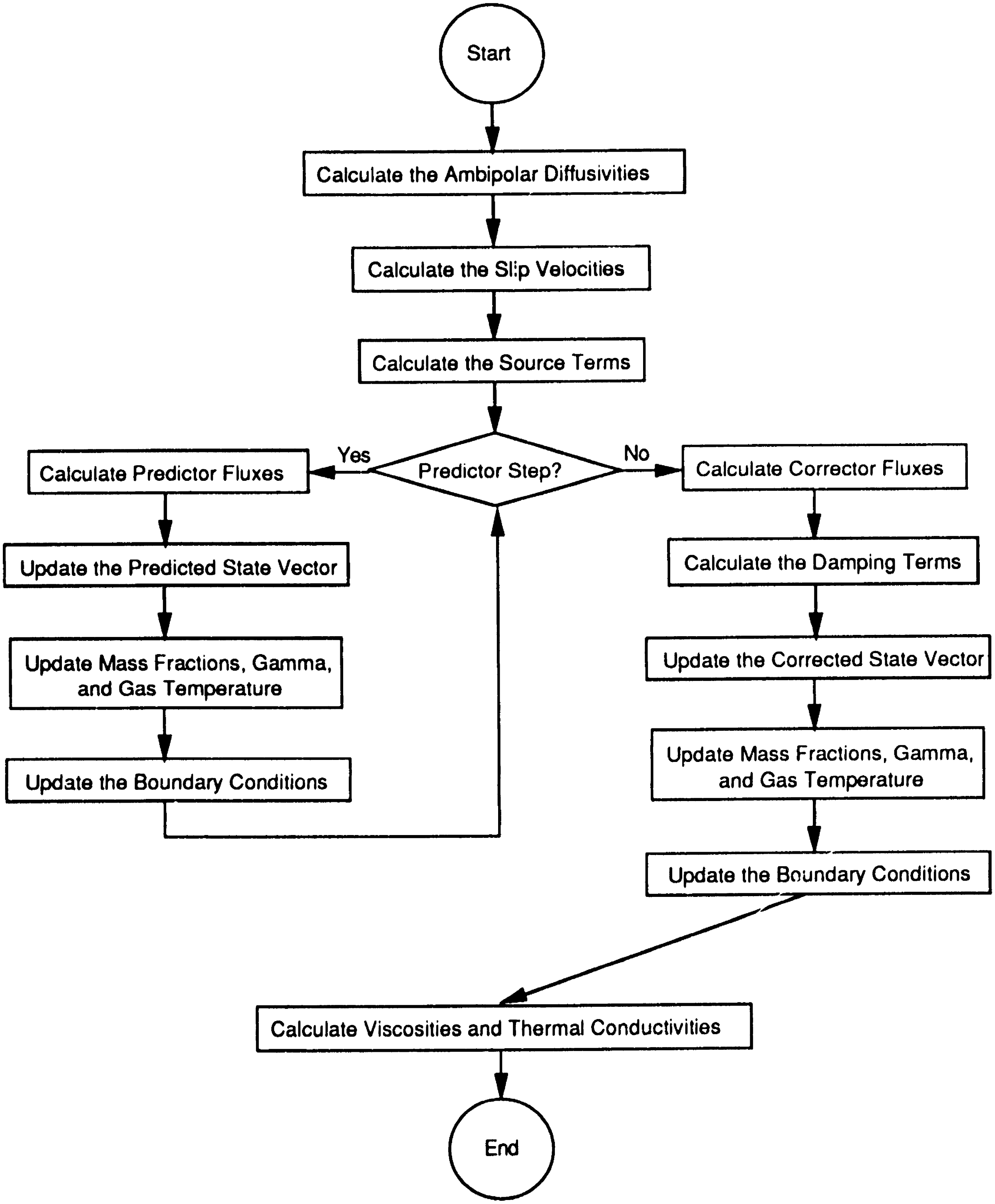

Figure 4.6: Flowchart for the Integration of the Global and Heavy Species Conservation Equations

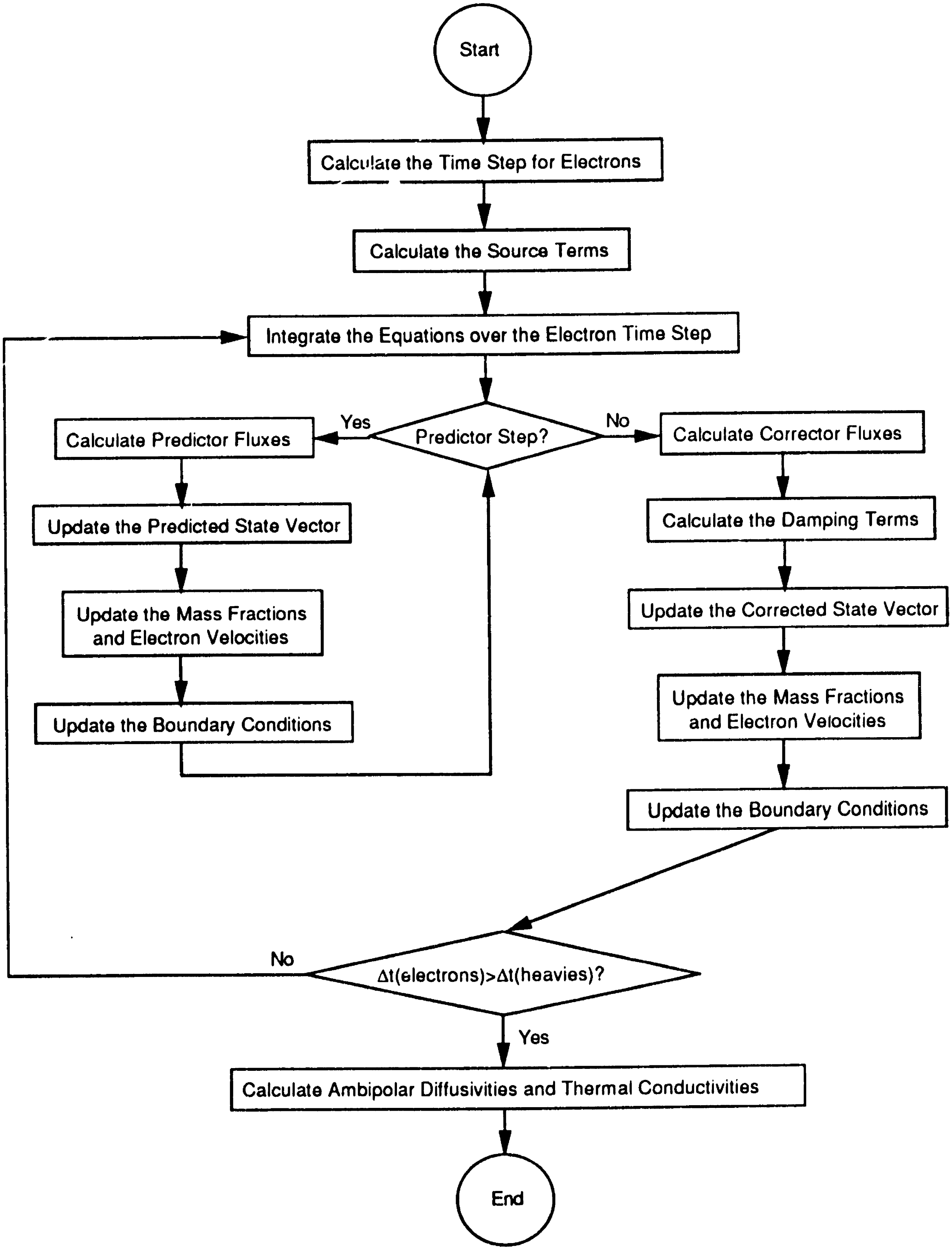

Figure 4.7: Flowchart for the Integration of the Electron Density and Electron Energy Equations

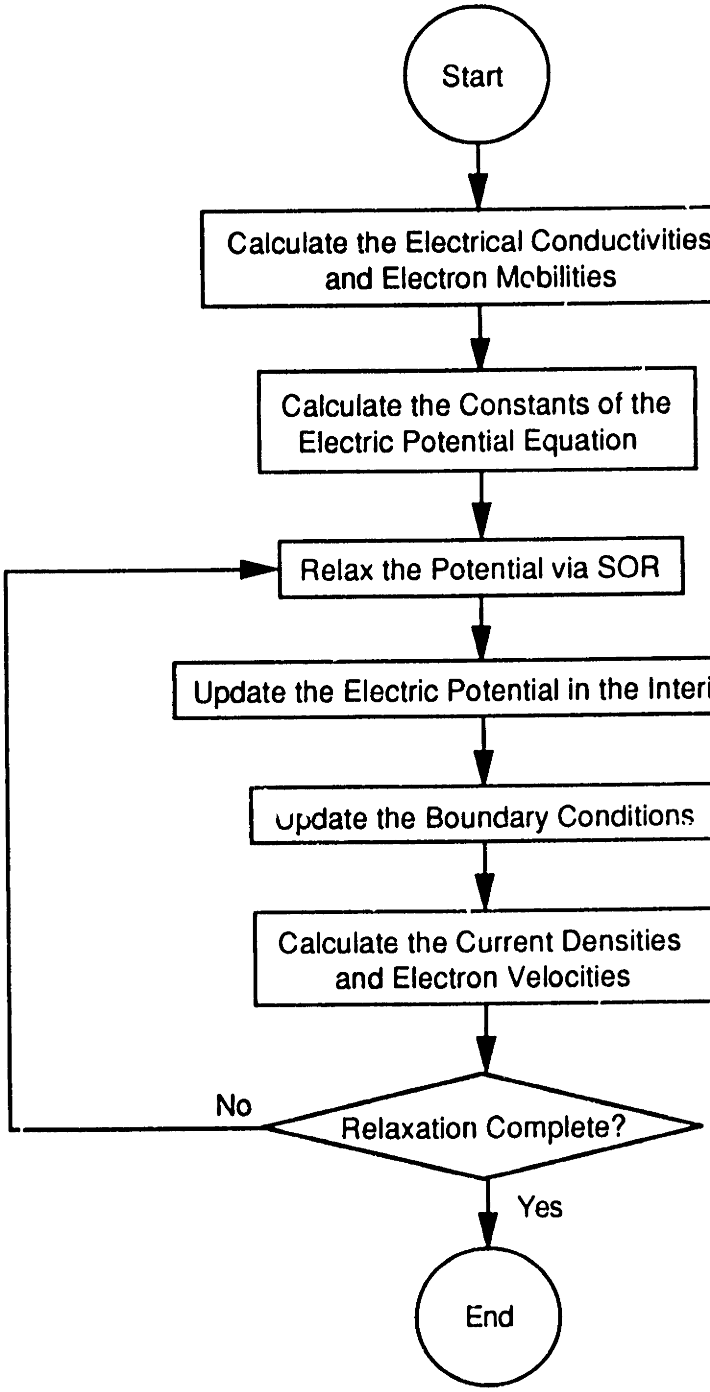

Figure 4.8: Flowchart for the Relaxation of the Electric Potential

Chapter 5

Electrothermal Arcjet Baseline Results

5.1 Model Verification

Parameters of the flow and arcjet geometry for model verification are listed in Table 5.1. A few geometric parameters in Table 5.1 warrant further description in order to clarify their meaning. The upstream anode half-angle describes the angle that the anode wall upstream of the cathode makes with respect to the axis of symmetry. The cathode diameter is the diameter of the cathode upstream of the point where it begins to contract toward the tip. The cathode tip angle is the angle that the contracting section makes with respect to the centerline axis, and the cathode gap is the minimum axial distance between the cathode and anode. Finally, the expansion nozzle may either be contoured as in this case or conical, in which case the nozzle half-angle describes the angle the outer anode wall maintains with respect to the axis of symmetry.

5.1.1 Flow Model

The integration scheme for the flow model was tested by simulating the case of H_2 flowing through the arcjet thruster with a wall and inlet temperature maintained at 1000°K, but with no electric current passing between the electrodes. Thus none of the electron or atomic hydrogen equations are solved in this instance, and the solution is that of purely diatomic hydrogen expanding to vacuum in a viscous axisymmetric nozzle. Initially, a solution was achieved without an azimuthal swirl velocity component. The effect of swirling flow will be examined in the following subsection. The RMS mass flow rate error was less than 1% for the converged solution, and satisfactory agreement

Table 5.1: Parameters for Arcjet Model Verification

Applied current	0A
Mass flow rate	0.2g/s
Propellant	H_2
Wall gas temperature	1000°K
Inlet gas temperature	1000°K
Upstream anode half-angle	45 degrees
Cathode diameter	4.0mm
Cathode gap	2.0mm
Cathode tip angle	45 degrees
Constrictor diameter	2.5mm
Constrictor length	5.0mm
Nozzle contour	bell-shaped
Exit diameter	25.0mm

with 1-D nozzle theory was obtained. Table 5.2 summarizes the calculated performance of this case, in mass-averaged, or bulk, terms for the thrust and specific impulse and in terms of centerline (CL) values for the exit flow conditions. A comparison is made to 1-D theoretical results for an inviscid, isentropic Laval nozzle with identical inlet conditions and exit area ratio. The 10% increased bulk performance in the computed case of this research results primarily from the fact that the flow is heated by the walls throughout the expansion process.

Representative contour plots of the converged solution for flow model verification are displayed in Figures 5.1 through 5.3. The Mach number contours show that the flow becomes supersonic within the constrictor region, and that a weak expansion wave originates at the end of the constrictor on the anode and reflects off the centerline boundary farther downstream. Similar behavior was reported by Pawlas and Keith[86] in a recent numerical simulation of gas flowing through an arcjet geometry without a central cathode. Velocity and temperature contours also show this expansion wave, while Figure 5.4 shows static pressure gradients emanating primarily from the corner points of the constrictor on the anode surface. The pressure is essentially uniform in the radial direction.

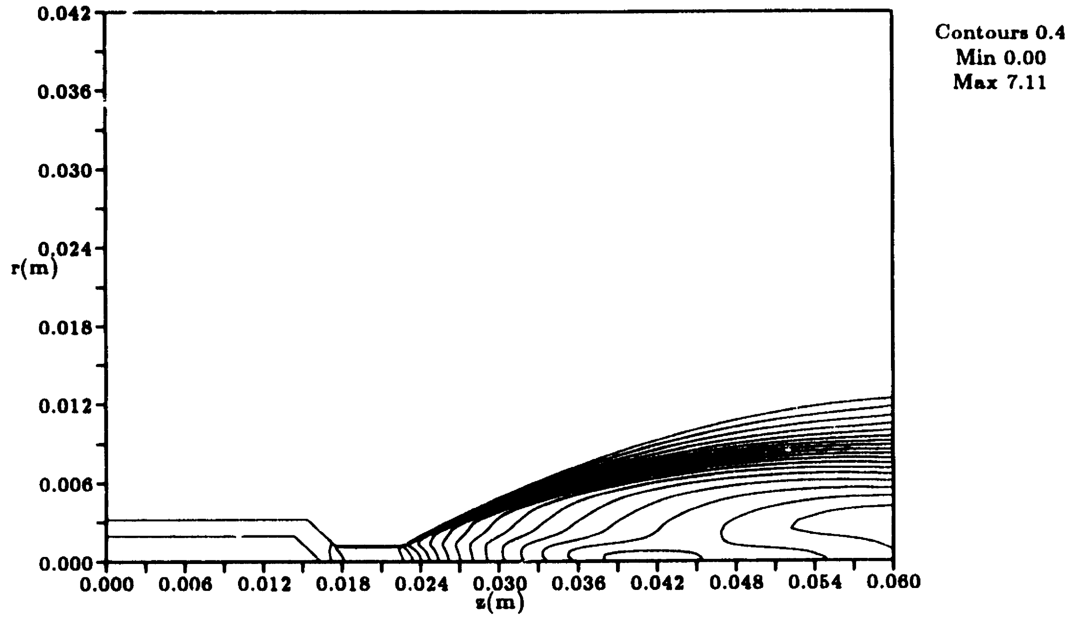

Figure 5.1: Mach Number Contours for Flow Model Verification

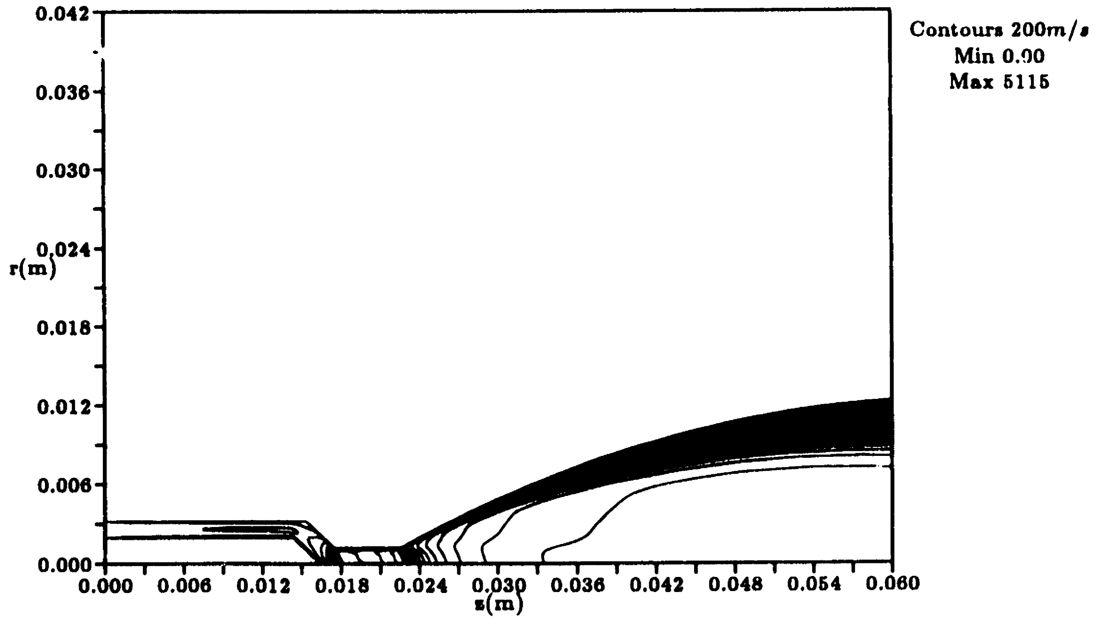

Figure 5 2: Velocity Contours for Flow Model Verification

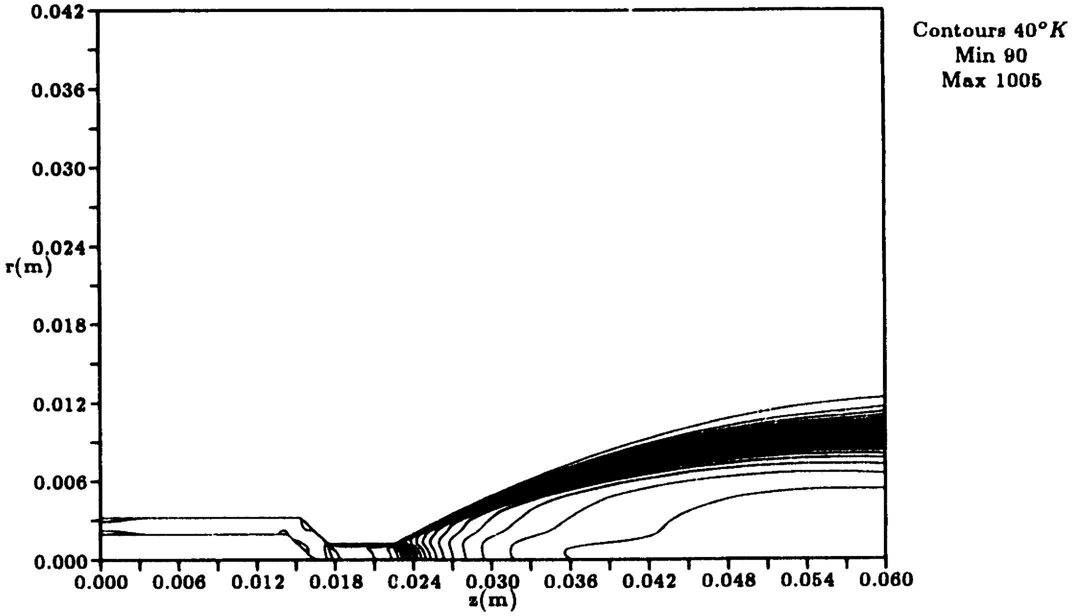

Figure 5.3: Gas Temperature Contours for Flow Model Verification

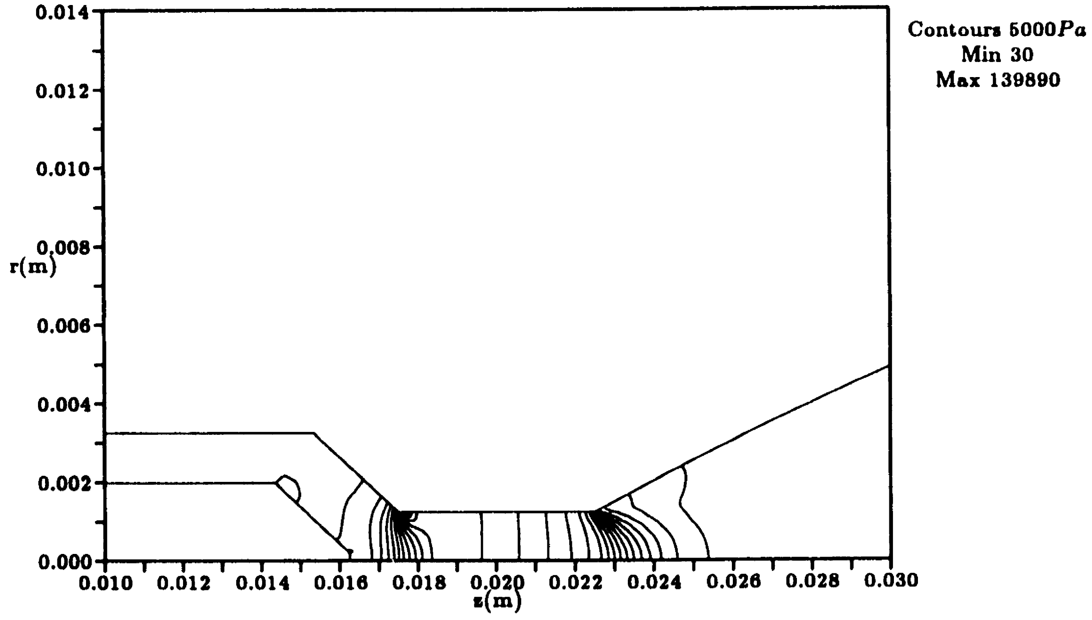

Figure 5.4: Pressure Contours for Flow Model Verification

Table 5.2: Flow Model Verification Results

	Arcjet Code	**Laval Nozzle**
Thrust	0.997N (bulk)	0.912N
Specific Impulse	509.7 sec (bulk)	465.3 sec
Exit Mach Number	6.8 (CL)	6.0
Exit Pressure	37.7Pa (CL)	36.2Pa
Exit Temperature	95.8^oK (CL)	96.3^oK
Exit Density	$9.5 \times 10^{-5} kg/m^3$ (CL)	$9.1 \times 10^{-5} kg/m^3$

5.1.2 Effect of Swirl Velocity

The flow model was also tested under the same parameters as the previous section but including a swirl, or azimuthal, velocity component. In this case the swirl velocity at the inlet boundary was specified by assuming a solid body rotation of the flow whose maximum velocity was 40% of the axial inlet flow velocity. Figure 5.5 shows the value of the swirl velocity as a function of axial distance for several radial mesh locations. Mesh location $j = 0$ is the geometric centerline; location $j = 8$ is one mesh point above the cathode outer radius; location $j = 18$ is at the midpoint of the grid upstream of the cathode tip; and location $j = 29$ is one grid point inside the anode wall. A total of 30 grid points span the mesh from the centerline to the anode wall, inclusive. By conservation of angular momentum, the swirl velocity is greatly increased as the channel cross-sectional area reaches a minimum in the constrictor region. The radial line plots of Figure 5.6 show the evolution of the swirl velocity profile as propellant flows through the arcjet thruster. The first profile (1) is the specified inlet distribution; the second (2) shows a viscosity-smoothed profile just before the cathode begins to narrow; and the last (3) represents the swirl velocity radial profile at the inlet of the constrictor. The last profile, while showing a large increase in swirl velocity magnitude as a result of the decreasing channel cross-sectional area, also displays a form similar to that of an ideal viscous vortex.

The increase in swirl velocity near the constrictor centerline is sufficient to cause the $\frac{\rho u_\theta^2}{r}$ source term in the radial momentum equation to become of the same order as the pressure gradient term. As a result, a lower pressure region is created along the constrictor centerline, as can be seen by comparing Figure 5.7 with Figure 5.4. The locally rapid decrease in pressure in this region then leads to the formation of a "jet"

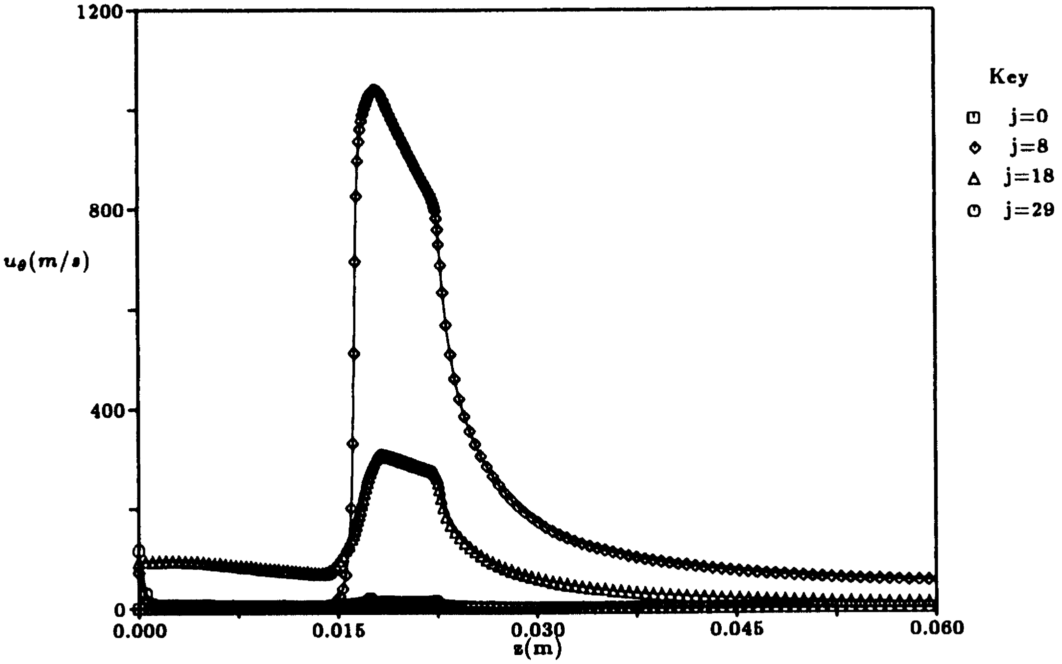

Figure 5.5: Swirl Velocity Axial Line Plot

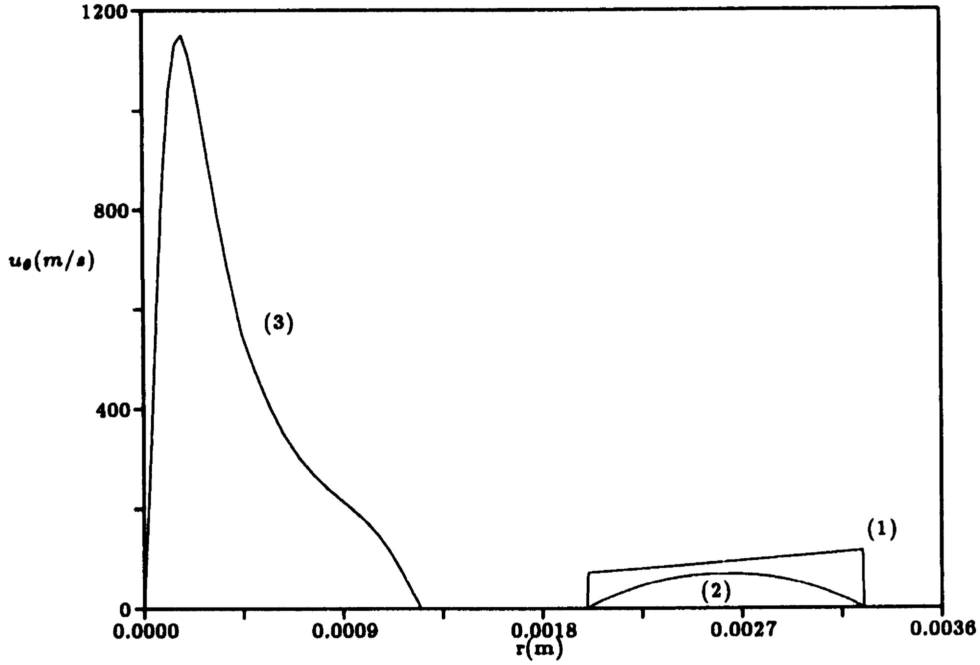

Figure 5.6: Swirl Velocity Radial Profiles

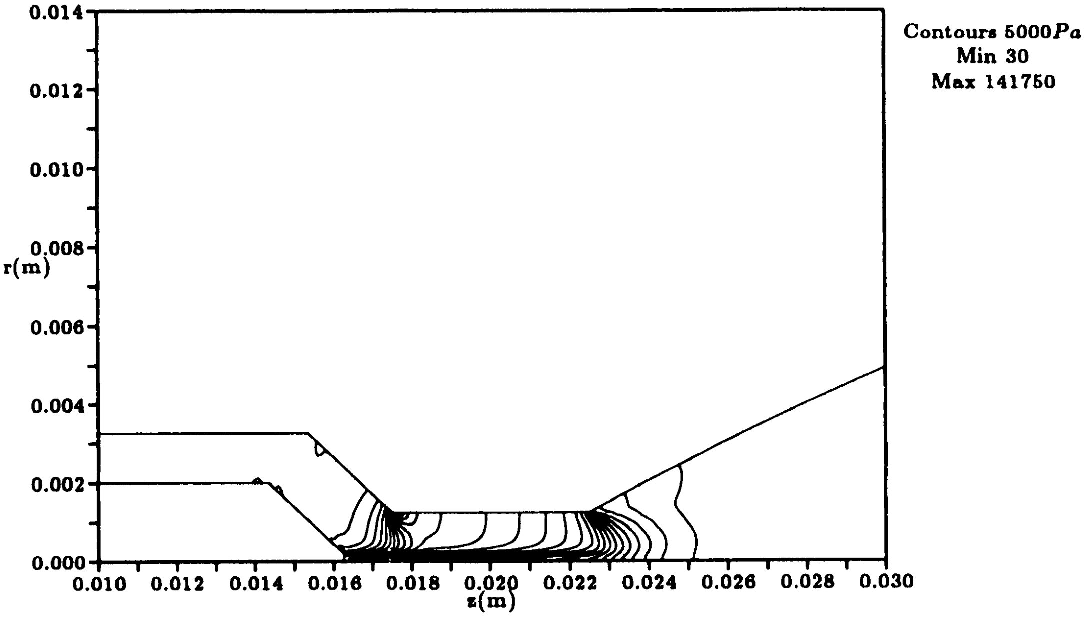

Figure 5.7: Pressure Contours with Swirl Velocity Component

in the axial velocity immediately downstream of the blunt cathode tip. This local high velocity jet, whose existence was predicted analytically by G.K. Batchelor for swirling inviscid flow past a blunt body[5], can be seen in the contour diagram of Figure 5.8.

Global performance parameters for the case with swirl were seen to differ from the case without swirl by less than 0.2%. The Isp for the swirling case was 508.9 seconds, the inlet pressure was 141,750Pa, and the thrust was 0.998N. Although including swirl did change the nature of the flow inside the constrictor region, the overall effect on performance was negligible.

5.1.3 Electric Current/Potential Model

The potential solver implemented in the arcjet code was verified by first solving Laplace's Equation on simple rectangular grids and then on the actual arcjet mesh. This application is analogous to solving the arcjet potential equation without gradients in electrical conductivity or electron pressure. For simple geometries, the numerical solutions were compared to analytic solutions. For the arbitrary mesh of the arcjet thruster, the numerical results were verified by checking that the flow of current from the anode to the cathode was constant and continuous. Figure 5.9 shows the potential contours for one of the actual geometry tests (V=80 volts), while Figure 5.10 shows a corresponding diagram of the current density vectors. Potential contours in Figure 5.9 are plotted every 4V. Note the large potential gradients formed near the cathode tip; this neces-

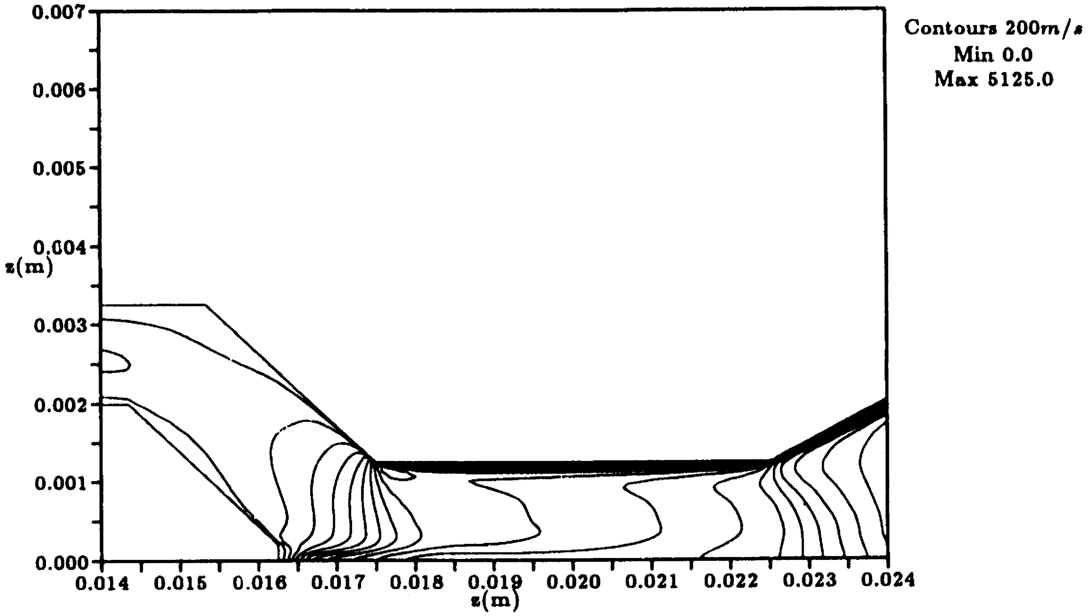

Figure 5.8: Axial Velocity Contours with Swirl Velocity Component

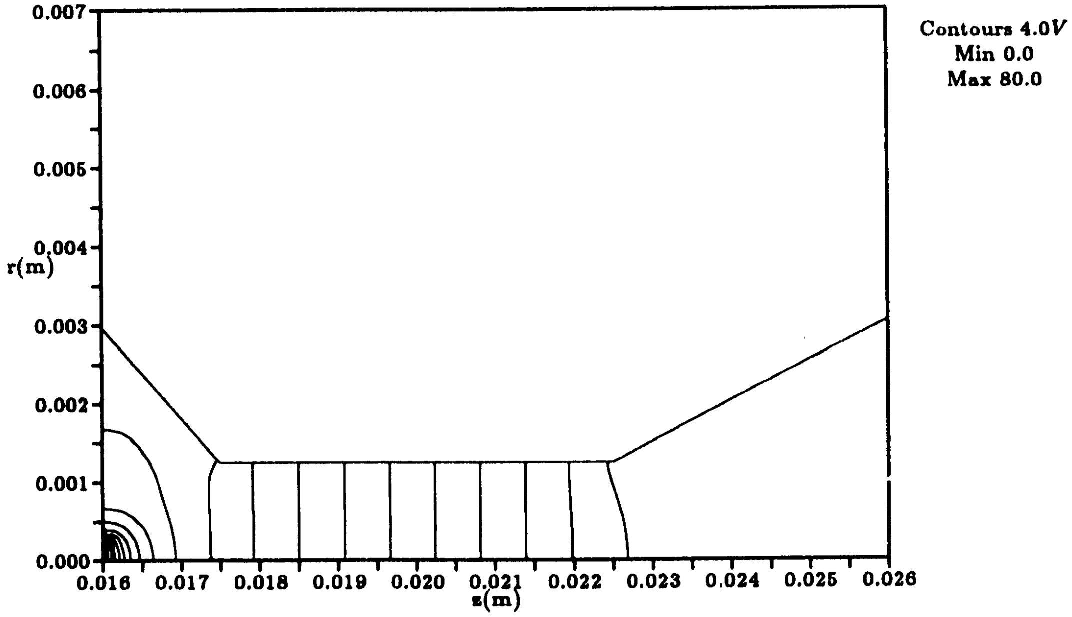

Figure 5.9: Electric Potential Contours for Potential Solver Verification

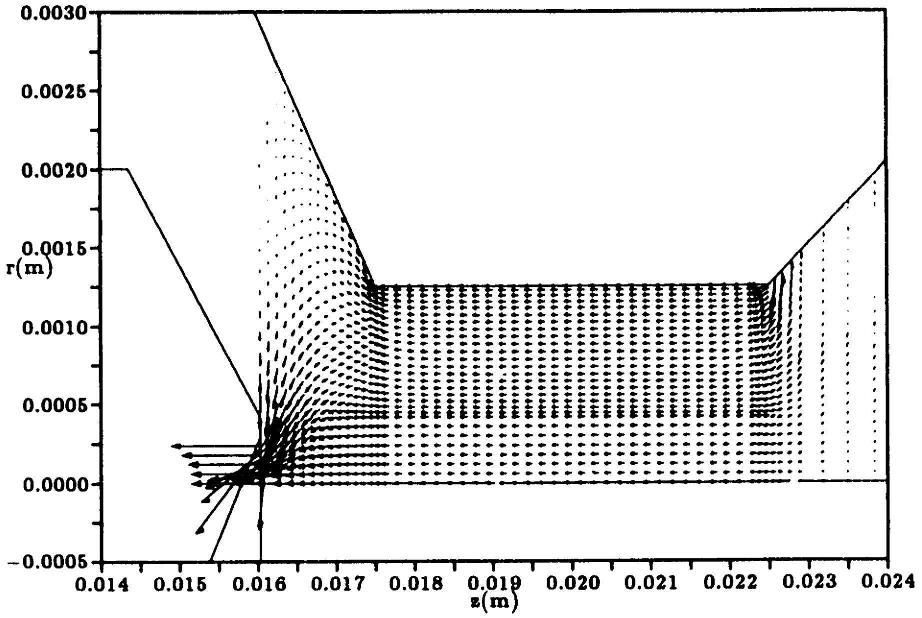

Figure 5.10: Current Density Vectors for Potential Solver Verification (r scale exaggerated)

sarily produces a concentration of current density in the vicinity of the cathode tip, as seen in Figure 5.10.

With an even distribution of electron pressure and electrical conductivity as in these tests, the current density tends to spread itself evenly over the mesh, as expected from fundamental electrodynamics. When these simplifications are removed, however, the distribution of current becomes markedly different. In the fully consistent arcjet model, strong ionization at the cathode tip and along the constrictor centerline will preferentially constrain the current to flow through this central arc region.

5.2 Baseline Arcjet Thruster Case

The baseline arcjet thruster modeled in this simulation is the German TT1 thruster [33], which has the geometrical characteristics listed in Table 5.3. The geometry is similar to that used for the flow model verification, except that the nozzle is conical rather than bell-shaped and the cathode tip angle and upstream anode half-angle are slightly different. The mass flow rate for this case is 0.1g/s, and the applied current is 100A.

Bulk performance parameters predicted by the model are listed in Table 5.4 and compared to experimentally obtained results[35, 36]. Voltage is calculated by adding a cathode sheath voltage drop equal to the ionization potential plus one half the disso-

Table 5.3: German TT1 Radiatively-Cooled Arcjet Thruster Geometry

Upstream anode half-angle	50 degrees
Cathode diameter	4.0mm
Cathode gap	2.0mm
Cathode tip angle	30 degrees
Constrictor diameter	2.5mm
Constrictor length	5.0mm
Nozzle half-angle	17.5 degrees
Nozzle length	35.7mm
Exit diameter	25.0mm

Table 5.4: Comparison of Predicted and Experimental Results for Baseline Case

	Predicted	Experimental	Difference
Voltage (V)	115	112	2.7%
Power (kW)	11.5	11.2	2.7%
Thrust (N)	1.01	0.94	7.3%
Specific Impulse (s)	1030	960	7.3%
Efficiency	0.442	0.395	11.8%

ciation potential of the propellant gas to the voltage measured in the simulation, then subtracting an anode sheath drop equal to the potential necessary to balance electron and ion random thermal currents with the actual current arriving at the anode. Thrust is calculated by integrating the quantity $\rho u_z^2 + P$ over the exit plane of the nozzle, and efficiency is given by the following formula:

$$\eta = \frac{\frac{1}{2}\dot{m}c^2}{VI}. \tag{5.1}$$

There is excellent agreement in the voltage between the predicted and experimental results and good agreement between the thrust and specific impulse results. The accuracy in voltage prediction shows that the model appears to be accurately modeling arc growth, conductivity, and current attachment given the assumptions made concerning electrode voltage drops. One possible reason for the discrepancy in thrust prediction is that the specified inlet gas temperature is probably too high. Using an anode heat balance model, described in Chapter 7 of this thesis, it is shown that the inlet temperature is about 850°K rather than 1000°K for the baseline case based on the heat flux to the anode wall and the TT1 thruster anode/casing design. Since the thrust scales as the plenum total pressure, which scales as $\sqrt{T_0}$, a 15% decrease in the inlet gas temperature could translate into a 7% reduction in thrust, which would bring the simulation results into very close agreement with experimental data. Other effects such as self-consistent positioning of the initial anodic arc attachment point, line radiation losses, or vibrational nonequilibrium could also result in a decreased thrust if incorporated into the model. There is some uncertainty in the predicted voltage, since the cathode sheath drop is of the order 15.8V for hydrogen, but not necessarily exactly equal to that value. The cathode sheath drop may also scale with operating parameters such as the current and mass flow rate. In addition, grid resolution may be lacking in the steep potential gradient regions near electrode surfaces. Reasonable assumptions have been made, however, in formulating the potential model, boundary conditions, and electrode sheath voltage drops. While previous models required heuristic fixes and empirical relations just to give reasonable voltage predictions, this simulation achieves great success in predicting discharge voltage by instead properly incuding the relevant physics.

5.2.1 Characterization of the Flow

The characterization of results for the baseline case is begun by examining the current-potential distributions. Figure 5.11 shows an axial line plot of the electric potential from the cathode tip to the anode attachment. The reference line follows those grid points just inside the anode wall. The anode voltage is maintained at 100V throughout the simulation, while the cathode potential is adjusted to maintain the correct applied current over the cathode tip. The near-cathode voltage drop $\triangle V_c$, shown in the leftmost portion of the figure, is composed of a 15.8V drop assigned to the cathode sheath $(V_i + \frac{1}{2}V_d)$ and an 8V drop calculated in the first few grid points downstream of the tip. The potential increases in a nearly linear fashion upstream of and inside the constrictor. In the current attachment region just beyond the constrictor exit, the near-anode voltage drop $\triangle V_a \approx 15V$ is composed of an approximately 22V drop captured by the simulation and a -7V drop associated with the electron-repelling anode sheath. This net anode voltage drop can be associated with the energy that is deposited into the anode block in the attachment zone by heavy species heat conduction and by the impingement of current-carrying electrons. Assuming that the energy transferred per

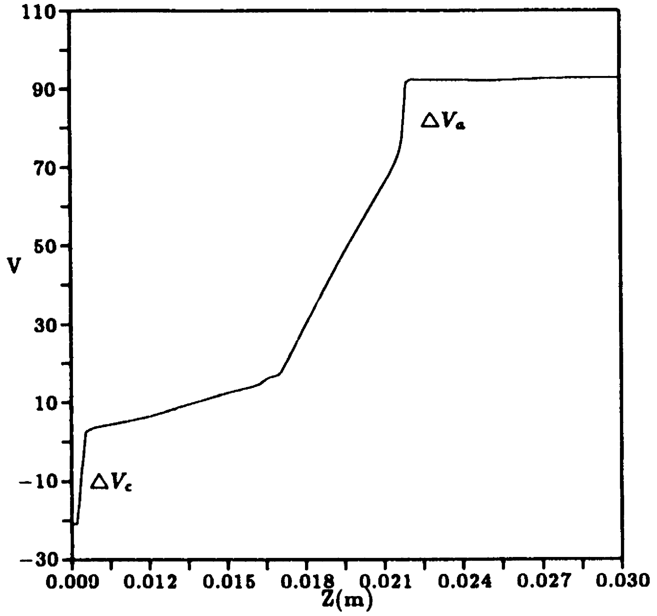

Figure 5.11: Electric Potential Axial Profile for the Baseline Case Arcjet Simulation

unit area is of the form

$$j_a \Delta V_a = -k_g \frac{dT_g}{d\hat{n}} + u_{e\hat{n}} \left[\frac{5}{2} p_e + \frac{1}{2} \rho_e u_e^2 + E_i n_e \right], \tag{5.2}$$

using the results of the baseline flow simulation yields an equivalent voltage of 14.5V for this deposited power, which agrees well with the ΔV_a seen in the potential profile.

Current streamlines are plotted in Figure 5.12. In this case, the bulk of the current attaches within the first quarter of the nozzle, peaking just downstream of the constrictor exit. Contours and axial line plots of current density ($|\vec{j}|$) are shown in Figures 5.13 and 5.14 respectively. In Figure 5.14 and in all subsequent axial line plots, the key shows that each line represents the value of the plotted quantity at the j^{th} grid point in the radial direction. Up to four radial locations may be plotted at once, including the centerline ($j = 0/30$), the grid line just outside of the cathode boundary ($j = 8/30$), the mid-channel line ($j = 18/30$), and the grid line just inside of the anode wall ($j = 29/30$). The location of these lines is shown in Figure 5.15. As would be expected, there is a maximum at the cathode tip and the current density decreases both axially and radially downstream of the cathode. This reflects both the radial growth of the arc in the constrictor region and the concentration of charge carriers in the highly ionized core of the arc which is initiated at the cathode tip.

This highly ionized core of the arc can be seen in Figures 5.16 through 5.18. The radial profiles of Figure 5.17 compare radial ionization fraction distributions at five axial locations in the thruster: the cathode tip, the constrictor inlet, the constrictor

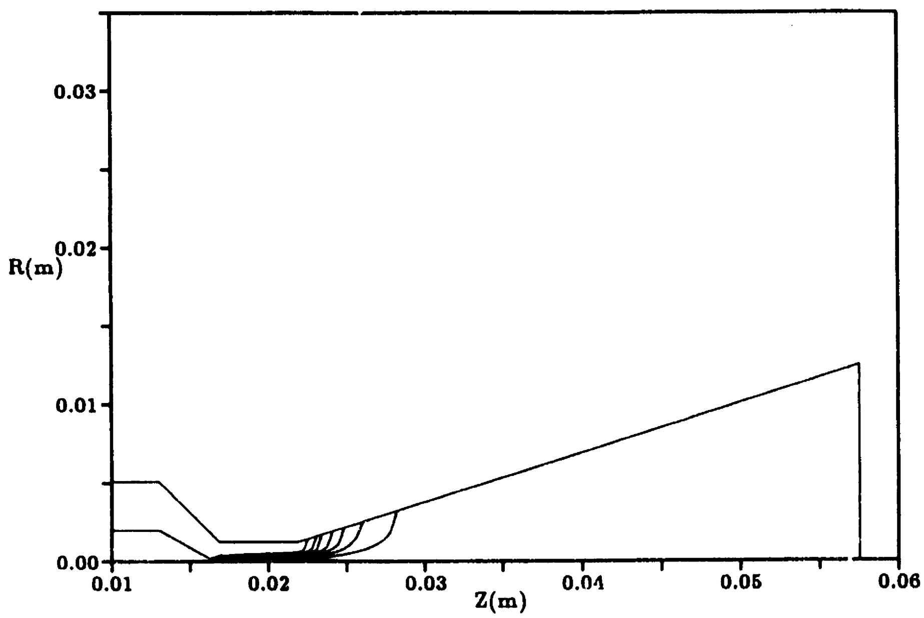

Figure 5.12: Current Streamlines for the Baseline Case Arcjet Simulation

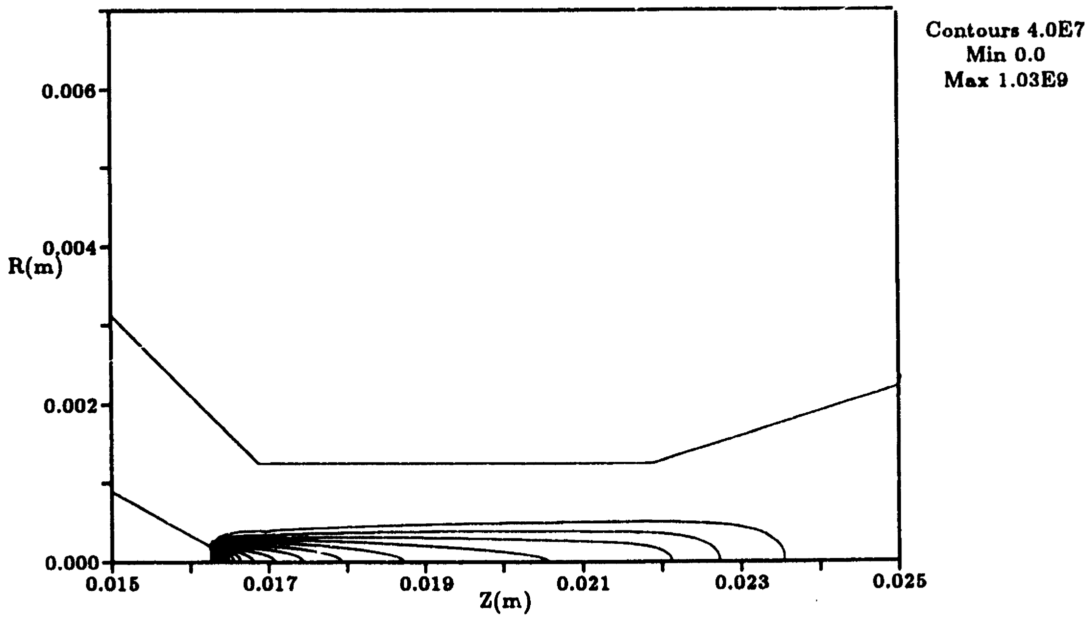

Figure 5.13: Current Density Contours for the Baseline Case Arcjet Simulation

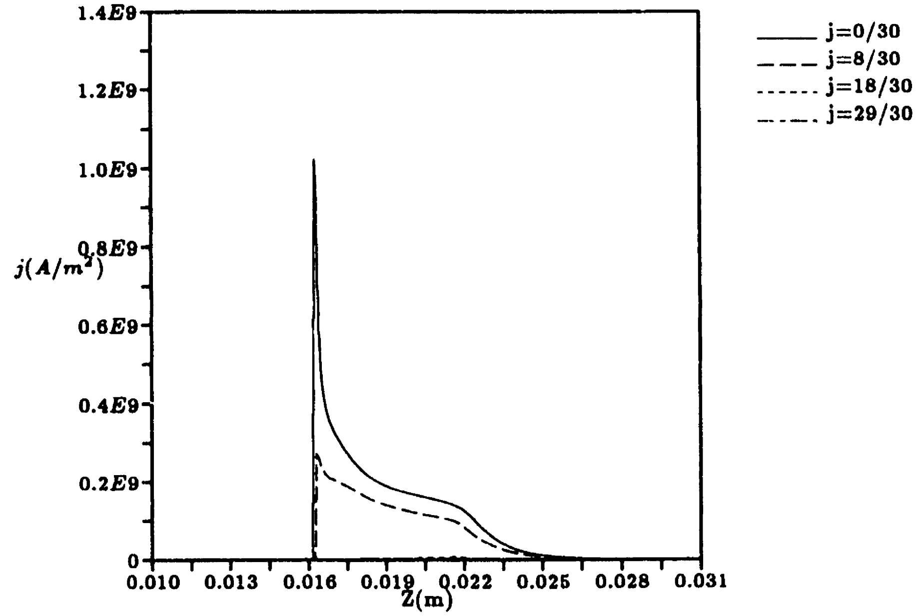

Figure 5.14: Axial Line Plots of $|\vec{j}|$ for the Baseline Case Arcjet Simulation

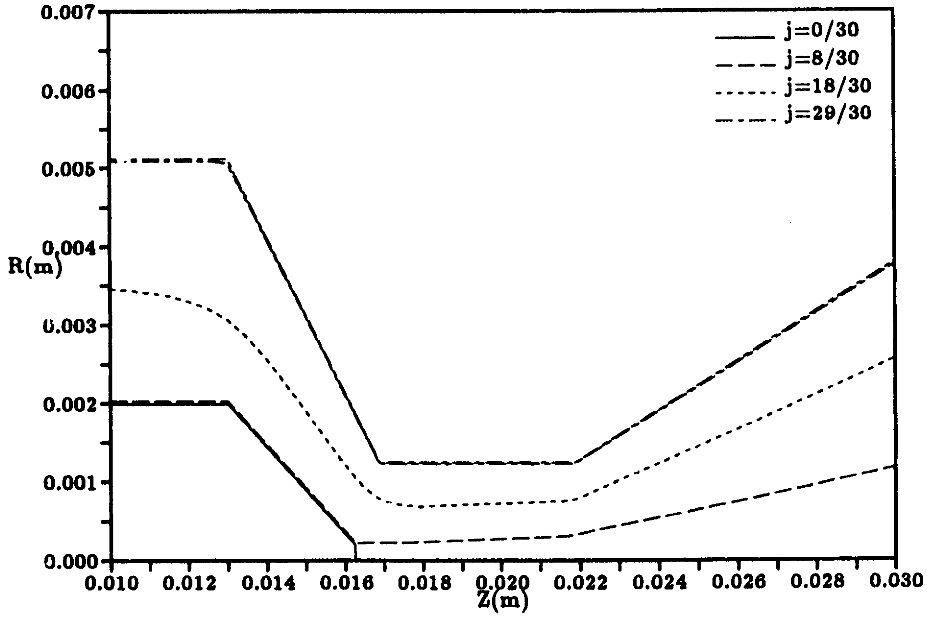

Figure 5.15: Radial Location of Grid Lines Used in Axial Line Plots

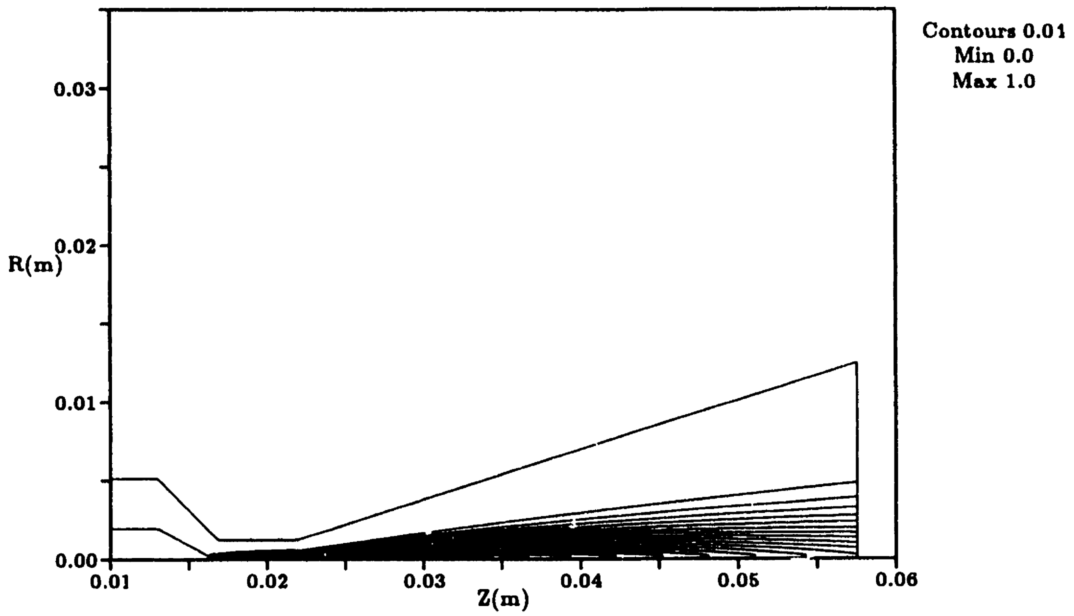

Figure 5.16: Ionization Fraction Contours for the Baseline Case Arcjet Simulation

midpoint, the constrictor exit, and the location one third of the way into the nozzle. The flow is fully ionized along the centerline immediately downstream of the cathode tip and remains so through the first part of the nozzle expansion, after which there is some recombination. The breadth of the partially ionized region grows to approximately 50% of the channel width by the constrictor exit, and this region is essentially entrained in the flow throughout the nozzle.

The primary heating mechanism is ohmic dissipation, which peaks locally along the constrictor centerline and near the anode just beyond the constrictor exit. This is evidenced by the local maxima in electron temperature in these regions (Figures 5.19, 5.20). Near the cathode tip the electron temperature hits the imposed upper limit of 40,000°K, as shown in Figure 5.21. Downstream of the cathode tip T_e decreases monotonically in the core of the arc. This occurs because ohmic dissipation decreases, energy is collisionally transferred from the electrons to the propellant gas, and in the nozzle the flow expands. In the near-anode attachment zone a peak electron temperature of 29,500°K is attained, while the average electron temperature in this region near the wall is approximately 20,000°K. Upstream of the constrictor, where the only source of energy for the electrons is heat conduction from the downstream arc, the temperature reaches a minimum of 1400°K. At the exit plane the peak electron temperature is about 4500°K at the centerline, falling off to 2200°K at the nozzle wall.

Hoskins et al. measured the electron temperature distribution 3mm downstream of the nozzle exit for two similar radiation-cooled 10kW class hydrogen arcjets[51].

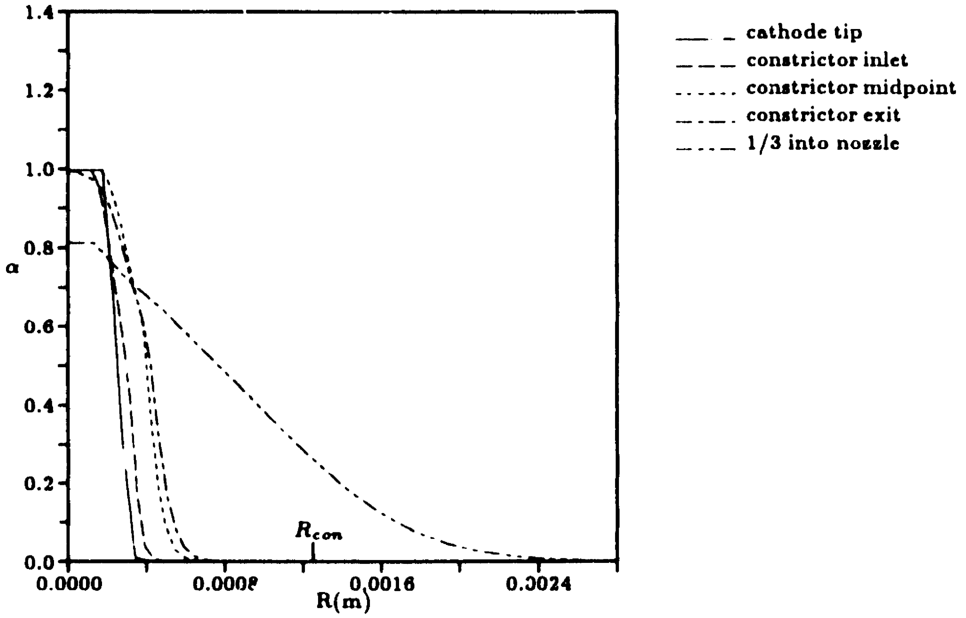

Figure 5.17: Radial Ionization Fraction Profiles for the Baseline Case Arcjet Simulation

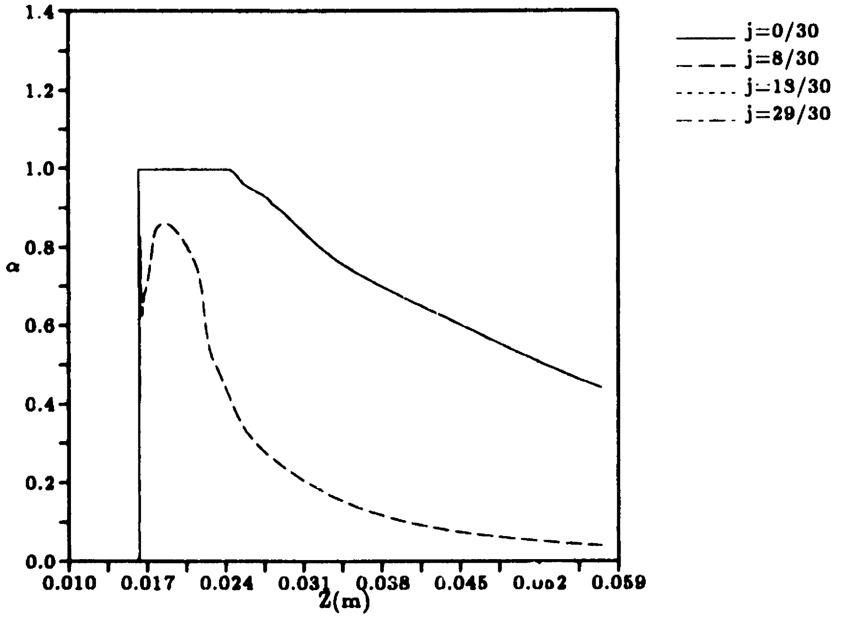

Figure 5.18: Axial Line Plots of α for the Baseline Case Arcjet Simulation

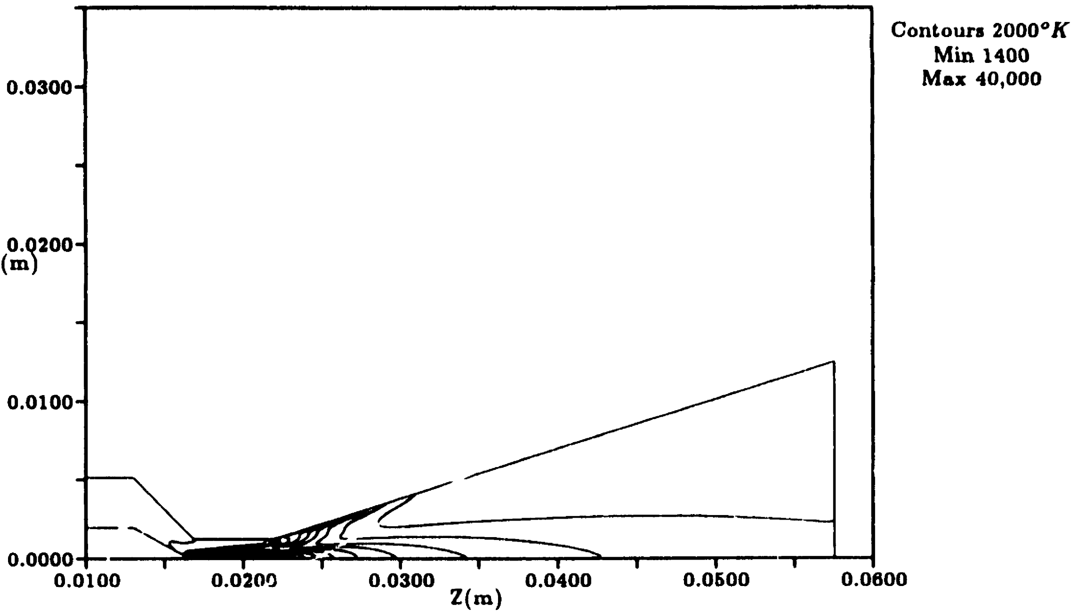

Figure 5.19: Electron Temperature Contours for the Baseline Case Arcjet Simulation

One thruster had a constrictor length and diameter of 1.27mm, a nozzle half-angle of 10°, and an expansion ration of 100:1; the other thruster had a constrictor length and diameter of 1.75mm, a nozzle half-angle of 20°, and an expansion ration of 250:1. The thrusters were then tested at power levels of 6-14kW and mass flow rates of 0.040-0.093g/s. Despite the different configurations, the measured electron temperature just beyond the exit plane varied by no more than about 10% between the two arcjets over the range of operating points. The plots in Figure 5.22 show that the electron temperature distributions measured by Hoskins et al. are relatively insensitive to variations in the input power for the thrusters studied and also that the model of this research predicts an electron temperature distribution very close to the one measured experimentally.

The primary source of energy for the heavy species is collisional energy transfer from electrons. In the core region of the arc where the electron temperature and electron number density are highest, the electron and gas temperatures are closely coupled. In the weakly ionized flow outside of the arc, however, the two temperatures are essentially uncoupled. This is clearly evidenced in Figure 5.23, which compares radial profiles of the gas and electron temperatures just beyond the constrictor exit. Axial profiles of the two temperatures along the centerline are plotted in Figure 5.24. The electron and gas temperatures are nearly equal in the core of the arc, particularly in the nozzle where there is little or no ohmic dissipation once the current has completely attached. In the constrictor and the first quarter of the nozzle, the presence of ohmic dissipation

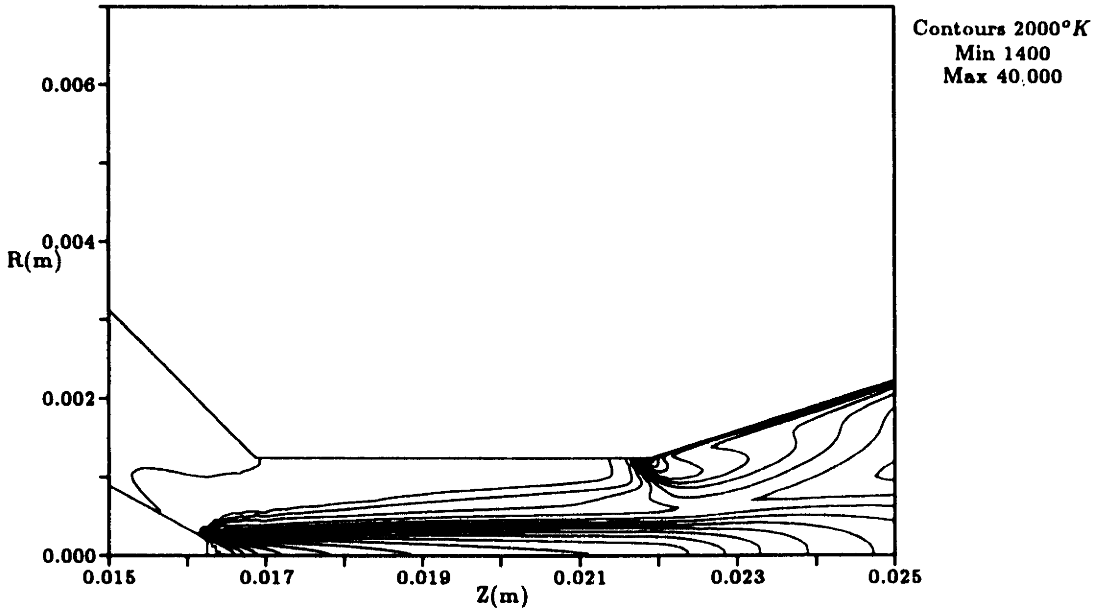

Figure 5.20: Electron Temperature Contours for the Baseline Case Arcjet Simulation: Closeup of the Constrictor Region

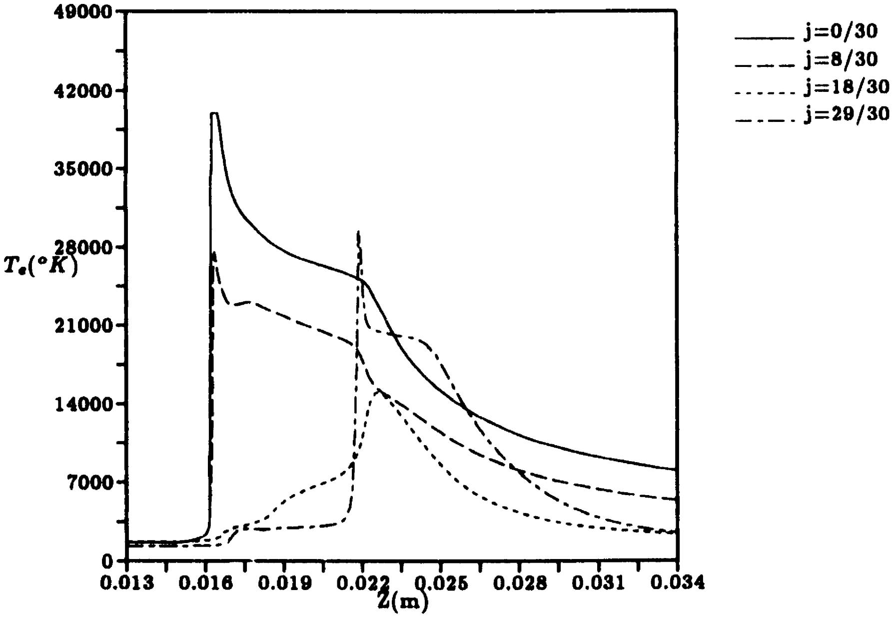

Figure 5.21: Axial Line Plots of T_e for the Baseline Case Arcjet Simulation

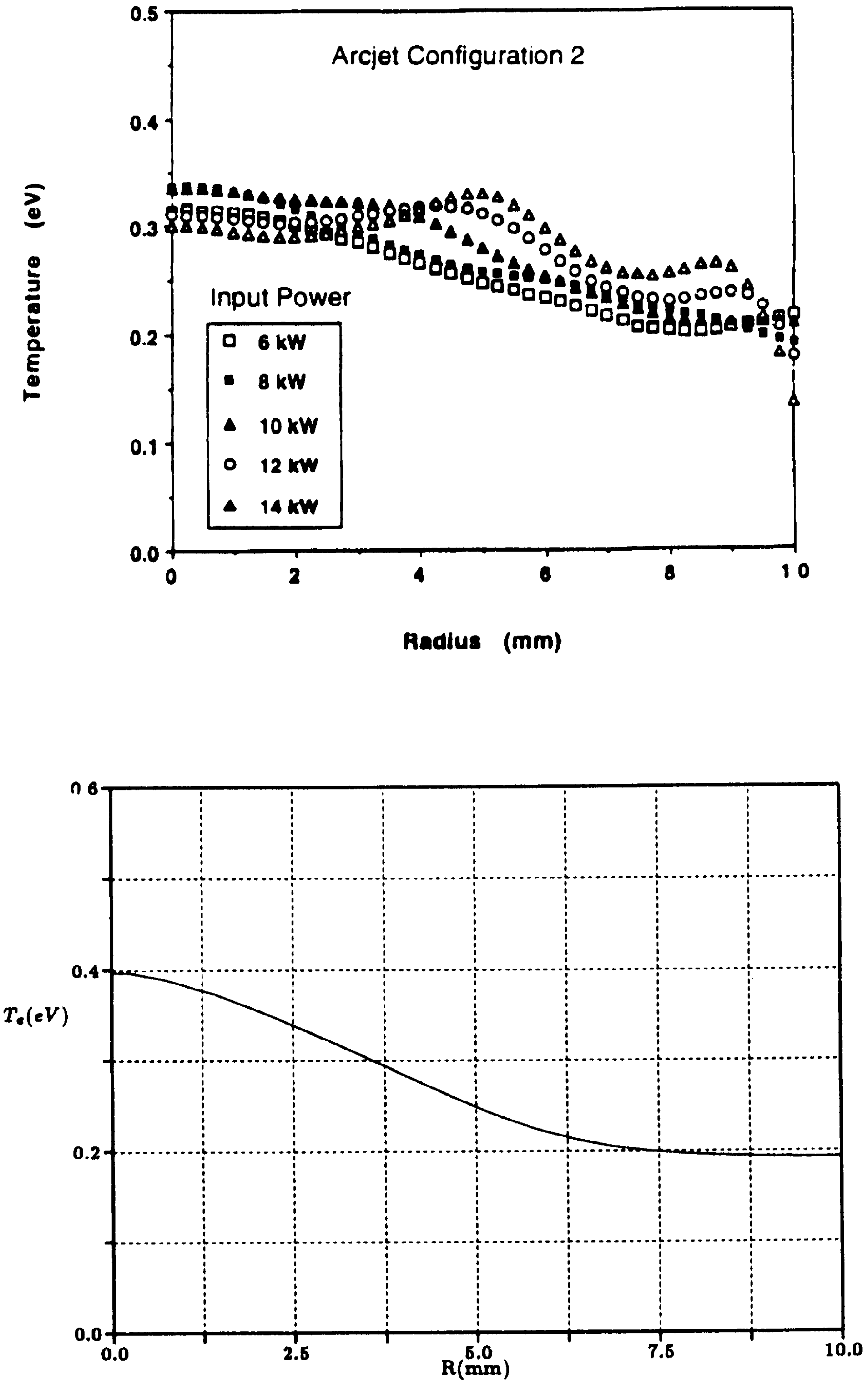

Figure 5.22: Comparison of Predicted Electron Temperature Distribution at Exit Plane to Experimental Measurements of Hoskins et al.

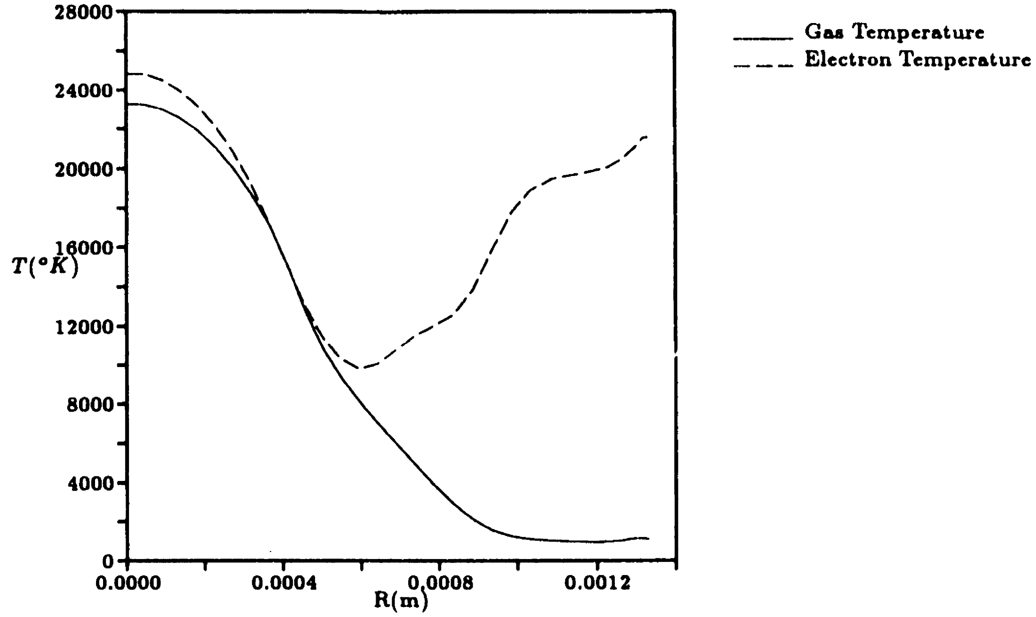

Figure 5.23: Radial Profiles of Gas and Electron Temperatures 0.25mm Downstream of the Constrictor Exit for the Baseline Case Arcjet Simulation

keeps the electron temperature 1000 – 2000°K higher than the gas temperature due to the finite collisional time scales involved.

Contours and line plots of the heavy species temperature for the baseline case are shown in Figures 5.25 through 5.27. Most of the heating of the gas occurs inside and just beyond the constrictor, after which the flow expands and cools in the arcjet nozzle. Figures 5.25 and 5.26 show two distinct regions of the flow: the inner hot core region and the outer cool gas region. The temperature of the outer region remains at or near that of the anode wall since the ionization fraction is too low to provide any significant thermal coupling to the electrons. This illustrates the importance of the inlet gas temperature and the anode wall temperature in determining the overall performance of the arcjet thruster. Since, as will be seen, most of the propellant flows outside of the arc core in the surrounding cooler gas flow, the inlet and wall temperatures directly impact the thrust and specific impulse achieved by the arcjet. Consequently, an accurate arcjet simulation should include either a good estimation of these two temperatures for a variety of operating points or a coupled, self-consistent model of the heat balance in the anode itself. Results presented in this chapter and the next were achieved with a specified anode (and cathode) temperature distribution. Chapter 7 describes the integration of an anode heat balance model with the flow solver and the resulting effects on predicted performance.

While characteristics of the flow such as temperature and composition vary greatly

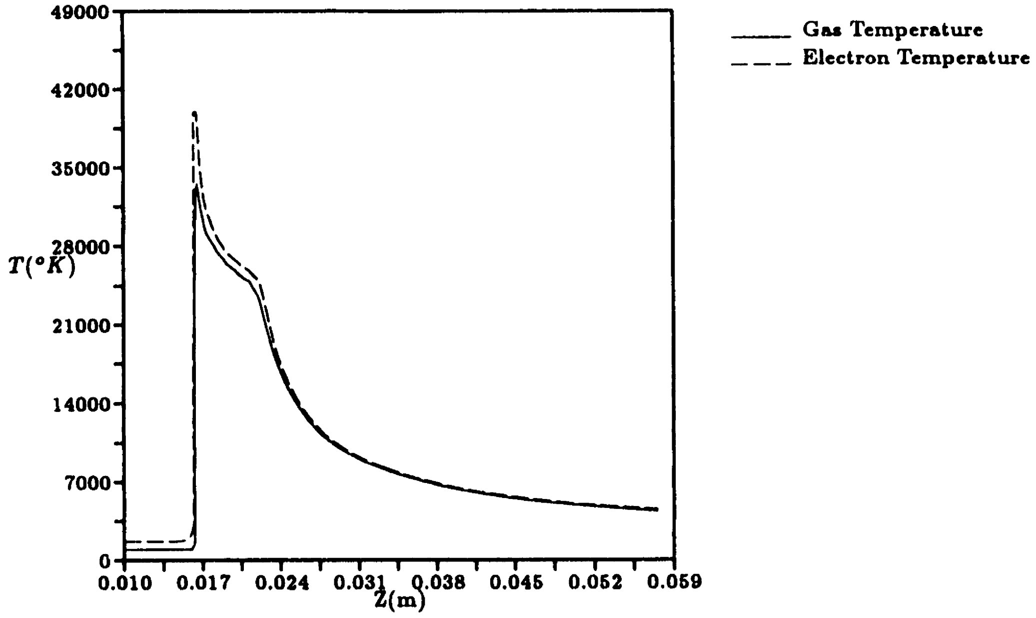

Figure 5.24: Centerline Axial Profiles of Gas and Electron Temperatures for the Baseline Case Arcjet Simulation

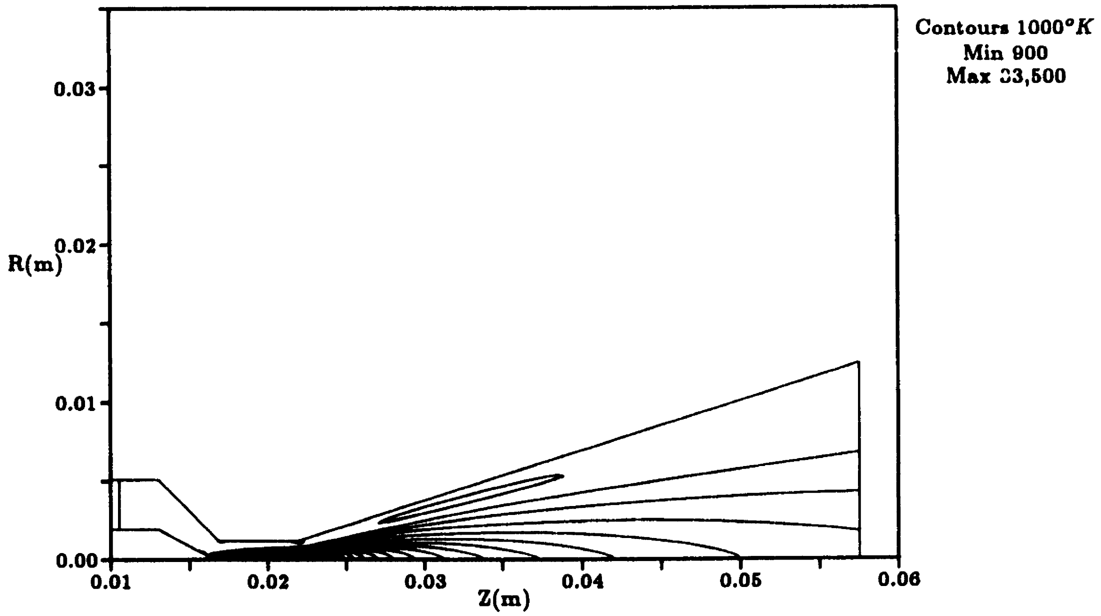

Figure 5.25: Gas Temperature Contours for the Baseline Case Arcjet Simulation

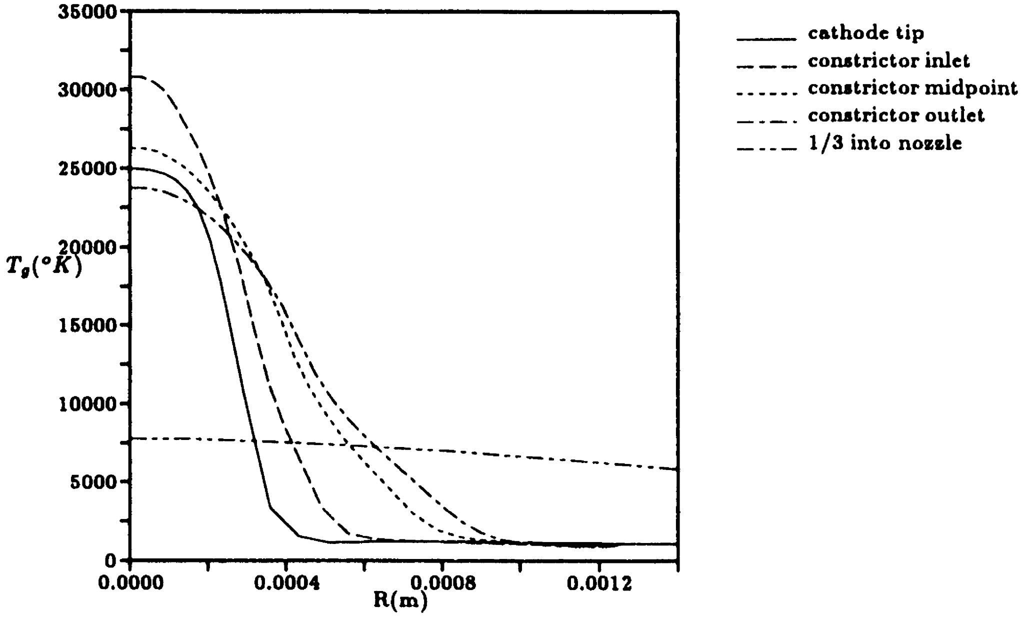

Figure 5.26: Radial Gas Temperature Profiles for the Baseline Case Arcjet Simulation

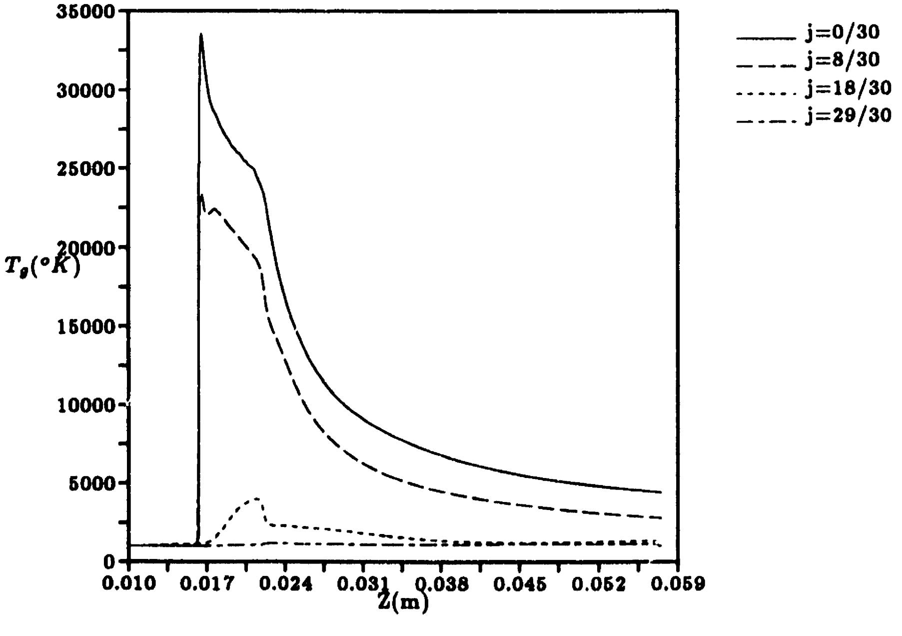

Figure 5.27: Axial Line Plots of T_g for the Baseline Case Arcjet Simulation

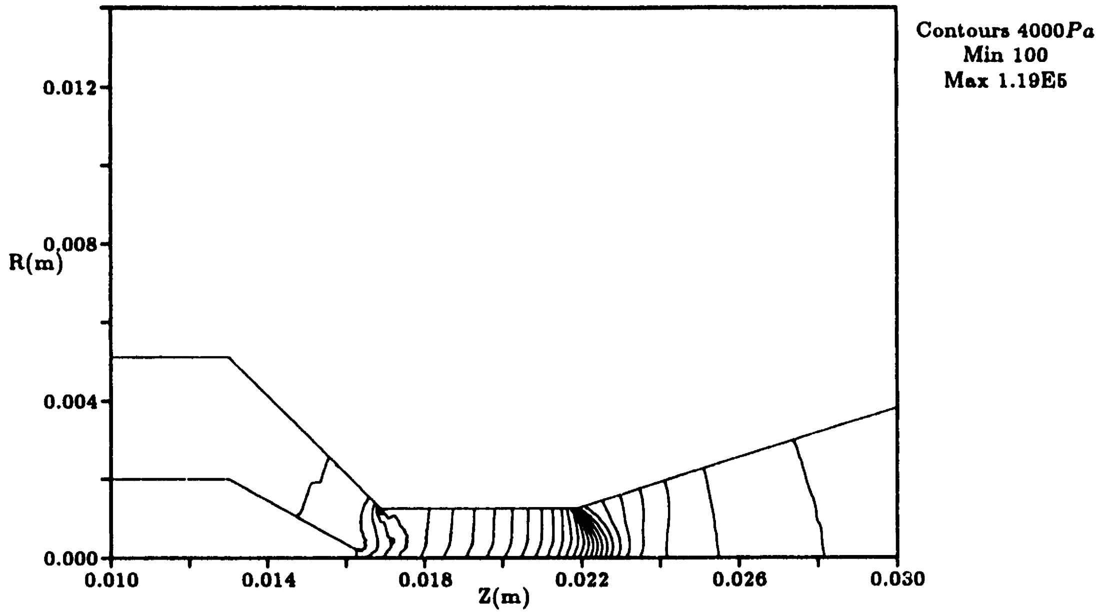

Figure 5.28: Pressure Contours for the Baseline Case Arcjet Simulation

in the radial direction due to the presence of the arc, the pressure is nearly uniform over the flow cross-section. Slight nonuniformities are present near the centerline due to swirl and viscous forces. Figure 5.28 shows pressure contours in the constrictor and surrounding areas. Most of the pressure expansion work is expended in the constrictor and in the first third of the nozzle, especially in the expansion fan at the constrictor exit. Since the pressure is nearly constant in the radial direction but the gas temperature and electron pressure are very high in the core, the density of the flow is much higher in the cooler outer gas flow than in the central flow region. Figure 5.29 illustrates this fact with a contour plot, while Figure 5.30 shows radial density distributions at several axial locations. One interesting result of this density "hole" in the core of the flow is that the electron density in the constrictor peaks radially in the outer portion of the arc, not along the centerline. As previously shown, the arc core is fully ionized. Because the fluid density increases with increasing radius, however, a local maximum in the electron density occurs in the transition region between full and partial ionization, 0.3 to 0.6 mm from the centerline axis. This can be seen clearly in Figures 5.31 through 5.33.

The propellant velocity in the arcjet thruster is influenced greatly by the nonuniformities in other flow variables. In particular, low density in the core region leads to much higher acceleration in the center as opposed to the surrounding higher density, low temperature flow. The reason for this is that while the pressure work term is nearly constant over the cross-section, there is very little propellant in the core of the arc com-

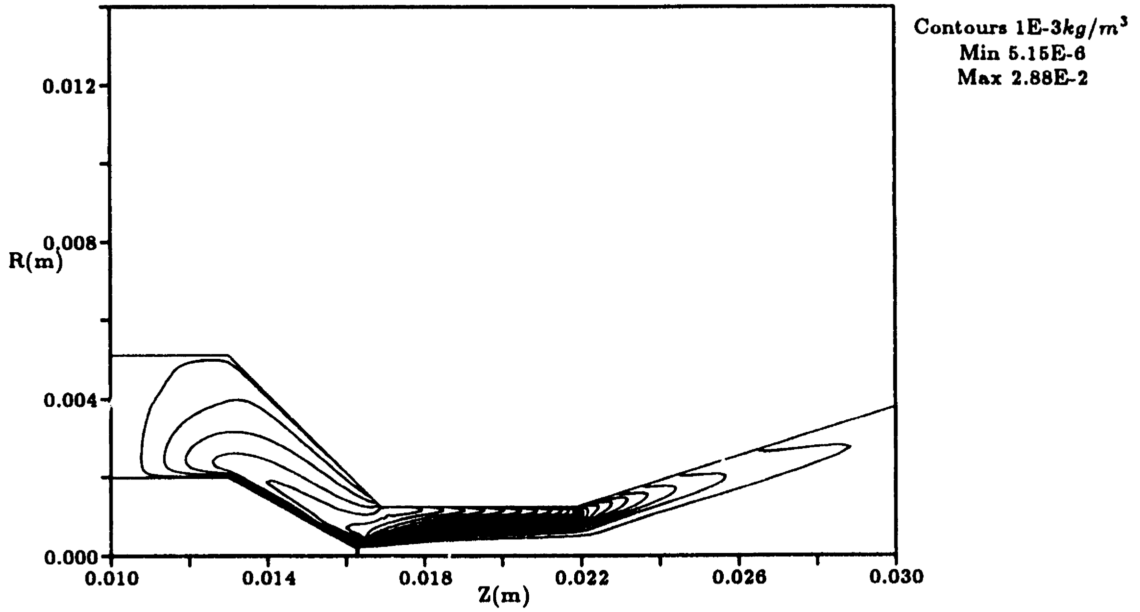

Figure 5.29: Density Contours for the Baseline Case Arcjet Simulation

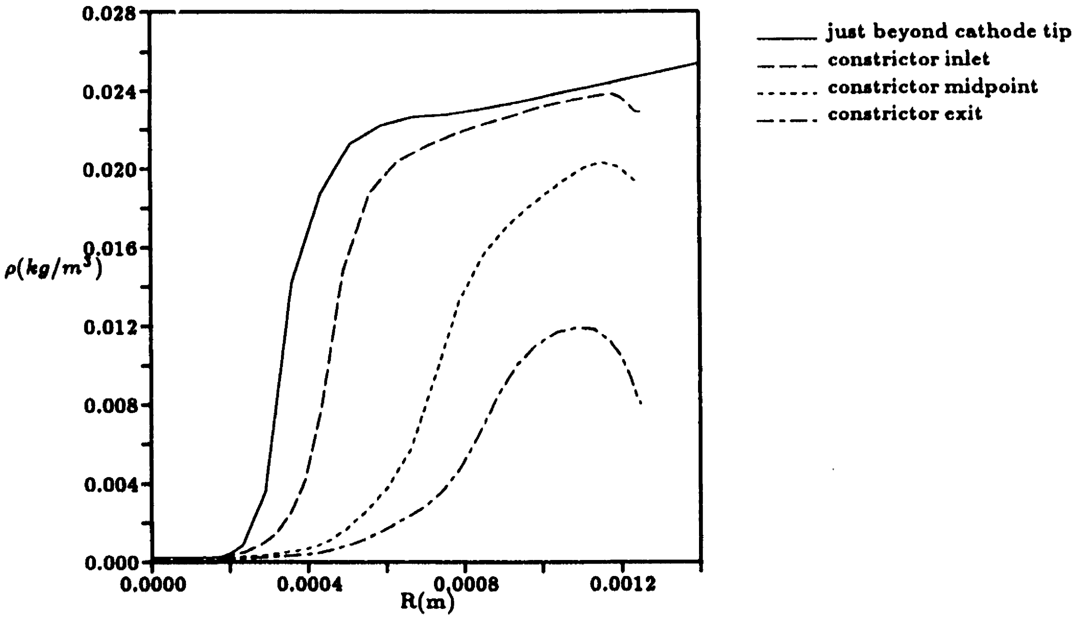

Figure 5.30: Radial Density Profiles for the Baseline Case Arcjet Simulation

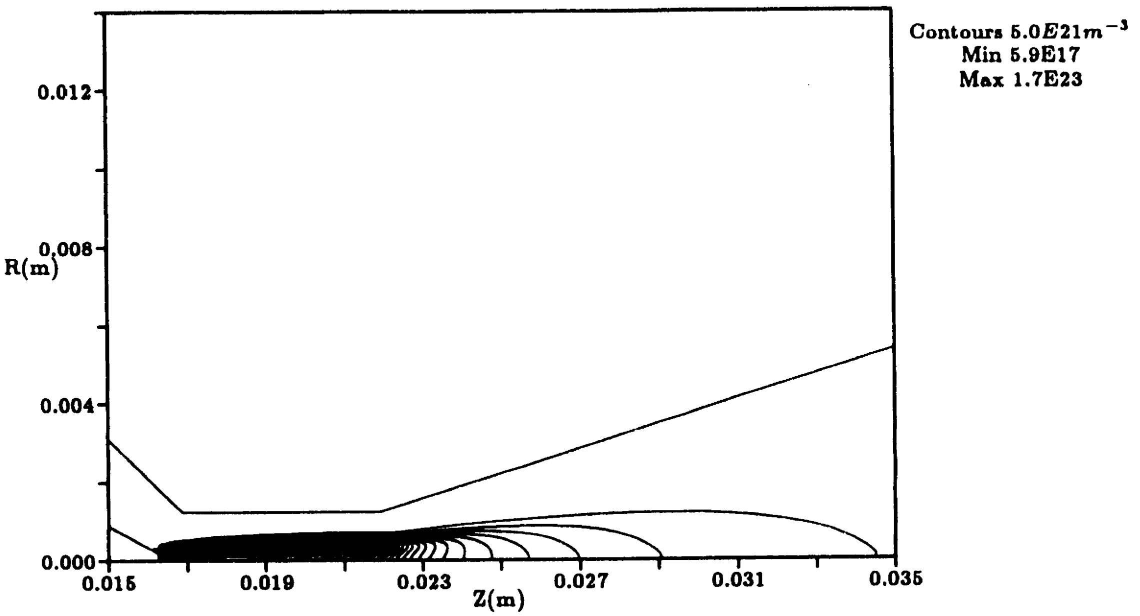

Figure 5.31: Electron Number Density Contours for the Baseline Case Arcjet Simulation

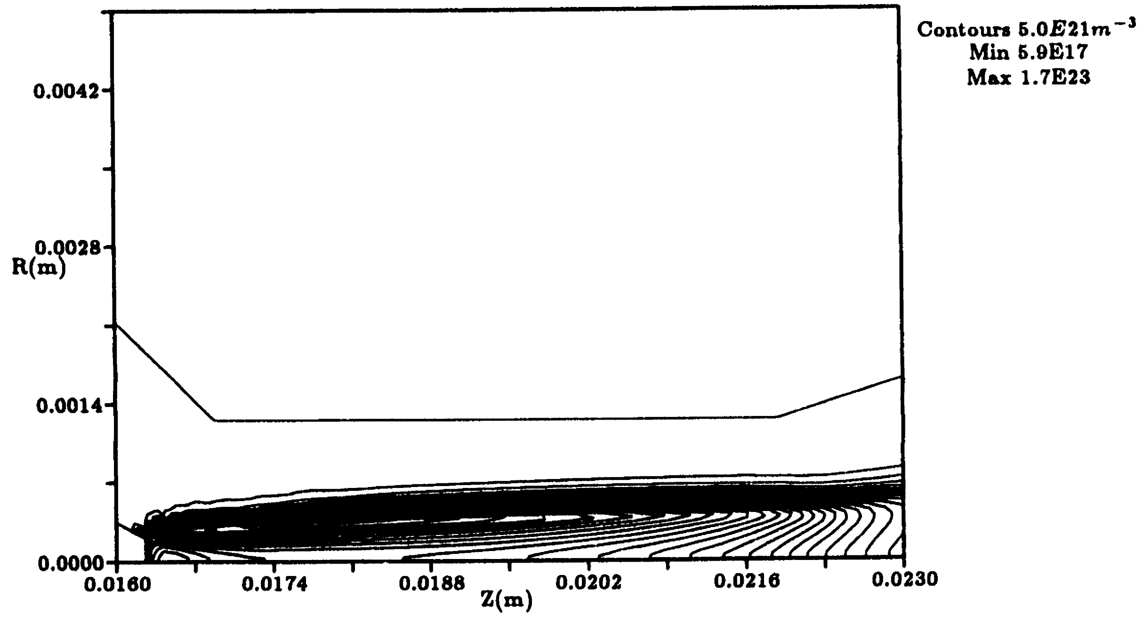

Figure 5.32: Electron Number Density Contours for the Baseline Case Arcjet Simulation: Closeup of the Constrictor Region

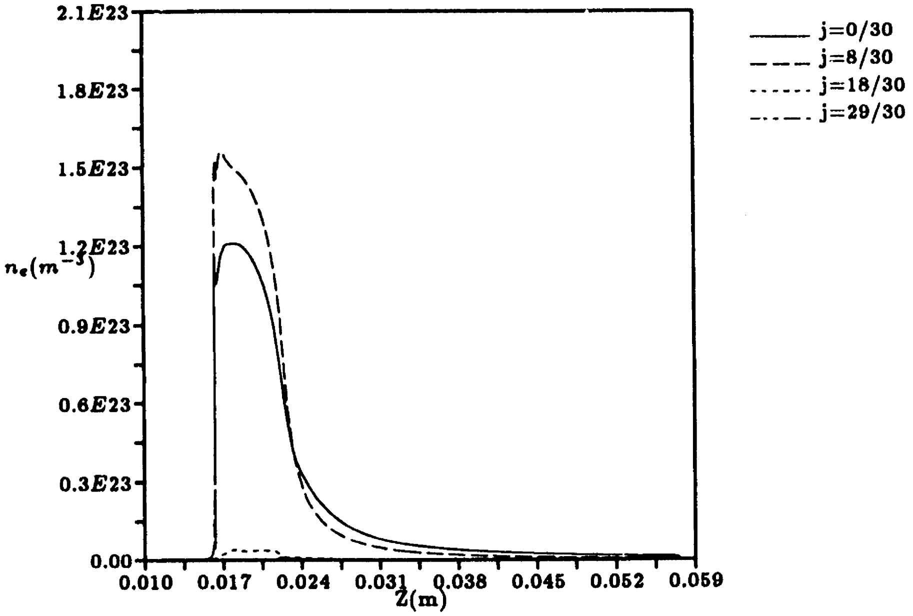

Figure 5.33: Axial Line Plots of n_e for the Baseline Case Arcjet Simulation

pared to the outer flow. As a result, the core gas is accelerated at a proportionally higher rate. The contour plots of Figures 5.34 and 5.35 show this rapid acceleration region within and just beyond the constrictor. In this case the centerline velocity reaches a maximum of over 26,000m/s. The separation between the high and low acceleration regions is clearly shown in these figures. The two regions remain essentially uncoupled through the constrictor and the first part of the nozzle expansion, beyond which the boundary is smoothed out by viscous forces.

Although the axial velocity is very high in the core of the flow, the mass flux in that region is initially small due to the extremely low density. Figure 5.36 shows mass flux (ρu_z) contours for the baseline case in the region of the constrictor. The exclusion of mass flow from the core arc region in the constrictor can be seen clearly in the detail of this contour plot. A more relevant way of illustrating this effect, however, is to integrate the mass flux over the cross-section at a particular axial location, thereby taking into account the axisymmetric geometry. A resultant mass flow ($\rho u_z dA$) radial distribution obtained at the constrictor exit is shown in Figure 5.37. The mass flow fraction inside the arc region (defined by an ionization fraction greater than 0.01) as a function of axial distance is shown in Figure 5.38. It can be seen that the mass flux in the arc grows from zero at the cathode tip to 5% at the constrictor inlet, 25% at the constrictor exit, and 80% at the nozzle exit plane. The most rapid growth occurs in the constrictor, where the boundary of the arc moves radially outward by heat diffusion and the arc mass flow is increased by axial convection. In the nozzle

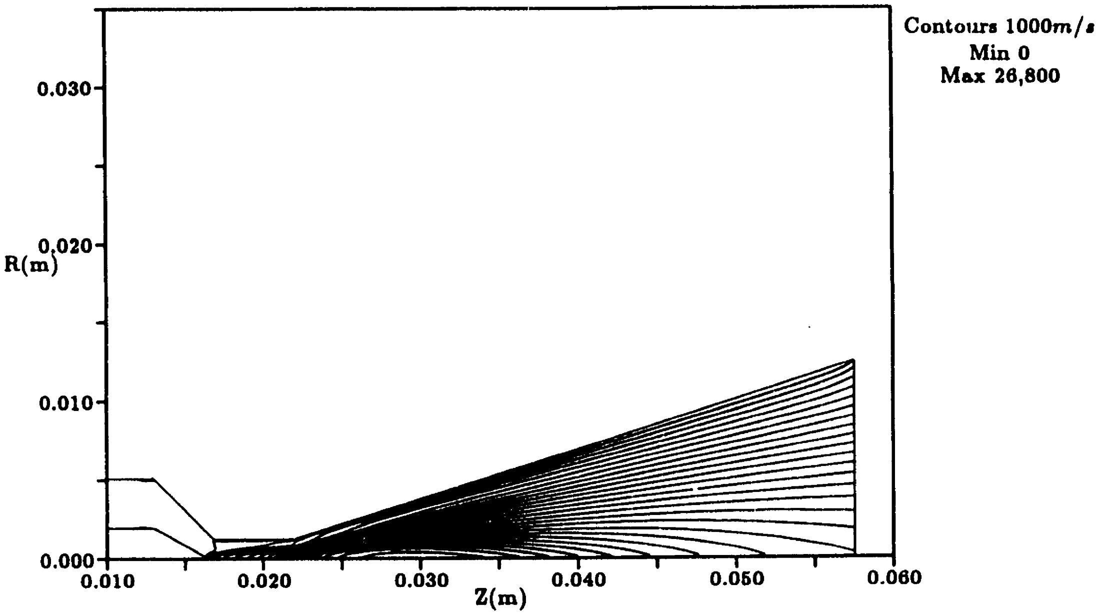

Figure 5.34: Axial Velocity Contours for the Baseline Case Arcjet Simulation

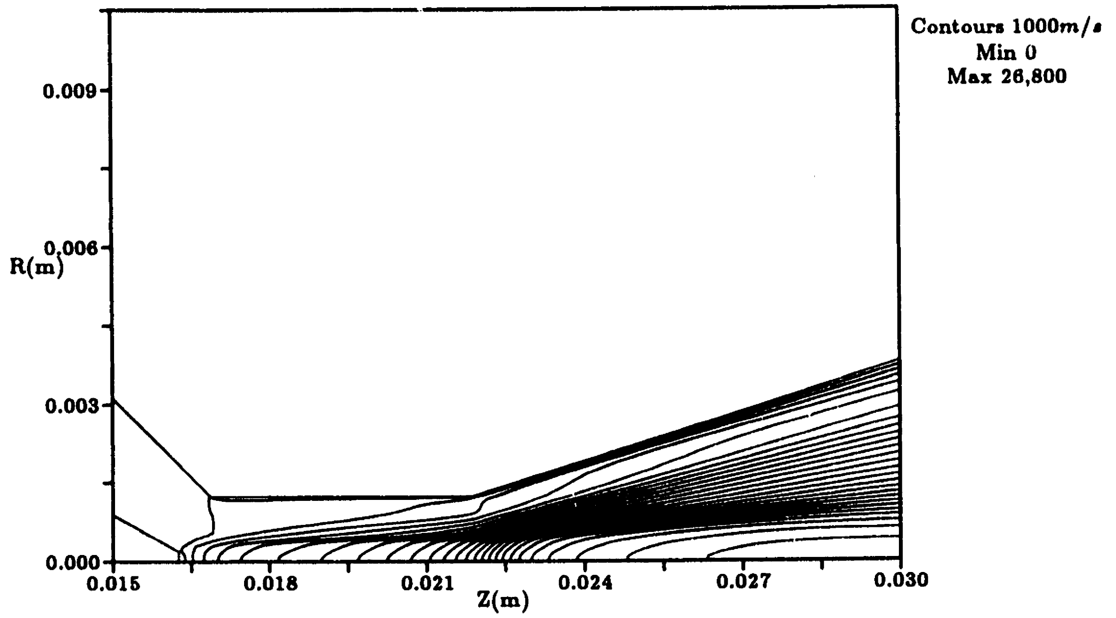

Figure 5.35: Axial Velocity Contours for the Baseline Case Arcjet Simulation: Closeup of the Constrictor Region

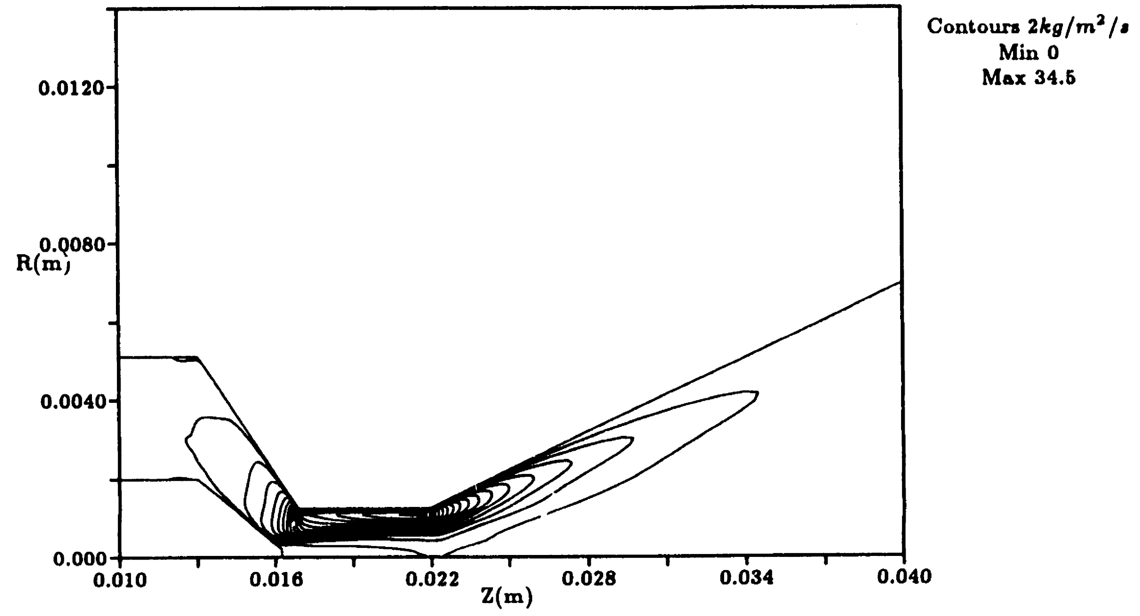

Figure 5.36: Mass Flux (ρu_z) Contours for the Baseline Case Arcjet Simulation (r-Coordinate Expanded)

ambipolar diffusion widens the ionized region and viscous and diffusive forces further smooth out the nonuniformities in velocity, density, and temperature. This is evidenced by the radial mass flow distribution at the thruster exit shown in Figure 5.39.

Momentum flux (ρu_z^2) contours are displayed in Figures 5.40 and 5.41. The momentum flux, like the mass flux, is seen to peak radially in the outer flow near the anode wall, although in this case a significant fraction is present in the arc core due to the high centerline velocity. The ratio of the momentum flux at the centerline to its maximum in the outer flow is approximately 0.1 at the constrictor inlet, 0.3 at the constrictor exit, and 0.5 in the nozzle. The nonuniformity of the momentum flux in the radial direction is due chiefly to viscous drag on the high speed core of the flow. Variations, or ripples, in the contour plots of Figures 5.40 and 5.41 result from radial gradients in temperature, density, and flow composition in the region of the arc edge, all of which affect the magnitude of viscous forces. Viscosity and diffusion smooth out these gradients in the nozzle expansion, so that by the thruster exit the momentum flux varies smoothly over the cross-section. The peak value at the exit occurs in mid-channel because the density is at a minimum at the centerline axis, while the axial velocity reaches a minimum at the anode wall. Figures 5.42 and 5.43 show integrated momentum flux distributions at the constrictor and nozzle exits, respectively. This quantity $\rho u_z^2 dA$, when summed over each point in the distribution, represents the kinetic contribution to the thrust. When the momentum flux is integrated over the

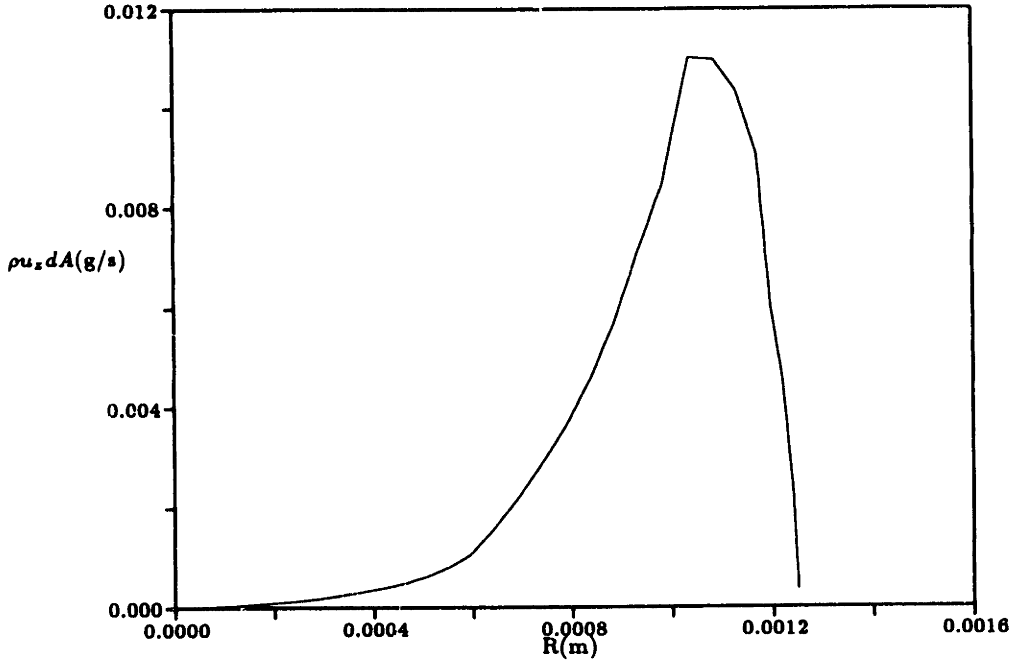

Figure 5.37: Radial Distribution of the Mass Flow Rate at the Constrictor Exit for the Baseline Case Arcjet Simulation

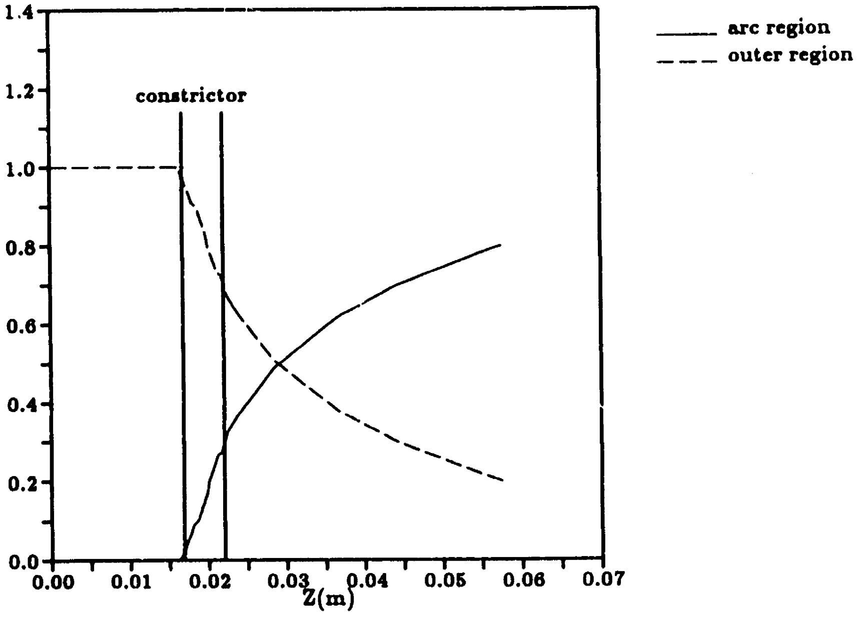

Figure 5.38: Mass Flow Fraction Inside the Arc ($\alpha > 0.01$) as a Function of Axial Location for the Baseline Case Arcjet Simulation

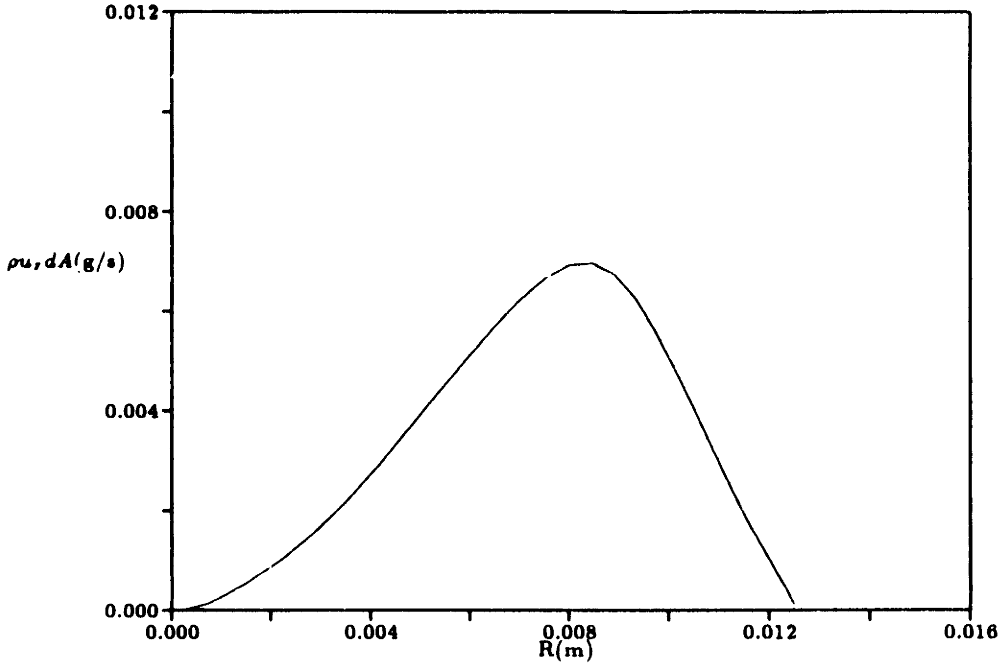

Figure 5.39: Radial Distribution of the Mass Flow Rate at the Thruster Exit for the Baseline Case Arcjet Simulation

cross-section to take into account the cylindrical geometry, it can be seen that the bulk of the kinetic thrust in the constrictor is actually pushed outward toward the walls by the presence of the central arc.

The mass and momentum flux distributions detailed in the previous two paragraphs point out an interesting way of describing how an arcjet works. Many people would explain the operation of an arcjet thruster by saying that an electric arc is passed through a specially designed rocket and imparts some of its dissipation energy to the flowing gas. This additional thermal heating of the propellant is then converted to kinetic energy in the nozzle expansion to produce increased thrust. The results shown in this chapter, however, show that while a very high temperature core is produced by the arc in the constrictor region, very little mass actually flows within this core. In reality, the effect of the central arc is to produce an electrothermal, or fluid dynamic, "plug" which forces most of the mass flow outward into the relatively low temperature region near the anode wall. This process then decreases the effective throat area, thereby increasing the stagnation pressure of the plenum and increasing the thrust of the device. This is not the full explanation, because there is heating of the flow by the arc in the core and transition region and there is some finite amount of propellant flowing within the arc core which then transfers a portion of its energy to the outer flow by diffusion and mixing in the nozzle.

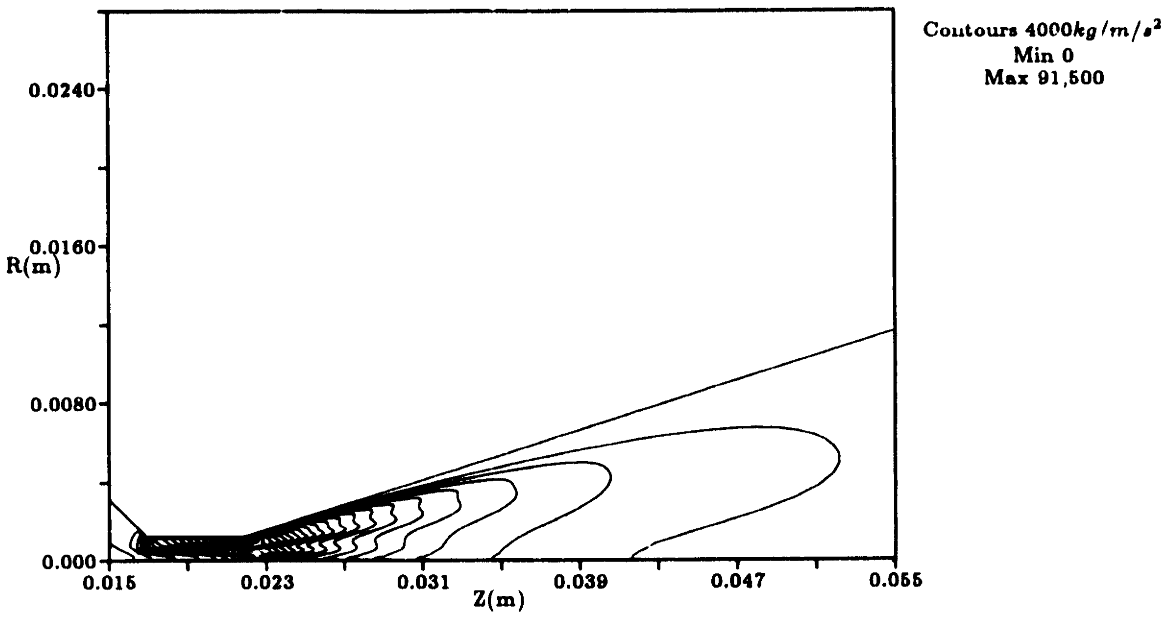

Figure 5.40: Momentum Flux (ρu_z^2) Contours for the Baseline Case Arcjet Simulation

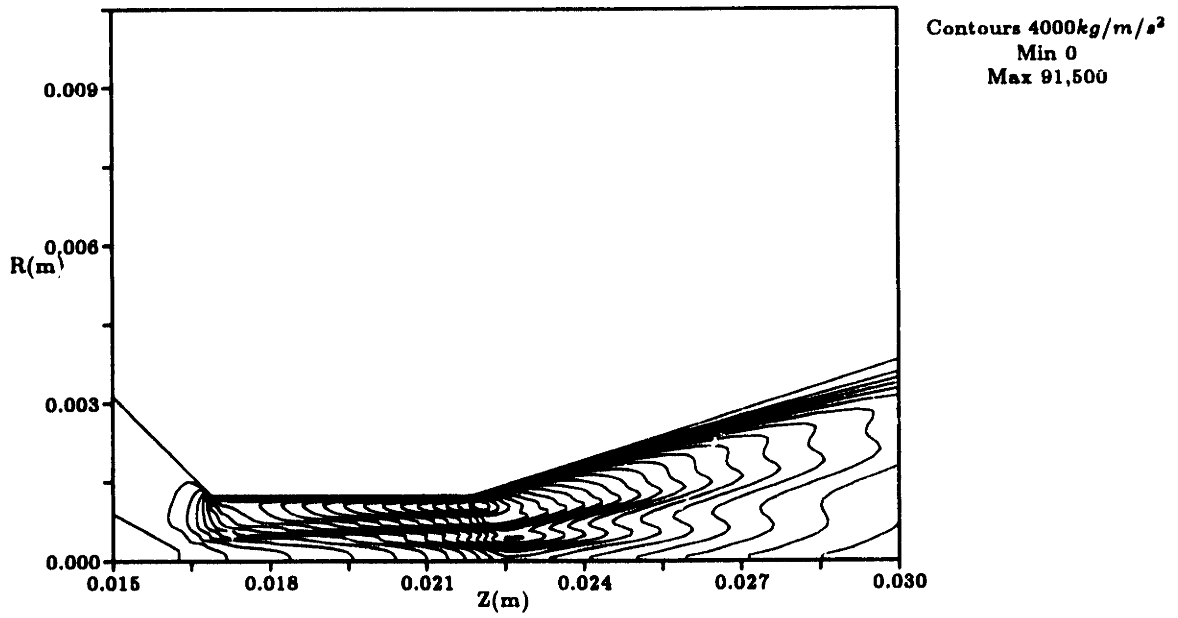

Figure 5.41: Momentum Flux (ρu_z^2) Contours for the Baseline Case Arcjet Simulation: Closeup of the Constrictor Region

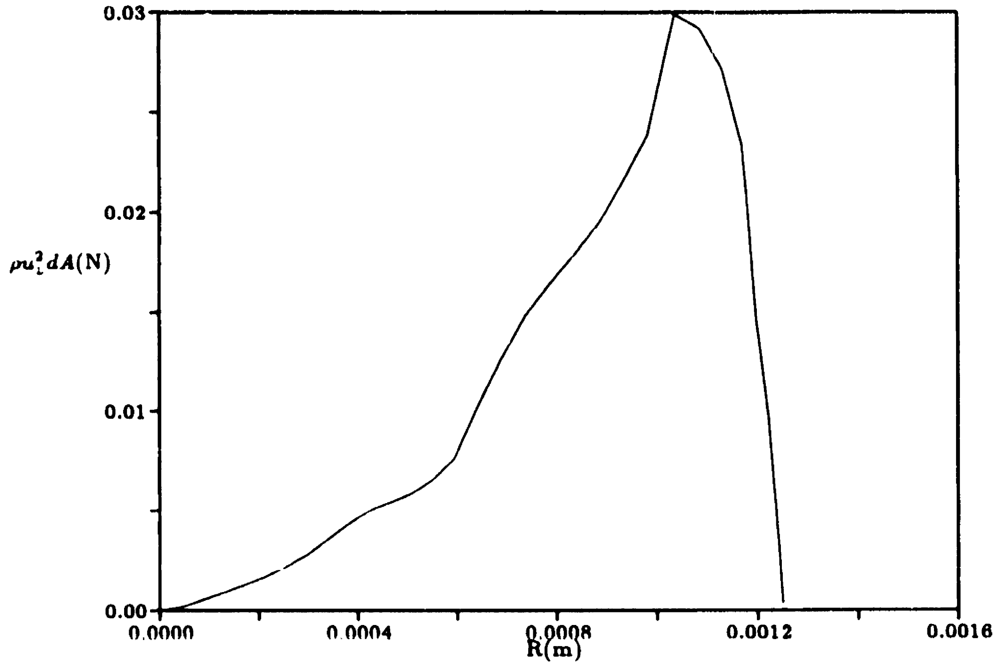

Figure 5.42: Radial Distribution of the Kinetic Thrust at the Constrictor Exit for the Baseline Case Arcjet Simulation

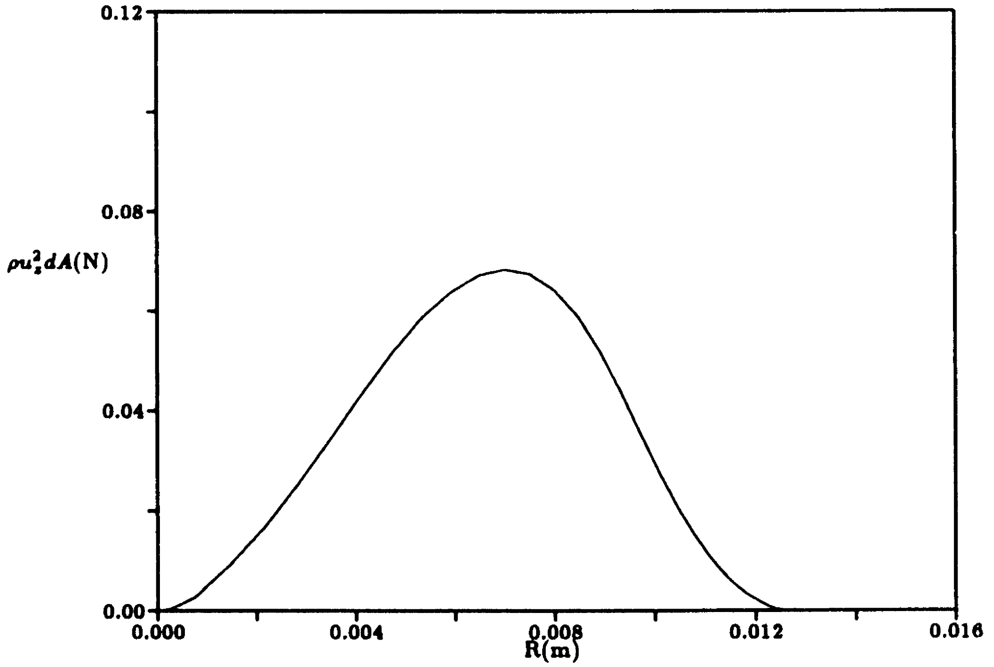

Figure 5.43: Radial Distribution of the Kinetic Thrust at the Thruster Exit for the Baseline Case Arcjet Simulation

An interesting feature of the nozzle flow is that viscous forces decrease the flow velocity substantially in the core region. This effect arises from the steep gradients in both the axial and radial velocities in the core. An axial line plot of the centerline velocity is plotted in Figure 5.44. The equation which governs the momentum along this streamline is

$$\frac{\partial \rho u_z}{\partial t} + \frac{\partial \rho u_z^2}{\partial z} + \frac{\partial p}{\partial z} = \mu \left[\frac{\partial^2 u_z}{\partial r^2} + \frac{4}{3}\frac{\partial^2 u_z}{\partial z^2} + \frac{1}{3}\frac{\partial^2 u_r}{\partial r \partial z} \right]. \tag{5.3}$$

In steady state this equation can be rewritten as

$$\frac{du_z}{dz} = -\frac{1}{\rho u_z}\frac{\partial p}{\partial z} + \frac{\mu}{\rho u_z}\left[\frac{\partial^2 u_z}{\partial r^2} + \frac{4}{3}\frac{\partial^2 u_z}{\partial z^2} + \frac{1}{3}\frac{\partial^2 u_r}{\partial r \partial z} \right]. \tag{5.4}$$

As stated in Section 4.4, the boundary condition on axial velocity at the centerline is that a zero gradient is imposed. Alternatively, Equation 5.4 may be integrated at each point on the axis in order to calculate the true axial momentum at this boundary. This was done for the baseline case, and results differed by at most 1% in u_z between the two boundary condition methods. The advantage of using the integration method is that each of the terms in Equation 5.4 may then be examined to see which are important at each axial location. Figure 5.45 is a plot of $\frac{du_z}{dz}$ at each grid point on the centerline. Up to about z=0.026m the pressure work term dominates, resulting in the rapid acceleration seen in Figure 5.44. Between z=0.026m and z=0.032m the pressure and viscous terms nearly balance, so that little change in the core flow velocity occurs. Beyond z=0.032m, however, viscous terms dominate and the flow is decelerated. Viscous forces therefore play an important role not only in the boundary layers at the walls, but also in the core of the nozzle expansion due to the steep gradients in propellant velocity located there. This core deceleration actually matters little in terms of the the overall operation of the thruster, however, since (1) there is much less propellant flow in the central region of the arc than there is farther away from the centerline; and (2) much of this deceleration represents a redistribution of the axial momentum from the high velocity centerline outward toward the lower velocity regions, so not all of the momentum is lost.

Both the inner and outer flows accelerate smoothly through sonic conditions at and just beyond the constrictor exit. Figure 5.46 shows Mach number contours for the baseline case arcjet simulation. Due to the large radial gradients in temperature and composition, the peak Mach number occurs in the interior region of the flow rather than at the centerline, where the velocity is highest. The maximum Mach number for this case is approximately 2.85.

Figures 5.47 through 5.49 show the distribution of the azimuthal swirl velocity in

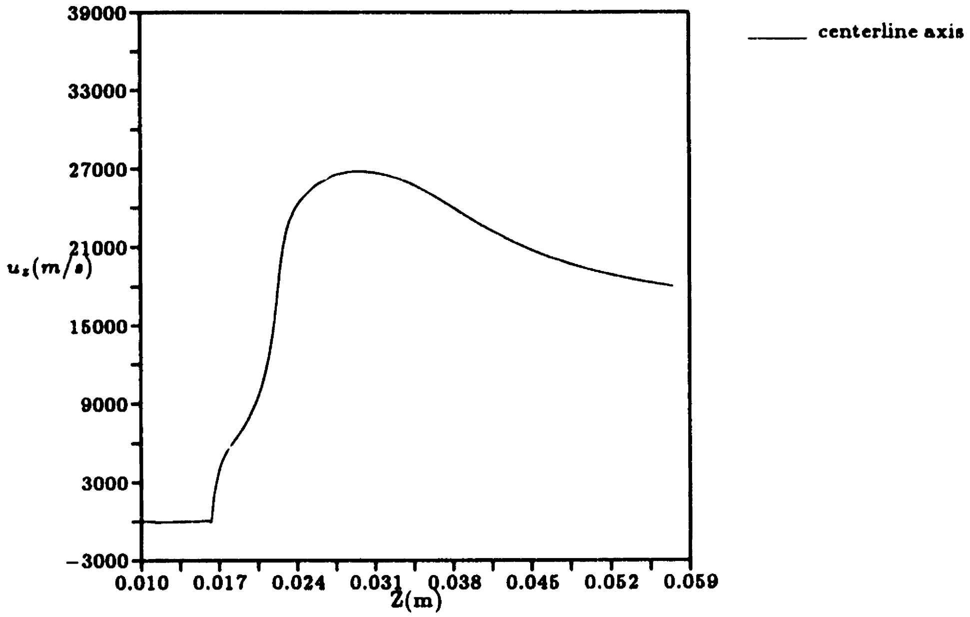

Figure 5.44: Axial Line Plot of u_z at the Centerline for the Baseline Case Arcjet Simulation

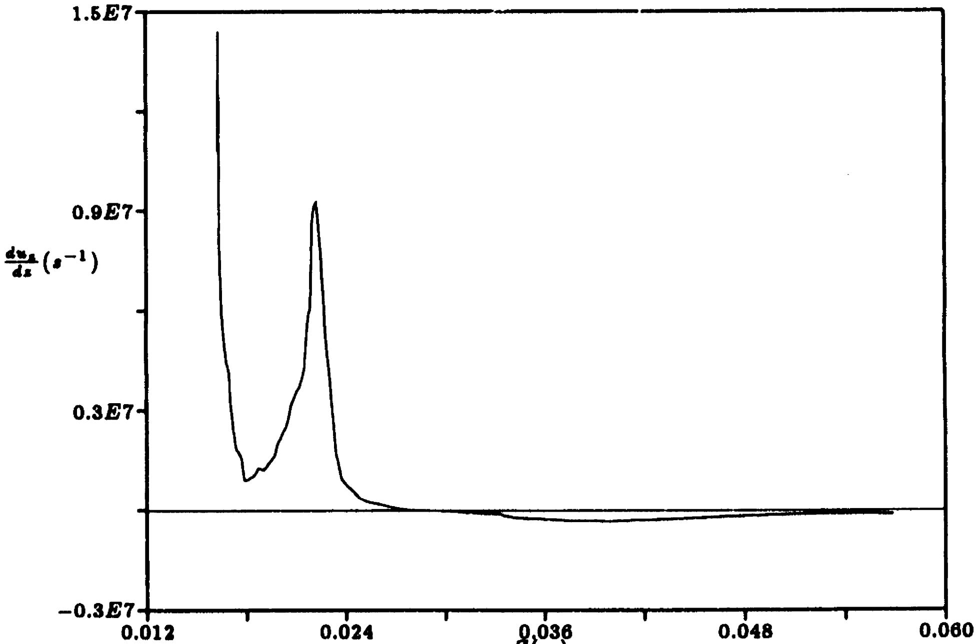

Figure 5.45: Axial Plot of $\frac{du_z}{dz}$ at the Centerline

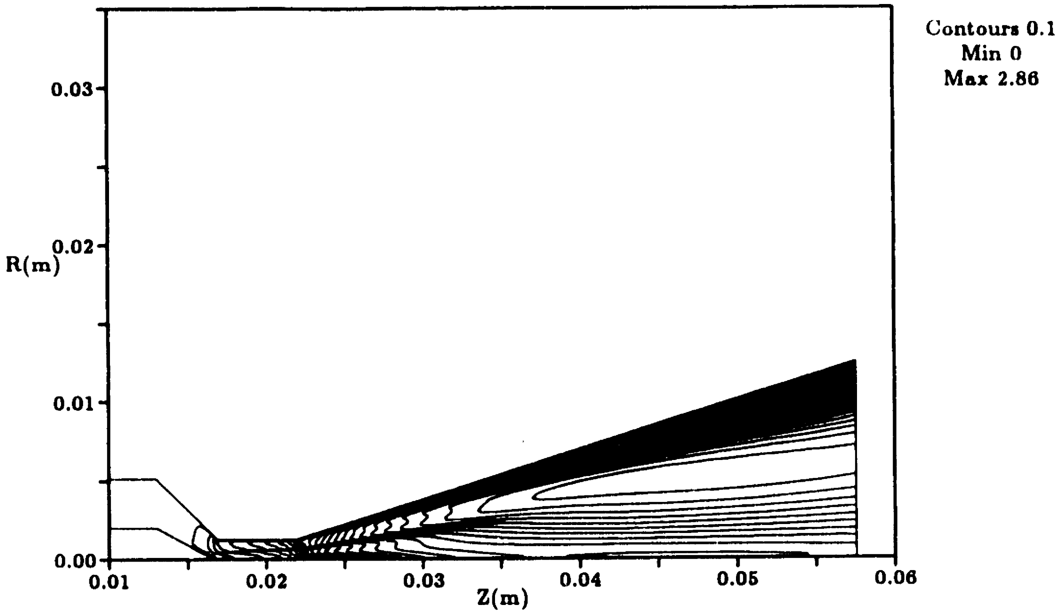

Figure 5.46: Mach Number Contours for the Baseline Case Arcjet Simulation

the arcjet thruster for the baseline case. The maximum swirl velocity of 90m/s in the arcjet simulation is an order of magnitude smaller than that in the flow verification case of Section 5.1.1. For the arcjet simulation case the mesh-averaged value of $\frac{u_\theta}{|\vec{u}|}$ is 0.05, varying between 3×10^{-5} and 3.0. For the verification test the mesh-averaged value of $\frac{u_\theta}{|\vec{u}|}$ is 0.15, with a range of 6×10^{-5} to 1.6. There are several reasons for this difference. First, the inlet area of the verification geometry is smaller and the specified mass flow rate is twice as large, resulting in an inlet swirl velocity that is four times larger than that of the arcjet simulation baseline case. Second, the much higher axial velocity in the core of the arcjet thruster minimizes the effect of increasing or decreasing cross-sectional area on the azimuthal velocity. To see this the azimuthal momentum equation can be recast into the following form:

$$\rho\frac{\partial u_\theta}{\partial t} + \rho u_r\frac{\partial u_\theta}{\partial r} + \rho u_z\frac{\partial u_\theta}{\partial z} = -\frac{2\rho u_r u_\theta}{r} + \frac{1}{r}\frac{\partial \tau_{r\theta} r}{\partial r} + \frac{\partial \tau_{\theta z}}{\partial z}. \qquad (5.5)$$

Neglecting for the moment viscous terms and radial gradients, in steady state Equation 5.5 can be rewritten as

$$\frac{du_\theta}{dz} = -\frac{2u_r u_\theta}{u_z r}. \qquad (5.6)$$

The axial velocity, which appears in the denominator of the above equation, varies from 0-2500m/s in constrictor of the flow verification case. Due to the low density region in the core of the arcjet simulation, however, the axial velocity in the constrictor of this case varies from 0-16,000m/s, thereby significantly reducing axial gradients in

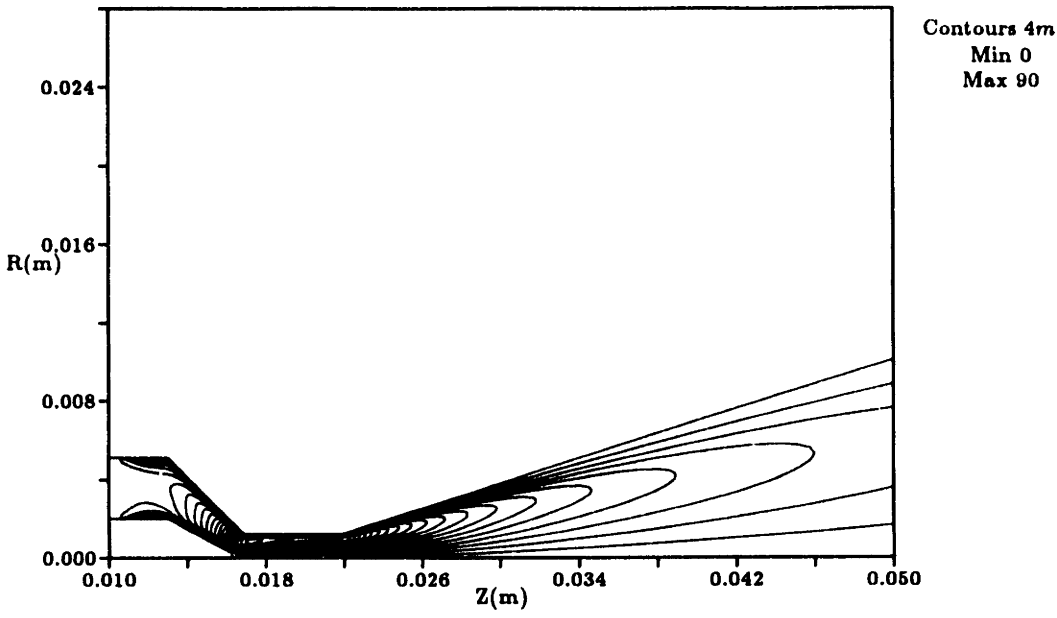

Figure 5.47: Swirl Velocity Contours for the Baseline Case Arcjet Simulation

the swirl velocity, especially in the core of the flow. This is essentially another way of saying that the flow is excluded by the arc from the near-axis region, where it would otherwise reach the highest u_θ values. Finally, viscous forces in the core of the flow are substantially higher in the arcjet simulation due to steeper gradients in velocity, causing additional swirl velocity reduction in this region. Therefore, aside from geometry differences between the two cases, it is the presence of the arc core in the arcjet simulation which effectively prevents the flow in that region from "spinning up" as seen in the flow verification test. The outer flow, however, still experiences an increase in swirl velocity in the constrictor of the same order as that for the case in which no arc is present.

5.2.2 Relative Importance of Effects

5.2.2.1 Ratios of Terms in the Governing Equations

One way to examine the relative importance of effects in the model is to compare the average ratios of terms to the dominant term in each equation. This is accomplished as follows. First the simulation is divided into two regions, the arc core ($\alpha > 0.01$) and the outer flow ($\alpha < 0.01$). For each region and each governing equation, at every grid point the ratio of each term in the equation to the term of largest magnitude is calculated. Each term ratio is then averaged over every point in the region, yielding a number between 0 and 1 which represents the mesh-averaged importance of each term

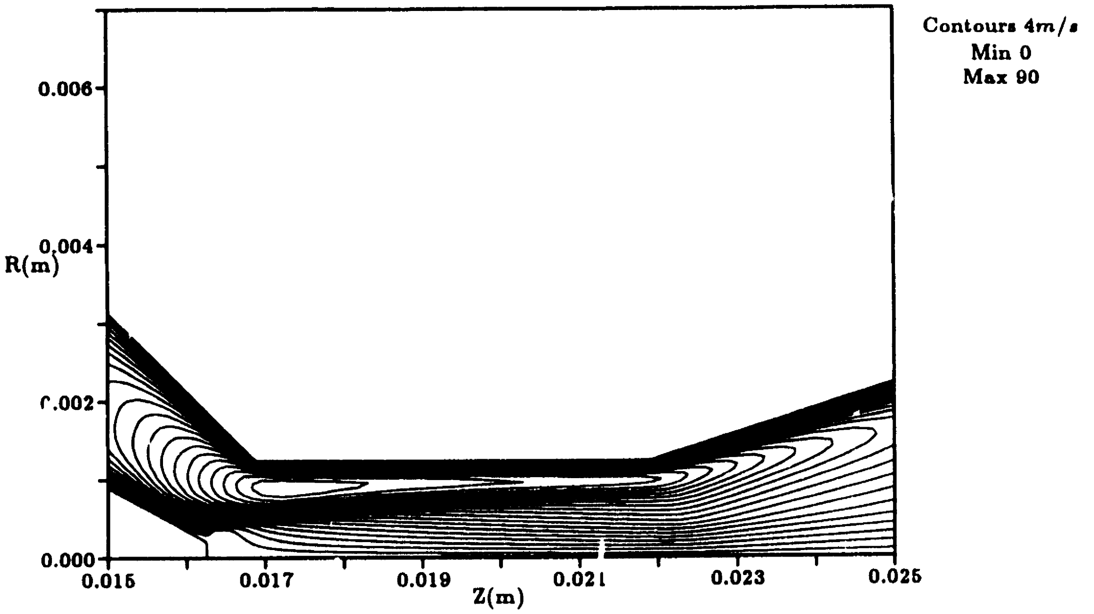

Figure 5.48: Swirl Velocity Contours for the Baseline Case Arcjet Simulation: Closeup of the Constrictor Region

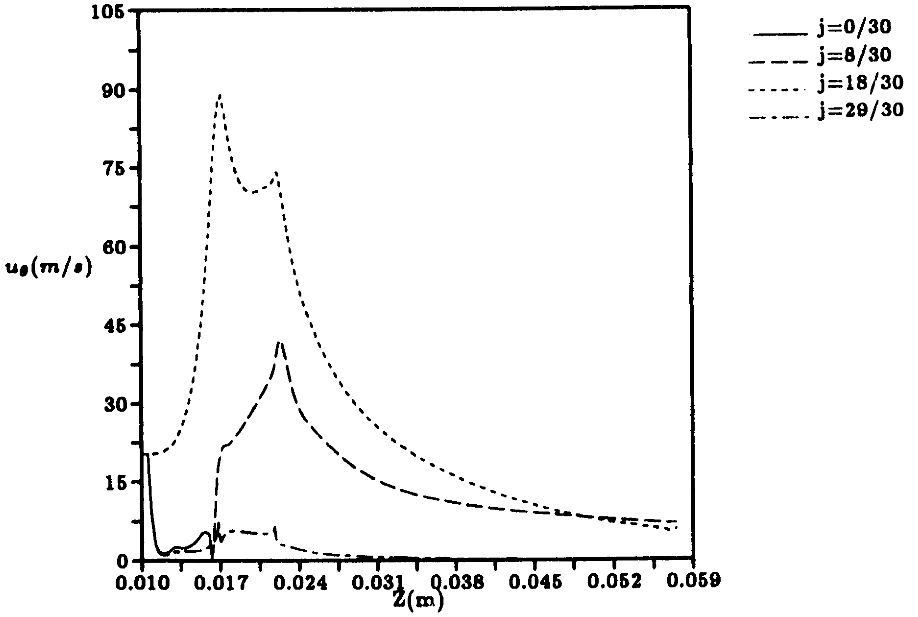

Figure 5.49: Axial Line Plots of u_θ for the Baseline Case Arcjet Simulation

in each equation. For reference, the equations discussed below are listed in Section 3.5 of this document.

The relative magnitudes of terms in the continuity equations are listed in Tables 5.5 and 5.6. For the overall continuity equation, both the axial and radial divergence terms are important in all regions of the flow. This result is expected and therefore not displayed. For the electron density equation, Table 5.5 lists the average ratio of each term to the dominant term for each simulated effect. In this case in addition to the divergence terms, radial ambipolar diffusion and net ionization are found to be important both inside and outside of the arc. Although the relative magnitude of radial ambipolar diffusion is 50% less outside the arc compared to inside, the average importance of net ionization is greater in the cooler outer flow than in the ionized arc itself. Axial ambipolar diffusion is almost negligible throughout the thruster. Relative sizes of terms in the atomic hydrogen density equation are listed in Table 5.6. In this case radial diffusion is found to be important only in the arc region, while axial diffusion is negligible everywhere. Net ionization is seen to be important in both flow regions, although its average relative magnitude is only one third as large in the outer flow as it is in the inner arc region. In terms of dissociation, however, while both electron and heavy species collision processes are factors in the arc, electron impact dissociation is the primary dissociation mechanism in the outer flow. Although the relative magnitude of electron impact dissociation is only 0.04 in the outer flow region, this result is skewed by the fact that this effect is concentrated in the high temperature ($T_e \approx 20,000^o$K) anode arc attachment zone in the first quarter of the nozzle. On the other hand, since the gas temperature of the outer region is essentially that of the anode wall, $1000 - 1100^o$K, the net dissociation rate by heavy species collisions is about the same throughout the region except for variations in the gas density. The fact that this model allows large numbers of charge carriers to be supplied to the outer flow region through ambipolar diffusion and electron impact dissociation and ionization is of great importance in understanding the anode current attachment process. This topic will be discussed in more detail in the next subsection.

Average ratios of terms in the three momentum equations are displayed in Tables 5.7 through 5.9. In the axial momentum equations all terms are seen to be significant in both regions of the flow. Of note is the fact that viscous forces are roughly twice as large when compared to the dominant term in the arc core as in the outer flow. This is a consequence of the much higher velocities and steep gradients in the central region of the thruster. The usual convective and pressure gradient terms are also the dominant terms in the radial momentum equation in both flow regions (Table 5.8). Again the

Table 5.5: Average Ratio of Terms to Dominant Term in Electron Density Equation

TERM	ARC ($\alpha > 0.01$)	OUTER ($\alpha < 0.01$)
Radial Divergence	0.604	0.636
Axial Divergence	0.830	0.788
Radial Ambipolar Diffusion	0.512	0.212
Axial Ambipolar Diffusion	0.019	0.009
Net Ionization	0.240	0.301

Table 5.6: Average Ratio of Terms to Dominant Term in Atomic Hydrogen Density Equation

TERM	ARC ($\alpha > 0.01$)	OUTER ($\alpha < 0.01$)
Radial Divergence	0.545	0.664
Axial Divergence	0.487	0.910
Radial Diffusion	0.265	0.001
Axial Diffusion	0.016	0.000
Net Dissociation ($H - H_2$)	0.131	0.019
Net Dissociation ($e - H_2$)	0.157	0.038
Net Ionization	0.332	0.139

viscous shear forces are more important in the inner core than in the outer region of the arcjet, in this case by a factor of three. The centrifugal force effect is negligible in the core and of minor importance in the outer flow. This is because the azimuthal swirl velocity is much less than the net flow velocity in most of the thruster for the injected swirl fraction of $0.4u_0$. Therefore, given this model's assumption of axisymmetry in the flow and in the electric arc, swirl as an arc stabilization device is irrelevant. If in actuality the propellant flow and arc are not uniform in the azimuthal direction due to instabilities or other physical effects, then injected swirl may still play a role. The balancing of the azimuthal momentum equation is dominated by the convective terms, as can be seen in Table 5.9. The Coriolis force, however, is also an important effect. Viscous forces are significant but not as large as in the other two momentum equations.

The relative sizes of terms in the electron energy equation are listed in Table 5.10. The primary source of energy is of course ohmic dissipation. Note however that the

Table 5.7: Average Ratio of Terms to Dominant Term in Axial Momentum Equation

TERM	ARC ($\alpha > 0.01$)	OUTER ($\alpha < 0.01$)
Radial Convection	0.532	0.648
Axial Convection	0.684	0.802
Axial Pressure Gradient	0.564	0.454
Viscous Shear	0.428	0.201

Table 5.8: Average Ratio of Terms to Dominant Term in Radial Momentum Equation

TERM	ARC ($\alpha > 0.01$)	OUTER ($\alpha < 0.01$)
Radial Convection	0.419	0.617
Axial Convection	0.521	0.766
Radial Pressure Gradient	0.581	0.493
Viscous Shear	0.346	0.103
Centrifugal Force	0.001	0.028

Table 5.9: Average Ratio of Terms to Dominant Term in Azimuthal Momentum Equation

TERM	ARC ($\alpha > 0.01$)	OUTER ($\alpha < 0.01$)
Radial Convection	0.924	0.876
Axial Convection	0.731	0.845
Viscous Shear	0.213	0.097
Coriolis Force	0.196	0.206

Table 5.10: Average Ratio of Terms to Dominant Term in Electron Energy Equation

TERM	ARC ($\alpha > 0.01$)	OUTER ($\alpha < 0.01$)
Radial Convection	0.338	0.423
Axial Convection	0.528	0.444
Radial Conduction	0.400	0.216
Axial Conduction	0.007	0.056
Ohmic Dissipation	0.508	0.504
Transfer to Heavy Species	0.023	0.069
Net Dissociation	0.006	0.007
Net Ionization	0.345	0.207
Radiation	0.001	0.001

relative magnitude of this term is nearly as large outside of the arc region as it is inside of it. The convective terms of this equation are seen to be among the most important in the energy balance, as is the radial conduction term. Radial conduction effects are greater inside the arc due to the higher coefficient of thermal conductivity there (resulting from the high electron temperatures) and to the steep gradients in electron temperature particularly at the edge of the ionized arc region. Axial heat conduction is of minor importance. Collisional energy transfer to the heavy species is of small relative magnitude in both flow regions, but this does not mean it is not important. The relative size of this term in the arc core is small only because the electron and heavy species temperatures are closely coupled. Collisional energy transfer would become a large energy sink for the electrons if these two temperatures were further apart because of the high electron number densities in the ionized arc region. Outside the arc, however, the electron density is so low that collisional energy coupling between electrons and heavy species is minimal. In terms of the electron energy balance, energy lost through dissociation events is negligible while energy lost due to net ionization is significant, particularly in the core region. Energy lost through continuum radiation is insignificant in this application.

Table 5.11 lists the average ratio of terms to the dominant term in the heavy species energy equation. As in the electron energy equation, the convective terms and the radial conduction term, especially in the arc, are dominant. The primary source of energy for the heavy species is collisional transfer from the electrons. This process is much more

Table 5.11: Average Ratio of Terms to Dominant Term in Heavy Species Energy Equation

TERM	ARC ($\alpha > 0.01$)	OUTER ($\alpha < 0.01$)
Radial Convection	0.620	0.698
Axial Convection	0.566	0.925
Radial Conduction	0.650	0.217
Axial Conduction	0.025	0.009
Species Diffusion	0.068	0.001
Viscous Dissipation	0.106	0.146
Transfer from Electrons	0.021	0.020
Net Dissociation	0.088	0.010

effective inside the arc where the electron density is high than outside the arc where the electron density is relatively low, although T_e and T_g are so close in the arc that the magnitude of the collisional energy transfer term appears to be small everywhere in the flow. Viscous dissipation is also a source of energy for the heavy species, and is of relative magnitude 0.11 and 0.15 inside and outside of the arc respectively. Energy lost due to dissociation by heavy species collisions is of minor importance in this equation, while transport by species diffusion is of minor importance in regions of steep gradients in flow composition and negligible elsewhere. Axial conduction is basically negligible throughout the flow.

5.2.2.2 Equilibrium vs. Nonequilibrium

In the simulation of this research nonequilibrium dissociation and ionization are modeled by integrating the electron and atomic hydrogen continuity equations with source terms reflecting the finite rate processes. It is instructive to compare the flow composition calculated in the simulation to that of an equilibrium composition in order to identify the effect of nonequilibrium modeling on the predicted results. In making this comparison the baseline case is not re-run with an equilibrium composition solver. Instead, the nonequilibrium composition calculated by the simulation is compared to the equilibrium composition which would occur given the electron temperature, heavy species internal energy, and number density of the flow at each grid location. Consequently, the equilibrium results presented here are not fully consistent since they do not reflect the effect of the differing transport coefficients (which are a function of

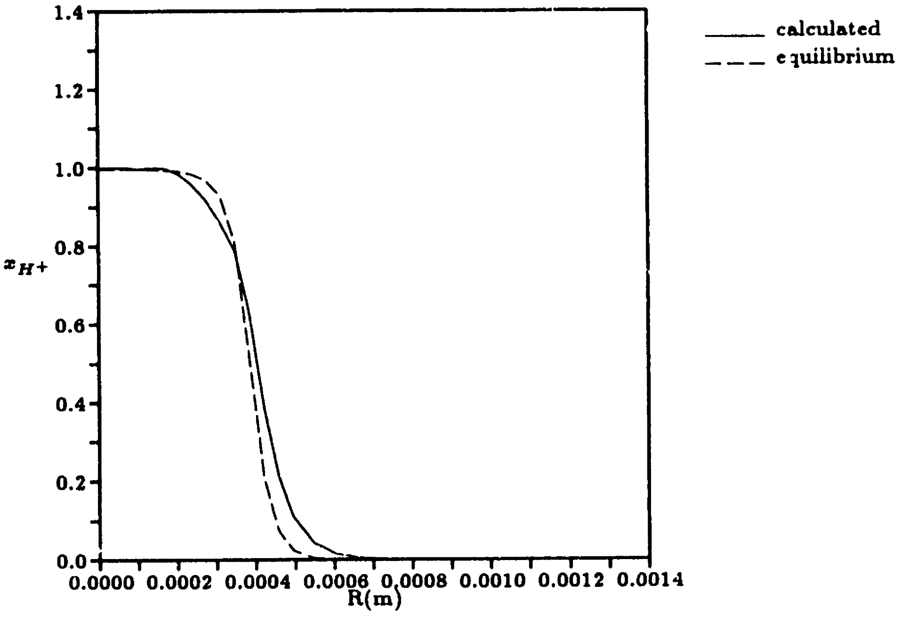

Figure 5.50: Equilibrium and Calculated Radial Profiles of Ion Mole Fraction at the Mid-Constrictor Axial Location

composition) on the behavior of the flow. The results are consistent enough, however, so that qualitative comparisons can be made.

Comparisons between equilibrium and nonequilibrium ion mole fractions are shown in Figures 5.50 and 5.51. Both figures plot radial profiles of x_{H^+} at the midpoint of the constrictor. The main difference in the full channel plot of Figure 5.50 is that the steep gradient of the equilibrium profile is smoothed out by ambipolar diffusion in the calculated profile. In the close-up of the near-anode region, however (Figure 5.51), the difference between the two cases is much greater. This comparison shows that in the outer, cooler region of the flow, the nonequilibrium model predicts a small but not insignificant ionization level of roughly 0.02%, while the equilibrium model predicts essentially no ionization (a lower limiter of 1×10^{-6} is reached). This difference, which is present throughout the outer flow region, is directly related to the finite rate source terms and ambipolar diffusion terms included in the model of this research. The fact that this model predicts some ionization in the outer flow allows the current to pass through this region and attach to the anode wall in a stable, consistent manner. The underlying reasons for this process are discussed in the next subsection.

Figures 5.52 and 5.54 compare equilibrium and nonequilibrium radial profiles of atomic hydrogen mole fraction, also at the midpoint of the constrictor. In this case the calculated nonequilibrium atomic hydrogen mole fraction is considerably lower than the equilibrium value. In the range $r = 0.0003\text{m}$ to $r = 0.0005\text{m}$ this is partly due to the

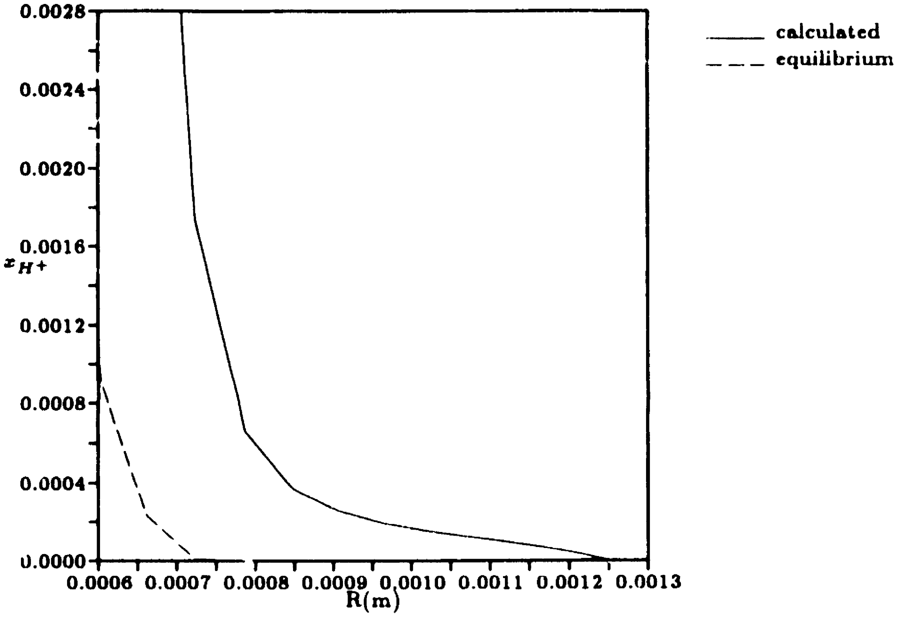

Figure 5.51: Equilibrium and Calculated Radial Profiles of Ion Mole Fraction at the Mid-Constrictor Axial Location and Near the Anode Wall

fact that the ion mole fraction is higher in the nonequilibrium case. Overall, the main reason for the difference is that the flow has already been accelerated significantly in the constrictor region for the calculated nonequilibrium case. Figure 5.53 shows that the axial velocity in the range of appreciable x_H values varies between 2000m/s and 7500m/s. As a result, the finite dissociation rate model of the simulation lags behind the equilibrium composition because the flow is moving rapidly downstream. Residence times in the constrictor for this case vary from 10^{-6} to 10^{-7}sec in the core flow where substantial quantities of atomic hydrogen are present. These times are of the same order as the reaction times for hydrogen dissociation under the thermodynamic conditions in the core. In the outer flow the nonequilibrium level of atomic hydrogen is substantially higher than the associated equilibrium level, except very near the anode wall. Figure 5.54 illustrates this near-anode behavior. The agreement is close near the wall because the boundary condition on atomic hydrogen mole fraction in the nonequilibrium simulation is that x_H is set equal to its equilibrium value.

Figures 5.55 and 5.56 compare calculated nonequilibrium and estimated equilibrium values of ion and atomic hydrogen mole fractions, respectively, at the nozzle exit. Under equilibrium conditions, since the electron temperature varies between only 2000°K and 4500°K over the nozzle exit plane, no ionization of the gas is expected. Of course, the gas in the core of this arcjet thruster is moving at 15,000-25,000m/s in the nozzle, so much of the ionization produced in the constrictor is entrained in the flow. This

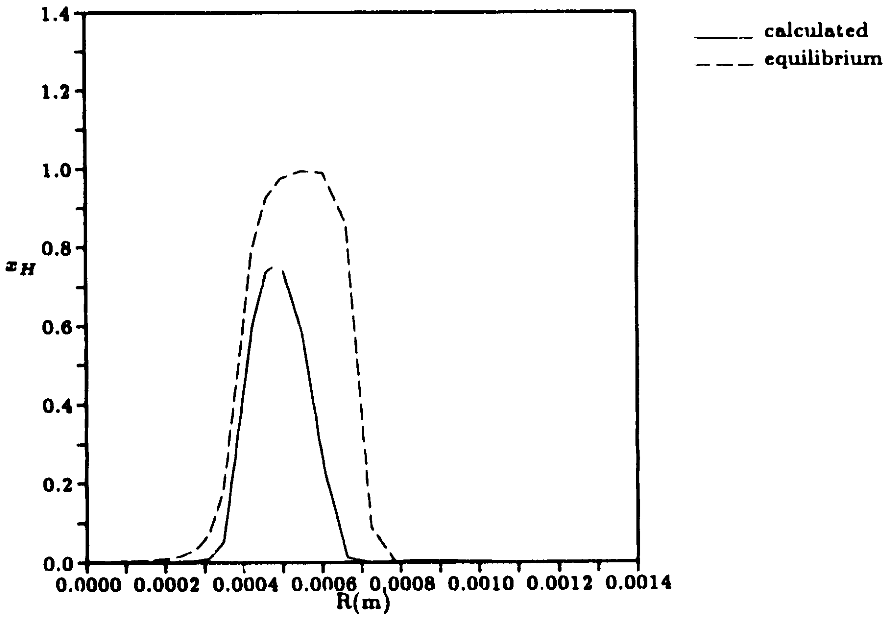

Figure 5.52: Equilibrium and Calculated Radial Profiles of Atomic Hydrogen Mole Fraction at the Mid-Constrictor Axial Location

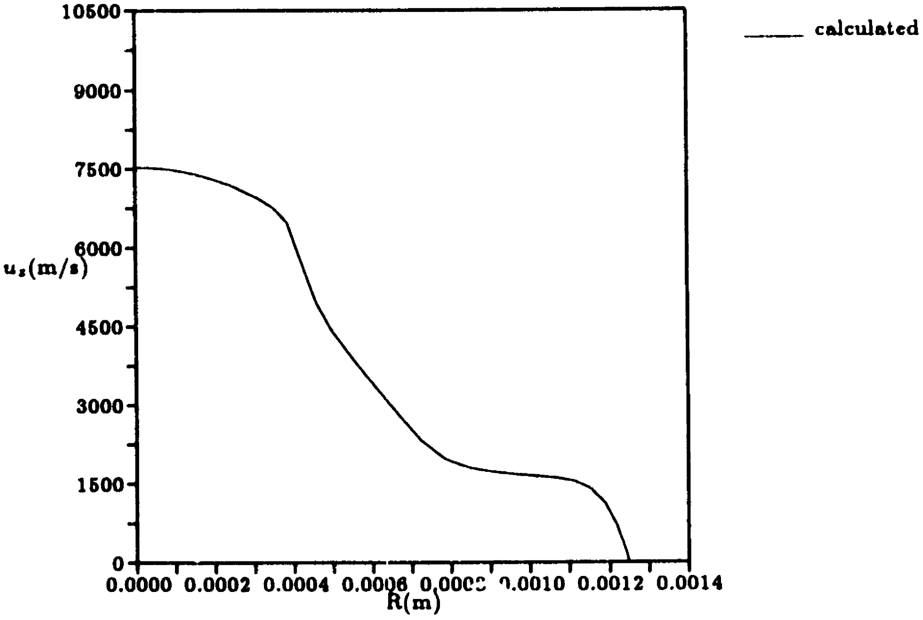

Figure 5.53: Calculated Radial Profile of Axial Velocity at the Mid-Constrictor Axial Location

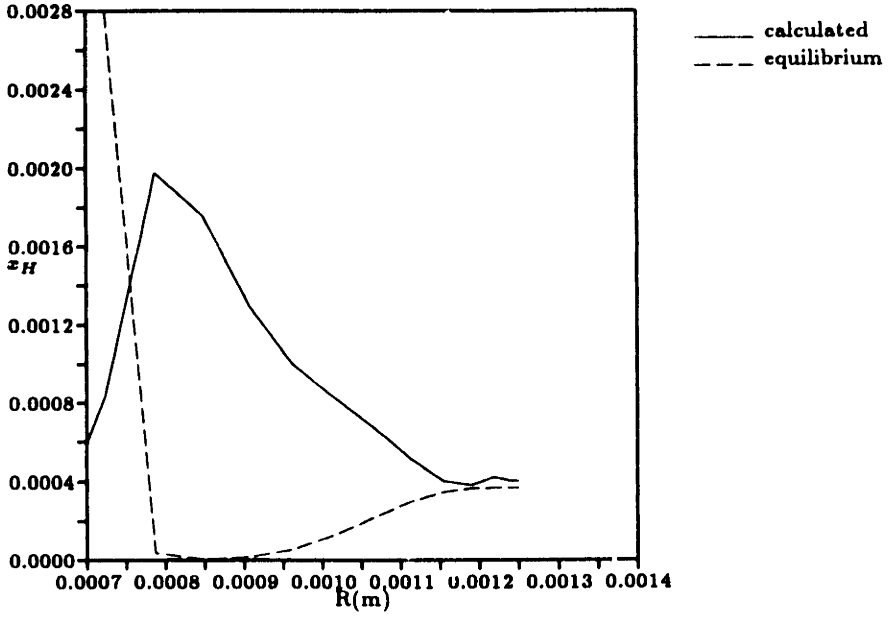

Figure 5.54: Equilibrium and Calculated Radial Profiles of Atomic Hydrogen Mole Fraction at the Mid-Constrictor Axial Location and Near the Anode Wall

residual ionization, 46% in ion mole fraction at the centerline, represents a frozen flow loss which decreases overall thruster efficiency. Figure 5.56 shows that the calculated atomic hydrogen mole fraction is lower than the equilibrium level in the ionized core and greater than the equilibrium level in the outer flow. Given the number of ions in the core flow at the nozzle exit, the calculated level of dissociation in the inner flow is close to the equilibrium level, except for smoothing due to ambipolar diffusion. In the outer region, the increased level of dissociation in the nonequilibrium case results from the radial convection and diffusion of species in the nozzle expansion.

5.2.2.3 Current Attachment

Simulating the current attachment at the anode realistically and self-consistently has been a major difficulty in previous arcjet simulations. The effectiveness of this model in simulating this region is due to the incorporation of separate energy equations for the heavy species and electrons, and to the use of nonequilibrium dissociation and ionization finite rate equations. In the previous section, the electron temperature was found to be significantly higher than the heavy species temperature in the outer current attachment region (Figures 5.20 and 5.23). It has also been shown that the nonequilibrium model of this research predicts outer flow levels of atomic hydrogen and hydrogen ions which are much higher than would be the case if the flow were in equilibrium (Figures 5.51 and 5.54). And finally, ohmic dissipation, ambipolar diffusion, and finite-rate

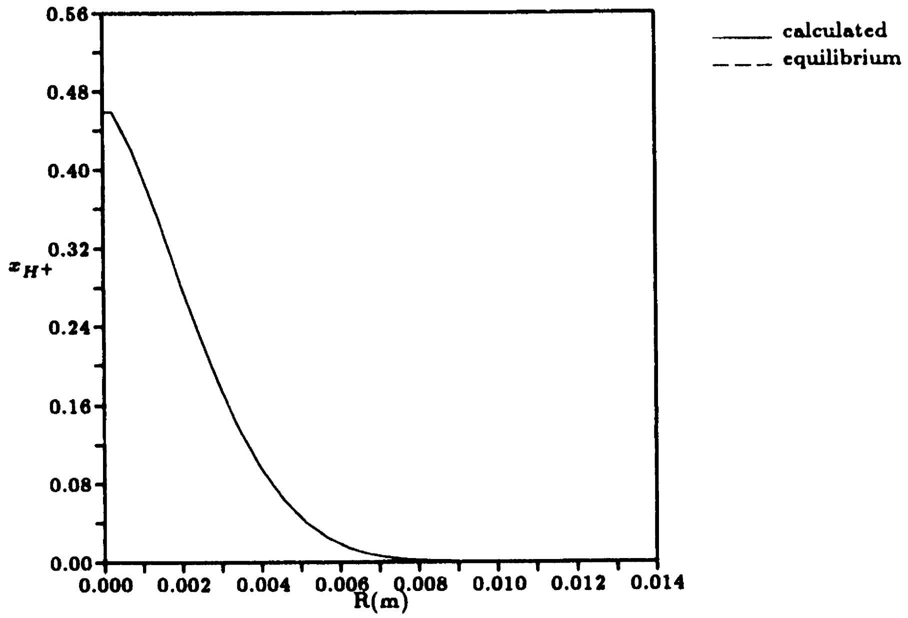

Figure 5.55: Equilibrium and Calculated Radial Profiles of Ion Mole Fraction at the Nozzle Exit

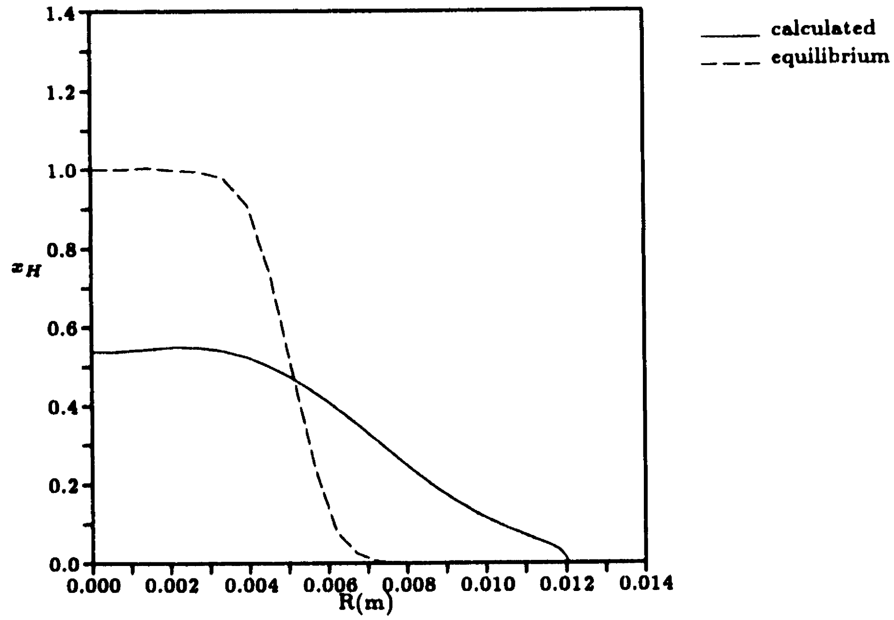

Figure 5.56: Equilibrium and Calculated Radial Profiles of Atomic Hydrogen Mole Fraction at Nozzle Exit

dissociation and ionization have been identified as mechanisms which could explain this difference. The importance of these effects in the anode attachment region is now examined in order to confirm this supposition.

Figure 5.57 contains radial profiles of some terms in the electron energy equation at an axial location just beyond the constrictor exit. The two most important energy sinks, radial and axial convection, have been omitted from this diagram in order to more clearly show the behavior of the remaining effects. Clearly, ohmic dissipation is the primary electron heating mechanism in the outer flow region. This process is simulated realistically by the model of this research by the use of separate energy equations for the electrons and heavy species. If only one energy equation were used, as has been the case in previous arcjet simulations, the temperature in the anode attachment zone would be on the order of the wall temperature, 1000 – 2000°K. This would not support the creation of ions and electrons as charge carriers, and numerical difficulties would arise in the attachment region. Previous models got around this problem by setting an artificial lower limit on the electrical conductivity in the gas. This allowed current attachment to occur, but resulted either in attachment over the entire anode wall (which is not what happens physically, and therefore led to inaccurate voltage predictions) or in the requirement that the current path be specified to achieve reasonable accuracy (which arbitrarily reduces the consistency and hence the predictive accuracy of the model). The use of two separate energy equations shifts the direct effect of ohmic dissipation to the electrons only and allows the electron temperature to be as much as 20,000°K higher than the gas temperature, as it is in the current attachment region near the anode.

The elevated electron temperature in the attachment zone then produces enough electron impact dissociation and ionization to create the necessary charge carriers for electrical conduction between the outer arc boundary and the anode. Figure 5.58 shows a contour plot of the net rate of ionization in the vicinity of the constrictor and anode attachment zone. Because this rate varies by several orders of magnitude in the arcjet, this contour plot does not reveal much detail. It can be noted, however, that the region of net ionization covers not only the core of the arc in the constrictor, but also a wide path from this central core to the anode wall downstream of the constrictor exit. Another important process, radial ambipolar diffusion, is shown in the contour plot of Figure 5.59. The magnitude of this effect also varies widely inside the arcjet, so the main function of this diagram is to show the sign of the term. Near the centerline in the constrictor an inward diffusive flux of charged species occurs, since the flow there is fully ionized and density decreases toward the axis. Along the edge of the arc core ions

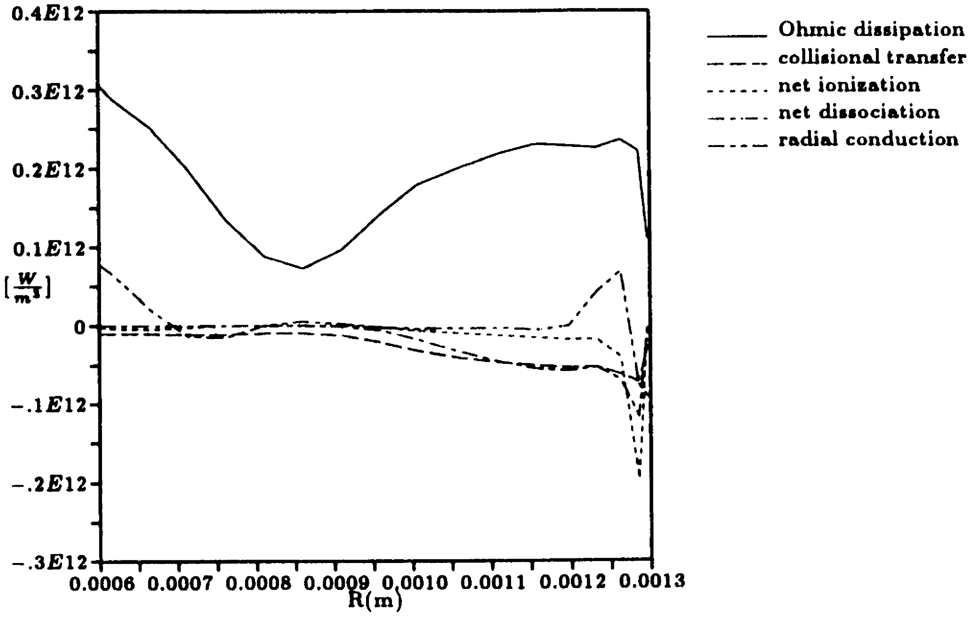

Figure 5.57: Radial Profiles of Some Terms in the Electron Energy Equation in the Current Attachment Region Just Beyond the Constrictor Exit

and electrons diffuse outward, particularly in the constrictor region where the edge of the arc is very steeply defined. In the middle region the ambipolar diffusion term is small but positive, while near the anode charged particles diffuse toward the wall.

For a closer look at the near-anode region, radial profiles of some terms in the electron density equation in the attachment area are shown in Figure 5.60. Radial ambipolar diffusion is seen to be important in moving ions and electrons outward from the arc into the surrounding cooler gas flow. Nearer to the wall, net ionization due to the locally elevated electron temperature provides additional charge carriers for conduction. Very near the wall, a layer exists in which ambipolar diffusion causes electrons and ions to diffuse toward the anode. This ambipolar loss of charge carriers to the wall is offset by a local maximum in net ionization. Figure 5.61 shows a similar plot for the atomic hydrogen density equation. Of the terms displayed, net dissociation is of primary importance in the outer flow and a local maximum is present near the anode wall. This locally high dissociation rate is tied to the high ionization rate necessary to replenish electrons and ions which diffuse to the wall. From Table 5.6 it is clear that the dissociation process in the outer flow region is due almost entirely to electron impact.

The physical effects, then, which allow the model of this research to consistently simulate current attachment in the relatively cool outer gas flow are clear. The fact that the voltage predicted by the model is very close to the experimentally measured

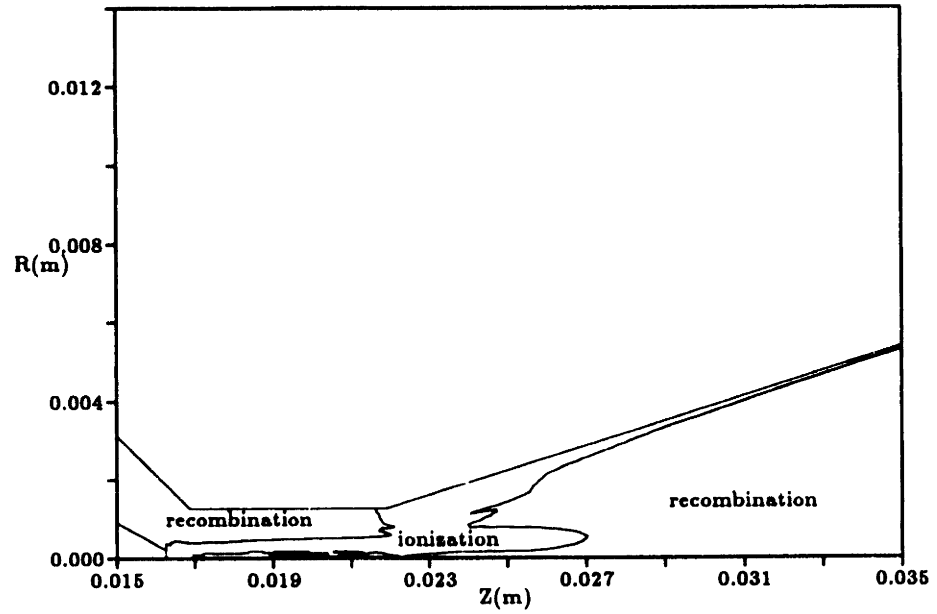

Figure 5.58: Net Ionization Rate Contours for the Baseline Case Arcjet Simulation

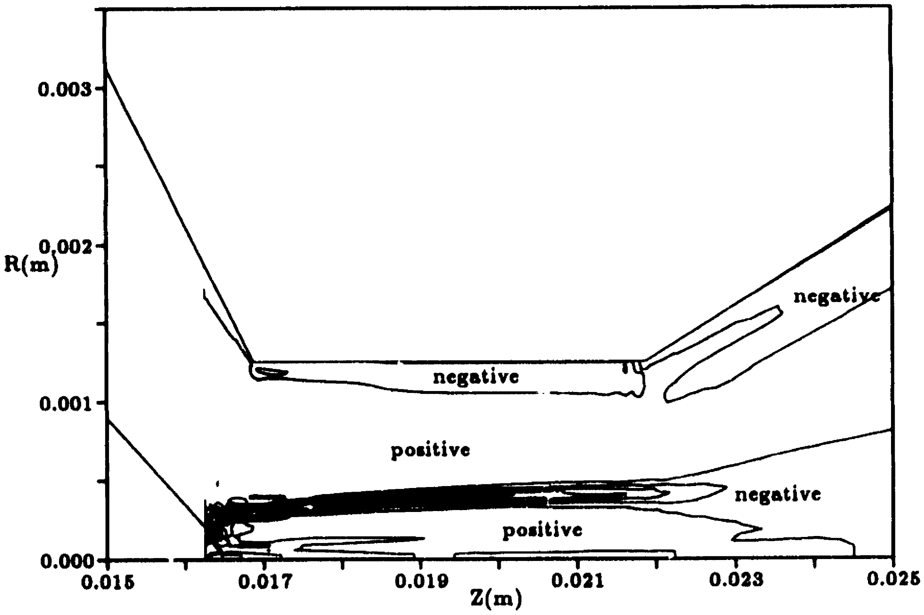

Figure 5.59: Negative Radial Ambipolar Diffusion Contours for the Baseline Case Arcjet Simulation (Positive = Diffusion Inwards Toward $r = 0$)

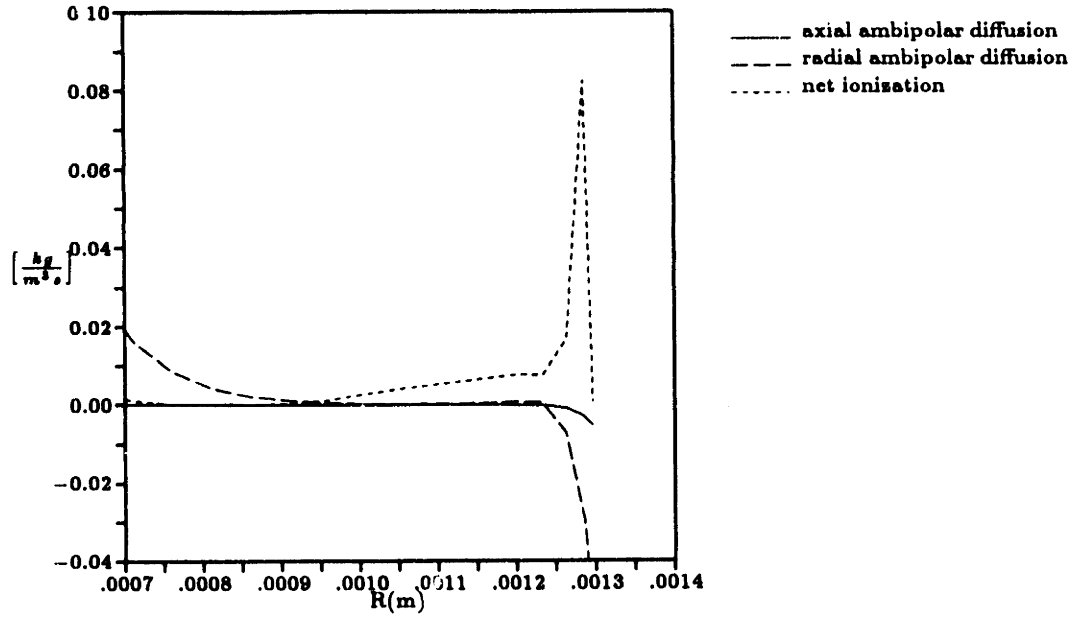

Figure 5.60: Radial Profiles of Some Terms in the Electron Density Equation in the Current Attachment Region Just Beyond the Constrictor Exit

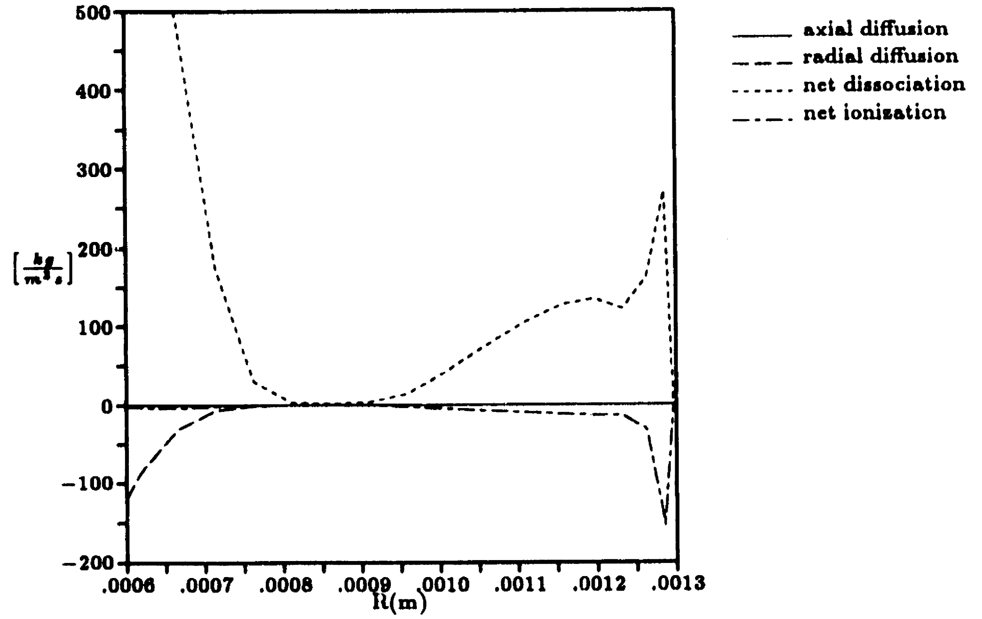

Figure 5.61: Radial Profiles of Some Terms in the Atomic Hydrogen Density Equation in the Current Attachment Region Just Beyond the Constrictor Exit

Table 5.12: Distribution of Energy in the Exit Flow for the Baseline Case Arcjet Simulation

Energy State	**Expression**	**Power(W)**	**% of Total**
Axial kinetic	$(\frac{1}{2}\rho u_z^2 + p)u_z A$	5720	39.2
Radial kinetic	$\frac{1}{2}\rho u_r^2 u_z A$	89	0.6
Azimuthal kinetic	$\frac{1}{2}\rho u_\theta^2 u_z A$	< 1	0.0
Ionization	$n_e E_i u_z A$	2546	17.5
Dissociation	$\frac{1}{2}(n_H + n_e)E_d u_z A$	4367	30.0
Electron thermal	$\frac{3}{2}p_e u_z A$	88	0.6
Heavy sp. thermal	$\left[\frac{3}{2}(p_H + p_{H^+}) + \frac{5}{2}p_{H_2} + \frac{\rho_{H_2} R_{H_2} \theta_v}{e^{\theta_v/T_g} - 1}\right] u_z A$	1769	12.1
Total		14580	100.0

voltage shows that these effects are likely the ones which act in the actual arcjet thruster as well. One remaining problem, however, is that the initial position of the anode current attachment region is not self-consistently determined by the physics included in the numerical simulation. In the present results the current is required to attach downstream of the constrictor exit. This is the situation observed in experiments using comparable arcjet thrusters, and the accuracy of the voltage predictions of this model reflect the plausibility of this choice. When the initial allowable attachment point is moved by the user, however, the code predicts current attachment wherever the initial point is set, resulting in widely varying predictions of thrust and voltage. Future research should be directed toward finding the physical mechanism which sets the initial attachment point of the arc on the anode surface in order to remove this final degree of arbitrariness.

5.2.2.4 Loss Mechanisms

To gain an understanding of the loss mechanisms involved in this particular arcjet thruster design, the partition of energy in the flow at the exit plane is examined. By conservation of energy, the total power in the exiting flow for the baseline case is equal to the electrical input power (11.50kW) minus the power lost to the walls (1.46kW) plus the power inherent in the inlet flow, for a total of 14.58kW. Table 5.12 catalogs the distribution of this power in the various energy states of the exiting flow. As the table shows, in this case only 39% of the exit plane energy is in the form of useful thrust. Fully 47% of the energy is tied up in dissociation and ionization, while 13% is classified as thermal energy. In particular, the energy bound in dissociation and ionization represents a significant frozen loss.

Chapter 6

Performance Mapping Results

The arcjet simulation code developed in this research has been used to obtain numerical solutions for a number of different operating points of the TT1 radiation-cooled arcjet tested at the University of Stuttgart. Numerically obtained performance parameters are summarized in Appendix G for reference. Figure 6.1 compares predicted and experimental specific impulse at three mass flow rates and over a range of applied currents. The simulated specific impulse is seen to be approximately 5-10% higher than that measured by experiment. Table 6.1 compares predicted and experimentally measured discharge voltage for the cases presented in Figure 6.1. Voltage predictions from the arcjet simulation fall from within 1-3% of experiment for the intermediate mass flow rate to within 10-12% for the high mass flow rate, and the negative slope of the V-I relationship is captured. The differences in predictive voltage accuracy between mass flow rates probably result from the boundary condition which requires the current to attach downstream of the constrictor exit. In reality this attachment point is a function of the operating conditions and may also be affected by sheath layers or instabilities not addressed by this research. The following two sections discuss the the results of this parametric study in more detail.

6.1 Effect of Applied Current Variation

Important operational characteristics of electrothermal arcjets can be identified and examined by studying the numerical solution as a function of input power per unit mass. This quantity can be varied by changing the applied current and/or the mass flow rate. Changes in the mass flow rate, however, alter not only $\frac{P}{\dot{m}}$ but also the physics of the outer flow region, and in particular the behavior of arc attachment at the anode.

Table 6.1: Comparison of Discharge Voltages for the Cases in Figure 6.1

Case		Voltage	
I(A)	$\dot{m}$(g/s)	Numerical	Experiment
70	0.05	89	85
100	0.05	85	78
120	0.05	83	77
60	0.10	118	117
100	0.10	115	112
130	0.10	113	111
60	0.15	140	127
95	0.15	138	120
130	0.15	137	118

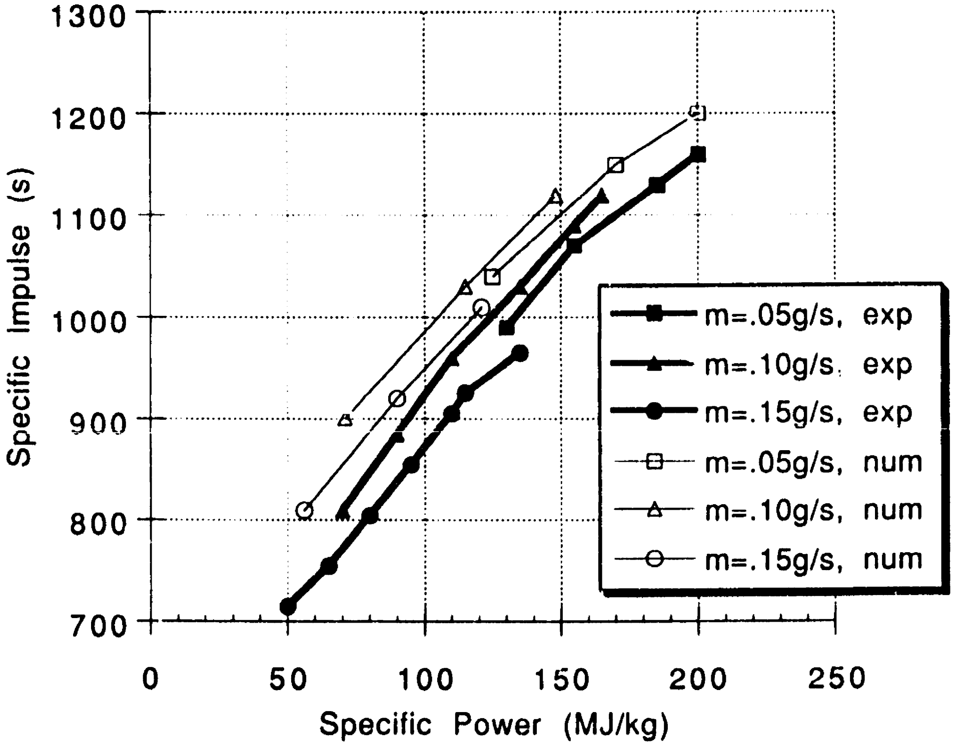

Figure 6.1: Comparison of Predicted Specific Impulse to Experimental Data for German TT1 Radiation-Cooled Arcjet

Consequently, the effect of varying the specific power will be examined by comparing three numerical solutions obtained at three different applied currents (60A, 100A, and 130A) but at the same mass flow rate of 0.1g/s.

Enclosed current contours for the three cases are shown in Figure 6.2. There is very little difference between the three contour plots, as would be expected both from experimental measurements and from physical considerations. Experimental voltage measurements vary only from 117V at 60A to 111V at 130A, suggesting that the pattern of current is very similar for each of these cases. Nearly identical voltages, varying between 118V and 113V, are predicted by the arcjet simulation. Physically, the distribution of current is controlled primarily by the behavior of current passage through the outer cooler gas layer, which in turn is governed by the heat diffusivity $\alpha = \frac{\kappa}{\rho c_p}$. Since the heat diffusivity is essentially the same for each of these cases ($\dot{m}$ is the same, as is $T_g \approx T_{wall}$), the current patterns and discharge voltages are nearly identical as well. The slightly negative voltage-current characteristic suggested by the three cases is due to the fact that the electron temperature, and therefore the electrical conductivity, increases with increasing current (Figure 6.3). In addition, the arc width increases as the current is increased (Figure 6.4), thus decreasing the width of the outer layer. This makes it easier for current to pass through the outer layer, so as the current is increased the arc attaches earlier in the nozzle and the voltage is decreased.

The effects of arc widening and increasing temperature with increasing current result indirectly from the greater ohmic dissipation produced by higher current levels. This increased dissipation then causes additional heating of the electrons, as shown in the centerline plots of electron temperature in Figure 6.3. Higher electron temperatures cause not only increased collisional energy transfer to the heavy species, thereby elevating gas temperatures (Figure 6.5), but also higher finite-rate dissociation and ionization rates and increased ambipolar diffusion, which cause the ionized region of the arc core to widen. Interestingly, the electron temperature in the flow outside the main arc is little affected by variations in the applied current, as shown in Figure 6.6.

Since the temperature increases and the arc core expands radially as the current is increased, the central region of low mass flow necessarily deepens and widens. This can be seen in Figure 6.7, which shows mass flux radial profiles at the constrictor exit, and in Figure 6.8, which tracks the mass flow fractions inside the arc as a function of axial location. The inlet pressure also increases with the applied current, rising from 1.13atm at 60A to 1.37atm at 130A. These two related effects produce increased thrust as the current is increased. Figure 6.9 compares axial velocity profiles at the constrictor exit for the three current levels, showing the net velocity increase. Figure 6.10 shows

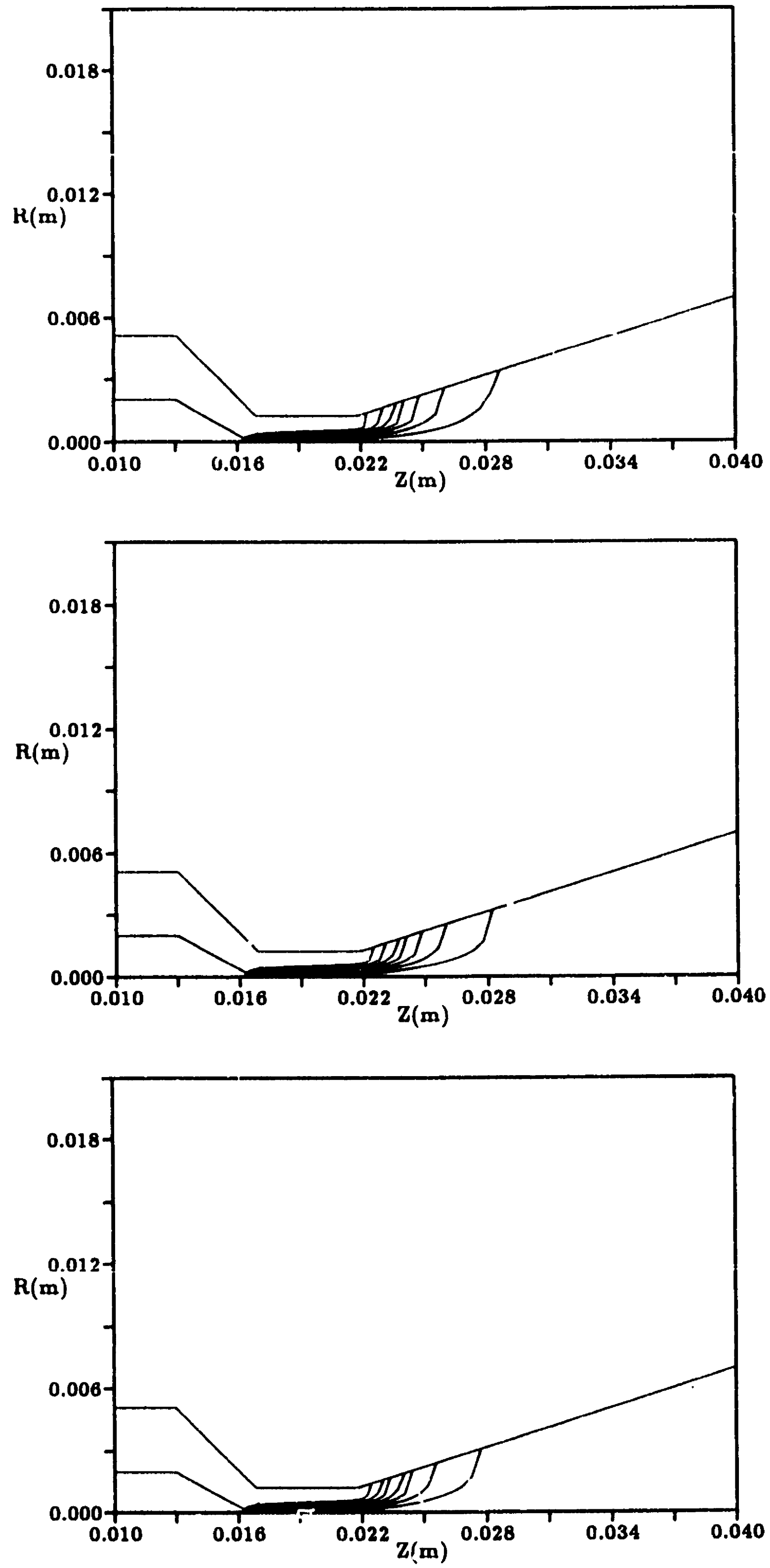

Figure 6.2: Enclosed Current Contours for $\dot{m} = 0.1$g/s: I=60A (top), I=100A (middle), and I=130A (bottom)

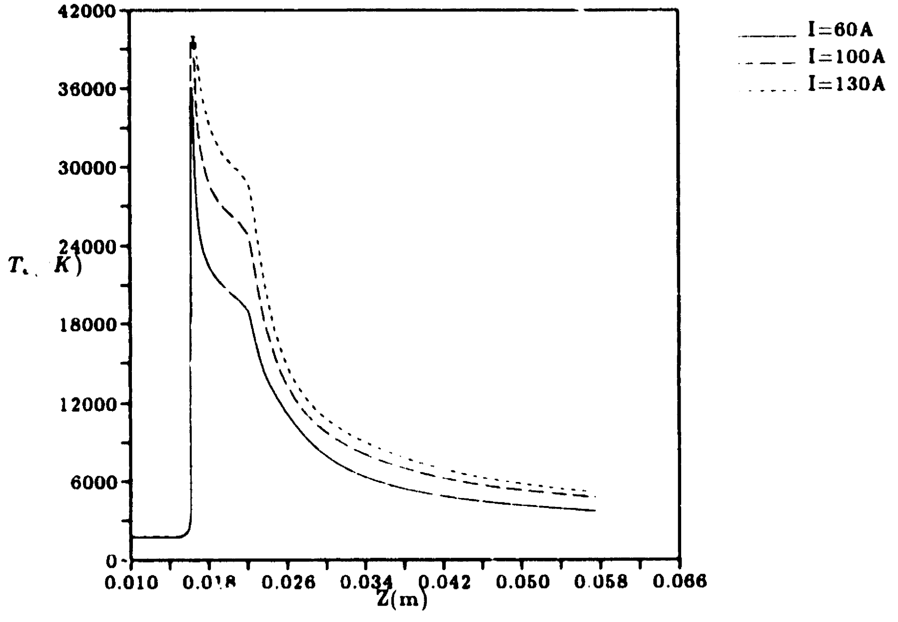

Figure 6.3: Centerline Axial Electron Temperature Profiles for $\dot{m} = 0.1$g/s at Three Applied Currents

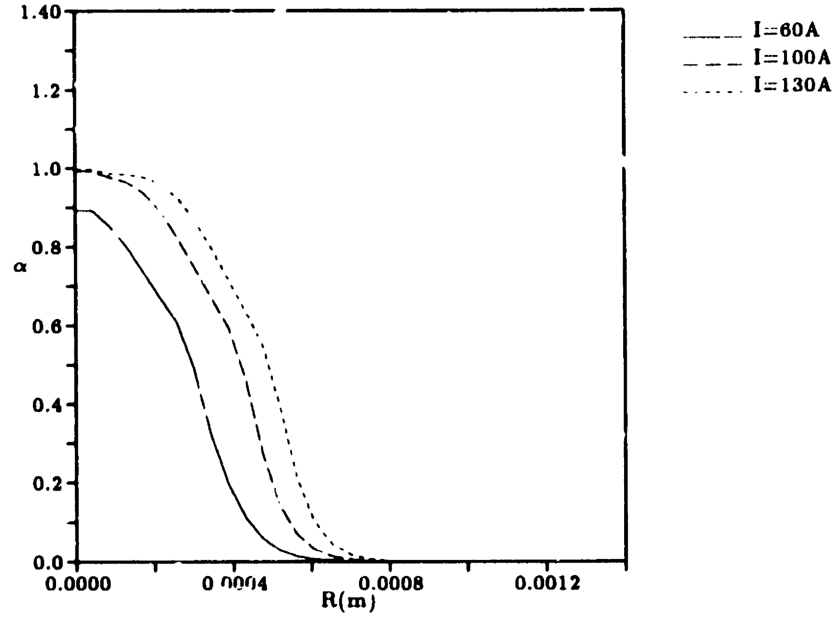

Figure 6.4: Ionization Fraction Radial Profiles at the Constrictor Exit for $\dot{m} = 0.1$g/s at Three Applied Currents

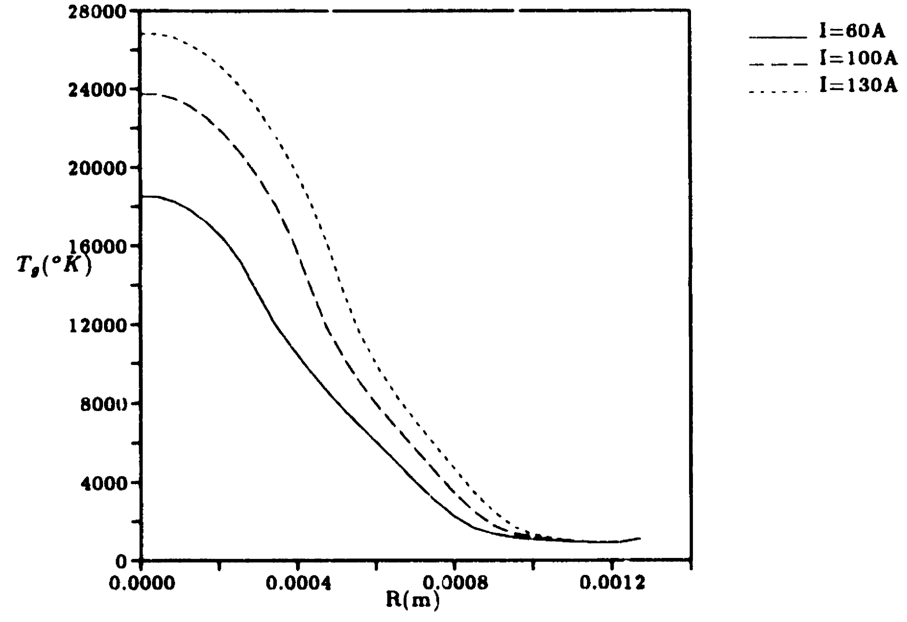

Figure 6.5: Radial Gas Temperature Profiles at the Constrictor Exit for $\dot{m} = 0.1$g/s at Three Applied Currents

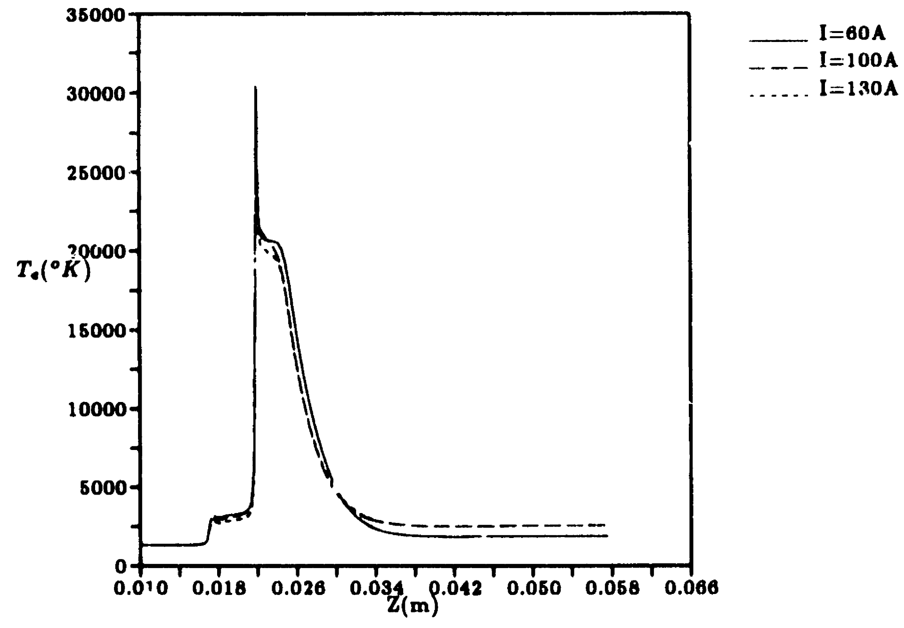

Figure 6.6: Anode Wall Axial Electron Temperature Profiles for $\dot{m} = 0.1$g/s at Three Applied Currents

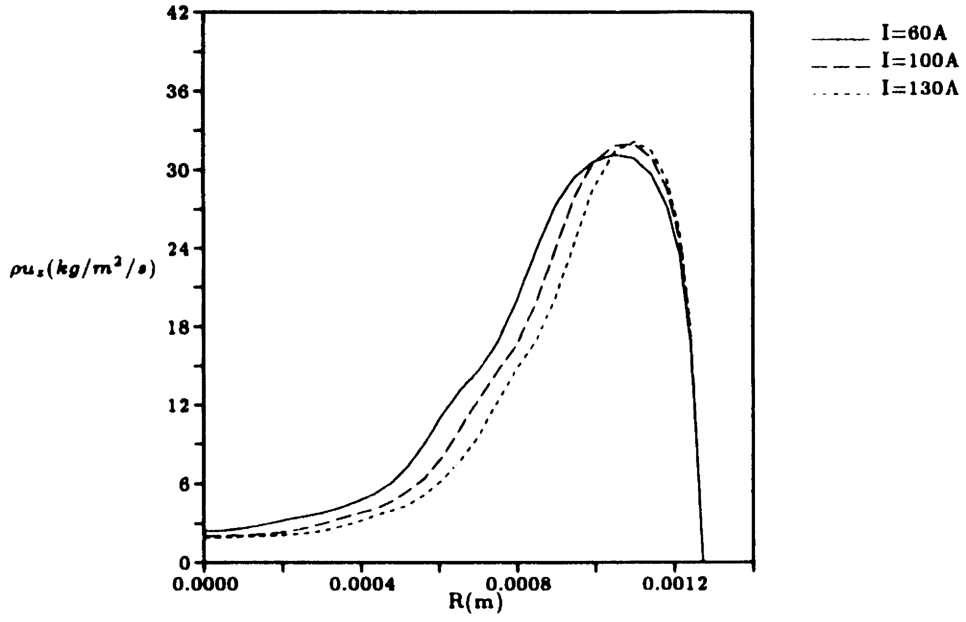

Figure 6.7: Mass Flux (ρu_z) Radial Profiles at the Constrictor Exit for $\dot{m} = 0.1$g/s at Three Applied Currents

profiles of the kinetic power ($u_z[\frac{1}{2}\rho u_z^2 + p]$), which are indicative of the power converted to useful thrust, at the same axial location.

A breakdown of the distribution of energy at the thruster exit plane is provided for each of the three current levels in Table 6.2. As detailed in the previous chapter, the total power at the exit plane is equal to the inherent power of the incoming gas flow plus the electrical input power minus the power transferred to the electrode walls. In this model the inlet boundary conditions are identical for each of the three cases examined here, so the total energy of the inlet flow is identical in each case. The power transferred to the anode wall, however, increases with increasing current, as shown in Table 6.3. This anode power loss rises from 0.85kW at 60A to 1.98kW at 130A, primarily due to the increased flux of current-carrying electrons at the anode surface. The effective anode voltage drop, however, defined by $V_a = \frac{\dot{q}}{I}$, increases only slightly from 14.1V at the lower current to 15.2V at the higher current. With regard to the distribution of energy at the exit plane, Table 6.2 shows that the fraction of energy tied thermally to the electrons and heavy species increases from 9.6% to 12.8% as the current is increased from 60A to 130A. Over the same range the fraction of energy frozen into dissociation and ionization remains nearly constant, actually decreasing from 48.9% to 47.0%. As the current increases, however, the fraction of that frozen energy which is associated with ionization rather than dissociation rises from 32% to 45%. Thus the net decrease in axial kinetic energy fraction with increasing current is

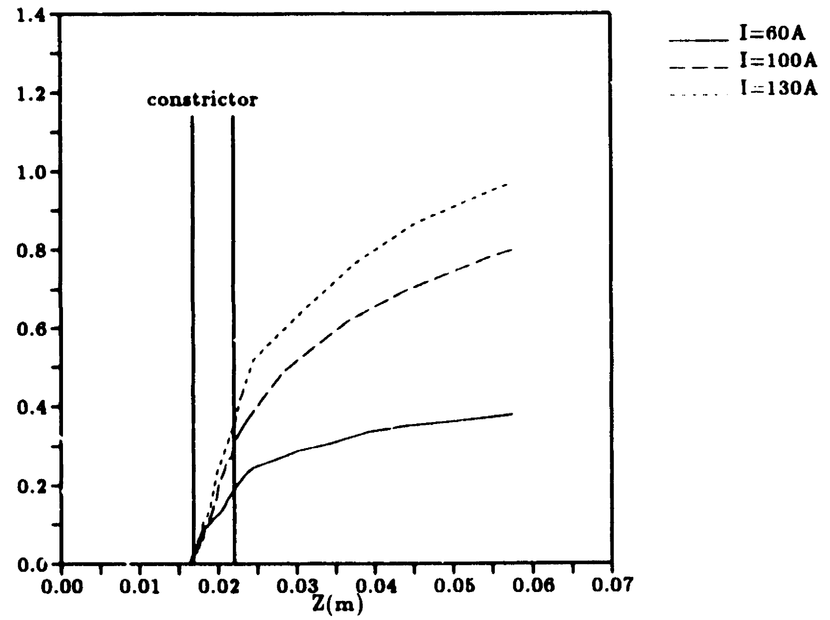

Figure 6.8: Mass Flow Fraction Inside the Arc ($\alpha > 0.01$) as a Function of Axial Location for $\dot{m} = 0.1$g/s at Three Applied Currents

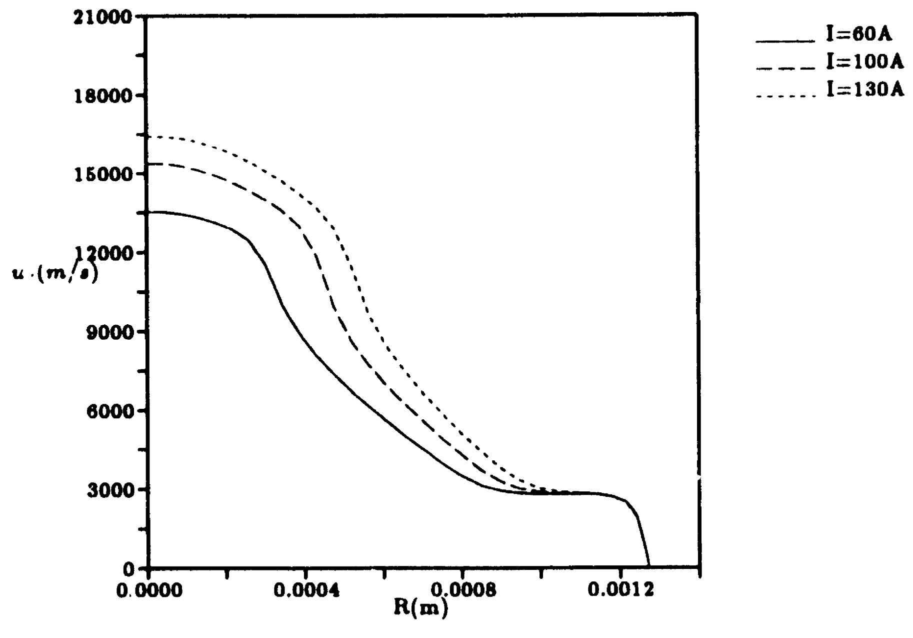

Figure 6.9: Axial Velocity (u_z) Radial Profiles at the Constrictor Exit for $\dot{m} = 0.1$g/s at Three Applied Currents

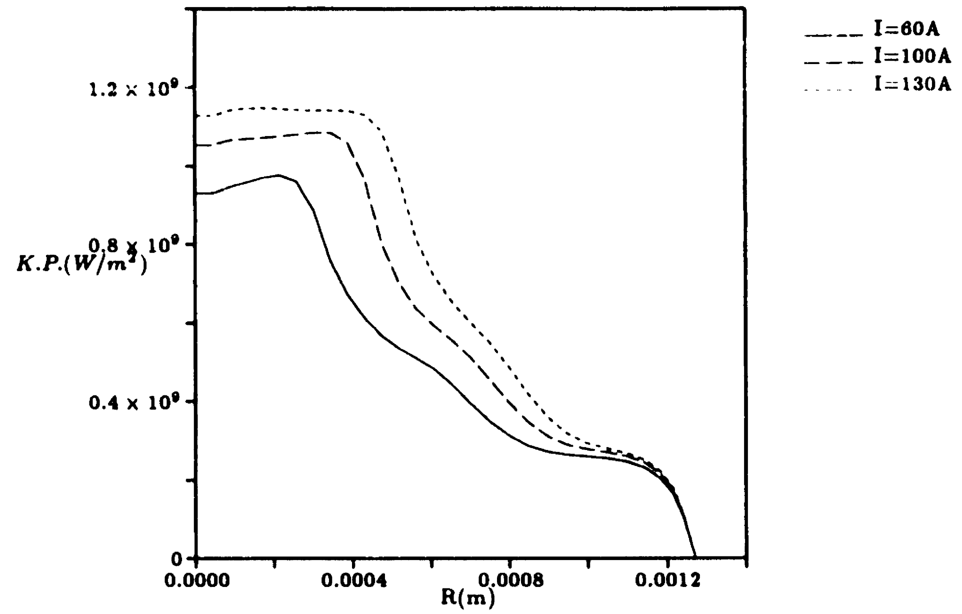

Figure 6.10: Kinetic Power ($u_z[\frac{1}{2}\rho u_z^2 + p]$) Radial Profiles at the Constrictor Exit for $\dot{m} = 0.1$g/s at Three Applied Currents

essentially the difference between the fractional thermal energy gain and the fractional dissociation/ionization energy loss. Including the power lost to the anode wall as part of the total power of the exiting flow would provide a more realistic picture of the energy partitioning. Unfortunately, using the simulated anode power losses mentioned above would not be consistent unless an anode heat balance model were developed to properly calculate the resulting total energy of the inlet gas in the plenum, which would vary with the applied current. Such a model is developed and evaluated in the next chapter.

6.2 Effect of Mass Flow Variation

The effect of varying the mass flow rate on arcjet performance can be isolated to some degree by comparing the three cases in Table 6.1 with different mass flow rates but similar specific powers. The first, fifth, and last cases listed in that table have specific powers of 120 MJ/kg and specific impulses of 1030 seconds, plus or minus a few percent. These three cases are defined by the following operating points: (1) I=60A, $\dot{m} = 0.05$g/s; (2) I=100A, $\dot{m} = 0.10$g/s; and (3) I=130A, $\dot{m} = 0.15$g/s.

The first major difference between these cases lies in their resulting current distributions, shown in Figure 6.11. Since increasing the mass flow rate increases the density, which directly decreases the heat diffusivity ($\alpha = \frac{\kappa}{\rho c_p}$), the arc becomes more

Table 6.2: Distribution of Energy in the Exit Flow for $\dot{m} = 0.1$g/s at Three Applied Currents

Energy State	% of Total		
	I=60A	I=100A	I=130 A
Axial kinetic	40.4	39.2	38.8
Radial kinetic	0.7	0.6	0.6
Azimuthal kinetic	0.0	0.0	0.0
Ionization	12.6	17.5	21.0
Dissociation	36.3	30.0	26.0
Electron thermal	0.4	0.6	0.8
Heavy sp. thermal	9.6	12.1	12.8

Table 6.3: Anode Wall Power Losses for $\dot{m} = 0.1$g/s at Three Applied Currents

Current (A)	Power to Anode (kW)	Effective Voltage Drop (V)
60	0.85	14.1
100	1.46	14.6
130	1.98	15.2

constricted. This can be seen qualitatively in Figure 6.11 and quantitatively in Figure 6.12. The latter figure displays radial plots of the ionization fraction at the constrictor exit for each of the three mass flow rates. The edge of the arc, defined by an ionization fraction on the order of 10^{-3}, moves inward about 1.5mm as the mass flow rate is increased from 0.05g/s to 0.15g/s. An additional effect is that the ionization fraction in the core increases with increasing mass flow rate. Although the specific power for each of these cases is the same, the decreasing width of the arc means that more energy per unit mass is being dissipated in the arc as the mass flow is increased. This increased dissipation then causes more ionization to occur in the arc core.

In fact, as the energy dissipated in the arc increases with increasing mass flow, the electron temperature increases due to ohmic dissipation and this elevated electron temperature then leads to increased ionization. Radial plots of the electron temperature at the constrictor exit are pictured in Figure 6.13 for each of the three cases. This figure shows that the electron temperature increase in the arc core is also accompanied by a corresponding decrease in temperature in the outer flow. The behavior of the gas temperature is similar (Figure 6.14). Lower temperatures and higher densities in the outer flow produce a lower heat diffusivity in that region. Combined with the fact that the width of the outer layer also increases with the mass flow rate, this leads to increased convection in the current attachment region and consequently to a broader attachment zone as the mass flow is increased. This effect can be seen clearly in the enclosed current contours of Figure 6.11. Increasing convection in the anodic arc attachment zone translates into a higher prediction of discharge voltage, from 89V at 0.05g/s to 115V at 0.10g/s to 137V at 0.15g/s.

The current and temperature distributions of each of these three cases look quite different, yet the specific impulse is known to be nearly the same for each mass flow rate. The reason for this can be discerned by comparing mass and velocity distributions for the three flows. Figure 6.15 shows normalized mass flux profiles for the three cases at the constrictor exit, while Figure 6.16 shows axial velocity profiles at the same axial location. Because the temperature inside the arc increases and the width of the arc decreases as the mass flow rate is increased, the normalized mass flow inside the arc decreases. When the mass flow in the arc proportionally decreases the axial velocity in the arc increases, as shown in Figure 6.16. Conversely, when the mass flow in the outer flow proportionally increases the axial velocity in that region decreases. As mentioned previously, this effect occurs because a nearly uniform pressure gradient acts over the flow cross-section. Thus as the mass flow increases while the specific power is held constant, the velocity in the the arc is increased but less mass flows through the core,

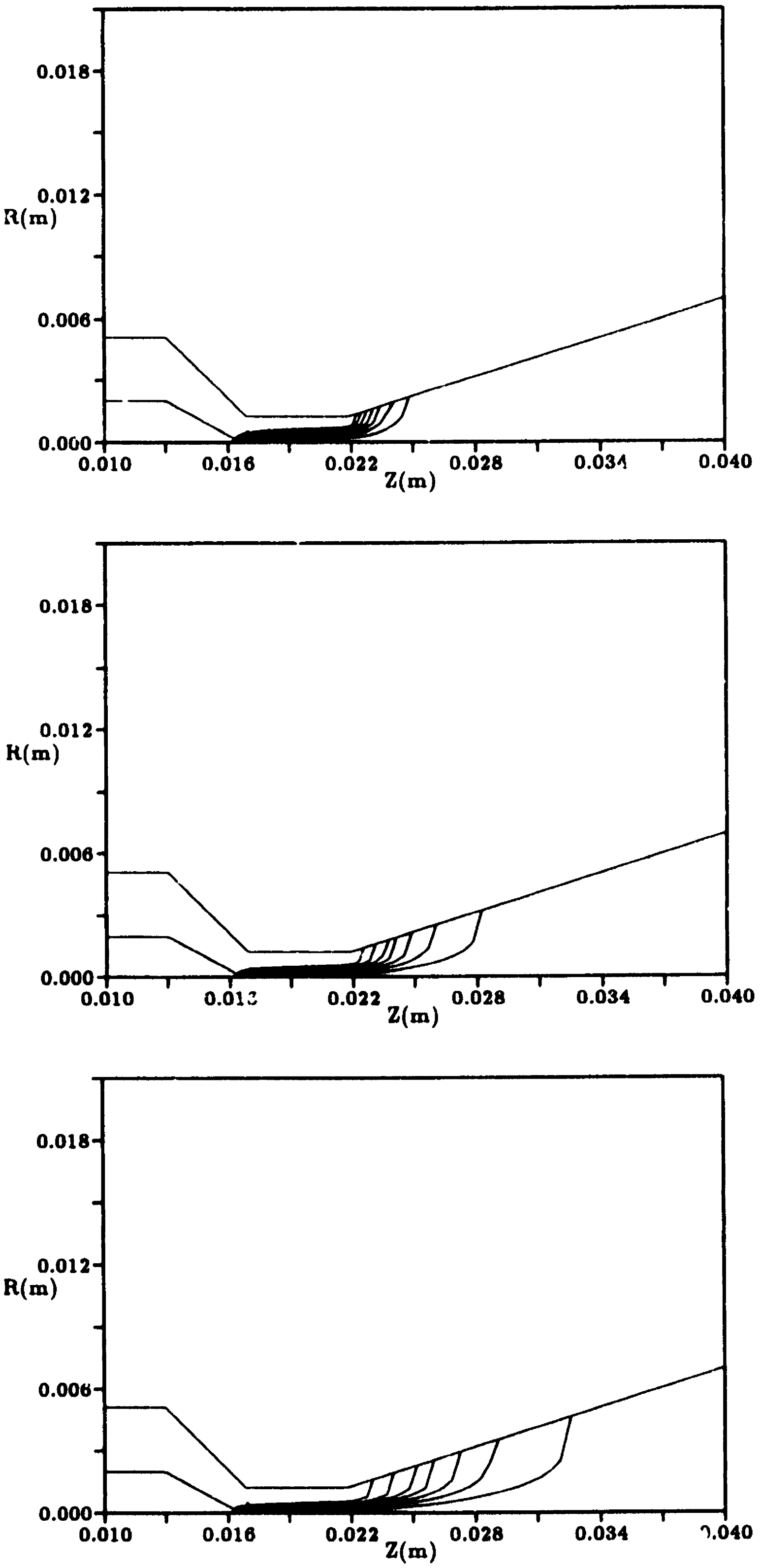

Figure 6.11: Enclosed Current Contours for $\frac{P}{\dot{m}} \approx$ 115MJ/kg : I=60A, $\dot{m}$ = 0.05g/s (top); I=100A, $\dot{m}$ = 0.10g/s (middle); and I=130A, $\dot{m}$ = 0.15g/s (bottom)

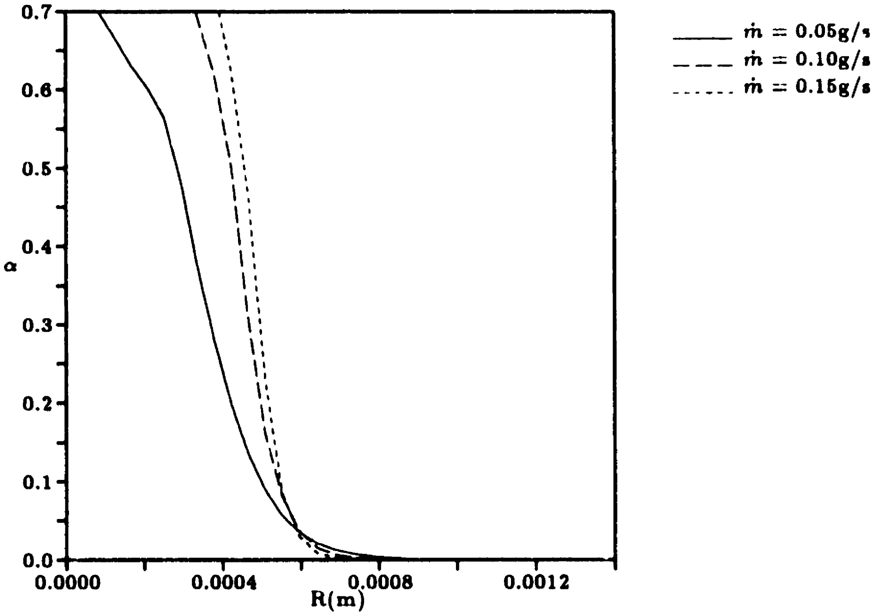

Figure 6.12: Ionization Fraction Radial Profiles at the Constrictor Exit for $\frac{P}{\dot{m}}$ = 120MJ/kg at Three Mass Flow Rates

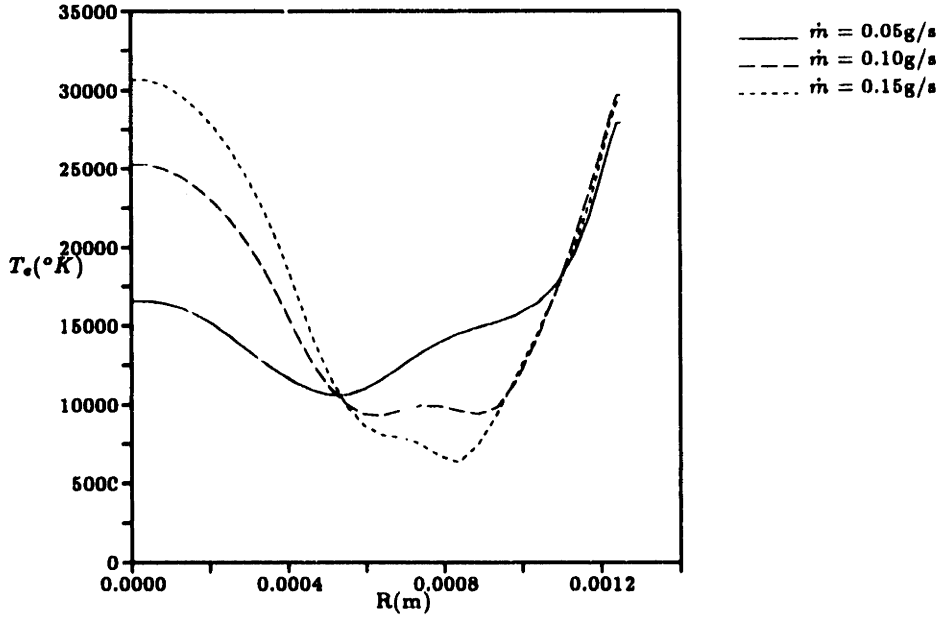

Figure 6.13: Electron Temperature Radial Profiles at the Constrictor Exit for $\frac{P}{\dot{m}}$ = 120MJ/kg at Three Mass Flow Rates

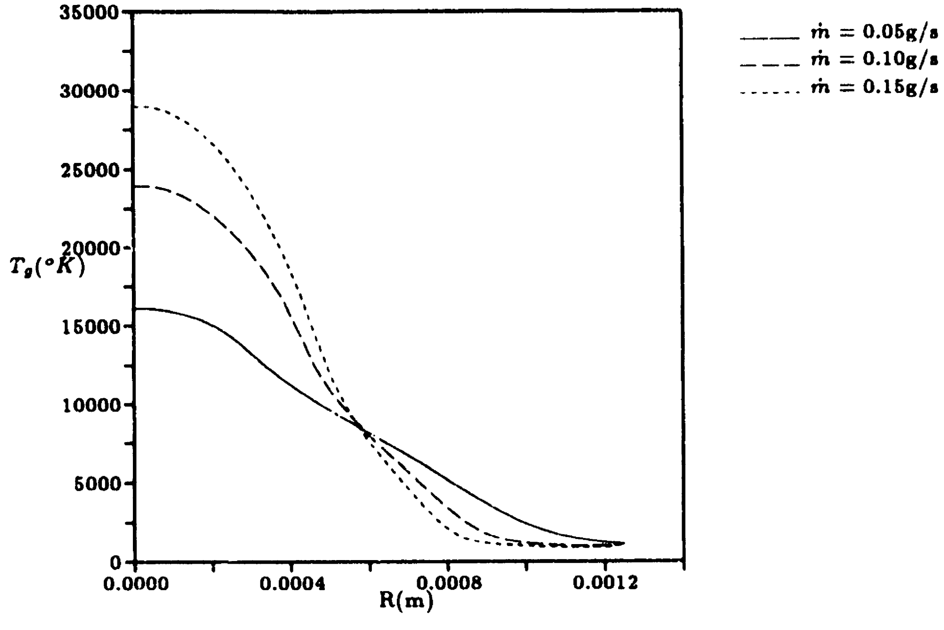

Figure 6.14: Gas Temperature Radial Profiles at the Constrictor Exit for $\frac{P}{\dot{m}}$ = 120MJ/kg at Three Mass Flow Rates

and the velocity in the outer flow is decreased and more mass flows through the outer region. This compensating effect results in specific impulses for the three cases which are nearly the same.

Of course viscosity and diffusion in the nozzle expansion tend to smooth out gradients in the flow, so a nozzle exit comparison is warranted. Figures 6.17 and 6.18 show radial profiles of axial velocity and momentum flux (ρu_z^2) at the exit plane, respectively. In an inviscid, homogeneous expansion to vacuum the specific impulse of a device would be calculated by simply dividing the exit velocity by the standard acceleration $g_0 = 9.8m/s^2$. In this case, however, the expanding flow is both viscous and nonuniform, so the specific impulse is determined by first integrating the quantity $\rho u_z^2 + P$ over the nozzle to produce thrust and then dividing by the mass flow rate and by g_0. This procedure weights the calculation of specific impulse by the thrust, so flow regions which contain the most kinetic energy will necessarily determine the overall specific impulse of the device. Figure 6.17 shows that the exit velocity increases at all radial locations as the mass flow rate is increased at constant specific power. The following figure, however, demonstrates that the maximum momentum flux occurs farther from the centerline as the mass flow is increased. This behavior is even more pronounced when a more relevant quantity is examined, namely the integrated momentum flux (Figure 6.19). The net effect is that while the exit velocity increases with increasing mass flow rate, more of the flow is actually farther from the centerline.

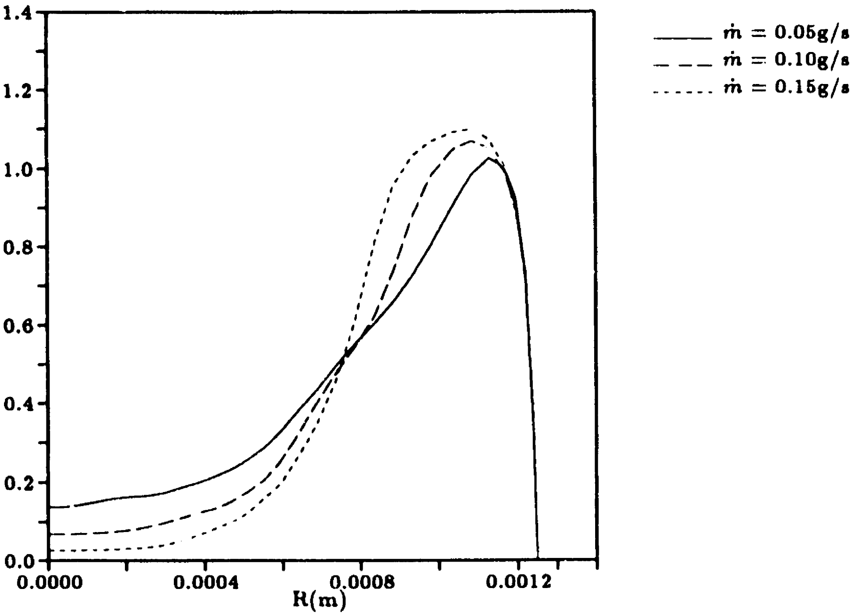

Figure 6.15: Normalized Mass Flux (ρu_z) Radial Profiles at the Constrictor Exit for $\frac{P}{\dot{m}} = 170MJ/kg$ at Three Mass Flow Rates

Therefore the effective specific impulse is relatively constant for a constant specific power, as would be expected from energy conservation principles. Minor physical effects due to the influence of density and current attachment keep the performance from being exactly the same in each case.

The distribution of energy in the exit flow for the three cases is detailed in Table 6.4. As the mass flow rate is increased from 0.05g/s to 0.15g/s at constant specific power, the fraction of energy in the axial kinetic mode increases from 34.1% to 44.4%. At the same time the fraction of energy frozen into dissociation and ionization decreases from 52.8% to 41.6%, implying that the recovery or minimization of these losses is more efficient at higher mass flow rates. This occurs because increasing the mass flow rate (1) increases the overall density, which tends to drive the system toward equilibrium, and (2) increases the propellant flow outside the arc, leaving a proportionally smaller amount of propellant in the core to be dissociated and ionized. Somewhat higher percentages of the exit flow energy are stored in the radial kinetic and electron thermal modes as the mass flow rate is increased, while the heavy species thermal energy fraction remains relatively unchanged.

Anode wall power losses for the three mass flow rates are listed in Table 6.5. As the mass flow rate is increased the power transmitted to the anode increases, mainly due to the fact that the anode arc attachment zone is spread out over a wider portion of the nozzle. The anode power loss for the lowest mass flow rate is not quite as

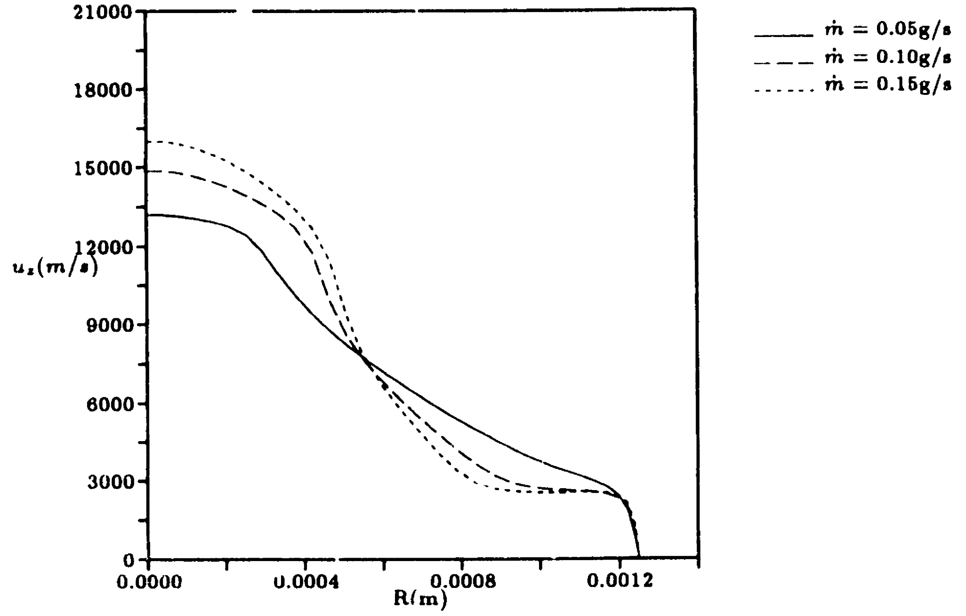

Figure 6.16: Axial Velocity (u_z) Radial Profiles at the Constrictor Exit for $\frac{P}{\dot{m}}$ = 120MJ/kg at Three Mass Flow Rates

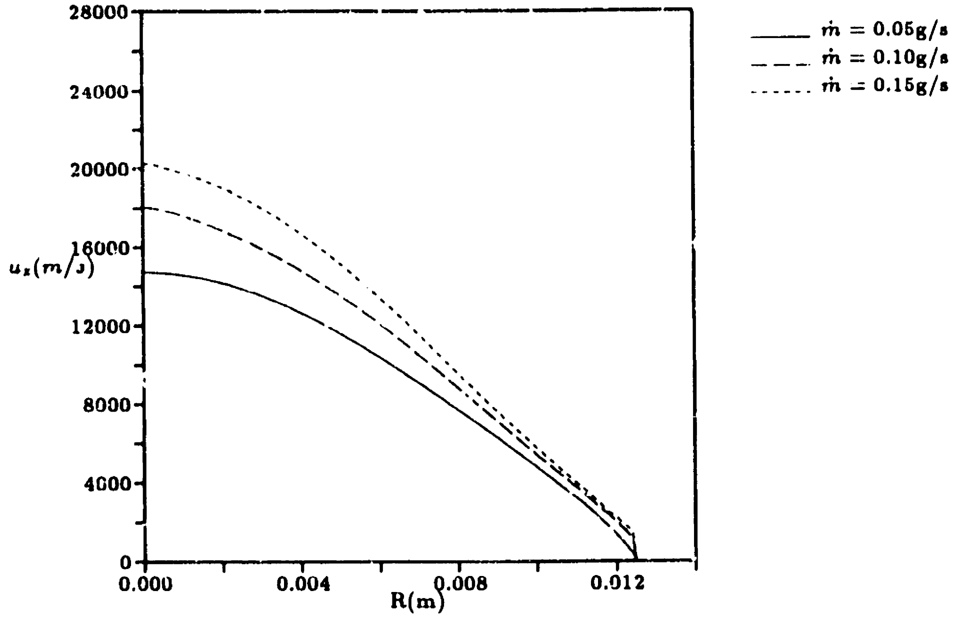

Figure 6.17: Axial Velocity (u_z) Radial Profiles at the Thruster Exit for $\frac{P}{\dot{m}}$ = 120MJ/kg at Three Mass Flow Rates

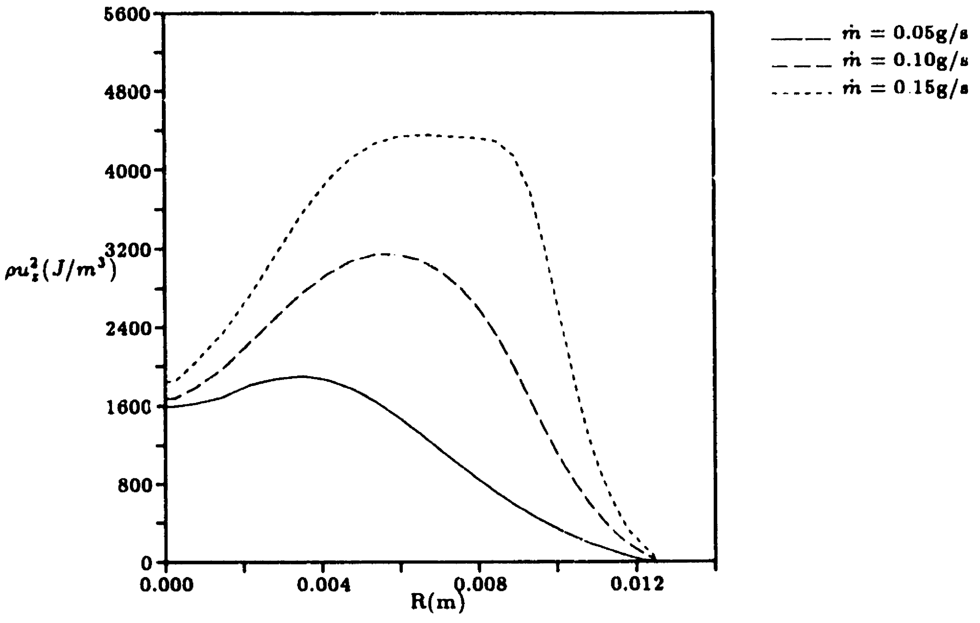

Figure 6.18: Momentum Flux (ρu_z^2) Radial Profiles at the Thruster Exit for $\frac{P}{\dot{m}}$ = 120MJ/kg at Three Mass Flow Rates

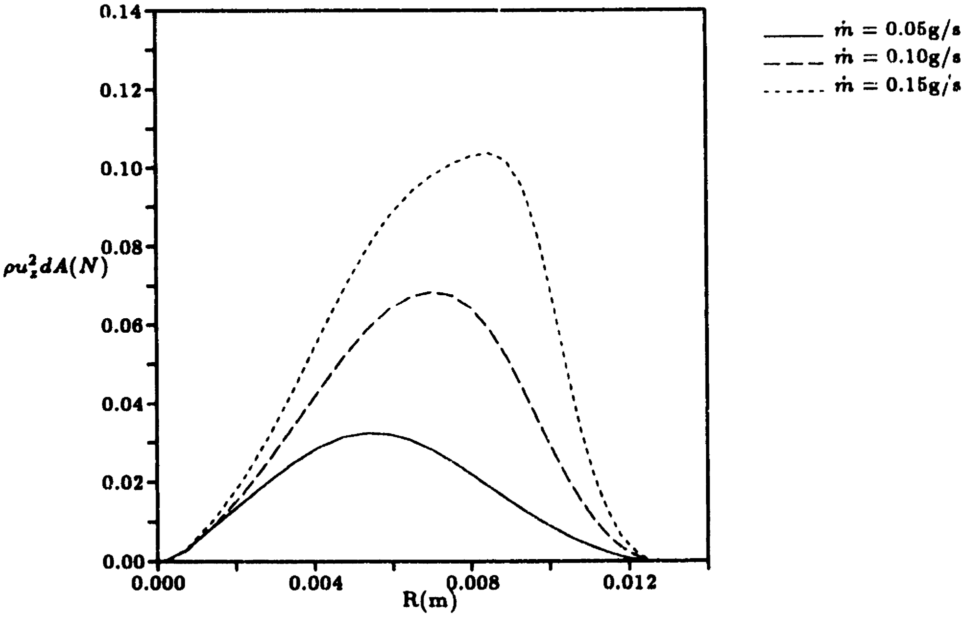

Figure 6.19: Radial Distribution of the Kinetic Thrust ($\rho u_z^2 dA$) at the Thruster Exit for $\frac{P}{\dot{m}}$ = 120MJ/kg at Three Mass Flow Rates

Table 6.4: Distribution of Energy in the Exit Flow for $\frac{P}{\dot{m}}$ = 120MJ/kg at Three Mass Flow Rates

Energy State	% of Total		
	$\dot{m} = 0.05$g/s	$\dot{m} = 0.10$g/s	$\dot{m} = 0.15$g/s
Axial kinetic	34.1	39.2	44.4
Radial kinetic	0.5	0.6	0.8
Azimuthal kinetic	0.0	0.0	0.0
Ionization	15.0	17.5	21.1
Dissociation	37.8	30.0	20.5
Electron thermal	0.4	0.6	0.9
Heavy sp. thermal	12.2	12.1	12.2

Table 6.5: Anode Wall Power Losses for $\frac{P}{\dot{m}}$ = 120MJ/kg at Three Mass Flow Rates

$\dot{m}$ (g/s)	**Power to Anode (kW)**	**Effective Voltage Drop (V)**
0.05	1.25	17.8
0.10	1.46	14.6
0.15	1.78	13.7

small as might be expected. The reason is that although the anodic arc attachment region is smaller, much higher heat fluxes are achieved in that region and there is a significant amount of heat lost to the constrictor wall as well. These points are illustrated in Figure 6.20, which plots anode wall heat flux distributions for the three cases studied. The results of this section suggest two methods for improving arcjet performance. Arcjet thrusters could be designed for higher pressures by decreasing the constrictor diameter in order to drive the flow more towards equilibrium and recover more of the frozen losses. Alternatively, higher mass flow rates and higher applied currents could be used to increase the fraction of propellant which flows outside the arc, thereby improving thrust efficiency.

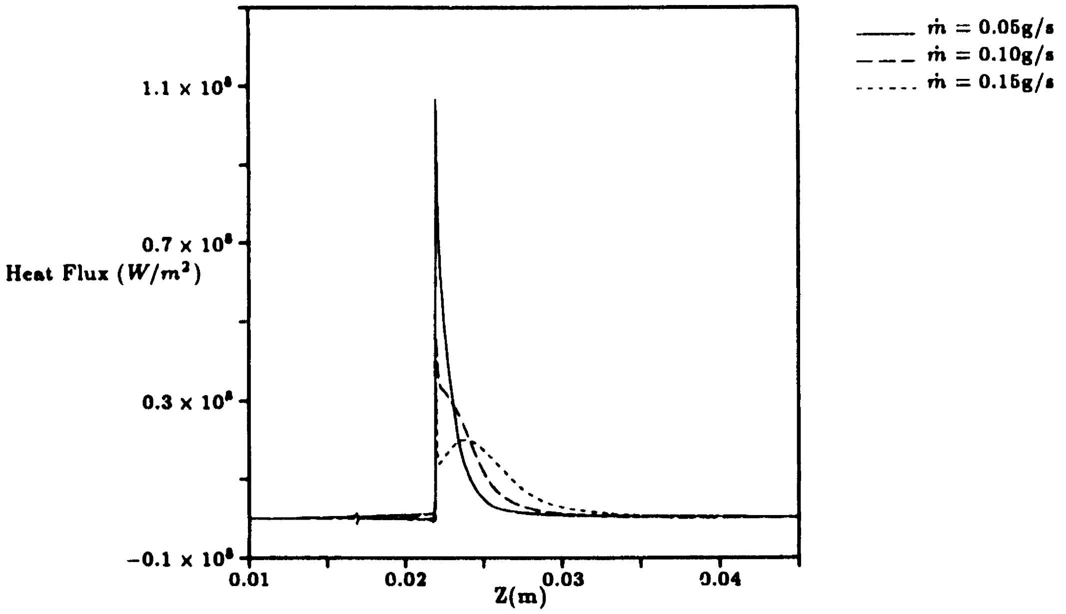

Figure 6.20: Axial Heat Flux Distributions Along the Anode Wall for $\frac{P}{\dot{m}}$ = 120MJ/kg at Three Mass Flow Rates

Chapter 7

Integration of an Anode Heat Balance Model

7.1 Formulation

Since it has been shown that the temperature of the cooler flow outside the electric arc has an important effect on overall arcjet performance[76], a model of the heat balance in the anode was deemed necessary in order to gain a more accurate estimate of the gas temperature at the anode wall boundary. For consistency, this model should include not only the anode block but also the cathode, insulator, propellant feed passages, and refractory casing in order to accurately determine both the anode wall temperature and the gas temperature at the plenum inlet, which directly influence the thrust of the device. This problem is governed by the heat flow equation

$$-\frac{\partial}{\partial z}\left(k_A\frac{\partial T}{\partial z}\right)-\frac{1}{r}\frac{\partial}{\partial r}\left(rk_A\frac{\partial T}{\partial r}\right)=\frac{j^2}{\sigma} \tag{7.1}$$

in an axisymmetric coordinate system, where k_A is the thermal conductivity of the anode material. For medium power arcjet thruster anodes the ohmic dissipation term is negligible, adding no more than a few watts of power to the 1-3kW already supplied by the arc electrons in the attachment zone. High currents passing through the thin cathode rod, however, produce a small but not insignificant dissipation. For the geometry of the TT1 arcjet thruster modeled in this research, a tungsten cathode with a conductivity of $1.8 \times 10^7/\Omega/m$ will absorb on the order of 5W compared to 60-100W incident at the cathode tip.

A diagram of the German TT1 thruster assembly is pictured in Figure 7.1. The design of this thruster is typical of most radiatively-cooled arcjet thrusters. A tungsten

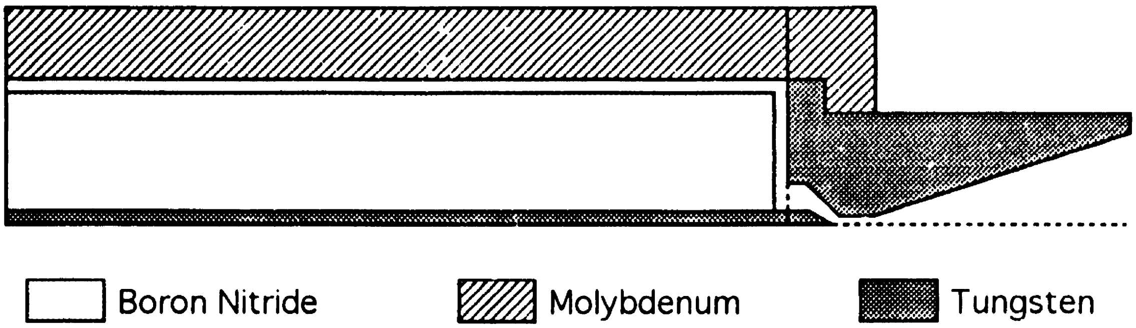

Figure 7.1: Anode Schematic of German TT1 Radiation-Cooled Arcjet

anode block is surrounded by a molybdenum casing, and separated from a cylindrical tungsten cathode by a boron nitride insulator. The propellant gas is injected at the rear of the thruster assembly and flows between the insulator and outer casing to the plenum just ahead of the constrictor. Heat conducted from the hot walls increases the gas temperature from approximately 300°K at the inlet to 700 – 900°K at the plenum. Using the transformation described in Section 3.3, this equation may be written in natural coordinates as

$$\begin{aligned} k_A \Bigg[\left(\xi_r^2 + \xi_z^2\right) \frac{\partial^2 T}{\partial \xi^2} + 2\left(\xi_r \eta_r + \xi_z \eta_z\right) \frac{\partial^2 T}{\partial \xi \partial \eta} \\ + \left(\eta_r^2 + \eta_z^2\right) \frac{\partial^2 T}{\partial \eta^2} + \left(\xi_{rr} + \xi_{zz}\right) \frac{\partial T}{\partial \xi} + \left(\eta_{rr} + \eta_{zz}\right) \frac{\partial T}{\partial \eta} \Bigg] \\ + \left(\frac{\partial T}{\partial \xi}\xi_r + \frac{\partial T}{\partial \eta}\eta_r\right)\left(\frac{k_A}{r} + \frac{\partial k_A}{\partial \xi}\xi_r + \frac{\partial k_A}{\partial \eta}\eta_r\right) \\ - \left(\frac{\partial T}{\partial \xi}\xi_z + \frac{\partial T}{\partial \eta}\eta_z\right)\left(\frac{\partial k_A}{\partial \xi}\xi_z + \frac{\partial k_A}{\partial \eta}\eta_z\right) + \frac{j^2}{\sigma} = 0, \end{aligned} \tag{7.2}$$

which is the equation to be solved in the computational domain.

The preceding equation is seen to be of exactly the same form as the potential equation, Eqn. D.1, and thus may be solved by the SOR technique described in Section 4.2. For anode boundaries which are exposed to space, the temperature is calculated to satisfy the relation

$$k_A \frac{dT}{d\hat{n}} = \epsilon \sigma_{SH} T^4, \tag{7.3}$$

where ϵ is the emissivity of the material and $\sigma_{SB} = 5.67 \times 10^{-8} \frac{W}{^oK^4 m^2}$ is the Stefan-Boltzmann constant. Emissivities for anode refractory materials vary from 0.37 for Molybdenum to 0.43 for Tungsten[100]. The temperature of the upstream or left-hand boundary of the thruster assembly is set to 300°K, a figure consistent with experi-

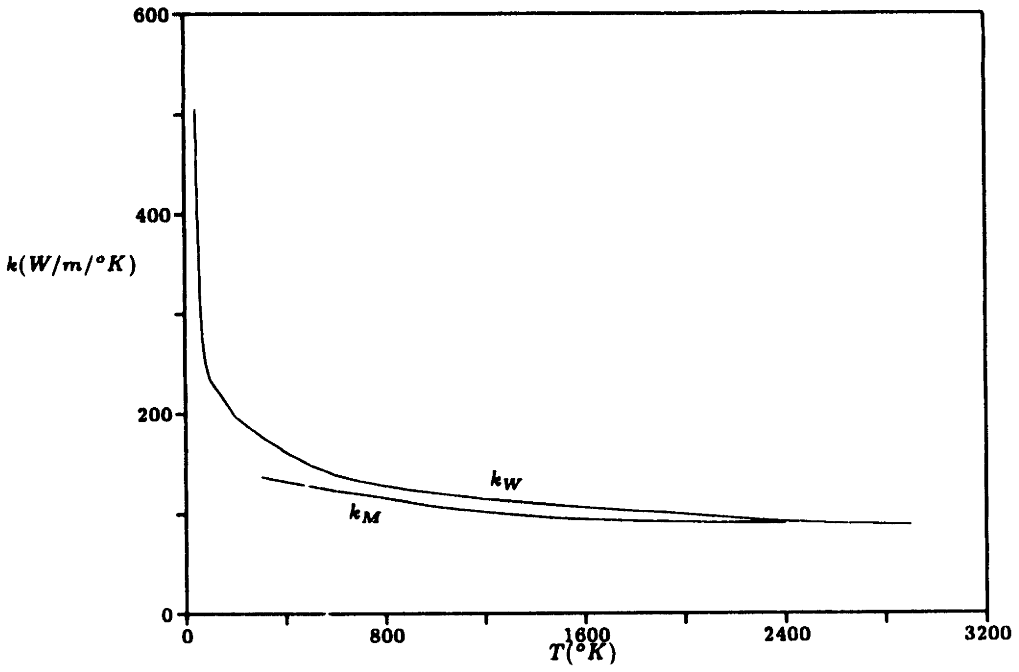

Figure 7.2: Tungsten and Molybdenum Thermal Conductivity vs. Temperature

mental measurements of the TT1 arcjet. On the inside anode wall, the temperature is found by equating the heat flux to the wall from the electrons and heavy species to the heat conducted away from the wall into the metal. This involves iteratively reconciling the results of the main arcjet flow code with the solution from the anode heat balance model. Measurements have been made of the heat flux to the cathode for the water-cooled TT1 arcjet thruster[35, 36], and these results are used to determine the temperature at the cathode boundary of the model. A more self-consistent method is not used because of the numerical and theoretical difficulties involved in making an accurate determination of the heat flux at the cathode tip. This simplification should not be of great importance in calculating the anode wall temperature, however, because the gas flow between the anode and cathode/insulator tends to isolate these two regions thermally.

The model uses different approaches to solve for the temperature in the flowing gas and in the solid materials. The transformed heat equation is used in the solid regions with the appropriate thermal conductivity for each material. The coefficient of thermal conductivity for both tungsten and molybdenum is plotted in Figure 7.2 over the range of electrode temperatures expected. For reference, numerical values of k_W and k_M are tabulated for selected temperatures in Appendix H. Of note is that the thermal conductivity of these refractory metals is a decreasing function of temperature at least to very near the melting point of the materials. The thermal conductivity of boron

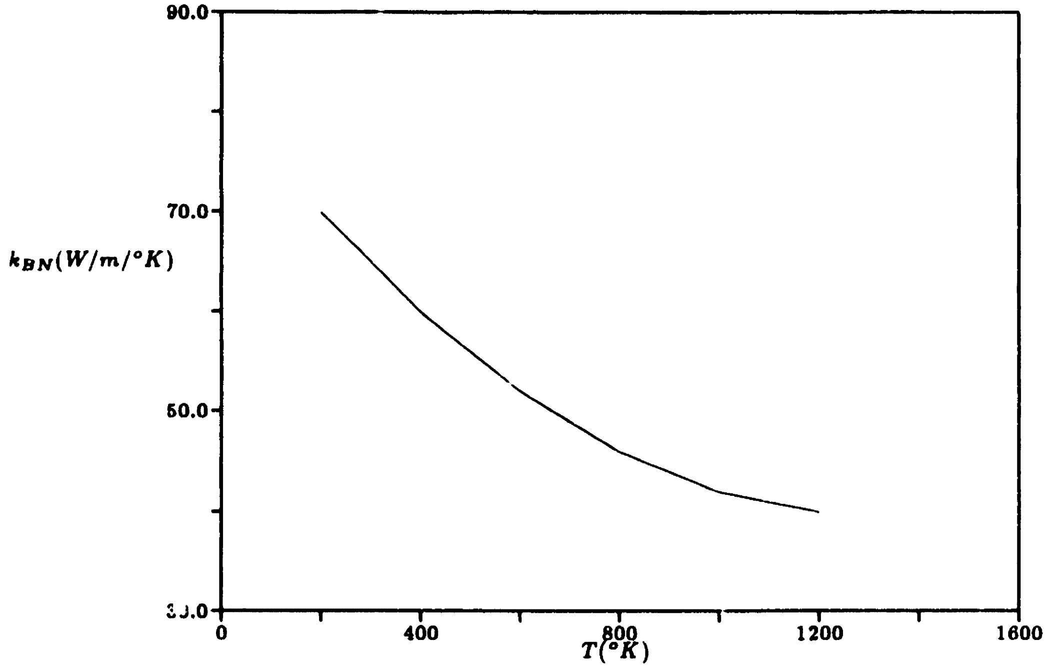

Figure 7.3: Combat HP Boron Nitride Thermal Conductivity vs. Temperature

nitride varies considerably depending on the grade of the material. In addition, properties are different in the directions parallel and perpendicular to the pressing direction. The boron nitride of this simulation is assumed to be Combat Boron Nitride Grade HP, which is manufactured by the Carborundum Company[16]. This grade is designed specifically for ion engines, plasma arcs, and similar applications. It has a higher thermal conductivity, thermal shock resistance, and chemical inertness than other boron nitride solids and a lower thermal expansion ratio. The thermal conductivity of Combat HP is plotted versus temperature in Figure 7.3, and is seen to be about one third that of tungsten and molybdenum. The parallel thermal conductivity, which is that of the longitudinal thruster direction, is used for all calculations.

The addition of heat to the flowing propellant gas is essentially a one-dimensional problem, so in order to simplify calculations a 1-D model is used to determine the temperature distribution in the gas passages. The equations

$$\rho u c_p \frac{\partial T}{\partial z} = k_g \frac{\partial^2 T}{\partial r^2} \qquad \mathit{and} \qquad \rho v c_p \frac{\partial T}{\partial r} = k_g \frac{\partial^2 T}{\partial z^2} \tag{7.4}$$

are employed, the former for the axial flow section and the latter for the radial flow section. A parabolic gas temperature distribution is assumed, which for example yields the following ordinary differential equation to be solved in the axial direction:

$$\frac{\dot{m} c_p}{A} \frac{dT}{dz} = \frac{6k_g}{H} \left[\frac{T_M - T}{L_M} + \frac{T_{BN} - T}{L_{BN}} \right] \tag{7.5}$$

where A is the cross-sectional area of the channel, T is the bulk average gas temperature, H is the channel width, T_M is the outer molybdenum temperature, T_{BN} is the inner boron nitride temperature, and L_M and L_{BN} are effective lengths for heat transfer across the two channel surfaces. A fourth order Runge-Kutta scheme is used to integrate this equation from the rear of the thruster assembly to the radial flow segment, after which the following equation is integrated to the plenum entrance:

$$\frac{\dot{m}c_p}{A}\frac{dT}{dr} = -\frac{6k_g}{H^2}\left[T_T + T_{BN} - 2T\right] \tag{7.6}$$

where T_T is the temperature of the tungsten anode in contact with the propellant gas. After each integration of the gas temperature, the edge temperatures T_M, T_{BN}, and T_T are updated by equating the heat fluxes across the flow boundary at each grid point.

7.2 Verification

The anode thermal model was verified by using the specified wall temperatures from the cases of the previous chapter as boundary conditions on the anode and cathode. The model was further simplified by eliminating the propellant gas passages. Overall conservation was then verified by calculating the heat flow through each boundary of the simulated thruster. Figure 7.4 shows the temperature distribution in the anode and in the upstream electrodes and insulator. The temperature varies smoothly between 300°K at the backplate to 1000°K at the cathode and 1000 – 1200°K on the interior anode surface except for minor discontinuities at the boundaries between different materials. The distribution is nearly one-dimensional from the backplate to 1.5 cm to the left of the thruster plenum. Boundaries between thruster materials can be seen clearly in the contour plot of thermal conductivity (Figure 7.5), which follows the behavior of the temperature plot closely. A total power of 1.73kW is delivered to the arcjet body in this case, 1.71kW through the anode and 0.02kW through the cathode. Of this total 0.33kW, or 19%, is radiated to space and the rest is conducted to the backplate.

The full anode heat balance model was tested by using realistic heat fluxes to set the electrode boundary conditions on temperature. At the cathode an input power of 0.1kW is assumed for this case and all subsequent simulations. At the anode the heat flux into the wall boundary is taken from simulation results for the baseline case of Chapter 5 (I=100A, $\dot{m}$ = 0.1g/s), based on the specified wall temperature of 1000 – 1100°K. This is therefore not a self-consistent solution, but rather the first step in the anode model - flow model iteration process. The results, however, do serve to

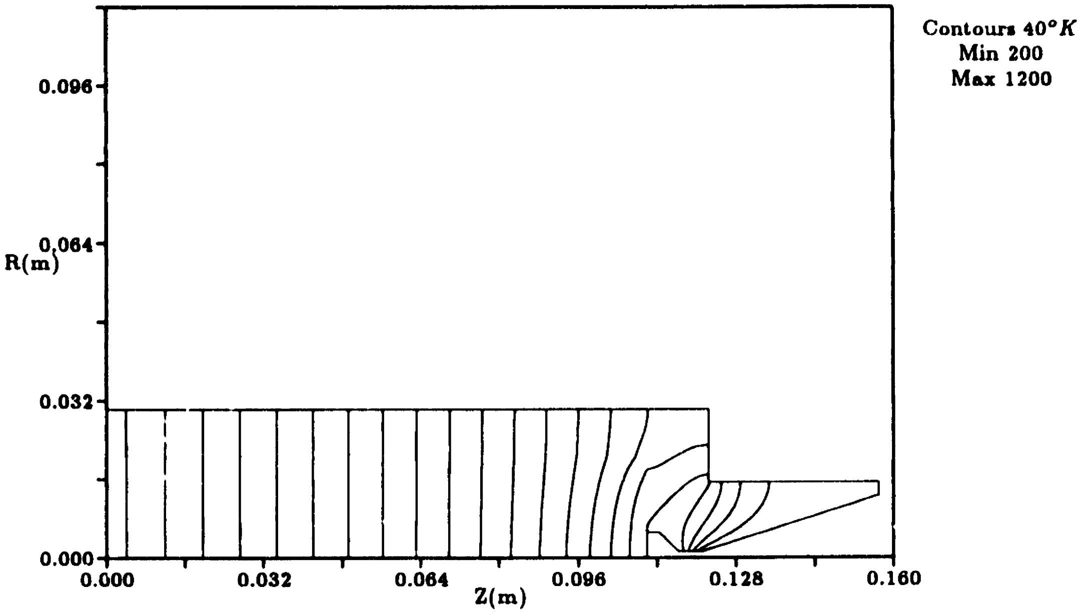

Figure 7.4: Anode Model Verification: Temperature Distribution for $T_W = 1000 - 1200^oK$

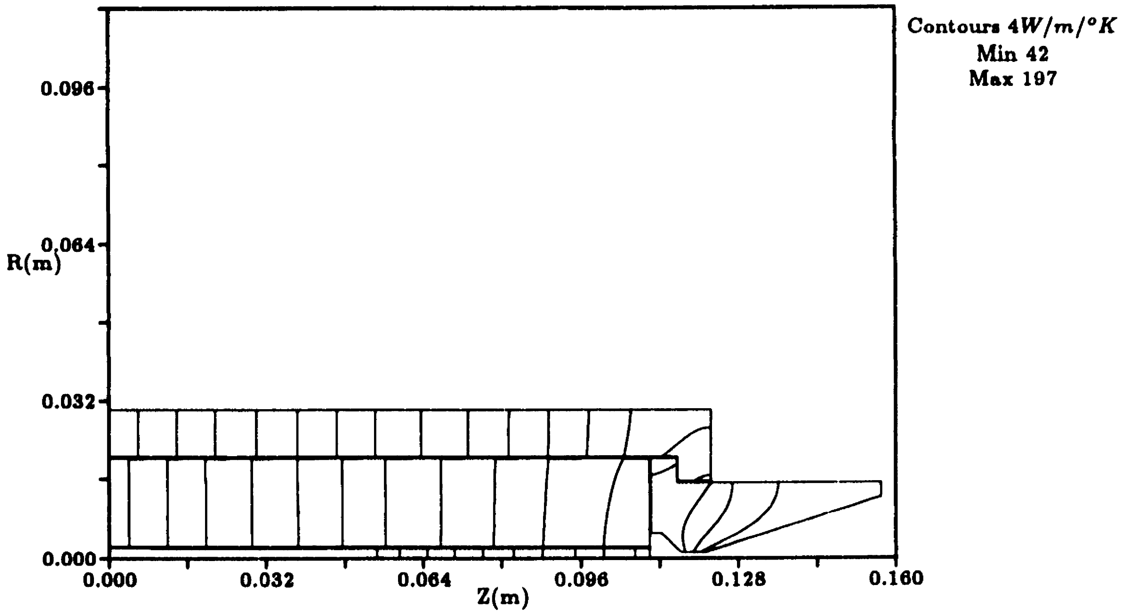

Figure 7.5: Anode Model Verification: Thermal Conductivity Distribution for $T_W = 1000 - 1200^oK$

indicate qualitatively the behavior of the fully consistent solution.

A line plot of the heat flux into the anode surface as a function of axial location is shown in Figure 7.6. Energy transfer is assumed to take place by heavy species heat conduction and by the deposition of the thermal, kinetic, and ionization energy of electrons impinging on the anode surface. Current-carrying electrons are the primary source of energy transferred to the anode wall. Some electron energy is transferred in the constrictor but the majority is deposited in the arc attachment region just beyond the constrictor exit. Upstream of the constrictor exit energy is lost from the walls via heat conduction to the heavy species, while downstream in the nozzle the reverse is true. The resulting temperature distribution in the thruster body is shown in Figure 7.7. Temperature maxima occur at the cathode and in the arc attachment region on the anode just beyond the constrictor exit, where the wall temperature reaches 1550°K. The temperature concentration in the anode arc attachment zone represents a significant difference between this case and the previous case, in which the anode wall temperature was specified. Outside of the attachment region, however, the anode wall temperature in Figure 7.7 varies from 990°K at the plenum entrance to 1080°K at the anode tip, which is relatively close to the previously specified distribution. The temperature at the cathode root is 875°K and conduction from the thruster body heats the propellant in the gas passages from 300°K to 825°K in the bulk-averaged sense. Thermal conductivity for this case, shown in Figure 7.8, varies predictably with temperature. This plot does serve, however, to delineate the different material regions of the simulation.

The diagram of Figure 7.9 illustrates the flow of energy through the arcjet thruster body for this baseline verification case. Here 49% of the power deposited into the thruster body is transferred to the flowing propellant, while 17% is radiated to space and the rest is conducted to the backplate. While beneficial recovery of one half of the anode power loss is achieved with this design, performance could be improved by using insulating materials to increase the temperature of the tungsten/molybdenum anode assembly even further.

7.3 Effect on Arcjet Performance Calculations

In order to obtain a more self-consistent simulation of arcjet performance, temperature distributions produced by the anode thermal model were then used as new boundary conditions for the arcjet flow solver. Three cases were studied at a mass flow rate of 0.1g/s. The applied currents were 60A, 100A, and 130A. Heat flux distributions corre-

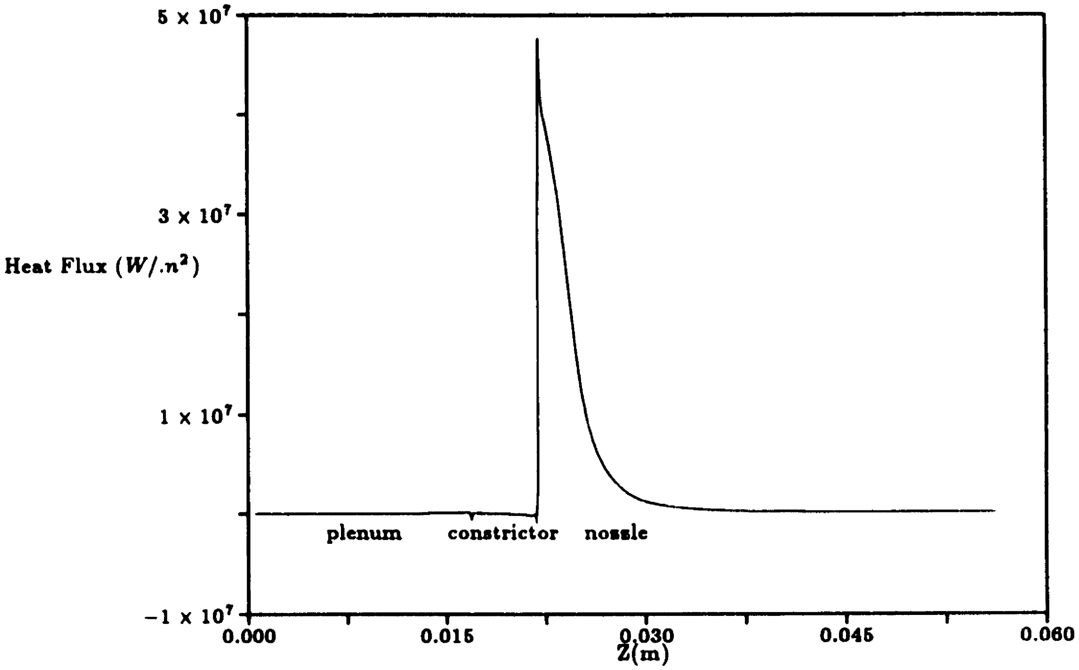

Figure 7.6: Anode Model Verification: Heat Flux to Anode from Baseline Case Flow Simulation Results ($\dot{m}$ = 0.1g/s, I=100A)

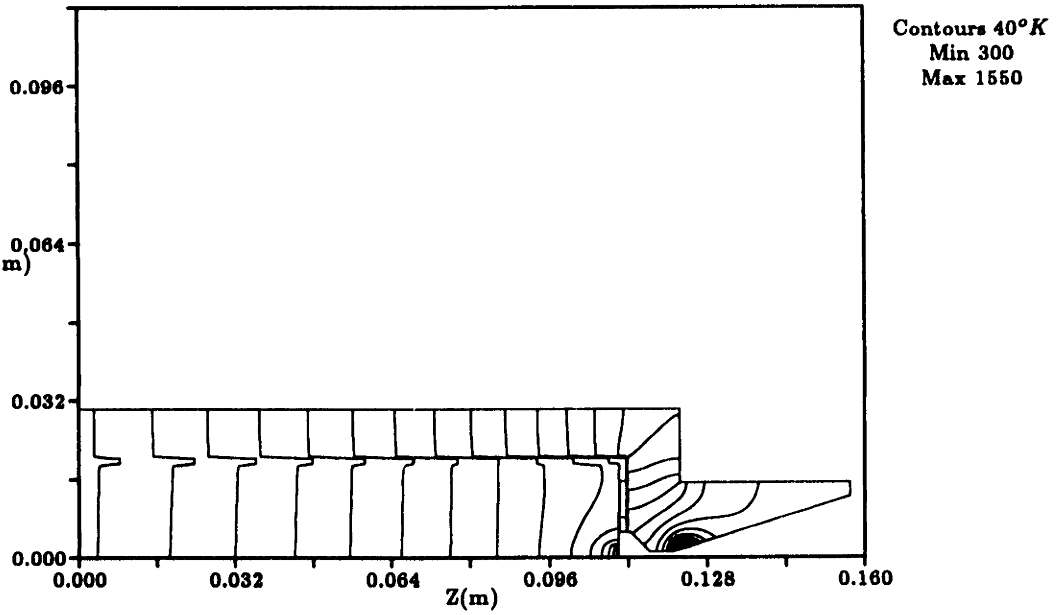

Figure 7.7: Anode Model Verification: Temperature Distribution for Baseline Case Heat Flux

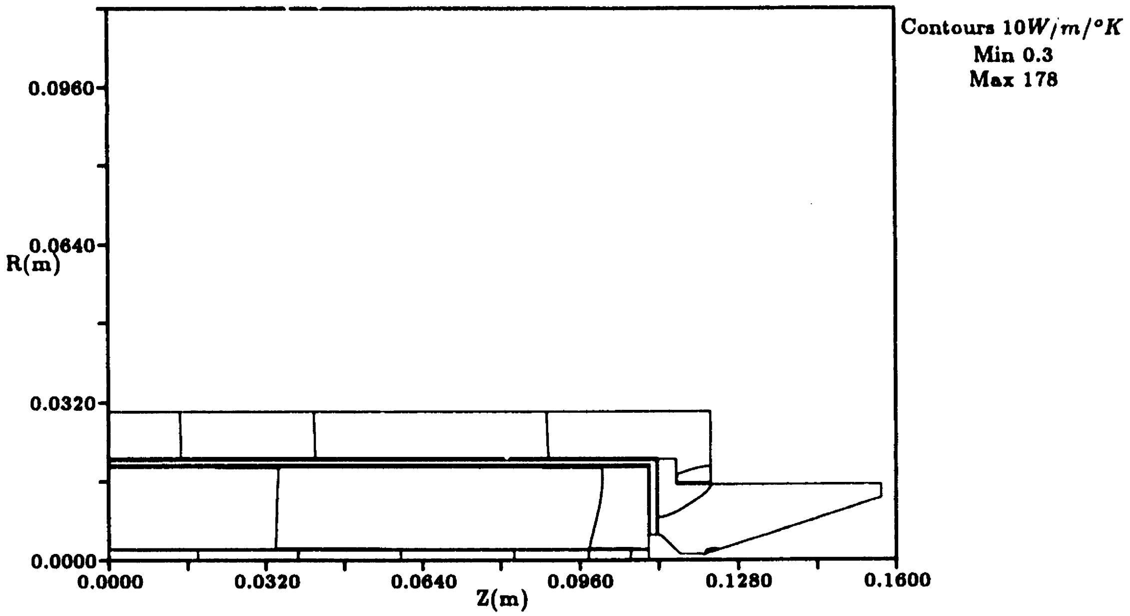

Figure 7.8: Anode Model Verification: Thermal Conductivity Distribution for Baseline Case Heat Flux

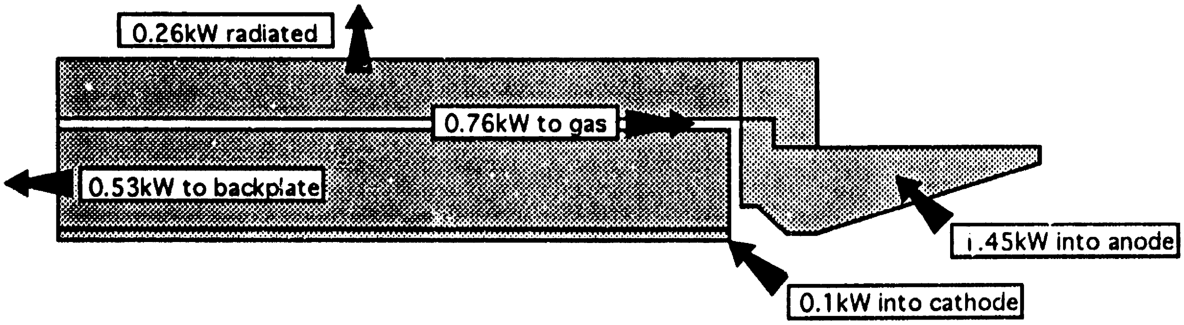

Figure 7.9: Anode Model Verification: Heat Flow Diagram

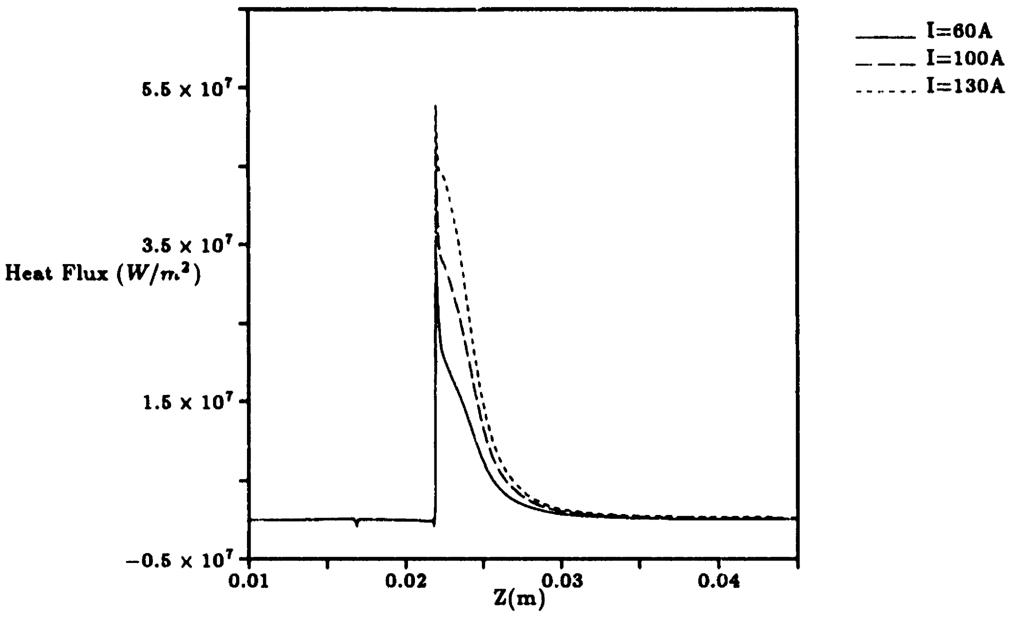

Figure 7.10: Heat Flux to Anode at $\dot{m}$ = 0.1g/s for Three Applied Currents

sponding to the three cases are plotted in Figure 7.10. This figure demonstrates that for a given mass flow rate the increase in current produces a change in the magnitude but not in the shape of the heat flux distribution.

The anode thermal model yields thruster assembly temperature distributions for these cases which are all qualitatively similar to that pictured in Figure 7.7 for the I=100A case. Temperature profiles along the inner anode surface for the three cases are shown in Figure 7.11. It can be seen that as the current is increased the temperature at all locations on the anode wall increases and the temperature maximum in the current attachment region becomes more pronounced. Table 7.1 lists key temperatures predicted by the anode heat balance model for each of the applied currents. In each case, the inlet gas temperature is less than the 1000°K specified as an original boundary condition of the flow simulation. Except for the current attachment regions, the anode wall temperature is everywhere less than the originally specified 1000 – 1100°K for the 60A case, about the same as the original boundary condition for the 100A case, and everywhere greater than the original boundary condition for the 130A case.

The net effect of incorporating the new temperature boundary conditions into the arcjet flow simulation is shown in the performance comparison of Figure 7.12. While the anode model shows closer agreement with experimentally measured specific impulse at low currents, it does worse in terms of accuracy at higher currents. For the 60A case the inlet and wall temperatures calculated by the heat balance model are 200 -- 300°K less than those specified in the original simulation, so the thrust and specific impulse are

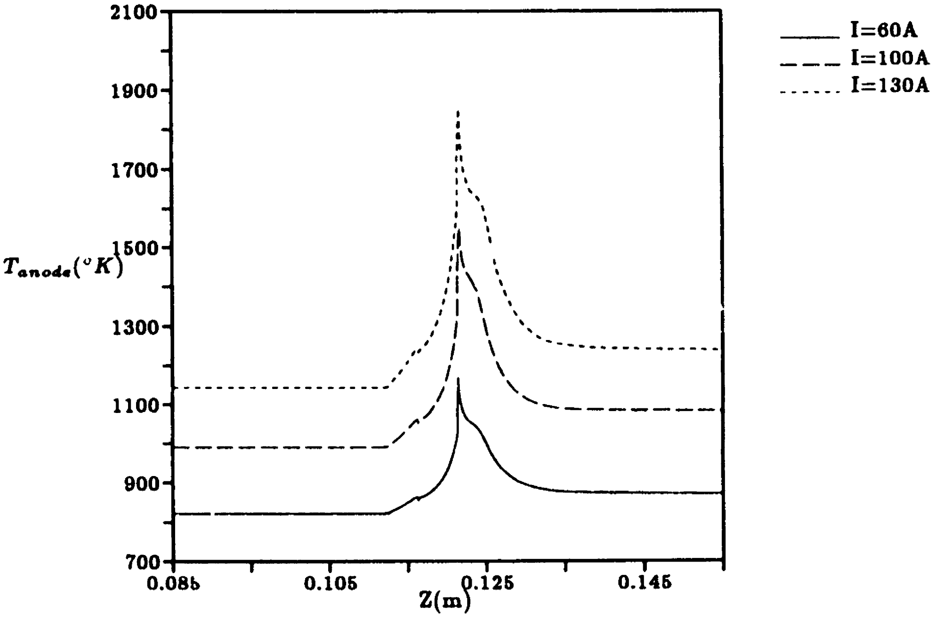

Figure 7.11: Anode Wall Temperature at $\dot{m} = 0.1$g/s for Three Applied Currents

Table 7.1: Temperatures Predicted by the Thermal Model for $\dot{m} = 0.1$g/s and Three Applied Currents

Location	**Temperature (^oK)**		
	I=60A	I=100A	I=130A
Inlet gas	710	825	910
Cathode root	825	875	950
Anode inlet	825	990	1140
Anode exit	875	1080	1240
Anode maximum	1170	1550	1850

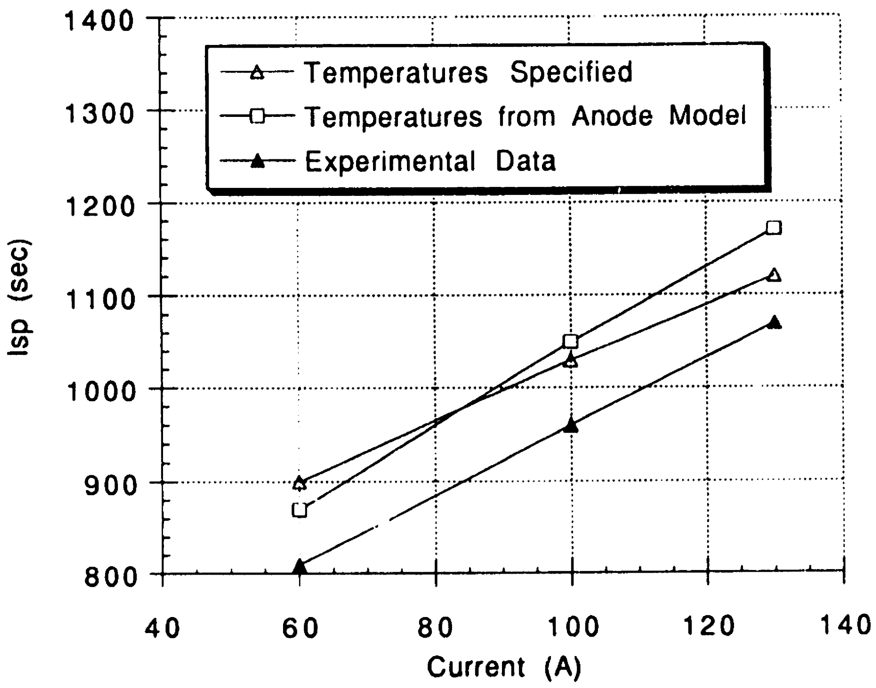

Figure 7.12: Effect of Anode Model Coupling on Predicted Performance for $\dot{m} = 0.1 \mathrm{g/s}$

lower. For the 100A case the lower inlet gas temperature predicted by the heat balance model is offset by increased heating of the flow by the anode wall in the constrictor exit and current attachment regions. This results in a specific impulse prediction which is slightly higher than that made with the original flow model boundary conditions. For the 130A case the inlet gas temperature is still lower than originally specified (910°K), but the anode wall temperatures are much higher (1150°K at the inlet and 1250°K at the exit, peaking at 1850°K). This produces a substantially higher performance prediction. The predicted voltages for these cases with a coupled anode thermal model are slightly lower than those calculated with the previously specified boundary temperatures, as shown in Table 7.2. This is due to preferential concentration of the anodic arc attachment in the region of elevated wall temperature.

In summary, use of the coupled heat balance model results in a slightly better prediction of voltage but no significant improvement in specific impulse prediction, leaving a gap of 5-10% between predicted and experimentally measured I_{sp}. An anode heat balance model such as the one described above, however, does have the additional potential to allow further thermal optimization of the thruster design.

Table 7.2: Predicted Voltages from Coupled Anode Thermal Model for $\dot{m} = 0.1$g/s at Three Applied Currents

Current(A)	Temperatures Specified	Temperatures from Anode Model
60	118	115
100	115	111
130	113	110

Chapter 8

Linearized Stability Analysis of the Anode Attachment Region

In the preceding chapters it has been shown that the model of this research can accurately predict the performance of an electrothermal arcjet using hydrogen propellant. Of some concern, however, is the fact that the anode attachment is still somewhat arbitrary in that the current is required to attach downstream of the constrictor. While this is expected to be the case for the experimental thruster considered, the fact that the model predicts initial current attachment wherever the initial boundary condition is set shows that the attachment process is still not completely understood. This has ramifications for the overall performance of the model since the location of the attachment zone has a direct effect on the discharge voltage and on the length of the core ohmic dissipation region, which relates to the amount of thermal energy transferred to the propellant. One possible reason for the difficulty in fixing the anode current attachment zone is that instabilities may be present in this region. This possibility is examined in this chapter by performing a linearized stability analysis on the relevant governing equations.

8.1 Governing Equations

In this analysis a conducting anode infinite in length and width is assumed, with current arriving normal to the surface as shown in Figure 8.1. It is also assumed that the heavy species do not participate in the instability, so their perturbations are small compared to perturbations of the electron and electrical variables. For simplicity, the degree of dissociation is assumed to be given in order to reduce the number of variables

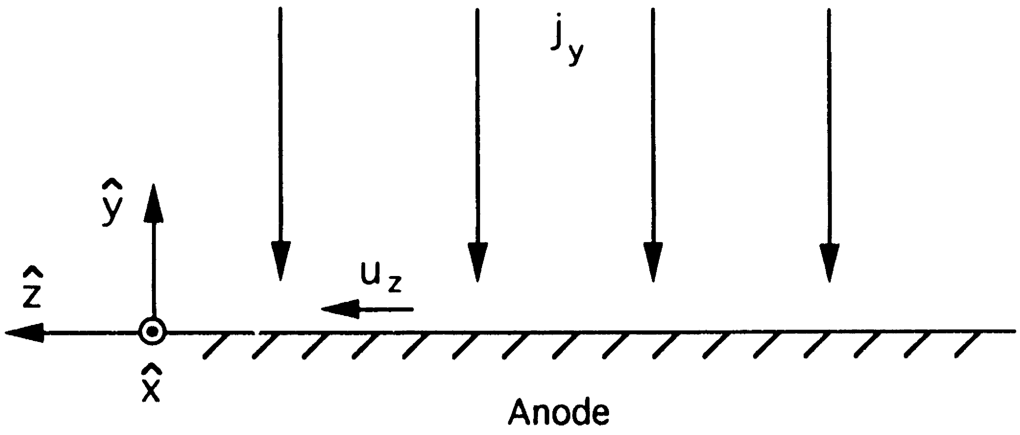

Figure 8.1: Coordinate System for the Linearized Stability Analysis

and allow a solution to be obtained. In addition, the flow velocity in the axial direction only is retained in order to model the effect of convection. The zeroth order solution of the governing equations is assumed to be uniform in space and time. Given these assumptions, the analysis is considered to be applicable in the region near the anode nozzle wall in an arcjet thruster, perhaps within 0.1 radii of the wall. The perturbation equations which govern this problem are the electron density equation, the electron energy equation, the electric potential equation, and the equation of state, together with Maxwell's equations which relate the electric potential to the current density.

The electron density equation is given by Equation 3.42. In this coordinate system it can be written as

$$\frac{\partial n_e}{\partial t}+\frac{\partial n_e u_z}{\partial z}-\nabla\cdot(D_a\nabla n_e)=\dot{n}_e=Rn_e\left(Sn_H-n_e^2\right). \tag{8.1}$$

The electron energy equation is given by Equation 3.83. Written in terms of temperature and neglecting radiation and dissociation loss rates, this equation becomes

$$\frac{3}{2}n_e k\left(\frac{\partial T_e}{\partial t}+u_z\frac{\partial T_e}{\partial z}\right)-\nabla\cdot(k_e\nabla T_e)=\frac{j^2}{\sigma}-3n_e k\left(T_e-T_g\right)\sum_r \nu_{er}$$
$$-\left(E_i+\frac{3}{2}kT_e\right)\dot{n}_e. \tag{8.2}$$

The equation for the electric potential is given by Equation 3.29. Neglecting electron pressure gradients, this equation becomes

$$\nabla^2\phi=-\nabla ln\sigma\cdot\nabla\phi. \tag{8.3}$$

Finally, the current density is defined as

$$\vec{j}=-\sigma\nabla\phi \tag{8.4}$$

and the equation of state is

$$p = n_e k T_e \left(1 + \frac{T_g}{T_e}\right) + (n_H + n_{H_2})\, k T_g. \tag{8.5}$$

8.2 Equilibrium Ionization Model

8.2.1 Derivation of the Dispersion Relation

First the limit of equilibrium ionization is considered. In this case, the electron density equation reduces to the Saha equation,

$$n_e^2 = S n_H = \overline{S} n_H T_e^{\frac{3}{2}} e^{-\frac{E_i}{kT_e}}, \tag{8.6}$$

where $\overline{S}$ is a constant. Letting $n_e = n_{e_0} + n_{e_1}$, $n_H = n_{H_0} + n_{H_1}$, and $T_e = T_{e_0} + T_{e_1}$, where $n_{e_1} \ll n_{e_0}$, $n_{H_1} \ll n_{H_0}$ and $T_{e_1} \ll T_{e_0}$, the perturbed electron density is then given by

$$\frac{n_{e_1}}{n_{e_0}} = \frac{1}{2}\left[\frac{n_{H_1}}{n_{H_0}} + X\frac{T_{e_1}}{T_{e_0}}\right], \tag{8.7}$$

where

$$X = \frac{E_i}{kT_{e_0}} + \frac{3}{2}. \tag{8.8}$$

From the equation of state, for $p \approx$const. and neglecting perturbations of n_{H_2} implies that

$$\frac{n_{H_1}}{n_{H_0}} = -\frac{n_{e_0} T_{e_0}}{n_{H_0} T_g}\left[\frac{n_{e_1}}{n_{e_0}}\left(1 + \frac{T_g}{T_{e_0}}\right) + \frac{T_{e_1}}{T_{e_0}}\right]. \tag{8.9}$$

This expression, together with Equation 8.7 gives

$$\frac{n_{e_1}/n_{e_0}}{T_{e_1}/T_{e_0}} = \frac{1}{2}\frac{\left(X - \frac{\alpha_0\theta_0}{\Delta-\alpha_0}\right)}{\left(1 + \frac{\alpha_0\theta_0}{\Delta-\alpha_0}\left(1 + \frac{1}{\theta_0}\right)\right)} = N, \tag{8.10}$$

where $\Delta = \frac{n_H+n_e}{n_H+n_e+2n_{H_2}}$ is the dissociation fraction, $\alpha = \frac{n_e}{n_H+n_e+2n_{H_2}}$ is the ionization fraction, and θ is the ratio of the electron temperature to the heavy species temperature.

The electric potential equation can be linearized as follows. The results of Chapter 5 indicate that the ionization fraction in the current attachment region near the anode is very low (10^{-5} to 10^{-4}), so the electron - molecular hydrogen collision frequency dominates over the electron - atomic hydrogen and coulomb collision frequencies. Consequently, using the $e - H_2$ collision data, the electrical conductivity can be written as

$$\sigma = \overline{\sigma} n_e T_e^{-\frac{1}{4}}, \tag{8.11}$$

where $\overline{\sigma}$ is a constant. The perturbed potential equation is then given by

$$\nabla^2\phi_1 = \frac{j_{y0}}{\sigma_0}\left(\frac{1}{n_{e_0}}\frac{\partial n_{e_1}}{\partial y} - \frac{1}{4T_{e_0}}\frac{\partial T_{e_1}}{\partial y}\right) \tag{8.12}$$

since a zeroth order current exists only in the y-direction and $\frac{\partial \phi_0}{\partial y} = -\frac{j_{y0}}{\sigma_0}$.

In the electron temperature equation, again considering only electron - molecular hydrogen collisions,

$$E_l = 3n_e k\left(T_e - T_g\right)\nu_{eH_2} = 3n_e k\left(T_e - T_g\right)\overline{\nu}_{eH_2}T_e^{\frac{3}{2}} \tag{8.13}$$

where $\overline{\nu}_{eH_2}$ is a constant, and

$$\frac{j^2}{\sigma} = \sigma\vec{E}^2 = \overline{\sigma}n_e T_e^{-\frac{1}{4}}\left(\nabla\phi\right)^2. \tag{8.14}$$

Linearizing the electron temperature equation and using Equations 8.1 and 8.10, it is found that

$$\begin{aligned}\left(\frac{3}{2} + XN\right)n_{e_0}k\left(\frac{\partial\theta_1}{\partial t} + u_z\frac{\partial\theta_1}{\partial z}\right) - k_{e_0}\nabla^2\theta_1 - n_{e_0}kXND_a\nabla^2\theta_1 \\ = \overline{\sigma}n_{e_0}T_{e_0}^{-\frac{1}{4}}T_g^{-1}\left[\frac{j_{y0}^2}{\sigma_0^2}\left(N - \frac{1}{4}\right)\frac{\theta_1}{\theta_0} - 2\frac{j_{y0}}{\sigma_0}\frac{\partial\phi_1}{\partial y}\right] \\ - 3n_{e_0}k\left(1 - \frac{1}{\theta_0}\right)\overline{\nu}_{eH_2}T_{e0}^{\frac{3}{2}}\left(N + \frac{1}{1 - 1/\theta_0} + \frac{3}{2}\right)\theta_1,\end{aligned} \tag{8.15}$$

where again $\theta = \frac{T_e}{T_g}$.

We now have two linear equations in the perturbed electron temperature and the perturbed electric potential. Substituting for solutions of the form $(\theta_1, \phi_1) = (\hat{\theta}_1(y), \hat{\phi}_1(y))e^{i(\omega t + k_x x + k_z z)}$, these two equations can be rewritten as

$$D_H\frac{\partial^2\hat{\theta}_1}{\partial y^2} - \left[i\left(\omega + k_z u_z\right) + D_H k_\perp^2 - \frac{\left(N - \frac{1}{4}\right)}{\tau_D} + \frac{\left(N + \frac{1}{1-1/\theta_0} + \frac{3}{2}\right)}{\tau_C}\right]\hat{\theta}_1 = -\frac{2\theta_0\sigma_0}{j_{y0}\tau_D}\frac{\partial\hat{\phi}_1}{\partial y} \tag{8.16}$$

and

$$\frac{\partial^2\hat{\phi}_1}{\partial y^2} - k_\perp^2\hat{\phi}_1 = \frac{j_{y0}}{\sigma_0}\left(N - \frac{1}{4}\right)\frac{1}{\theta_0}\frac{\partial\hat{\theta}_1}{\partial y}, \tag{8.17}$$

where

$$D_H = \frac{k_{e0}}{\left(\frac{3}{2} + XN\right)n_{e_0}k} + \frac{XND_a}{\left(\frac{3}{2} + XN\right)} \tag{8.18}$$

is the heat diffusivity, $k_\perp^2 = k_x^2 + k_z^2$ is the wave vector tangent to the anode surface,

$$\tau_D = \left(\frac{\overline{\sigma}T_{e_0}^{-\frac{5}{4}}}{\left(\frac{3}{2} + XN\right)k}\frac{j_{y0}^2}{\sigma_0^2}\right)^{-1} \tag{8.19}$$

is the dissipation time scale, and

$$\tau_C = \left[2\left(\frac{3}{\frac{3}{2}+XN}\right)\left(1-\frac{1}{\theta_0}\right)\overline{\nu}_{eH_2}T_{e_0}^{\frac{3}{2}}\right]^{-1} \tag{8.20}$$

is the collisional time scale. The 4th order characteristic equation for these two coupled equations is

$$D_H D^4 - \left[i\left(\omega + k_z u_z\right) + 2D_H k_\perp^2 + \frac{\left(N-\frac{1}{4}\right)}{\tau_D} + \frac{\left(N+\frac{1}{1-1/\theta_0}+\frac{3}{2}\right)}{\tau_C}\right] D^2$$

$$+ \left[i\left(\omega + k_z u_z\right) + D_H k_\perp^2 - \frac{\left(N-\frac{1}{4}\right)}{\tau_D} + \frac{\left(N+\frac{1}{1-1/\theta_0}+\frac{3}{2}\right)}{\tau_C}\right] = 0, \tag{8.21}$$

where $D = \frac{\partial}{\partial y}$.

The boundary conditions in the y-direction are as follows. Far from the anode wall, the perturbations are assumed to die out. At the wall, equipotential considerations require that the perturbed electric potential goes to zero and a zero gradient condition is imposed on the perturbed electron temperature, just as in the fluid model of the steady-state solution. The boundary conditions can be summarized explicitly as

$$\hat{\theta}_1\left(y \to \infty\right) = 0 \qquad \frac{\partial \hat{\theta}_1}{\partial y}\left(y = 0\right) = 0$$

and

$$\hat{\phi}_1\left(y \to \infty\right) = 0 \qquad \hat{\phi}_1\left(y = 0\right) = 0. \tag{8.22}$$

The characteristic equation (Eqn. 8.21) has four roots, two of which give exponentially increasing functions in y and are therefore ruled out by the boundary conditions. The boundary conditions at $y = 0$ require that the remaining two roots be equal. If these roots are equal but nonzero, then a dispersion relation results which always predicts stable behavior. If the roots are both zero, however, the following dispersion relation results:

$$i\left(\omega + k_z u_z\right) = \frac{\left(N-\frac{1}{4}\right)}{\tau_D} - D_H k_\perp^2 - \frac{\left(N+\frac{1}{1-1/\theta_0}+\frac{3}{2}\right)}{\tau_C}. \tag{8.23}$$

In the anode attachment region N is on the order of of 5 and θ_0 is on the order of 15. This implies that the perturbations are damped by heat diffusion and collisional energy transfer and unstable if neither of these effects are present. The effect of flow convection in the z-direction is that disturbances travel at the velocity u_z as they grow. Assuming $k_\perp$ is real, the imaginary part of the frequency can be written in nondimensional form as

$$\nu_i = -N + \frac{1}{4} + K_\perp^2 + \Gamma_C \left(N + \frac{1}{1 - 1/\theta_0} + \frac{3}{2} \right), \tag{8.24}$$

where $\nu_i = \omega_i \tau_D$, $K_\perp = k_\perp \sqrt{D_H \tau_D}$, and $\Gamma_C = \tau_D / \tau_C$.

This instability can be described as a "layer" ionization instability. The instability is present only in planes perpendicular to the direction of the current. Physically, the flow begins to go unstable when a localized increase in the electron temperature appears. This increases the local degree of ionization and the electrical conductivity, which then creates a current concentration. The current concentration increases the local rate of ohmic heating, which feeds the electron temperature increase, and an unstable situation results.

8.2.2 Results

Using the dispersion relation of Equation 8.24, the behavior of the instability can be examined numerically as a function of the steady-state zeroth order solution. Table 8.1 lists zeroth order parameters for the instability analysis based on the numerical solution for the baseline case arcjet simulation of Chapter 5, at a typical point near the anode in the current attachment region. For these baseline zeroth order parameters, Figure 8.2 plots ν_i vs. $K_\perp$ according to the dispersion relation. A negative value of ν_i indicates instability. With no damping, the model predicts an unstable mode with a growth rate of $|\nu_i| \approx 3$. Collisional energy transfer for these zeroth order conditions, however, is sufficient to completely damp out the instability. As shown in Figure 8.2, the magnitude of the collisional damping term is approximately ten times that of the ohmic dissipation source term, so that $\nu_i \approx 28$ even before heat diffusion is accounted for. It can therefore be concluded that under the zeroth order conditions of the baseline case specified in Table 8.1, the linearized equilibrium perturbation analysis predicts stability for all possible wave numbers.

The behavior of the instability is now examined with respect to variations in the zeroth order parameters. Figure 8.3 shows neutral stability lines ($\nu_i = 0$) as a function of electron temperature and current density, with the remaining zeroth order quantities given by their values in Table 8.1. Neutral stability lines are generated by identifying the minimum wave number necessary to ensure stability of the system. The system is unconditionally stable if no heat diffusion is necessary to guarantee stability. In Figure 8.3, the area above and to the right of each curve represents stability and the area below and to the left of each curve represents instability. Each curve describes the behavior of the system at a specific zeroth order current density. Clearly as the

Table 8.1: Baseline Zeroth Order Parameters from Numerical Arcjet Simulation

Electron Temperature (T_{e_0})	$20,000^o K$
Ionization Fraction (α_0)	1.0×10^{-4}
Current Density (j_{y_0})	$3 \times 10^6 A/m^2$
Gas Temperature (T_g)	$1100^0 K$
Dissociation Fraction (Δ)	5×10^{-3}
Density (ρ)	$6 \times 10^{-3} kg/m^3$

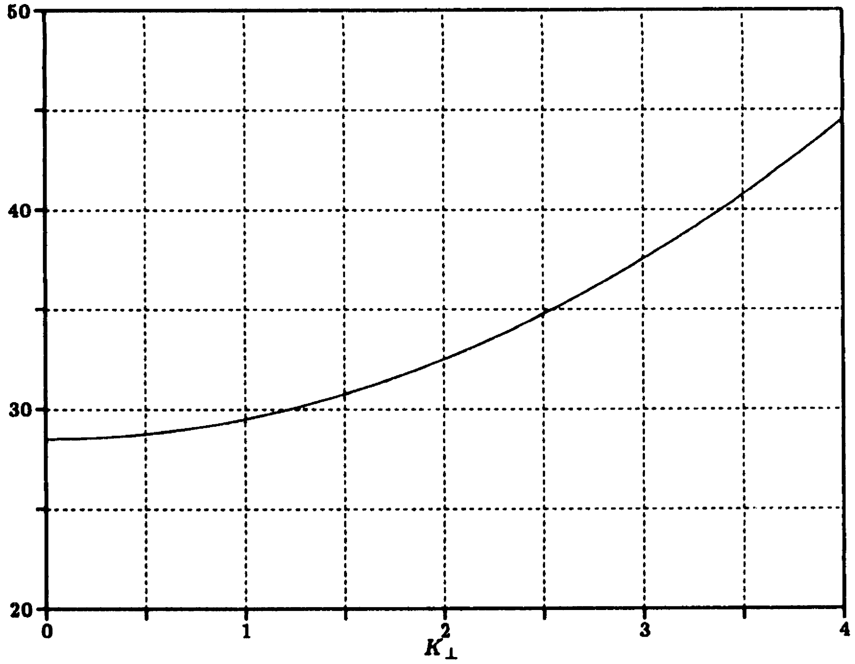

Figure 8.2: Nondimensional Imaginary Frequency versus Nondimensional Perpendicular Wave Number for the Baseline Zeroth Order Parameters with Equilibrium Ionization

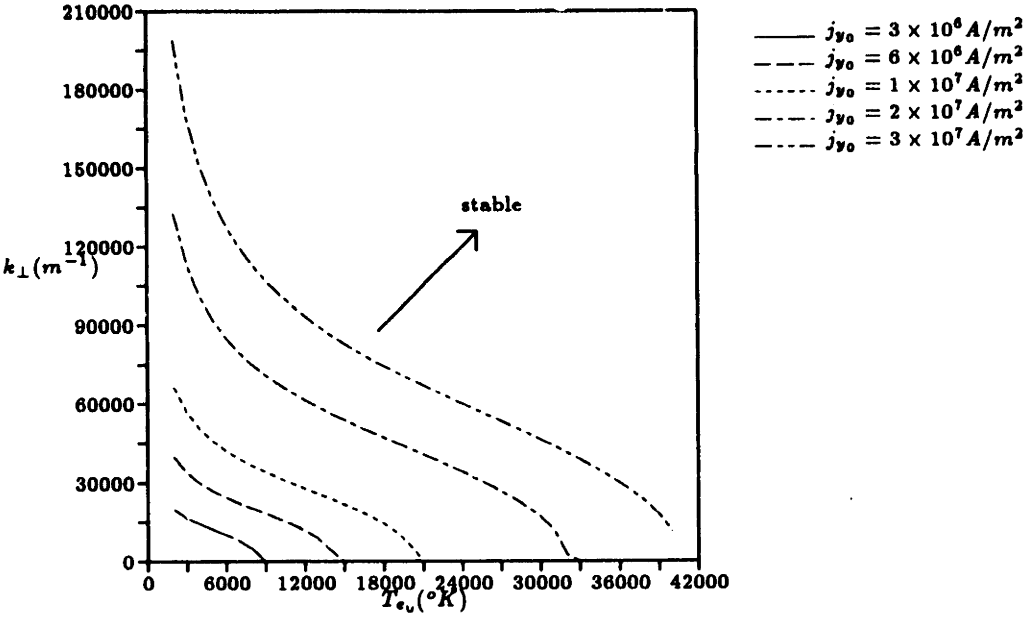

Figure 8.3: Neutral Stability Lines as a Function of the Zeroth Order Electron Temperature and Current Density with Equilibrium Ionization

zeroth order current density is increased the system becomes more unstable at all temperatures, because the source energy of the instability is increased. The system becomes less unstable as the zeroth order electron temperature is increased because the dissipation term is proportional to $T_{e_0}^{-1/4}$, while the collisional term is proportional to $T_{e_0}^{3/2}$, and the heat diffusion term is proportional to $T_{e_0}^{1/2}$ for thermal conduction and to T_{e_0} for ambipolar diffusion. The model predicts stability for the specified zeroth order current density $j_{y_0} = 3 \times 10^6 \frac{A}{m^2}$ when $T_{e_0} > 9000^\circ K$, and for the specified zeroth order electron temperature $T_{e_0} = 20,000^\circ K$ as long as $j_{y_0} < 9 \times 10^6 \frac{A}{m^2}$. For the baseline zeroth order conditions of this analysis, heat diffusion via ambipolar diffusion dominates over heat conduction. This is because the value of k_{e_0} is only about 0.02W/m/°K due to low ionization in the near-anode attachment region.

Similar curves for different values of the zeroth order ionization fraction are depicted in Figure 8.4. As can be seen in the figure, as the zeroth order ionization fraction decreases the system becomes more unstable. From the dispersion relation it is apparent that the dissipation term is proportional to α_0^{-2} while the damping terms are both independent of α_0. In terms of the physics, decreasing the background ionization fraction reduces the electrical conductivity of the gas, thus increasing the amount of energy dissipated by ohmic heating for a given applied current. At the same time, the collisional energy transfer rate and the electron thermal conductivity are decreased since fewer electrons are present. For the other specified zeroth order conditions in

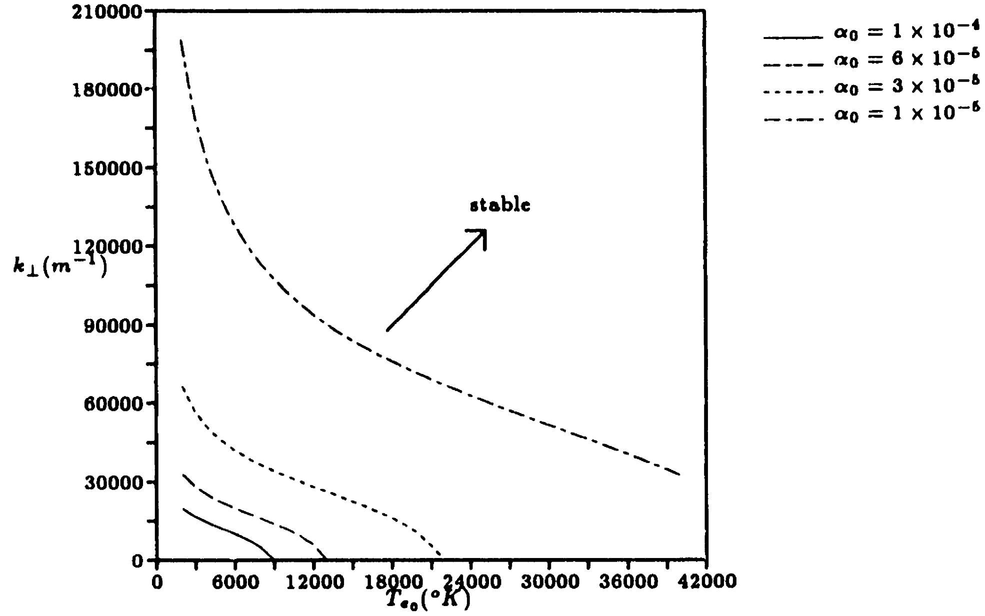

Figure 8.4: Neutral Stability Lines as a Function of the Zeroth Order Electron Temperature and Ionization Fraction with Equilibrium Ionization

Table 8.1, a minimum ionization fraction of 4×10^{-5} is required to guarantee stability at all wave numbers.

Neutral stability curves for different values of the background gas parameters from Table 8.1 are shown in Figures 8.5-8.7. In this model, over the range of expected values the gas temperature and dissociation fraction have minimal effects on the stability of the system. As can be seen in the first two figures, stability behavior varies only slightly from the baseline result when T_g is varied from $300^\circ K$ to $3000^\circ K$ and $\triangle$ is varied by two orders of magnitude. Increasing the gas temperature promotes instability by decreasing the energy collisionally transferred and decreasing the ambipolar diffusion coefficient, while increasing the dissociation fraction promotes instability by decreasing the frequency of energy-transferring collisions. The gas density, however, has a more pronounced effect on stability. From Figure 8.7, as the density is decreased the system becomes more unstable. Both the dissipation and heat diffusion terms of the dispersion relation are proportional to ρ^{-1} while the collisional term is proportional to ρ, so that for a given wave number the range of unstable behavior increases when the density decreases. Physically, decreasing the gas density decreases the collisional coupling between the electrons and the heavy species, which reduces collisional damping of the instability. At large wave numbers when the diffusion term is much larger than the collisional term, varying the density has no effect and all the curves in Figure 8.7 collapse onto one.

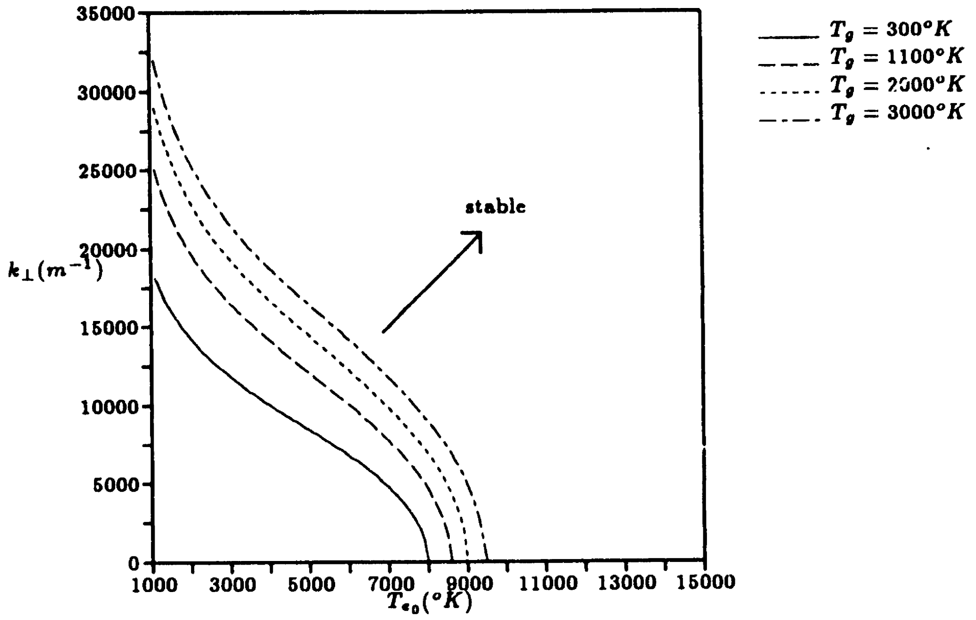

Figure 8.5: Neutral Stability Lines as a Function of the Zeroth Order Electron Temperature and Gas Temperature with Equilibrium Ionization

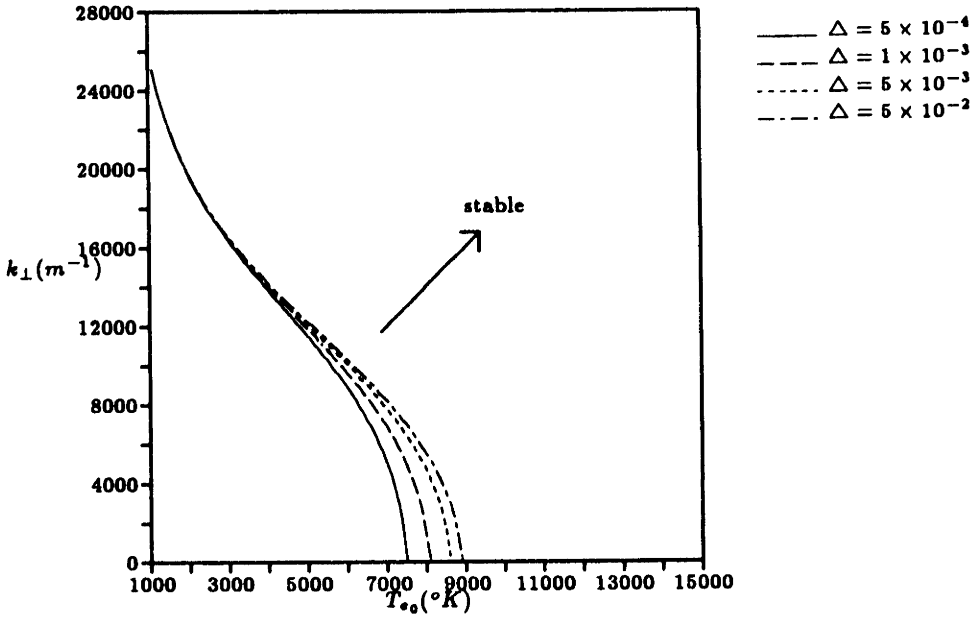

Figure 8.6: Neutral Stability Lines as a Function of the Zeroth Order Electron Temperature and Dissociation Fraction with Equilibrium Ionization

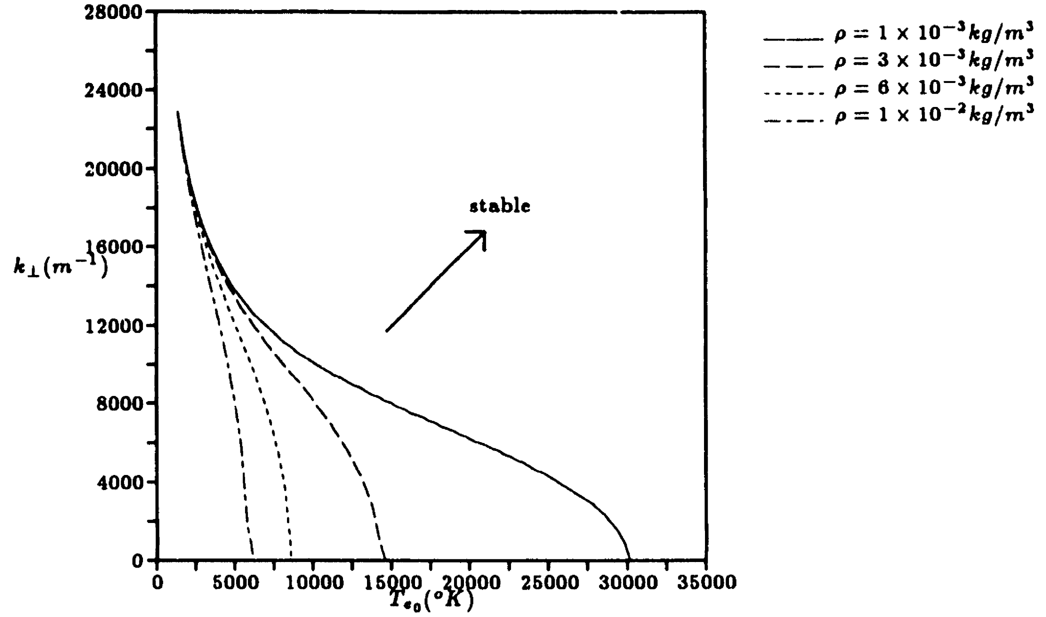

Figure 8.7: Neutral Stability Lines as a Function of the Zeroth Order Electron Temperature and Density with Equilibrium Ionization

In summary, the linearized perturbation analysis for the case of equilibrium ionization reveals an ionization instability driven by ohmic dissipation and damped by collisional energy transfer and heat diffusion. For zeroth order conditions corresponding to the near-anode region of the baseline TT1 arcjet simulation of Chapter 5, the model predicts stable behavior. This guarantee of stability, however, depends on the values of the zeroth order parameters. Increasing the current density, decreasing the ionization fraction, decreasing the electron temperature, or decreasing the density by less than an order of magnitude from the baseline parameters in Table 8.1 could lead to instability. In fact, if only one overall energy equation were used as in models developed prior to the research of this thesis, the simulated state of the near-anode flow would almost assuredly lie in the unstable region of this perturbation analysis. It is the use of a separate electron energy equation in this research which allows an elevated electron temperature to produce sufficient ionization, thermal conduction, and electrical conduction to ensure a stable mode of operation.

8.3 Nonequilibrium Ionization Model

8.3.1 Derivation of the Dispersion Relation

For the case of nonequilibrium ionization the electron density equation is given by Eqn. 8.1. Using the Hinnov-Hirshberg model of the recombination coefficient, this equation can be expanded as

$$\frac{\partial n_e}{\partial t}+\frac{\partial n_e u_z}{\partial z}-\nabla\cdot\left(D_a\nabla n_e\right)=\overline{R}T_e^{-\frac{9}{2}}n_e\left(\overline{S}T_e^{\frac{3}{2}}e^{-\frac{B_i}{kT_e}}n_H-n_e^2\right), \qquad (8.25)$$

where for hydrogen $\overline{R}=1.09\times10^{-20}m^6degK^{\frac{9}{2}}s^{-1}$ and $\overline{S}=2.42\times10^{21}m^{-3}degK^{-\frac{3}{2}}$. The perturbed form of the electron density equation is then given by

$$\frac{\partial n_{e_1}}{\partial t}+\frac{\partial n_{e_1}u_z}{\partial z}-\nabla\cdot\left(D_{a_0}\nabla n_{e_1}\right)$$

$$=\overline{R}\overline{S}T_{e_0}^{-3}n_{H_0}e^{-\frac{B_i}{kT_{e_0}}}\left[\left(1-\frac{n_{e_0}T_{e_0}}{n_{H_0}T_g}\right)n_{e_1}+\frac{n_{e_0}}{T_{e_0}}\left(X-\frac{9}{2}-\frac{n_{e_0}T_{e_0}}{n_{H_0}T_g}\right)T_{e_1}\right]$$

$$-\overline{R}T_{e_0}^{-\frac{9}{2}}\left[3n_{e_0}^2n_{e_1}-\frac{9}{2}\frac{n_{e_0}^3}{T_{e_0}}T_{e_1}\right]. \qquad (8.26)$$

Substituting for the ionization fraction and non-dimensional temperature, and defining the ionization and recombination time scales as

$$\tau_I=\left(\overline{R}\overline{S}T_{e_0}^{-3}n_{H_0}e^{-\frac{B_i}{kT_{e_0}}}\right)^{-1} \qquad (8.27)$$

and

$$\tau_R=\left(\overline{R}T_{e_0}^{-\frac{9}{2}}n_{e_0}^2\right)^{-1} \qquad (8.28)$$

respectively, the electron continuity perturbation equation can be rewritten as

$$\frac{\partial\alpha_1}{\partial t}+\frac{\partial\alpha_1u_z}{\partial z}-\nabla\cdot\left(D_{a_0}\nabla\alpha_1\right)$$

$$=\frac{1}{\tau_I}\left[\left(1-\frac{\alpha_0\theta_0}{\Delta-\alpha_0}\right)\alpha_1+\frac{\alpha_0}{\theta_0}\left(X-\frac{9}{2}-\frac{\alpha_0\theta_0}{\Delta-\alpha_0}\right)\theta_1\right]-\frac{1}{\tau_R}\left[3\alpha_1-\frac{9}{2}\frac{\alpha_0}{\theta_0}\theta_1\right]. \qquad (8.29)$$

The electric potential equation for the nonequilibrium case is identical to that of the equilibrium case, and is given by Eqn. 8.12. In terms of α and θ, the equation is

$$\nabla^2\phi_1=\frac{j_{y_0}}{\sigma_0}\left(\frac{1}{\alpha_0}\frac{\partial\alpha_1}{\partial y}-\frac{1}{4\theta_0}\frac{\partial\theta_1}{\partial y}\right). \qquad (8.30)$$

For the case of nonequilibrium ionization the electron temperature equation is given by Eqn. 8.2. Using the previously-defined time scales and non-dimensional variables, the perturbed form of this equation is given by

$$\frac{\partial\theta_1}{\partial t}+u_z\frac{\partial\theta_1}{\partial z}-D_H\nabla^2\theta_1=\frac{1}{\tau_D}\left[\frac{\theta_0}{\alpha_0}\alpha_1-\frac{1}{4}\theta_1-\frac{2\theta_0\sigma_0}{j_{y_0}}\frac{\partial\phi_1}{\partial y}\right]$$

$$-\frac{1}{\tau_c}\left[\frac{\theta_0}{\alpha_0}\alpha_1+\left(\frac{3}{2}+\frac{1}{1-\frac{1}{\theta_0}}\right)\theta_1\right]$$

$$-\frac{2X}{3\tau_I}\left[\left(1-\frac{\alpha_0\theta_0}{\Delta-\alpha_0}\right)\frac{\theta_0}{\alpha_0}\alpha_1+\left(X+\frac{3}{2X}-\frac{9}{2}-\frac{\alpha_0\theta_0}{\Delta-\alpha_0}\right)\theta_1\right]$$

$$+\frac{2X}{3\tau_R}\left[3\frac{\theta_0}{\alpha_0}\alpha_1-\left(\frac{9}{2}-\frac{3}{2X}\right)\theta_1\right]. \qquad (8.31)$$

We now have three second order linear differential equations in the perturbed ionization fraction, electron temperature, and electric potential. Again substituting for solutions of the form $(\alpha_1,\phi_1,\theta_1)=(\hat{\alpha}_1(y),\hat{\phi}_1(y),\hat{\theta}_1(y))e^{i(\omega t+k_x x+k_z z)}$, these three equations can be rewritten as

$$-D_a\frac{\partial^2\hat{\alpha}_1}{\partial y^2}+\left[i\left(\omega+k_z u_z\right)+D_a k_\perp^2-\frac{1}{\tau_I}\left(1-\frac{\alpha_0\theta_0}{\Delta-\alpha_0}\right)+\frac{3}{\tau_R}\right]\hat{\alpha}_1$$

$$-\left[\frac{1}{\tau_I}\left(X-\frac{9}{2}-\frac{\alpha_0\theta_0}{\Delta-\alpha_0}\right)-\frac{9}{2\tau_R}\right]\frac{\alpha_0}{\theta_0}\hat{\theta}_1=0, \qquad (8.32)$$

$$\frac{\partial^2\hat{\phi}_1}{\partial y^2}-k_\perp^2\hat{\phi}_1=\frac{j_{y0}}{\sigma_0}\left(\frac{1}{\alpha_0}\frac{\partial\hat{\alpha}_1}{\partial y}-\frac{1}{4\theta_0}\frac{\partial\hat{\theta}_1}{\partial y}\right), \qquad (8.33)$$

and

$$-D_H\frac{\partial^2\hat{\theta}_1}{\partial y^2}+\left[i\left(\omega+k_z u_z\right)+D_H k_\perp^2+\frac{1}{4\tau_D}+\frac{1}{\tau_C}\left(\frac{3}{2}+\frac{1}{1-\frac{1}{\theta_0}}\right)\right.$$

$$\left.+\frac{2X}{3\tau_I}\left(X+\frac{3}{2X}-\frac{9}{2}-\frac{\alpha_0\theta_0}{\Delta-\alpha_0}\right)+\frac{2X}{3\tau_R}\left(\frac{9}{2}-\frac{3}{2X}\right)\right]\hat{\theta}_1$$

$$+\left[-\frac{1}{\tau_D}+\frac{1}{\tau_C}+\frac{2X}{3\tau_I}\left(1-\frac{\alpha_0\theta_0}{\Delta-\alpha_0}\right)-\frac{2X}{\tau_R}\right]\frac{\theta_0}{\alpha_0}\hat{\alpha}_1=-\frac{2\theta_0\sigma_0}{j_{y0}\tau_D}\frac{\partial\hat{\phi}_1}{\partial y}. \qquad (8.34)$$

These equations can be combined into one 6th order characteristic equation similar to Eqn. 8.21 which is satisfied by the following boundary conditions:

$$\hat{\alpha}_1\left(y\to\infty\right)=0 \qquad D_a\frac{\partial\hat{\alpha}_1}{\partial y}\left(y=0\right)=\hat{\alpha}_1 v_B\left(y=0\right),$$

$$\hat{\phi}_1\left(y\to\infty\right)=0 \qquad \hat{\phi}_1\left(y=0\right)=0,$$

and

$$\hat{\theta}_1\left(y\to\infty\right)=0 \qquad \frac{\partial\hat{\theta}_1}{\partial y}\left(y=0\right)=0. \qquad (8.35)$$

The boundary condition on the perturbed ionization fraction at $y=0$ comes from a balance between the flux of ions arriving at the sheath edge by ambipolar diffusion and the flux of ions arriving at the wall by virtue of their thermal energy at the Bohm velocity. The remaining boundary conditions are identical to those of the equilibrium case. The 6th order polynomial which represents Eqns.8.33-8.34 can be reduced to a 3rd order polynomial after elimination of the roots which grow exponentially in y and therefore violate the boundary conditions. Unfortunately, because the solution of an arbitrary 3rd order polynomial is significantly more complicated than that of a 2nd order polynomial no further simplifications are readily apparent, as was the case for the equilibrium stability analysis.

The stability of a purely layered geometry independent of y, however, can be examined, and it was this geometry which was in fact found to be the unstable mode in the equilibrium ionization case. This leads to a dispersion relation of the form

$$-\left(\omega + k_z u_z\right)^2 + i\left(\omega + k_z u_z\right) B + C = 0, \tag{8.36}$$

where B and C are assumed to be real functions of the perpendicular wave number and the zeroth order parameters. Setting $\omega = \omega_r + i\omega_i$ implies that the imaginary frequency has one or two roots depending on the values of the constants B and C:

$$\omega_i = \frac{B}{2} \quad \left(B^2 < 4C\right) \qquad and \qquad \omega_i = \frac{B}{2} \pm \frac{\sqrt{B^2 - 4C}}{2} \quad \left(B^2 > 4C\right). \tag{8.37}$$

The requirement for stability is that all imaginary roots must be positive. As in the equilibrium ionization case, flow convection in the z-direction causes perturbations to travel at velocity u_z as they grow.

8.3.2 Results

Using the zeroth order parameters listed in Table 8.1, the nondimensional imaginary frequencies which solve Eqn. 8.37 are plotted versus nondimensional perpendicular wave number in Figure 8.8. The behavior of the roots is identical to that of the equilibrium case (Figure 8.2), although the magnitude of ν_i is smaller. The smallest root has a magnitude of $\nu_i = 1.6 \times 10^{-2}$ when $K_\perp = 0$, implying unconditional stability for these zeroth order conditions.

Neutral stability lines as a function of zeroth order electron temperature and current density are shown for the nonequilibrium ionization case in Figure 8.9. As expected, increasing the zeroth order current density causes the system to become more unstable. In this case, however, the unstable region expands at different rates depending on the zeroth order electron temperature. For electron temperatures less than $3000^o K$ and in the range $8000 - 40,000^o K$, the expansion of the unstable region with increasing current density is readily apparent. In the other two regions, though, neutral stability lines are relatively unaffected by varying j_{y_0}. The difference between this behavior and the simpler behavior seen in the results of the equilibrium ionization stability analysis

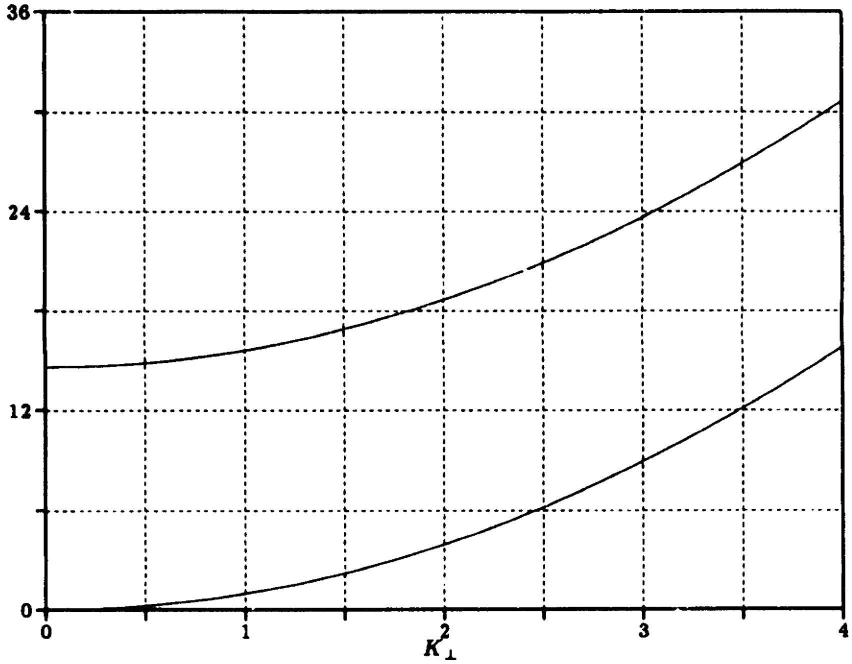

Figure 8.8: Nondimensional Imaginary Frequency versus Nondimensional Perpendicular Wave Number for the Baseline Zeroth Order Parameters with Nonequilibrium Ionization

lies in the balance between the ionization and recombination processes. At very low electron temperatures, the system becomes more unstable because ohmic dissipation dominates over the other effects. Between $3000^\circ K$ and $8000^\circ K$ system behavior is dominated by recombination. Within this electron temperature range, no matter how much energy is channeled into the system there is no mechanism by which charge carriers can be produced to form current concentrations and instability. This does not necessarily mean that a flow under these conditions is stable, however. One possibility is that without the capability for ionization, current could be diverted from the region and stability ensured. But that diverted current has to go somewhere because decreased current density in one region means increased current density in another. A second possibility in this recombination-dominated region is that the electron temperature would be increased by ohmic dissipation until enough electrons could be produced to carry the required current. Consequently the region $8000^\circ K < T_{e_0} < 40,000^\circ K$ is most indicative of the expected system stability behavior under these zeroth order conditions. At very high electron temperatures, higher than any expected in the near-anode current attachment zone, the effect on stability of increased current is much diminished. This is because collisional damping and heat diffusion increase greatly at higher temperatures while the form of the recombination coefficient causes net ionization to decrease. The nonequilibrium model predicts stability for the specified zeroth order current density

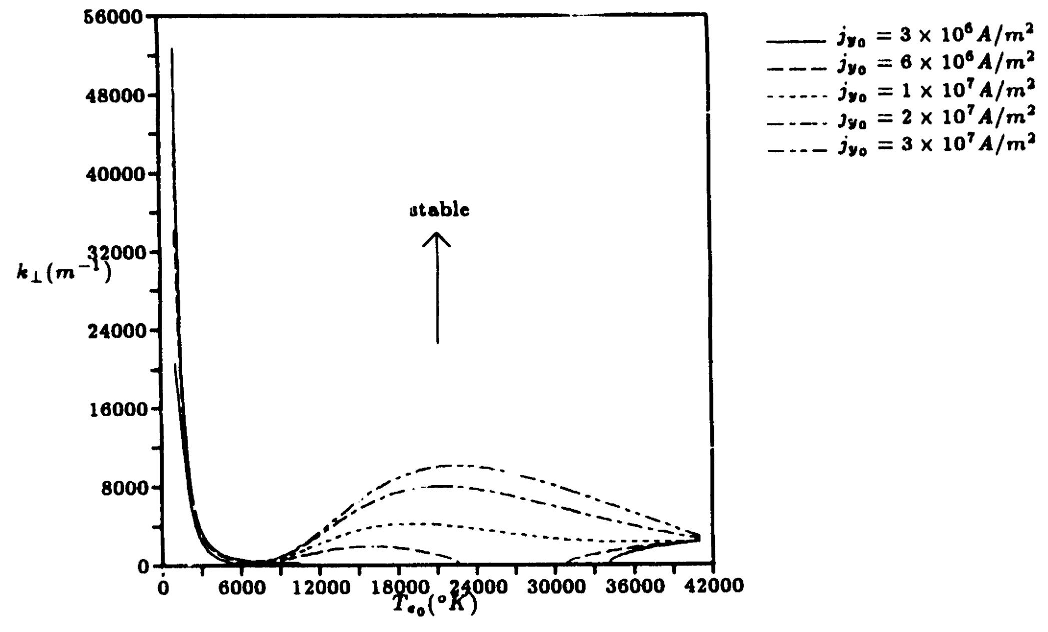

Figure 8.9: Neutral Stability Lines as a Function of the Zeroth Order Electron Temperature and Current Density with Nonequilibrium Ionization

$j_{y_0} = 3 \times 10^6 \frac{A}{m^2}$ when $11{,}000^\circ K < T_{e_0} < 34{,}000^\circ K$, and for the specified zeroth order electron temperature $T_{e_0} = 20{,}000^\circ K$ provided that $j_{y_0} < 5 \times 10^6 \frac{A}{m^2}$.

The effect of the zeroth order ionization fraction on lines of neutral stability is shown in Figure 8.10. Apart from the region where recombination is dominant, the system becomes more unstable as the ionization fraction is decreased. Increasing α_0 decreases the electrical conductivity of the gas and therefore increases the ohmic dissipation, and decreases the collisional energy transfer and the thermal conductivity since fewer electrons are present, thereby enhancing instability. For the other specified zeroth order parameters, a minimum ionization fraction of 5×10^{-5} is required to insure stable behavior at all wave numbers.

Neutral stability curves for different values of the background gas parameters are shown in Figures 8.11-8.13. Stability is basically insensitive to variations in the gas temperature, except at electron temperatures above $30{,}000^\circ K$. At these high electron temperatures two things happen: (1) the collisional energy transfer becomes large enough that increasing the gas temperature significantly decreases the energy transferred; and (2) the ambipolar diffusivity, which now scales as $T_g^{-\frac{1}{2}}$, also decreases with increasing gas temperature. Both of these effects make the system less stable as the gas temperature is increased. Figure 8.12 shows that as the dissociation fraction is increased the system becomes less stable, particularly at high electron temperatures. This occurs because increasing the dissociation fraction decreases the collisional energy

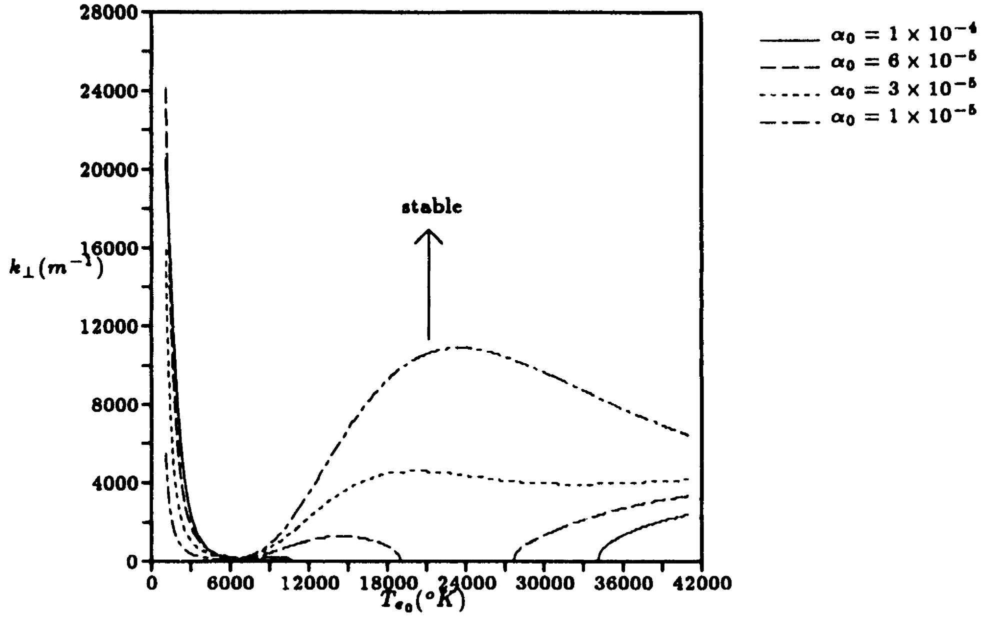

Figure 8.10: Neutral Stability Lines as a Function of the Zeroth Order Electron Temperature and Ionization Fraction with Nonequilibrium Ionization

transferred and increases the rate of ionization. For the wide range of T_g and $\triangle$ examined, there is no effect on the stability of the baseline zeroth order state of Table 8.1. The effect of varying the density on stability behavior is shown in Figure 8.13. At electron temperatures above the those of recombination-dominated region, decreasing the density promotes instability. For electron temperatures below $6000^o K$ the reverse is true. Collisional energy transfer is reduced relative to dissipation and heat diffusion when the density is decreased, resulting in a more unstable situation. At the same time, the net ionization term is reduced relative to the ambipolar diffusion term in the electron density equation when the density is decreased, which promotes stability. The former effect dominates at high electron temperatures while the latter dominates at low electron temperatures. In all, the density effects are much milder in the nonequilibrium case than in the equilibrium case. This is due to the incorporation into the dispersion relation of a density equation which is dependent on the diffusion and finite rate ionization processes rather than on the Saha equilibrium.

It has been shown that the stability analysis with nonequilibrium ionization produces results similar to those obtained with the equilibrium analysis. The difference lies in the balance between ionization and recombination in the electron density equation. Like the equilibrium model, the nonequilibrium model predicts unconditional stability for the baseline zeroth order state suggested by the results of Chapter 5. In the nonequilibrium case, however, it was found that system stability is somewhat more

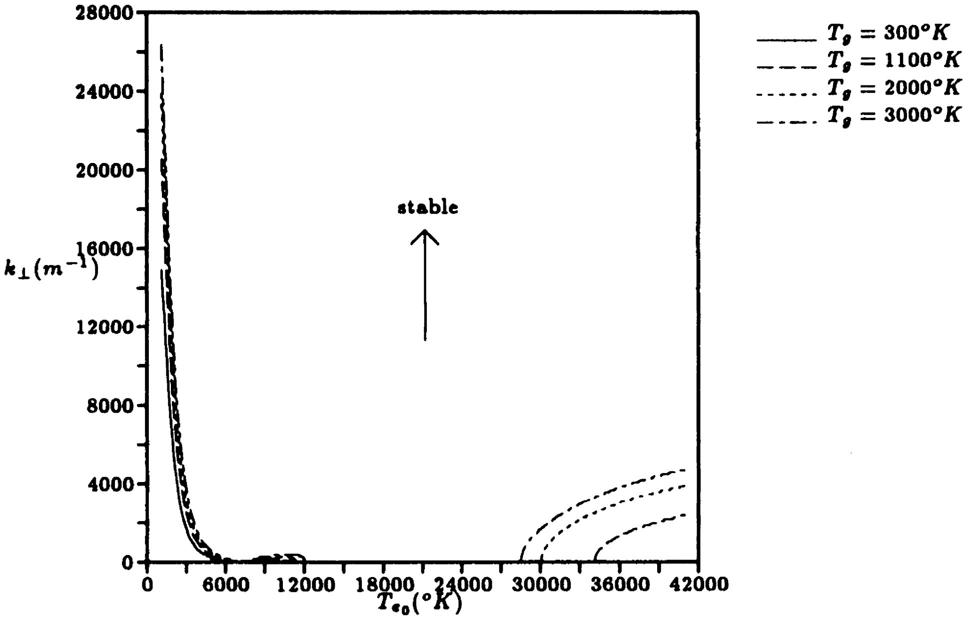

Figure 8.11: Neutral Stability Lines as a Function of the Zeroth Order Electron Temperature and Gas Temperature with Nonequilibrium Ionization

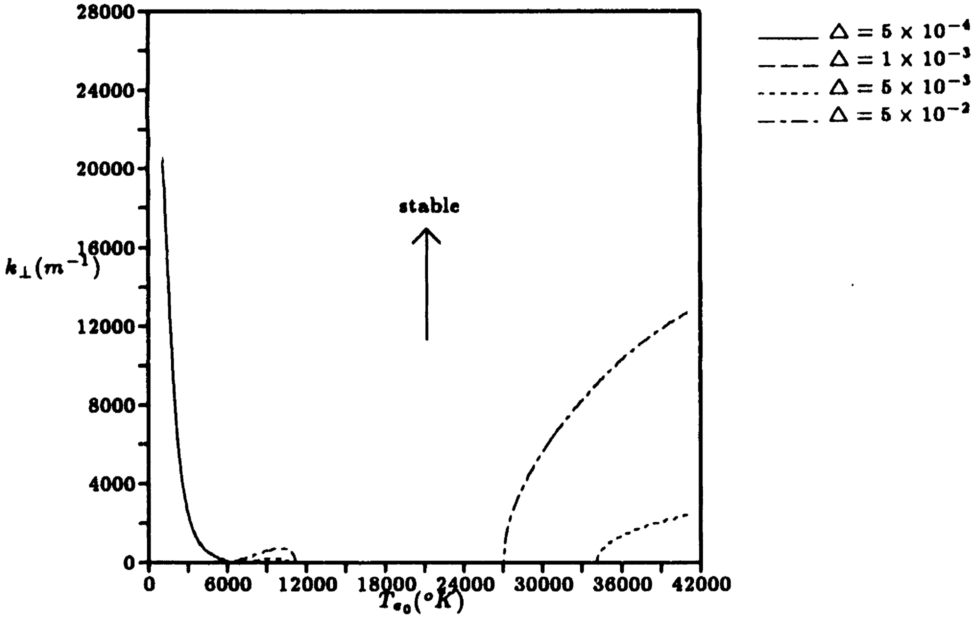

Figure 8.12: Neutral Stability Lines as a Function of the Zeroth Order Electron Temperature and Dissociation Fraction with Nonequilibrium Ionization

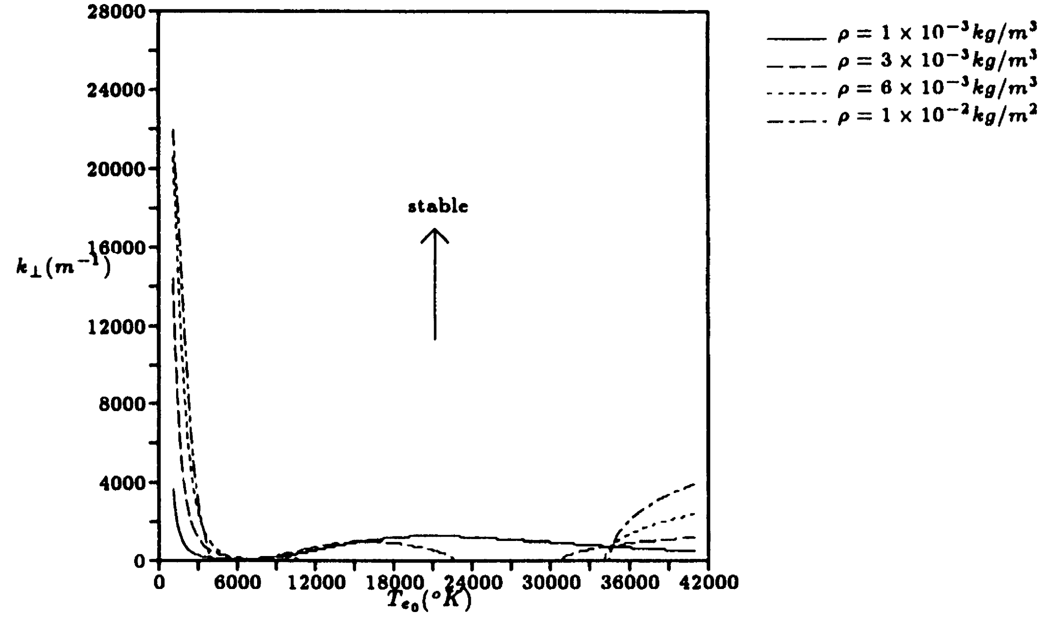

Figure 8.13: Neutral Stability Lines as a Function of the Zeroth Order Electron Temperature and Density with Nonequilibrium Ionization

sensitive to variations in the zeroth order parameters.

The analysis of this chapter has shown that given the predicted state of the flow in the near-anode current attachment region by the arcjet simulation of this research, the arc is physically stable to perturbations perpendicular to the arc direction in the nonequilibrium case, and stable irrespective of direction in the equilibrium case. Stability is relatively unaffected by changes in the gas parameters, while variations in the zeroth order electron temperature and current density can lead to instability within a reasonable range of values. Additional analyses beyond the scope of this thesis could be performed in the future to confirm these results in a broader sense. These analyses might include solving the complete dispersion relations with numerical techniques or examining the effects of different boundary conditions such as a resistive layer near the anode wall.

Chapter 9

Conclusions

9.1 Achievements of this Research

This thesis has made a significant contribution to the state of the art in arcjet thruster modeling. A numerical simulation has been constructed which contains nearly all of the relevant physical processes in an arcjet thruster, including separate electron and heavy species temperatures, nonequilibrium dissociation and ionization, ambipolar diffusion, viscosity and heat conduction, ohmic dissipation, elastic and inelastic collisional energy transfer, continuum radiation, and accurate, local evaluation of the transport coefficients. A self-consistent set of boundary conditions have also been developed in conjunction with the derivation of the governing equations. Previous models did not include all of the aforementioned effects, and in particular no previous model successfully incorporated separate equations for the electron and heavy species temperatures. As a result, past simulations could not provide particularly accurate predictions of thruster performance, and in fact the accuracy of experimental comparisons was tied to a number of undesirable empirical assumptions and heuristic fixes. The only significant empirical assumption made in the model of this research is that the current must attach to the anode wall downstream of the constrictor exit.

Results of the arcjet simulation of this thesis are compared to experimental measurements of the German TT1 radiation-cooled thruster using hydrogen propellant. Predicted specific impulse is within 5-10% of experiment for a range of mass flow rates and applied currents. The accuracy of previous simulations varied from 5-25% even with empirical fixes not contained in the model of this research. Predicted discharge voltage is also compared to experimental measurements, and is found to be within 2-3% to 10-12% of experiment depending on the mass flow rate. Previous simulations, including some of the most advanced, produced voltage predictions which differed from experiment by as much as 20-50%. Perhaps the most impressive demonstration of the accuracy of this model is the comparison between the predicted electron temperature distribution at the nozzle exit and that measured by emission spectroscopy. The two temperature profiles are found to be similar in shape and nearly identical in magnitude. This type of prediction is much more difficult to make accurately than one of thrust or voltage, since it requires realistic simulation of the interior flow as opposed to matching of bulk parameters. The close experimental comparisons mentioned here suggest that the simulation is correctly accounting for the necessary physical effects.

Including the necessary physics in the model of this research has led to the most important contribution of this thesis to the field, namely the discovery of the mechanism by which current passes between the ionized arc core and the relatively cool outer flow to the anode wall. The problem is that the temperature of the outer flow is too low to produce enough ionization to allow the current to be conducted across it from the arc core to the anode. Previous numerical simulations either disregarded the anode current attachment process entirely or used some fix to resolve the issue, such as an artificially high conductivity or an ionization fraction floor. Self-consistent, realistic simulation of this conduction process is absolutely necessary, however, if accurate predictions of the voltage and power transmitted to the wall are to be made. The significant advance of the model of this thesis is the separation of the electron and heavy species temperatures. While it is true that the gas temperature is relatively low in the outer flow, the results of this research show that ohmic dissipation from the arc current produces very high electron temperatures in the outer flow as well as in the inner arc core. These elevated electron temperatures in the outer gas flow produce sufficiently high nonequilibrium dissociation and ionization rates to provide enough charge carriers for self-sustaining conduction of the current across the outer flow. Ambipolar diffusion of ions and electrons outward from the arc core also aids in this process. Self-consistent modeling of the arc attachment process allows the simulation to produce very good predictions of discharge voltage, the only qualification being that the upstream boundary of the anodic arc attachment is prescribed.

Being axisymmetric in formulation, the arcjet flow model is also useful in that it provides a detailed picture of the flow inside the thruster. This level of detail has brought to light a number of interesting effects, including the effect of swirl on arcjet operation, the fluid dynamic "plug" nature of the high temperature, low density arc core, the velocity reduction which occurs in the nozzle expansion due to viscous forces, and the magnitude of the near-anode and near-cathode voltage drops. In addition, the relative importance of each of the included physical effects is evaluated in the inner and outer regions of the thruster in order to determine which effects should be retained and which may be neglected. The distribution of energy in the exit plane is also calculated in order to gain some insight into the various frozen flow losses. Finally, having a detailed map of the flow inside the arcjet proves to be useful in explaining performance trends observed by varying the applied current and mass flow rate.

In order to obtain a more accurate estimate of the inlet gas and anode wall temperatures, a thermal model of the thruster assembly is developed which includes the electrodes, insulator, and propellant gas passages. The heat flux to the anode wall calculated by the flow solver is used as an input to the thermal model, which then solves for the temperature distribution in the thruster assembly. By using the temperature distributions produced by the heat balance model as new boundary conditions in the flow solver, a more consistent overall simulation is achieved. It is found that the inlet gas temperature is approximately $100 - 200^{o}$K lower than the anode temperature at the inlet, and that a temperature maximum occurs on the anode wall where the current attaches in the nozzle. While incorporation of the anode thermal model does not significantly improve overall performance predictions, it does provide a useful tool for making thruster assembly design improvements.

An additional contribution of this thesis is the evaluation of the stability of the near-anode attachment region by performing a linearized analysis of the governing equations. Equilibrium and nonequilibrium cases are studied, and a layer type of ionization instability is identified perpendicular to the direction of the current. The instability is activated by a local increase in the electron temperature, which then increases the local ionization fraction and conductivity, thereby creating a current concentration. This current concentration increases the local rate of ohmic heating, which then feeds the electron temperature increase to produce a runaway situation. The instability is fed by the current and damped by ambipolar diffusion, heat conduction, and collisional energy transfer. The near-anode region is shown to be stable for zeroth order parameters taken from the numerical arcjet simulation, but it becomes less stable when the current increases or when the electron temperature, ionization fraction, density, or gas temperature decrease. In particular, the near-anode conditions which would be predicted by a single temperature arcjet model would lead to instability based on this linearized analysis.

The results of this thesis have shown which physical processes must be incorporated in an arcjet model in order to properly simulate the flow. Any realistic arcjet model must include separate equations for the electron and heavy species temperatures, a least in the outer region of the flow where collisional coupling is low. Nonequilibrium models of dissociation and ionization are particularly important in the outer flow, where electron impact dissociation and ionization provide most of the charge carriers for electrical conduction between the ionized arc core and the anode wall. Equilibrium chemistry models may suffice in the high temperature, high pressure core of the arc in the constrictor, but probably not in the high speed, low pressure flow of the nozzle. Ambipolar diffusion in the radial direction has been shown to be important in terms of both anode arc attachment and overall performance. Due to the steep velocity gradients developed in the constrictor of an arcjet thruster, a viscous model is necessary to insure that the dominant viscous smoothing which occurs in the nozzle is properly accounted for. Since transport phenomena have been shown to play a major role in arc development and anode attachment as well as in the determination of overall performance, reasonably accurate models of the transport coefficients must be retained in a simplified arcjet model in order to maintain predictive accuracy. Effects such as radiation, the Lorentz force, axial conduction and diffusion, and azimuthal swirl could be neglected in a simpler model than the one developed in this research.

9.2 Recommendations for Further Work

There are a number of issues relating to arcjet research which can be explored by extending the work of this thesis. First and foremost is the determination of the arc attachment location on the anode surface. The results presented in this thesis have illuminated a mechanism by which the current in the central arc can penetrate the outer cooler gas layer and attach in a self-sustaining manner to the anode wall. The extreme upstream boundary of that attachment region, however, must be fixed a priori or else the simulation predicts an attachment location which disagrees with experimental results. It is believed that the solution to this problem lies in the physics of the anode sheath. A detailed analysis of this sheath layer might reveal the necessary physics which could be included in the arcjet simulation via boundary conditions or a coupled model to more self-consistently represent the anodic arc attachment process. The existence of a resistive layer near the anode surface might also explain how the attachment location is determined. The resolution of this problem is of great importance because the location of the anode current attachment zone influences not only the discharge voltage, and therefore the efficiency, but also the magnitude and distribution of the power transmitted to the anode block.

The second most important future task is the extension of the simulation to include other propellants, such as nitrogen, ammonia, and hydrazine. Hydrogen yields the highest specific impulse of any propellant, but it requires new technology storage tanks and feed systems to be developed and tested in order to be used as a long-term arcjet fuel in space. Ammonia and hydrazine, both easily storable and currently being used in space applications, are more desirable for near-term missions. Therefore, the development of a code which includes all the physics of this thesis and yet which is applicable to these other propellants is of considerable interest to the advanced propulsion community. The program is already being modified to simulate nitrogen propellant, since the only changes required concern collisional rate parameters and atomic weight corrections. Extension of the program to the simulation of ammonia or hydrazine, however, would represent a substantial increase in code complexity and computational intensiveness. The simulation would have to account for at least four more species than are currently incorporated, and probably more. In addition, many more collision cross-sections would have to be tabulated and calculation of the transport properties would become more complicated. This would likely render the program too slow to be usable on any of the computer workstations available today. Consequently, improvements in the way the code computes nonequilibrium species distributions and transport properties would have to be made in order for the simulation of ammonia and hydrazine to become feasible.

This last point brings up the issue of the computational speed and efficiency of the arcjet program. The numerical implementation of the model developed in this thesis was done in a relatively simple and robust way in order to more easily generate converged solutions. Now that the internal flow is more understood and the relevant physical processes have been identified, a new arcjet code can be written which takes advantage of advanced numerical techniques. The speed and efficiency of the program could be improved by utilizing adaptive gridding, multiple scales, partially or wholly implicit methods, and methods which use knowledge of local flow conditions to select the most appropriate integration technique. By decreasing the program run time, improvements such as these would allow extensions to the code to be incorporated and make optimization studies quicker to perform.

In its present form additional runs of the arcjet program could be made to assess its capacity to simulate other hydrogen arcjets currently being tested. These include the German TT1 water-cooled arcjet, the 1kW NASA Lewis arcjet, and the various configurations of the NASA Lewis 15kW arcjet. New measurements of plume properties have been made for the NASA Lewis arcjets, and these measurements could be used as additional consistency checks for the arcjet simulation. Future experimental diagnostics may yield even more opportunities for comparison. Of particular interest would be measurements of temperature, number density, and velocity at the exit plane and measurements of temperature and number density in the constrictor region. Detailed measurements of the temperature on the anode inner and outer surfaces could be used in conjunction with the anode heat balance model to compare the predicted and experimental current distributions on the constrictor and nozzle walls.

Some additional physics could be incorporated into the model, such as a thermal conductivity component which takes into account the transport of line radiation. A study of the degree of thermal nonequilibrium in the nozzle and how it might be accounted for, particularly for the case of nitrogen or nitrogen-based propellants, would also be desirable. Finally, a more complete instability analysis of the near-anode arc attachment zone could be undertaken in order to conclusively determine the stability of that region. Advanced numerical techniques would be required to allow solution of the full dispersion relations for this purpose. The ultimate goal of any analytical or numerical model is to identify the important physics of a particular system and then to consistently simulate those physical processes in order to accurately predict the real behavior of the system. By continually improving arcjet models such as the one developed in this thesis, additional physical insight can be gained and experimental thrusters can be optimized in terms of performance and thermal efficiency.

Bibliography

[1] C. Agte and J. Vacek, "Tungsten and Molybdenum", NASA Technical Translation F-135, Washington, 1963.

[2] D.A. Anderson, J.C. Tannehill, and R.H. Pletcher, *Computational Fluid Mechanics and Heat Transfer*, Hemisphere Publishing Corp., New York, 1984.

[3] M. Andrenucci et al., "Development of a Computer Programme for the Analysis of Arcjet Nozzles", IEPC 91-113, AIDAA/AIAA/DGLR/JSASS 22nd International Electric Propulsion Conference, Viareggio, Italy, October 1991.

[4] G.S. Bahn, *Reaction Rate Compilation for the H-O-N System*, Gordon and Breach, New York, 1968.

[5] G.K. Batchelor, *An Introduction to Fluid Mechanics*, Cambridge University Press, 1985, p.543-550.

[6] D.R. Bates, A.E. Kingston, and R.W.P. McWhirter, "Recombination Processes Between Electrons and Atomic Ions", Proc. Royal Society A, Vol.267; Vol.270, 1962.

[7] V.A. Belov, "Viscosity of Partially Ionized Hydrogen", High Temperature, Vol.5, 1967, p.31-6.

[8] R.J. Biasca, *Chemical Kinetics of Scramjet Propulsion*, S.M. Thesis, Massachusetts Institute of Technology, September 1988.

[9] J.A. Bittencourt, *Fundamentals of Plasma Physics*, Pergamon Press, New York, 1986.

[10] D. Brezing, "Transport Properties of Hydrogen", AIAA Journal Vol.3, No. 8, August 1965, p.1422-7.

[11] R.S. Brokaw, "Approximate Formulas for the Viscosity and Thermal Conductivity of Gas Mixtures", Journal of Chemical Physics, Vol.29, No.2, August 1958, p.391-7.

[12] J.W. Buddenberg and C.R. Wilke, "Calculation of Gas Mixture Viscosities", Industrial and Engineering Chemistry, Vol. 41, No. 7, 1949, p.1345-7.

[13] J.M. Burgers, *Flow Equations for Composite Gases*, Academic Press, New York, 1969.

[14] G.W. Butler, B.A. Kashiwa, and D.Q. King, "Numerical Modeling of Arcjet Performance", AIAA 90-1474, AIAA 21st Fluid Dynamics, Plasma Dynamics, and Lasers Conference, Seattle, June 1990.

[15] G.W. Butler and D.Q. King, "Single and Two Fluid Simulations of Arcjet Performance", AIAA 92-3104, AIAA/SAE/ASME/ASEE 28th Joint Propulsion Conference, Nashville, July 1992.

[16] Carborundum Company, "Combat Boron Nitride Technical Data", Niagara Falls, New York, 1991.

[17] G. Cruciani, W.D. Deininger, and C. Petagna, "Development of a 1N, Radiatively Cooled Arcjet", AIAA 90-2536, AIAA/DGLR/JSASS 21st International Electric Propulsion Conference, Orlando, July 1990.

[18] G. Cruciani and W.D. Deininger, "Development Testing of a 1kW Class Arcjet Thruster", AIAA 92-3114, AIAA/SAE/ASME/ASEE 28th Joint Propulsion Conference, Nashville, July 1992.

[19] F.M. Curran and S. Nakanishi, "Low Power dc Arcjet Operation with Hydrogen/Nitrogen Propellant Mixtures", AIAA 86-1505, AIAA/ASME/SAE/ASEE 22nd Joint Propulsion Conference, Huntsville, June 1986.

[20] F. M. Curran and T.W. Haag, "An Extended Life and Performance Test of a Low-Power Arcjet", NASA Technical Memorandum 100942, July 1988.

[21] F.M. Curran, A.J. Sovie, and T.W. Haag, "Arcjet Nozzle Design Impacts", NASA Technical Memorandum 102050, May 1989.

[22] F.M. Curran, T.W. Haag, and J.F. Raquet, "Arcjet Cathode Phenomena", NASA TM 102099, JANNAF Propulsion Meeting, Cleveland, May 1989.

[23] F.M. Curran and C.J. Sarmiento, "Low Power Arcjet Performance Characterization", AIAA 90-2578, AIAA/DGLR/JSASS 21st International Electric Propulsion Conference, Orlando, July 1990.

[24] F.M. Curran, D.H. Manzella, and E.J. Pencil, "Performance Characterization of a Segmented Anode Arcjet Thruster", AIAA 90-2582, AIAA/DGLR/JSASS 21st International Electric Propulsion Conference, Orlando, July 1990.

[25] C.F. Curtiss and J.O. Hirschfelder, "Transport Properties of Multicomponent Gas Mixtures", Journal of Chemical Physics, Vol.17, June 1949, p.550-5.

[26] W.D. Deininger, T.J. Pivirotto, and J.R. Brophy, "Effect of Nozzle and Cathode Configuration on Arcjet Performance", AIAA 87-1082, AIAA/DGLR/JSASS 19th International Electric Propulsion Conference, Colorado Springs, May 1987.

[27] W.D. Deininger, A. Chopra, and K.D. Goodfellow, "Cathode Erosion Tests for 30kW Arcjets", AIAA 89-2264, AIAA/ASME/SAE/ASEE 25th Joint Propulsion Conference, Monterey, July 1989.

[28] R.S. Devoto, "Transport Properties of Ionized Monatomic Gases", Physics of Fluids, Vol. 9, No. 6, June 1966, p.1230-40.

[29] R.S. Devoto, "Transport Coefficients of Partially Ionized Hydrogen", Journal of Plasma Physics, Vol. 2, 1968, p.617-31.

[30] H.W. Drawin and P. Felenbok, *Data for Plasmas in Local Thermodynamic Equilibrium*, Gauthier-Villars, Paris, 1965.

[31] A.C. Ducati, H. Pumpal, J. Meltzer, E. Muehlberger, J.P. Todd, and H. Waltzer, "1-kw Arcjet-Engine System-Performance Test", Journal of Spacecraft, Vol.1, No.3, May-June 1964, p.327-332.

[32] M.Giles, Assistant Professor of Aeronautics and Astronautics, Massachusetts Institute of Technology, private communication, May 1992.

[33] B. Glocker, M. Autweter-Kurtz, T.M. Goelz, H.L. Kurtz, and H.O. Schrade, "Medium Power Arcjet Thruster Experiments", AIAA 90-2531, AIAA/DGLR/JSASS 21st International Electric Propulsion Conference, Orlando, July 1990.

[34] B. Glocker, H.O. Schrade, and P.C. Sleziona, "Numerical Prediction of Arcjet Performance", AIAA 90-2612, AIAA/DGLR/JSASS 21st International Electric Propulsion Conference, Orlando, July 1990.

[35] B. Glocker, Th. Rosgen, and A. Laxander, "Medium Power Arcjet Analysis and Experiments", IEPC 91-016, AIDAA/AIAA/DGLR/JSASS 22nd International Electric Propulsion Conference, Viareggio, Italy, October 1991.

[36] B. Glocker and M. Auweter-Kurtz, "Radiation Cooled Medium Power Arcjet Experiments and Thermal Analysis", AIAA 92-3834, AIAA/SAE/ASME/ASEE 28th Joint Propulsion Conference, Nashville, July 1992.

[37] B. Glocker and M. Auweter-Kurtz, "Numerical and Experimental Constrictor Flow Analysis of a 10kW Thermal Arcjet", AIAA 92-3835, AIAA/SAE/ASME/ASEE 28th Joint Propulsion Conference, Nashville, July 1992.

[38] P.A. Gnoffo, R.N. Gupta, and J.L. Shinn, "Conservation Equations and Physical Models for Hypersonic Air Flows in Thermal and Chemical Nonequilibrium", NASA Technical Paper 2867, February 1989.

[39] T. Gölz, M. Autweter-Kurtz, H.L. Kurtz, and H.O. Schrade, "High Power Arcjet Thruster Experiments", IEPC 91-072, AIDAA/AIAA/DGLR/JSASS 22nd International Electric Propulsion Conference, Viareggio, Italy, October 1991.

[40] D.A. Gonzales and P.C. Varghese, "Vibrational Relaxation and Dissociation in Nitrogen", AIAA 91-1370, AIAA 26th Thermophysics Conference, Honolulu, June 1991.

[41] K.D. Goodfellow and J.E. Polk, "Throttling Capability of a 30-kW Class Ammonia Arcjet", AIAA 91-2577, AIAA/SAE/ASME/ASEE 27th Joint Propulsion Conference, Sacramento, June 1991.

[42] N.T. Grier, "Calculation of Transport Properties and Heat Transfer Parameters of Dissociating Hydrogen", NASA TN D-1406, October 1962.

[43] N.T. Grier, "Calculation of Transport Properties of Ionizing Atomic Hydrogen", NASA TN D-3186, April 1966.

[44] T. Haag and F. Curran, "High Power Hydrogen Arcjet Performance", AIAA 91-2226, AIAA/SAE/ASME/ASEE 27th Joint Propulsion Conference, Sacramento, June 1991.

[45] T.L. Hardy and F.M. Curran, "Low Power dc Arcjet Operation with Hydrogen/Nitrogen/Ammonia Mixtures", AIAA 87-1948, AIAA/SAE/ASME/ASEE 23rd Joint Propulsion Conference, San Diego, June 1987.

[46] D.J. Heimerdinger, *An Approximate Two-Dimensional Analysis of an MPD Thruster*, S.M. Thesis, Massachusetts Institute of Technology, June 1984.

[47] D.J. Heimerdinger, *Fluid Mechanics in a Magnetoplasmadynamic Thruster*, Doctoral Thesis, Massachusetts Institute of Technology, January 1988.

[48] P.G. Hill and C.R. Peterson, *Mechanics and Thermodynamics of Propulsion*, Addison-Wesley, Reading, Mass., 1970.

[49] E. Hinnov and J.G. Hirschberg, "Electron-Ion Recombination in Dense Plasmas", Physical Review, Vol.125, No.3.

[50] J.O. Hirschfelder, C.F. Curtiss, and R.B. Bird, *Molecular Theory of Gases and Liquids*, John Wiley & Sons, Inc, New York, 1954.

[51] W.A. Hoskins, A.E. Kull, and G.W. Butler, " Measurement of Population and Temperature Profiles in an Arcjet Plume", AIAA 92-3240, AIAA/SAE/ASME/ASEE 28th Joint Propulsion Conference, Nashville, July 1992.

[52] Y. Itikawa, "Momentum-Transfer Cross Sections for Electron Collisions with Atoms and Molecules", Atomic Data and Nuclear Tables Vol. 21, No. 1, January 1978.

[53] M.Y. Jaffrin, "Shock Structure in a Partially Ionized Gas", The Physics of Fluids, Vol.8, No.4, April 1965.

[54] R.K. Janev, W.D. Langer, K. Evans Jr., and D.E. Post Jr., *Elementary Processes in Hydrogen-Helium Plasmas*, Springer-Verlag, New York, 1987.

[55] S.W. Janson, R.P. Welle, D.R. Schulthess, and R.B. Cohen, "Arcjet Plume Characterization Part II: Optical Diagnostic Results", AIAA 90-2643, AIAA/DGLR/JSASS 21st International Electric Propulsion Conference, Orlando, July 1990.

[56] R.R. John, M. Chen, J. Connors, and J. Megrue, "Arc Jet Performance - Experiment and Theory IV", ARS 2345-62, ARS Electric Propulsion Conference, Berkeley, March 1962.

[57] R.R. John, S. Bennett, L.A. Coss, M.M. Chen, and J.F. Connors, "Energy Addition and Loss Mechanisms in the Thermal Arc Jet Engine", AIAA 63-022, AIAA Electric Propulsion Conference, Colorado Springs, March 1963.

[58] R.R. John, J.F. Connors, and S. Bennett, "Thirty Day Endurance Test of a 30kw Arc Jet Engine", AIAA 63-274, AIAA Summer Meeting, Los Angeles, June 1963.

[59] D.Q. King and G.W. Butler, "Modeling and Measurement of N_2 Arcjet Performance", AIAA 90-2626, AIAA/DGLR/JSASS 21st International Electric Propulsion Conference, Orlando, July 1990.

[60] S.C. Knowles, W.W. Smith, F.M. Curran, and T.W. Haag, "Performance Characterization of a Low Power Hydrazine Arcjet", AIAA 87-1057, AIAA/DGLR/JSASS 19th International Electric Propulsion Conference, Colorado Springs, May 1987.

[61] S.C. Knowles, S.E. Yano, and R.S. Aadland, "Qualification and Life Testing of a Flight Design Hydrazine Arcjet System", AIAA 90-2576, AIAA/DGLR/JSASS 21st International Electric Propulsion Conference, Orlando, July 1990.

[62] P. Kovitya, D.A. Scott, and G.N. Haddad, "Two-dimensional Modelling of Plasma Torches", CSIRO Division of Applied Physics, Final Report for AWRA Contract No. 123, July 1988.

[63] H.L. Kurtz, D.M. Zube, B. Glocker, and M. Autweter-Kurtz, "Low Power Hydrazine Arcjet Thruster Study", AIAA 92-3116, AIAA/SAE/ASME/ASEE 28th Joint Propulsion Conference, Nashville, July 1992.

[64] P. Kutler, L. Sakell, and G. Aiello, "On the Shock-On-Shock Interaction Problem", AIAA 74-524, AIAA 7th Fluid and Plasma Dynamics Conference, Palo Alto, June 1974.

[65] D. Landrum and G. Candler, "Vibration-Dissociation Coupling in Nonequilibrium Flows", AIAA 91-0466, AIAA 29th Aerospace Sciences Meeting, Reno, January 1991.

[66] W.T. Langan, J.D. Cresswell, and W.G. Browne, "Effect of Ablation Products on Ionization in Hypersonic Wakes", AIAA Journal, Vol.3, No.12, December 1965.

[67] D.A. Lichtin, S.W. Janson, J.E. Pollard, D.R. Schulthess, and R.B. Cohen, "Arcjet Plume Characterization Part 1: Mass/Velocity Analyzer Results", AIAA 90-2642,

AIAA/DGLR/JSASS 21st International Electric Propulsion Conference, Orlando, July 1990.

[68] J.G. Liebeskind, R.K. Hanson, and M.A. Cappelli, "Velocity Measurements in a Hydrogen Arcjet Using LIF", AIAA 91-2112, AIAA/SAE/ASME/ASEE 27th Joint Propulsion Conference, Sacramento, June 1991.

[69] R.W. MacCormack, "The Effect of Viscosity in Hypervelocity Impact Cratering", AIAA 69-354, 1969.

[70] R.W. MacCormack, "Numerical Solution of the Interaction of a Shock Wave with a Laminar Boundary Layer", *Lecture Notes in Physics*, Vol.8, Springer-Verlag, 1971.

[71] R.W. MacCormack and B.S. Baldwin, "A Numerical Method for Solving the Navier-Stokes Equations with Application to Shock-Boundary Layer Interactions", AIAA 75-1, AIAA 13th Aerospace Sciences Meeting, Pasadena, January 1975.

[72] J.S. Mankins, W.J. Harris, E.A. O'Hair, L.L. Hatfield, and M. Kristiansen, "Comparison of Erosion of Various Cathode Materials in a 30kWe Class Arcjet", AIAA 92-3839, AIAA/SAE/ASME/ASEE 28th Joint Propulsion Conference, Nashville, July 1992.

[73] D.H. Manzella, F.M. Curran, R.M. Myers, and D.M. Zube, "Preliminary Plume Characteristics of an Arcjet Thruster", AIAA 90-2645, AIAA/DGLR/JSASS 21st International Electric Propulsion Conference, Orlando, July 1990.

[74] D.H. Manzella and M.A. Cappelli, "Vacuum Ultraviolet Absorption in a Hydrogen Arcjet", AIAA 92-3564, AIAA/SAE/ASME/ASEE 28th Joint Propulsion Conference, Nashville, July 1992.

[75] J.S. Martinez and G.W. Elverum, Jr., "A Method of Calculating the Performance of Liquid-Propellant Systems Containing the Species C, H, O, N, F, and One Other Halogen, with Tables Required; Thermochemical Properties to $6000^o K$", JPL Memorandum No. 20-121, December 1955.

[76] M. Martinez-Sanchez, Professor of Aeronautics and Astronautics, Massachusetts Institute of Technology, private communication, July 1992.

[77] M. Martinez-Sanchez and A. Sakamoto, "Simplified Analysis of Arcjet Thrusters", AIAA 93-1904, AIAA/ASME/SAE/ASEE 29th Joint Propulsion Conference, Monterey, June 1993.

[78] S.A. Miller, *Viscous and Diffusive Effects in Magnetoplasmadynamic Flows*, S.M. Thesis, Massachusetts Institute of Technology, June 1990.

[79] S.A. Miller, "Viscous and Diffusive Effects in MPD Flows, AIAA 90-2606, AIAA/DGLR/JSASS 21st International Electric Propulsion Conference, Orlando, July 1990.

[80] S.A. Miller and M. Martinez-Sanchez, "Viscous and Diffusive Effects in Electrothermal and MPD Arcjet Thrusters", IEPC 91-060, AIDAA/AIAA/DGLR/-JSASS 22nd International Electric Propulsion Conference, Viareggio, Italy, October 1991.

[81] M. Mitchner and C. Kruger, *Partially Ionized Gases*, John Wiley and Sons, New York, 1973.

[82] J.C. Morris, R.P. Rudis, and J.M. Yos, "Measurements of Electrical and Thermal Conductivity of Hydrogen, Nitrogen, and Argon at High Temperatures", Physics of Fluids, Vol.13, No.2, March 1970, p.608-617.

[83] S. Nakanishi, "Experimental Performance of a 1-Kilowatt Arcjet Thruster", NASA Technical Memorandum 87131, October 1985.

[84] H. Okamoto, M. Nishida, and K. Tanaka, "Numerical Studies of the Flow Field in a Low Power DC Arcjet Thruster Using Navier-Stokes Equations", IEPC 91-112, AIDAA/AIAA/DGLR/JSASS 22nd International Electric Propulsion Conference, Viareggio, Italy, October 1991.

[85] C. Park, "Assessment of Two-Temperature Kinetic Model for Dissociating and Weakly-Ionizing Nitrogen", AIAA 86-1347, AIAA/ASME 4th Joint Thermophysics and Heat Transfer Conference, Boston, June 1986.

[86] G.E. Pawlas and T.G. Keith, "Analysis of a Swirl Stabilized Arcjet Thruster", AIAA 91-1995, AIAA/SAE/ASME/ASEE 27th Joint Propulsion Conference, Sacramento, June 1991.

[87] E. Pfender, "Electric Arcs and Gas Heaters", in *Gaseous Electronics*, Vol.1, edited by M.N. Hirsh and H.J. Oskam, Academic Press, 1978.

[88] T.J. Pivirotto and W.D. Deininger, "Velocity Measurements in the Plume of an Arcjet Engine", AIAA 87-1063, AIAA/DGLR/JSASS 19th International Electric Propulsion Conference, Colorado Springs, May 1987.

[89] T.J. Pivirotto, D.Q. King, and W.D. Deininger, "Long Duration Test of a 30-kW Class Thermal Arcjet Engine", AIAA 87-1947, AIAA/SAE/ASME/ASEE 23rd Joint Propulsion Conference, San Diego, June 1987.

[90] J.E. Polk and K.D. Goodfellow, "Results of a 1462 Hour Ammonia Arcjet Endurance Test", AIAA 92-3833, AIAA/SAE/ASME/ASEE 28th Joint Propulsion Conference, Nashville, July 1992.

[91] R.W. Powell, C.Y. Ho, and P.E. Liley, *Thermal Conductivity of Selected Materials*, NSRDS-NBS 8, 1966.

[92] W.H. Press, B.P. Flannery, S.A. Teukolsky, and W.T. Vetterling, *Numerical Recipes*, Cambridge University Press, New York, 1988.

[93] R. Rhodes and D. Keefer, "Numerical Modeling of an Arcjet Thruster", AIAA 90-2614, AIAA/DGLR/JSASS 21st International Electric Propulsion Conference, Orlando, July 1990.

[94] R. Rhodes and D. Keefer, "Modeling Arcjet Space Thrusters", AIAA 91-1994, AIAA/SAE/ASME/ASEE 27th Joint Propulsion Conference, Sacramento, June 1991.

[95] R. Rhodes and D. Keefer, "Comparison of Model Calculations With Experimental Data From Hydrogen Arcjets", IEPC-91-111, AIDAA/AIAA/DGLR/JSASS 22nd International Electric Propulsion Conference, Viareggio, Italy, October 1991.

[96] R. Richter, "Development Work on Plasma Arc Jet Engines", ARS 2347-62, ARS Electric Propulsion Conference, Berkeley, March 1962.

[97] P.J. Roache, *Computational Fluid Dynamics*, Hermosa Publishers, Albuquerque, 1985.

[98] R.C. Rogers and C.J. Schexnayder Jr., "Chemical Kinetic Analysis of Hydrogen-Air Ignition and Reaction Times", NASA Technical Paper 1856, 1981.

[99] W.M. Rohsenow and H.Y. Choi, *Heat, Mass, and Momentum Transfer*, Prentice-Hall, Inc., New Jersey, 1963.

[100] W.M. Rohsenow, J.P. Hartnett, and E.N. Ganic, *Handbook of Heat Transfer Applications*, 2nd Edition, McGraw-Hill, New York, 1985.

[101] J.M. Sankovic, "Investigation of the Arcjet Plume Near Field Using Electrostatic Probes", NASA Technical Memorandum 103638, October 1990.

[102] J.M. Sankovic and F.M. Curran, "Arcjet Thermal Characteristics", AIAA 91-2456, AIAA/SAE/ASME/ASEE 27th Joint Propulsion Conference, Sacramento, June 1991.

[103] H.O. Schrade and P.C. Sleziona, "Performance Calculation of an H_2 Arcjet by Means of a Dual Channel Model", IEPC 88-104, DGLR/AIAA/JSASS 20th International Electric Propulsion Conference, Garmisch-Partenkirchen, W. Germany, October 1988.

[104] E.J. Sheppard, *Nonequilibrium Ionization in Electromagnetic Accelerators*, Ph.D. Thesis, Massachusetts Institute of Technology, 1993.

[105] T.M. Shih, *Numerical Heat Transfer*, Hemisphere Publishing Corp., New York, 1984.

[106] M.A. Simon, S.C. Knowles, F.M. Curran, and T.L. Hardy, "Low Power Arcjet Life Issues", AIAA 87-1059, AIAA/DGLR/JSASS 19th International Electric Propulsion Conference, Colorado Springs, May 1987.

[107] W.W. Smith, R.D. Smith, S.E. Yano, K. Davies, and D. Lichtin, "Low Power Hydrazine Arcjet Flight Qualification", IEPC 91-148, AIDAA/AIAA/DGLR/JSASS 22nd International Electric Propulsion Conference, Viareggio, Italy, October 1991.

[108] L. Spitzer and R. Härm, "Transport Phenomena in a Completely Ionized Gas", Physical Review, Vol. 89, 1953.

[109] R. Spurrett and R.A. Bond, "Modelling Arcjet Thruster Performance", IEPC 91-110, AIDAA/AIAA/DGLR/JSASS 22nd International Electric Propulsion Conference, Viareggio, Italy, October 1991.

[110] G.W. Sutton and A. Sherman, *Engineering Magnetohydrodynamics*, McGraw-Hill, New York, 1965.

[111] H. Tahara, T. Sakakibara, K. Onoe, and T. Yoshikawa, "Discharge Characteristics and Inner Plasma Features of a High-Power DC Arcjet Thruster", AIAA 90-2534, AIAA/DGLR/JSASS 21st International Electric Propulsion Conference, Orlando, July 1990.

[112] H. Tahara, T. Sakakibara, K. Onoe, and T. Yoshikawa, "Experimental and Numerical Studies of a 10kW Water-Cooled Arcjet Thruster", IEPC 91-015, AIDAA/AIAA/DGLR/JSASS 22nd International Electric Propulsion Conference, Viareggio, Italy, October 1991.

[113] J.C. Tannehill, T.L. Holst, and J.V. Rakich, "Numerical Computation of Two-Dimensional Viscous Blunt Body Flows with an Impending Shock", AIAA Paper 75-154, Pasadena, 1975.

[114] J.F. Thompson, F.C. Thames, and C.W. Mastin, "Automatic Numerical Generation of Body-Fitted Curvilinear Coordinate System for Field Containing any Number of Arbitrary Two-dimensional Bodies", Journal of Computational Physics, Vol. 15, pp. 299-319, 1974.

[115] J.F. Thompson, F.C. Thames, C.W. Mastin, and S.P. Shanks, "Use of Numerically Generated Body-Fitted Coordinate Systems for Solution of the Navier-Stokes Equations", Proc. AIAA 2nd Computational Fluid Dynamics Conference, Hartford, 1975.

[116] J.P. Todd and R.E. Sheets, "Development of a Regeneratively Cooled 30-kw Arcjet Engine", AIAA 64-671, AIAA 4th Electric Propulsion Conference, Philadelphia, August 1964.

[117] J.T. Vanderslice, S. Weissman, E.A. Mason, and R.J. Fallon, "High-Temperature Transport Properties of Dissociating Hydrogen", Physics of Fluids, Vol.5, No.2, February 1962, p.155-64.

[118] W.G. Vincenti and C.H. Kruger, *Introduction to Physical Gas Dynamics*, Wiley, New York, 1965.

[119] J.J. Wang, *Electrodynamic Interactions Between Charged Space Systems and the Ionospheric Plasma Environment*, Doctoral Thesis, Massachusetts Institute of Technology, June 1991.

[120] V.R. Watson and E.B. Pegot, "Numerical Calculations for the Characteristics of a Gas Flowing Axially Through a Constricted Arc", NASA Technical Note TN D-4042, June 1967.

[121] C.R. Wilke, "A Viscosity Equation for Gas Mixtures", Journal of Chemical Physics, Vol.18, No.4, April 1950, p.517-9.

[122] T.Yamada, Y. Shimizu, K. Toki, and K. Kuriki, "Thermal Analysis and Thrust Performance of a Low Power Arcjet Thruster", AIAA 90-2581, AIAA/DGLR/JSASS 21st International Electric Propulsion Conference, Orlando, July 1990.

[123] T. Yoshikawa, K. Onoe, S.Tsuri, M. Ishii, and K. Uematsu, "Development of a Low Power Arcjet Thruster - Thrust Performance and Life Evaluation", IEPC 91-043, AIDAA/AIAA/DGLR/JSASS 22nd International Electric Propulsion Conference, Viareggio, Italy, October 1991.

[124] D.M. Zube and R.M. Myers, "Nonequilibrium in a Low Power Arcjet Nozzle", AIAA 91-2113, AIAA/SAE/ASME/ASEE 27th Joint Propulsion Conference, Sacramento, June 1991.

Appendix A

Fundamental Constants

Electric charge of a proton	$e = 1.602 \times 10^{-19} C$
Permittivity of vacuum	$\epsilon_0 = 8.854 \times 10^{-12} \frac{F}{m}$
Permeability of vacuum	$\mu_0 = 4\pi \times 10^{-7} \frac{H}{m}$
Planck's constant	$h = 6.626 \times 10^{-34} J - s$
Boltzmann constant	$k = 1.381 \times 10^{-23} \frac{J}{{}^oK}$
Stefan-Boltzmann constant	$\sigma_{SB} = 5.67 \times 10^{-8} \frac{W}{{}^oK^4/m^2}$
Avogadro's number	$\hat{N} = 6.022 \times 10^{23} \frac{molecules}{mole}$
Electron rest mass	$m_e = 9.11 \times 10^{-31} kg$
Atomic mass (Ar)	$m_{Ar} = 6.634 \times 10^{-26} kg$
Atomic mass (H)	$m_H = 1.674 \times 10^{-27} kg$
Atomic mass (N)	$m_N = 2.326 \times 10^{-26} kg$
1st ionization energy (Ar)	$E_i = 2.53 \times 10^{-18} J$
Ionization energy (H)	$E_i = 2.178 \times 10^{-18} J$
1st ionization energy (N)	$E_i = 2.328 \times 10^{-18} J$
Dissociation energy (H_2)	$E_d = 7.24 \times 10^{-19} J$
Dissociation energy (N_2)	$E_d = 1.57 \times 10^{-18} J$
Characteristic dissociation temperature (H_2)	$\theta_d = 52,400^o K$
Characteristic vibrational temperature (H_2)	$\theta_v = 6160^o K$
Characteristic dissociation temperature (N_2)	$\theta_d = 113,500^o K$
Characteristic vibrational temperature (N_2)	$\theta_v = 3390^o K$

Ratio of specific heats (monatomic)	$\gamma = 1.667$
Ratio of specific heats (diatomic)	$\gamma = 1.4$
Universal gas constant	$\hat{R} = 8.31435\frac{J}{mole^{\circ}K}$
Argon gas constant	$R_{Ar} = 208.13\frac{J}{kg^{\circ}K}$
Electron gas constant	$R_e = 1.516 \times 10^7\frac{J}{kg^{\circ}K}$
Hydrogen atom gas constant	$R_H = 8249.23\frac{J}{kg^{\circ}K}$
Hydrogen molecule gas constant	$R_{H_2} = 4124.62\frac{J}{kg^{\circ}K}$

Appendix B

Hydrogen Collision Cross-Section and Collision Integral Tables

Table B.1: Average Electron Collision Cross-Sections (Coulomb Cross-Section at 1 atm Pressure)

$\overline{Q}_{ej}(10^{-20}m^2)$			
$T_e(^\circ K)$	$\overline{Q}_{eH_2}$	$\overline{Q}_{eH}$	$\overline{Q}_{eH^+}$
1000	10.1	31.18	
2000	11.3	27.65	
3000	12.6	26.01	
4000	13.4	24.54	
5000	14.2	23.20	3817
6000	14.8	21.96	3243
7000	15.5	20.83	2750
8000	15.9	19.80	2350
9000	16.4	18.86	2026
10,000	16.9	17.99	1765
11,000	17.3	17.18	1550
12,000	17.6	16.44	1373
13,000	17.8	15.76	1225
14,000	18.0	15.11	1101
15,000	18.2	14.52	995
16,000	18.3	13.96	904
17,000	18.4	13.43	825
18,000	18.5	12.93	757
19,000	18.5	12.47	697
20,000	18.4	12.02	644
21,000	18.3	11.59	597
22,000	18.2	11.19	555
23,000	18.0	10.83	518
24,000	17.8	10.50	484
25,000	17.6	10.19	454

Table B.2: Average Effective Collision Integrals (Low Temperature)

$\overline{\Omega}_{ij}(10^{-20}m^2)$					
$T_g(^\circ K)$	$\overline{\Omega}^{(2,2)}_{H_2-H_2}$	$\overline{\Omega}^{(2,2)}_{H_2-H}$	$\overline{\Omega}^{(2,2)}_{H-H}$	$\overline{\Omega}^{(1,1)}_{H_2-H_2}$	$\overline{\Omega}^{(1,1)}_{H-H}$
300	7.34			6.50	
500	6.75			5.97	
1000	6.00	5.13	5.95	5.21	5.24
1500	5.59	4.52	5.22	4.66	4.57
2000	5.33	4.10	4.74	4.37	4.13
2500	5.02	3.79	4.39	4.04	3.82
3000	4.73	3.55	4.12	3.79	3.57
3500	4.50	3.35	3.90	3.59	3.37
4000	4.29	3.18	3.74	3.42	3.23
4500	4.12	3.03	3.61	3.27	3.12
5000	3.97	2.91	3.50	3.14	3.03
5500	3.83	2.80	3.39	3.03	2.96
6000	3.71	2.69	3.28	2.93	2.88
6500	3.60	2.60	3.17	2.83	2.82
7000	3.50	2.52	3.06	2.75	2.76
7500	3.41	2.44	2.97	2.67	2.70
8000	3.32	2.37	2.88	2.60	2.62
8500	3.24	2.31	2.80	2.53	2.55
9000	3.17	2.25	2.73	2.47	2.48
9500	3.10	2.19	2.66	2.41	2.42
10,000	3.03	2.14	2.60	2.36	2.36
11,000	2.91	2.04	2.49	2.26	2.25
12,000	2.81	1.95	2.42	2.17	2.15
13,000	2.71	1.87	2.34	2.09	2.07
14,000	2.62	1.80	2.25	2.02	1.99
15,000	2.54	1.74	2.18	1.95	1.92

Table B.3: Average Effective Collision Integrals (High Temperature) (Coulomb Integrals at 1 atm Pressure)

	$\overline{\Omega}_{ij}(10^{-20}m^2)$					
$T(°K)$	$\overline{\Omega}^{(2,2)}_{H-H}$	$\overline{\Omega}^{(2,2)}_{H-H^+}$	$\overline{\Omega}^{(2,2)}_{H^+-H^+}$	$\overline{\Omega}^{(2,2)}_{e-H}$	$\overline{\Omega}^{(1,1)}_{H^+-H^+}$	$\overline{\Omega}^{(1,1)}_{e-H}$	$\overline{\Omega}^{(1,1)}_{e-H_2}$
5000	3.50	13.60	3193	5.81	2174	6.85	3.55
5500	3.39	13.01	2434	5.53	2069	6.55	3.63
6000	3.28	12.49	1905	5.27	1619	6.29	3.70
6500	3.17	12.01	1525	5.04	1296	6.05	3.79
7000	3.06	11.58	1244	4.83	1057	5.82	3.89
7500	2.97	11.18	1031	4.64	876.4	5.62	3.93
8000	2.88	10.82	866.6	4.47	736.6	5.43	3.98
8500	2.80	10.48	737.7	4.30	627.0	5.26	4.04
9000	2.73	10.17	635.0	4.15	539.8	5.09	4.10
9500	2.66	9.87	552.0	4.02	469.2	4.94	4.16
10,000	2.60	9.60	484.2	3.89	411.6	4.80	4.23
11,000	2.49	9.10	373.2	3.65	317.2	4.54	4.33
12,000	2.42	8.66	309.4	3.45	263.0	4.31	4.40
13,000	2.34	8.26	257.3	3.27	218.7	4.11	4.46
14,000	2.25	7.90	219.0	3.11	186.2	3.92	4.51
15,000	2.18	7.57	190.4	2.97	161.8	3.76	4.55
16,000	2.09	7.27	168.6	2.84	143.3	3.61	4.58
17,000	2.02	6.99	151.6	2.73	128.9	3.47	4.61
18,000	1.96	6.73	137.8	2.63	117.1	3.34	4.62
19,000	1.89	6.50	126.2	2.54	107.3	3.23	4.62
20,000	1.84	6.27	116.3	2.46	98.86	3.13	4.60
21,000	1.78	6.07	107.7	2.39	91.55	3.03	4.57
22,000	1.73	5.87	100.0	2.33	85.00	2.94	4.53
23,000	1.68	5.69	93.26	2.27	79.27	2.86	4.49
24,000	1.63	5.51	87.18	2.23	74.10	2.79	4.45
25,000	1.59	5.35	81.70	2.19	69.45	2.72	4.41
26,000	1.55	5.19	76.75	2.15	65.24	2.66	4.36
27,000	1.51	5.04	72.25	2.12	61.41	2.60	4.31
28,000	1.47	4.90	68.16	2.10	57.94	2.55	4.25
29,000	1.44	4.77	64.41	2.08	54.75	2.51	4.18
30,000	1.40	4.64	60.97	2.06	51.82	2.46	4.10

Appendix C

Ambipolar Diffusion Coefficient

The coefficient of ambipolar diffusion (D_a) is calculated from the electron and ion species momentum equations. In general, for magnetoplasmadynamic flow these equations may be written in the following form:

$$m_s n_s \left[\frac{\partial \vec{u}_s}{\partial t} + (\vec{u}_s \cdot \nabla)\vec{u}_s\right] + \nabla \cdot \bar{\bar{p}}_s = q_s n_s \left(\vec{E} + \vec{u}_s \times \vec{B}\right) - m_s n_s \sum_r \nu_{sr}\left(\vec{u}_s - \vec{u}_r\right). \quad \text{(C.1)}$$

Let the coordinate system be Cartesian, with the main flow in the x-direction, the magnetic field in the z-direction, and transverse flow in the y-direction. Then in the steady state, neglecting inertial and viscous terms, the electron and ion transverse momentum equations become

$$\frac{dp_e}{dy} = -en_e(E_y - u_{ex}B_z) - m_e n_e \nu_{ei}(u_{ey} - u_{iy}) - m_e n_e \nu_{en}(u_{ey} - u_{ny}) \quad \text{(C.2)}$$

and

$$\frac{dp_i}{dy} = en_e(E_y - u_{ix}B_z) - m_i n_i \nu_{ie}(u_{iy} - u_{ey}) - \frac{1}{2} m_i n_i \nu_{in}(u_{iy} - u_{ny}). \quad \text{(C.3)}$$

Summing the previous two equations and noting that $m_i n_i \nu_{ie} = m_e n_e \nu_{ei}$ and $n_i = n_e$ (quasineutrality), we find that

$$\frac{d(p_e + p_i)}{dy} = (u_{ex} - v_{ix})B_z - m_e n_e \nu_{en}(u_{ey} - u_{ny}) - \frac{1}{2} m_i n_e \nu_{in}(u_{iy} - u_{ny}). \quad \text{(C.4)}$$

The electron-neutral collisional momentum transfer term is assumed to be much smaller than the term arising from ion-neutral collisions. For the electrothermal arcjet, in which case the magnetic field may be neglected, or for the MPD arcjet when the Hall parameter is sufficiently low that the axial current may be neglected, the Lorentz acceleration term may also be neglected. Thus

$$\frac{d(p_e + p_i)}{dy} = \frac{1}{2} m_i n_e \bar{c}_{in} n_n Q_{in}(v_{iy} - v_{ny}), \quad \text{(C.5)}$$

where

$$\bar{c}_{in} = \sqrt{\frac{8kT_g}{\pi \mu_{in}}} = \sqrt{\frac{16kT_g}{\pi m_i}}. \tag{C.6}$$

If there is no net heavy particle flux to the walls of the thruster, i.e. the walls return neutral particles when ions recombine there, then

$$n_e u_{iy} + n_n u_{ny} = 0, \tag{C.7}$$

which implies that $n_n(v_{iy} - v_{in}) = v_{iy}(n_e + n_n)$. Finally, assuming the temperatures are approximately constant in the transverse direction, Equation C.5 then becomes

$$k(T_e + T_g)\frac{dn_e}{dy} = -\frac{1}{2} m_i \bar{c}_{in} Q_{in} n_e v_{iy}(n_e + n_n). \tag{C.8}$$

This expression can then be written in the more illuminating form:

$$n_e v_{i_y} = -D_a \frac{dn_e}{dy}, \tag{C.9}$$

where D_a is the required form of the ambipolar diffusion coefficient,

$$D_a = \sqrt{\frac{\pi k T_g}{4 m_i}} \frac{(1 + \frac{T_e}{T_g})}{Q_{in}(n_e + n_n)}. \tag{C.10}$$

Appendix D

Governing Equations of Axisymmetric Arcjet Flow in Transformed Coordinates

$$
\begin{aligned}
&\sigma\left[\left(\xi_r^2+\xi_z^2\right)\frac{\partial^2\phi}{\partial\xi^2}+2\left(\xi_r\eta_r+\xi_z\eta_z\right)\frac{\partial^2\phi}{\partial\xi\partial\eta}+\left(\eta_r^2+\eta_z^2\right)\frac{\partial^2\phi}{\partial\eta^2}+\left(\xi_{rr}+\xi_{zz}\right)\frac{\partial\phi}{\partial\xi}+\left(\eta_{rr}+\eta_{zz}\right)\frac{\partial\phi}{\partial\eta}\right]\\
&\qquad+\left(\frac{\partial\phi}{\partial\xi}\xi_r+\frac{\partial\phi}{\partial\eta}\eta_r\right)\left(\frac{\sigma}{r}+\frac{\partial\sigma}{\partial\xi}\xi_r+\frac{\partial\sigma}{\partial\eta}\eta_r\right)-\left(\frac{\partial\phi}{\partial\xi}\xi_z+\frac{\partial\phi}{\partial\eta}\eta_z\right)\left(\frac{\partial\sigma}{\partial\xi}\xi_z+\frac{\partial\sigma}{\partial\eta}\eta_z\right)\\
&=\psi\left[\left(\xi_r^2+\xi_z^2\right)\frac{\partial^2 p_e}{\partial\xi^2}+2\left(\xi_r\eta_r+\xi_z\eta_z\right)\frac{\partial^2 p_e}{\partial\xi\partial\eta}+\left(\eta_r^2+\eta_z^2\right)\frac{\partial^2 p_e}{\partial\eta^2}+\left(\xi_{rr}+\xi_{zz}\right)\frac{\partial p_e}{\partial\xi}+\left(\eta_{rr}+\eta_{zz}\right)\frac{\partial p_e}{\partial\eta}\right]\\
&\quad+\left(\frac{\partial p_e}{\partial\xi}\xi_r+\frac{\partial p_e}{\partial\eta}\eta_r\right)\left(\frac{\psi}{r}+\frac{\partial\psi}{\partial\xi}\xi_r+\frac{\partial\psi}{\partial\eta}\eta_r\right)+\left(\frac{\partial p_e}{\partial\xi}\xi_z+\frac{\partial p_e}{\partial\eta}\eta_z\right)\left(\frac{\partial\psi}{\partial\xi}\xi_z+\frac{\partial\psi}{\partial\eta}\eta_z\right)
\end{aligned}
\tag{D.1}
$$

$$
\begin{aligned}
j_r&=\psi\left(\frac{\partial p_e}{\partial\xi}\xi_r+\frac{\partial p_e}{\partial\eta}\eta_r\right)-\sigma\left(\frac{\partial\phi}{\partial\xi}\xi_r+\frac{\partial\phi}{\partial\eta}\eta_r\right)\\
j_z&=\psi\left(\frac{\partial p_e}{\partial\xi}\xi_z+\frac{\partial p_e}{\partial\eta}\eta_z\right)-\sigma\left(\frac{\partial\phi}{\partial\xi}\xi_z+\frac{\partial\phi}{\partial\eta}\eta_z\right)
\end{aligned}
\tag{D.2}
$$

$$
\frac{\partial\rho r}{\partial t}+\frac{\partial\rho u_r r}{\partial\xi}\xi_r+\frac{\partial\rho u_r r}{\partial\eta}\eta_r+\frac{\partial\rho u_z r}{\partial\xi}\xi_z-\frac{\partial\rho u_z r}{\partial\eta}\eta_z=0
\tag{D.3}
$$

$$
\begin{aligned}
&\frac{\partial\rho s r}{\partial t}+\frac{\partial\rho s u_r r}{\partial\xi}\xi_r-\frac{\partial}{\partial\xi}\left(\frac{\rho s}{\left(\rho s+\rho s_2\right)}\frac{m s}{m_e}d_{er}r\right)\xi_r+\frac{\partial\rho s u_r r}{\partial\eta}\eta_r-\frac{\partial}{\partial\eta}\left(\frac{\rho s}{\left(\rho s+\rho s_2\right)}\frac{m s}{m_e}d_{er}r\right)\eta_r\\
&\quad+\frac{\partial\rho s u_z r}{\partial\xi}\xi_z-\frac{\partial}{\partial\xi}\left(\frac{\rho s}{\left(\rho s+\rho s_2\right)}\frac{m s}{m_e}d_{ez}r\right)\xi_z+\frac{\partial\rho s u_z r}{\partial\eta}\eta_z-\frac{\partial}{\partial\eta}\left(\frac{\rho s}{\left(\rho s+\rho s_2\right)}\frac{m s}{m_e}d_{ez}r\right)\eta_z\\
&\qquad=m s\left(\dot{n} s+<\sigma v>n_e n s_2-\dot{n}_e\right)r
\end{aligned}
\tag{D.4}
$$

$$\frac{\partial \rho_e r}{\partial t} + \frac{\partial\left(\rho_e u_r + d_{er}\right) r}{\partial \xi}\xi_r + \frac{\partial\left(\rho_e u_r + d_{er}\right) r}{\partial \eta}\eta_r + \frac{\partial\left(\rho_e u_z + d_{ez}\right) r}{\partial \xi}\xi_z$$

$$+ \frac{\partial\left(\rho_e u_z + d_{ez}\right) r}{\partial \eta}\eta_z = m_e \dot{n}_e r \tag{D.5}$$

$$d_{er} = -D_a\left(\frac{\partial \rho_e}{\partial \xi}\xi_r + \frac{\partial \rho_e}{\partial \eta}\eta_r\right) \qquad d_{ez} = -D_a\left(\frac{\partial \rho_e}{\partial \xi}\xi_z + \frac{\partial \rho_e}{\partial \eta}\eta_z\right) \tag{D.6}$$

$$\frac{\partial \rho u_r r}{\partial t} + \frac{\partial(\rho u_r^2 + p - \tau_{rr})r}{\partial \xi}\xi_r + \frac{\partial(\rho u_r^2 + p - \tau_{rr})r}{\partial \eta}\eta_r + \frac{\partial(\rho u_r u_z - \tau_{rz})r}{\partial \xi}\xi_z$$

$$+ \frac{\partial(\rho u_r u_z - \tau_{rz})r}{\partial \eta}\eta_z = \rho u_\theta^2 - \tau_{\theta\theta} + p \tag{D.7}$$

$$\frac{\partial \rho u_\theta r}{\partial t} + \frac{\partial(\rho u_r u_\theta - \tau_{r\theta})r}{\partial \xi}\xi_r + \frac{\partial(\rho u_r u_\theta - \tau_{r\theta})r}{\partial \eta}\eta_r + \frac{\partial(\rho u_\theta u_z - \tau_{\theta z})r}{\partial \xi}\xi_z$$

$$+ \frac{\partial(\rho u_\theta u_z - \tau_{\theta z})r}{\partial \eta}\eta_z = -\rho u_r u_\theta \tag{D.8}$$

$$\frac{\partial \rho u_z r}{\partial t} + \frac{\partial(\rho u_r u_z - \tau_{rz})r}{\partial \xi}\xi_r + \frac{\partial(\rho u_r u_z - \tau_{rz})r}{\partial \eta}\eta_r + \frac{\partial(\rho u_z^2 + p - \tau_{zz})r}{\partial \xi}\xi_z$$

$$+ \frac{\partial(\rho u_z^2 + p - \tau_{zz})r}{\partial \eta}\eta_z = 0 \tag{D.9}$$

$$\tau_{rr} = \frac{4}{3}\mu_g\left(\frac{\partial u_r}{\partial \xi}\xi_r + \frac{\partial u_r}{\partial \eta}\eta_r\right) - \frac{2}{3}\mu_g\left(\frac{\partial u_z}{\partial \xi}\xi_z + \frac{\partial u_z}{\partial \eta}\eta_z + \frac{u_r}{r}\right) \tag{D.10}$$

$$\tau_{\theta\theta} = \frac{4}{3}\mu_g\frac{u_r}{r} - \frac{2}{3}\mu_g\left(\frac{\partial u_r}{\partial \xi}\xi_r + \frac{\partial u_r}{\partial \eta}\eta_r + \frac{\partial u_z}{\partial \xi}\xi_z + \frac{\partial u_z}{\partial \eta}\eta_z\right) \tag{D.11}$$

$$\tau_{zz} = \frac{4}{3}\mu_g\left(\frac{\partial u_z}{\partial \xi}\xi_z + \frac{\partial u_z}{\partial \eta}\eta_z\right) - \frac{2}{3}\mu_g\left(\frac{\partial u_r}{\partial \xi}\xi_r + \frac{\partial u_r}{\partial \eta}\eta_r + \frac{u_r}{r}\right) \tag{D.12}$$

$$\tau_{r\theta} = \mu_g\left(\frac{\partial u_\theta}{\partial \xi}\xi_r + \frac{\partial u_\theta}{\partial \eta}\eta_r - \frac{u_\theta}{r}\right) \tag{D.13}$$

$$\tau_{rz} = \mu_g\left(\frac{\partial u_r}{\partial \xi}\xi_z + \frac{\partial u_r}{\partial \eta}\eta_z + \frac{\partial u_z}{\partial \xi}\xi_r + \frac{\partial u_z}{\partial \eta}\eta_r\right) \tag{D.14}$$

$$\tau_{\theta z} = \mu_g\left(\frac{\partial u_\theta}{\partial \xi}\xi_z + \frac{\partial u_\theta}{\partial \eta}\eta_z\right) \tag{D.15}$$

$$\frac{\partial \rho e_g r}{\partial t} + \frac{\partial\left(\rho u_r e_g + q_{gr}\right) r}{\partial \xi}\xi_r + \frac{\partial\left(\rho u_r e_g + q_{gr}\right) r}{\partial \eta}\eta_r + \frac{\partial\left(\rho u_z e_g + q_{gz}\right) r}{\partial \xi}\xi_z + \frac{\partial\left(\rho u_z e_g + q_{gz}\right) r}{\partial \eta}\eta_z$$

$$+\frac{\partial\left(\rho_{S_2} V_{S_2 r} e_{S_2} + \rho_S V_{S r} e_S + \rho_{S+} V_{S+r} e_{S+}\right) r}{\partial \xi}\xi_r + \frac{\partial\left(\rho_{S_2} V_{S_2 r} e_{S_2} + \rho_S V_{S r} e_S + \rho_{S+} V_{S+r} e_{S+}\right) r}{\partial \eta}\eta_r$$

$$+p_g\left(\frac{\partial u_r r}{\partial \xi}\xi_r + \frac{\partial u_r r}{\partial \eta}\eta_r + \frac{\partial u_z r}{\partial \xi}\xi_z + \frac{\partial u_z r}{\partial \eta}\eta_z\right) + p_{S_2}\left(\frac{\partial V_{S_2 r} r}{\partial \xi}\xi_r + \frac{\partial V_{S_2 r} r}{\partial \eta}\eta_r\right)$$

$$+p_S\left(\frac{\partial V_{S r} r}{\partial \xi}\xi_r + \frac{\partial V_{S r} r}{\partial \eta}\eta_r\right) + p_{S+}\left(\frac{\partial V_{S+ r} r}{\partial \xi}\xi_r + \frac{\partial V_{S+ r} r}{\partial \eta}\eta_r\right)$$

$$= \left(\Phi + E_l - \frac{1}{2}E_d \dot{n}_S\right) r \tag{D.16}$$

$$\Phi = \mu_g\left[2\left(\frac{\partial u_r}{\partial \xi}\xi_r + \frac{\partial u_r}{\partial \eta}\eta_r\right)^2 + 2\left(\frac{\partial u_z}{\partial \xi}\xi_z + \frac{\partial u_z}{\partial \eta}\eta_z\right)^2 + 2\left(\frac{u_r}{r}\right)^2\right.$$

$$+\left(\frac{\partial u_r}{\partial \xi}\xi_z + \frac{\partial u_r}{\partial \eta}\eta_z + \frac{\partial u_z}{\partial \xi}\xi_r + \frac{\partial u_z}{\partial \eta}\eta_r\right)^2$$

$$+\left(\frac{\partial u_\theta}{\partial \xi}\xi_r + \frac{\partial u_\theta}{\partial \eta}\eta_r - \frac{u_\theta}{r}\right)^2 + \left(\frac{\partial u_\theta}{\partial \xi}\xi_z + \frac{\partial u_\theta}{\partial \eta}\eta_z\right)^2$$

$$\left.-\frac{2}{3}\left(\frac{\partial u_r}{\partial \xi}\xi_r + \frac{\partial u_r}{\partial \eta}\eta_r + \frac{\partial u_z}{\partial \xi}\xi_z + \frac{\partial u_z}{\partial \eta}\eta_z + \frac{u_r}{r}\right)^2\right] \tag{D.17}$$

$$q_{gr} = -k_g\left(\frac{\partial T_g}{\partial \xi}\xi_r + \frac{\partial T_g}{\partial \eta}\eta_r\right) \qquad q_{gz} = -k_g\left(\frac{\partial T_g}{\partial \xi}\xi_z + \frac{\partial T_g}{\partial \eta}\eta_z\right) \tag{D.18}$$

$$\frac{\partial \rho_e E_e r}{\partial t} + \frac{\partial\left(\rho_e u_{er} H_e + q_{er}\right) r}{\partial \xi}\xi_r + \frac{\partial\left(\rho_e u_{er} H_e + q_{er}\right) r}{\partial \eta}\eta_r + \frac{\partial\left(\rho_e u_{ez} H_e + q_{ez}\right) r}{\partial \xi}\xi_z$$

$$+\frac{\partial\left(\rho_e u_{ez} H_e + q_{ez}\right) r}{\partial \eta}\eta_z = \left(\frac{j^2}{\sigma} - E_l - E_d < \sigma v > n_e n_{S_2} - E_i \dot{n}_e - \dot{R}\right) r \tag{D.19}$$

$$q_{er} = -k_e\left(\frac{\partial T_e}{\partial \xi}\xi_r + \frac{\partial T_e}{\partial \eta}\eta_r\right) \qquad q_{ez} = -k_e\left(\frac{\partial T_e}{\partial \xi}\xi_z + \frac{\partial T_e}{\partial \eta}\eta_z\right) \tag{D.20}$$

Appendix E

ARCAXI Arcjet Code Description

This appendix describes in some detail the axisymmetric arcjet code, named ARCAXI, from which the bulk of the results for this thesis were obtained. The run files, input and output files, data files, and program subroutines are detailed, as well as the major variables used in the code. The code was written in FORTRAN, and compiled using Makefiles on UNIX-based systems.

E.1 Subroutines

The following list summarizes the FORTRAN files required to compile and link ARCAXI and the subroutines contained in each file.

arcjet.f The main program.

boundc.f Updates the boundary conditions for all flow quantities.

common.inc Contains listing of all common blocks and the variables shared within each block.

constants.f Initializes all physical constants required by the program.

damp.f Contains subroutines which calculate the numerical smoothing for each of the flow equations.

decs.inc Contains declarations of the common block program variables.

efast.f Integrates the electron density and energy equations.

eflux.f Calculates the axial and radial fluxes for the electron density and energy discretized equations.

elecdt.f Calculates the maximum allowable time step for the electron density and energy equations.

error.f Calculates the RMS error in the heavy species pressure, electron pressure, and electric potential over the mesh after each integration step.

esource.f Calculates the source terms for the electron state vector.

funcs.f Contains subroutines which extract the gas temperature from the flow enthalpy, and which calculate the electrical conductivity, electron thermal conductivity, heavy species thermal conductivity, gas viscosity, ambipolar diffusivity, net dissociation rate, net ionization rate, various collision frequencies, and radiative transfer.

getcur.f Calculates the current density and electron velocities from the distributions of electric potential, electron pressure, and electron mobility.

getflow.f Initializes the simulation variables based on the saved variables in the run files.

getgrid.f Reads in the flow grid and the potential grid and calculates the grid metrics.

getinfo.f Reads in run information from the user such as run file names, grid file names, and run duration.

gflux.f Calculates the axial and radial fluxes for the global and heavy species discretized equations.

gsource.f Calculates the source terms for the global and heavy species state vector.

init.f Initializes the flow state vectors and electric potential for a new run case.

input.f Calls subroutines to get run information from the user and then to initialize the simulation variables based on that information.

integ.f Integrates the global and heavy species conservation equations.

output.f Writes data to the output files at the conclusion of a run.

perform.f Calculates the total voltage, thrust, specific impulse, and efficiency after each run has been completed.

phibound.f Updates the boundary conditions for the electric potential.

potential.f Performs the iterative relaxation of the electric potential.

readdata.f Reads in collisional and reaction rate data for use in calculating transport coefficients, collisional energy transfer, and net dissociation and ionization rates.

timestep.f Calculates the maximum allowable time step for the global and heavy species equations.

E.2 Data Files

The following data files must be present in the directory in which the arcjet simulation code is run. They contain data used in calculating the transport coefficients, dissociation and ionization rates, and collision frequencies for hydrogen propellant.

deltac.1 First order correction factor for electrical conductivity in the interval $5000 < T_e < 30,000^o K$ at $10^{-4} atm$ pressure.

deltac.2 First order correction factor for electrical conductivity in the interval $5000 < T_e < 30,000^o K$ at $10^{-2} atm$ pressure.

deltac.3 First order correction factor for electrical conductivity in the interval $5000 < T_e < 30,000^o K$ at $10^{0} atm$ pressure.

deltac.4 First order correction factor for electrical conductivity in the interval $5000 < T_e < 30,000^o K$ at $10^{2} atm$ pressure.

eh.c11 Electron-H average effective diffusion collision integral in the interval $5000 < T_e < 32,000^o K$.

eh.c22 Electron-H average effective momentum collision integral in the interval $5000 < T_e < 32,000^o K$.

eh.mom Electron-H momentum cross-section in the interval $3000 < T_e < 20,000^o K$.

eh2.mom Electron-H_2 momentum cross-section in the interval $0 < T_e < 30,000^o K$.

el.dat Inelastic correction factor for $e - H_2$ collisional energy transfer in the interval $1000 < T_e < 30,000^o K$.

hh.c11 H-H average effective diffusion collision integral in the interval $1000 < T_g < 15,000^o K$.

hh.c22 H-H average effective momentum collision integral in the interval $1000 < T_g < 30,000^o K$.

hhion.c22 H-H^+ average effective momentum collision integral in the interval $6000 < T_g < 30,000^o K$.

h2h.c22 H_2-H average effective momentum collision integral in the interval $1000 < T_g < 15,000^o K$.

h2h.logkp $Log_{10}(K_p)$ for hydrogen in the interval $1500 < T_g < 6000^o K$.

h2h2.c11 H_2-H_2 average effective diffusion collision integral in the interval $1000 < T_g < 15,000^o K$.

h2h2.c22 H_2-H_2 average effective momentum collision integral in the interval $300 < T_g < 15,000^o K$.

nhdote.dat $Log_{10}(<\sigma v>)$ for electron impact dissociation of hydrogen in the interval $0.1 < T_e < 4.0eV$.

E.3 Variables

In this section the main variables used in the arcjet simulation program are listed and described for reference. The units of all program variables are MKS.

amin Minimum ionization fraction limiter.

ancur Total current into the anode.

catcur Total current out of the cathode.

curmult Multiplier used to numerically set the proper current density on the cathode tip.

current Specified current density on the cathode tip.

da Ambipolar diffusivity.

detadr, detadz, dxidr, dxidz Grid metrics.

dt Integration time step for electron density and energy equations.

dtg Integration time step for global/heavy species equations.

e Proton charge.

ed Hydrogen dissociation energy.

eff Propulsive efficiency.

eih Hydrogen ionization energy.

enhdot Hydrogen dissociation rate due to electron impact.

erms Root mean square error in the electron pressure residual over the mesh.

etacat Radial grid station marking the cathode radius.

fe, fg, fh Axial flux vectors for electron, global/heavy species, and atomic hydrogen density state vectors.

fname Prefix identifying the run files of the current run.

ftheta0 Inlet flow swirl angle.

gamma Ratio of specific heats.

ge, gg, gh Radial flux vectors for electron, global/heavy species, and atomic hydrogen density state vectors.

grms Root mean square error in the heavy species pressure residual over the mesh.

inlet Logical variable which indicates whether the inlet density equation is to be integrated during this integration step.

isp Specific impulse.

iter Cumulative number of integration steps for the current run.

jacobian Jacobian of the coordinate transformation.

jr, jz Radial and axial current densities.

kb Boltzmann's constant.

ke, kg Electron and heavy species coefficients of thermal conductivity.

mdot Inlet mass flow rate per unit area.

me, mh, mh2 Electron, hydrogen atom, and hydrogen molecule masses.

mug Heavy species coefficient of viscosity.

na Avogadro's number.

nedot Net hydrogen ionization rate.

neta Number of grid points in the radial direction.

nhdot Net hydrogen dissociation rate.

nxi Number of grid points in the axial direction.

pe, pg Electron and heavy species pressures.

phi Potential.

power Current times voltage.

predictor Logical variable which indicates whether a predictor or corrector integration step is being performed.

prms Root mean square error in the electric potential residual over the mesh.

qer, qez Radial and axial electron heat fluxes.

qgr, qgz Radial and axial heavy species heat fluxes.

r Radial grid point location.

re Electron gas constant.

rgas Ideal gas constant.

rh2, rh, rnet Molecular hydrogen, atomic hydrogen, and net hydrogen mixture gas constants.

rhoemin Minimum electron density limiter.

rhoh Atomic hydrogen density.

rhomax Maximum density limiter.

rhomin Minimum density limiter.

se, sg, sh Source term vectors for electron, global/heavy species, and atomic hydrogen density state vectors.

sigma Electrical conductivity.

spcur Specified total current.

supersonic Logical variable which indicates whether the flow at this exit point is supersonic.

taurr, taurt, taurz, tautt, tautz, tauzz Viscous stresses.

te, tg Electron and heavy species temperatures.

temax Maximum electron temperature limiter.

temin Minimum electron temperature limiter.

tf Reference temperature $(298.16^{\circ}K)$.

time Total simulation time of current run.

thetad, thetav Hydrogen characteristic dissociation and vibration temperatures.

totcur Space-averaged current in the arc.

twall Temperature of the electrode walls.

ue Electron state vector: array consisting of electron density, axial momentum, radial momentum, internal energy, and pressure.

ug Global/heavy species state vector: array consisting of global density, axial momentum, radial momentum, azimuthal momentum, heavy species internal energy, and heavy species pressure.

umax Maximum velocity limiter.

vei, ven, ven2 Electron-hydrogen ion, electron-atomic hydrogen, and electron-molecular hydrogen collision frequencies.

ver, vez Radial and axial electron velocities.

voltage Potential difference between anode and cathode plus the ionization potential and one half the dissociation potential of the gas.

xh2, xh, xhion Molecular hydrogen, atomic hydrogen, and hydrogen ion mole fractions.

xianode Axial grid station marking the onset of the convergent channel section upstream of the constrictor.

xicathode Axial grid station marking the cathode tip.

xi1con Axial grid station marking the constrictor inlet.

xi2con Axial grid station marking the constrictor exit.

xmax Maximum mass/mole fraction limiter.

xmh2, xmh, xmhion Molecular hydrogen, atomic hydrogen, and hydrogen ion mass fractions.

xmin Minimum mass/mole fraction limiter.

z Axial grid point location.

E.4 Run Files

A number of files are produced which contain flow simulation data for each case run. The files are all prefixed by a five character string which serves to identify each particular case, such as *run12*, or *case4*. Each of these files is described below, with the dummy identifying prefix *fname*.

fname.cur Lists the total axial current in the simulation at each axial location from the cathode tip to the constrictor exit.

fname.hydro Lists the molecular hydrogen, atomic hydrogen, and hydrogen ion mole fractions at all mesh points.

fname.pcur Lists the total axial current in the simulation at each axial location on the potential grid from the cathode tip to the constrictor inlet.

fname.perf Lists the current, voltage, power, thrust, efficiency, and specific impulse of the run.

fname.phi Lists the voltage, cathode tip current density, and then the electric potential at all mesh points.

fname.stat Lists the number of grid points in the axial and radial directions, the cumulative number of integration steps run, the total simulation time, the wall temperature, the inlet mass flow rate per unit area, the z-coordinate of the cathode tip, the z-coordinate of the converging channel section upstream of the constrictor, the z-coordinate of the constrictor inlet, the z-coordinate of the constrictor exit, the r-coordinate of the cathode radius, the inlet swirl angle, the maximum and minimum electron temperature limiters, the minimum electron density limiter, the minimum and maximum density limiters, the minimum and maximum mass/mole fraction limiters, the maximum velocity limiter, the specified total current, the minimum ionization fraction limiter, the cathode tip current multiplier, and the inlet gas temperature, axial momentum, and ionization fraction profiles.

fname.trans Lists the electrical conductivity, electron thermal conductivity, heavy species thermal conductivity, and viscosity at all mesh points.

fname.ue Lists the electron state vector at all mesh points.

fname.ug Lists the global/heavy species state vector at all mesh points.

There are also two grid files which are read each time the program is run. The file *grid."gridname"* lists the r and z locations of each grid point of the physical mesh, and the file *grid.phi* lists the r and z coordinates of the more refined mesh used for relaxation of the electric potential.

E.5 Compiling, Linking, and Running the Code

On Unix based systems, the code may be compiled and linked using a Makefile, which produces *.o* object files and the executable image *arcaxi* The code is written in floating point single precision but must be compiled in double precision (-r8, -autodblpad, or similar compiler option) in order to insure correct results. When the code is run the user is prompted for the prefix of the run files and the suffix of the grid file, asked whether the run is a new or continued one, and prompted for the number of integration steps to perform. If the solution to a new set of arcjet operating parameters is desired, it is best to use the results from a previously converged solution as the starting point for the new run. Otherwise the code will generate an initial guess at the solution which may require smaller time steps, increased smoothing, additional limiters, and/or periodic checking to keep the code from going unstable as the simulation approaches the correct steady-state solution. Run times for the code are on the order of 500 hours for the computer workstations described in Section 4 6. In general when only global performance predictions such as specific impulse and efficiency are needed, the code does not need to be run nearly as long as when an accurate internal flow solution is required for detailed analysis. For the former case mass flow errors on the order of 3-8% can be tolerated, while for the latter case the mass flow rate error should be less than 1-2%. Since the fluid density converges last of all the flow variables, decreasing the mass flow rate error from 5% to 1% could double the simulation time required. One useful trick for speeding up convergence is to multiply the flux term which is used to update the inlet density in *boundc.f* by a factor of 2-10 until the mass flow rate error near the inlet has come close to convergence. This is particularly useful when starting new runs with different mass flow rates or different inlet conditions.

A number of simple programs have been written to analyze and plot the data from the arcjet simulation results. The program *plot2*, written with the GRAFIC subroutine library, generates axial line plots, contour plots, vector plots, and grid plots. Before running *plot2*, the program *convert* must first be run to convert the data in the run files to the format which is used by the plotting program. The program *out* creates files containing radial profiles of a number of flow quantities, which may then be plotted using one of three multiple line plotting programs: *graf*, *graf2*, or *graf3*. Simple line plots are produced by *graf*, while line plots with a key are created by *graf2*. Line plots with a background grid are produced by *graf3*. All three graphing programs were written using the GRAFIC subroutine library. The program *massflow* has been written to calculate the RMS error in the mass flow rate averaged over all axial grid stations. Average values and radial profiles of the sizes of terms in each of the governing equations are generated by the program *terms*. The program *heat* calculates the distribution of the heat flux to the anode wall, and also the total power transmitted.

Appendix F

Numerical Problems Encountered

This appendix is included primarily as a reference for researchers working on similar numerical programming projects. For most complex numerical fluid simulations, debugging and refining the code from an initial implementation to a final working state can be an arduous, time-consuming process. The arcjet simulation code of this research was no exception to the norm in this regard. During the debugging of the arcjet code a number of numerical issues arose, some of a very subtle nature, which needed to be resolved in order to achieve proper convergence and consistency. These issues can be grouped into three main categories: numerical implementation of the governing equations, grid generation and resolution, and variable limiters.

F.1 Numerical Implementation of the Governing Equations

The numerical implementation of the governing equations is described in some detail in Sections 4.2-4.5 of this thesis. One important consideration for the application of the finite difference algorithm of this research is the fact that the model is axisymmetric. It was found that if the axisymmetric $\frac{1}{r}$ source terms were included in the source vector on the right-hand sides of the equations, the simulation would converge but with conservation errors at the points near $r = 0$. The errors were particularly large in equations which included second order diffusion terms, such as the electron and atomic hydrogen continuity equations. This problem was solved by multiplying all of the fluid equations by r and incorporating the axisymmetric terms as much as possible into the fluxes of the left-hand sides of the equations.

A second problem encountered in the numerical application of the governing equations involved the grid metrics. The governing equations in transformed coordinates, as listed in Appendix D, contain flux terms multiplied by the metrics of the coordinate transformation. In the equations as listed, these metrics are of the form η_r, η_z, ξ_r, and ξ_z, and lie outside the spatial derivatives in what would seem to be a non-conservative manner. Three different implementations of the metric terms were tried, only one of which yielded satisfactory results. Initially, all metrics were evaluated by central differences of second order accuracy and applied as in Equations D.1-D.20. This led to conservation errors, however, which were particularly noticeable in the mass flux between axial stations. Central differencing was causing numerical smoothing of the grid points, which led to an inconsistent finite difference approximation of the governing equations. In an effort to resolve this problem, the metrics were rederived in the r_η, r_ξ, z_η, z_ξ form and moved inside the flux derivatives. This method decreased the amount of grid smoothing, but not to acceptable levels. The final solution involved returning the metrics to their original form but evaluating them by two point first order differences in the direction of the integration step being performed. In other words, a forward difference would be used for each MacCormack predictor step, and a backward difference would be used for each corrector step. Once the evaluation of the grid metrics was tied to the numerical method in this manner, conservation errors became negligible.

Some numerical smoothing of the difference equations was necessary for convergence, however, and this also proved to be problematic. As detailed in Section 4.1.3, two different smoothing approaches were tried without success before a third method was found which worked. Neither fourth order damping of the state variables based on a pressure switch, nor second order damping without a switch could insure proper stability without causing unreasonable errors in the solution. The complexity of the governing equations, the two-step numerical method, and the skewness of the physical grid all dictated that a simple grid point-based method be used for numerical smoothing, and it was the simplified method of Kutler, Sakell, and Aiello[64] that finally achieved the desired results.

One final issue regarding the implementation of the numerical method was the computational time required for convergence. In order to reduce the computational time per iteration, a number of different measures were taken. First, numerical smoothing was applied only after the corrector integration step, with the amount of damping calculated from variables at the previous time level. Second, the values of transport coefficients such as μ_g, k_g, k_e, D_a, and σ were updated only once each integration step or less. All major variables were placed in common blocks to eliminate long subroutine parameter lists, and no subroutine calls were made inside mesh-traversing DO-loops. In addition, the use if IF-THEN statements within DO-loops was minimized. Finally, the code was written in as vectorized a manner as as possible, with minimal reuse of a variable calculated in a given DO-loop.

F.2 Grid Generation and Resolution

The generation of a physical mesh to represent a complex geometry such as that of an arcjet is often a difficult problem in and of itself. One of the most important concerns is the elimination of internal mesh discontinuities. A grid generated by transfinite interpolation, for example, will propagate boundary discontinuities onto the interior points of the grid. It is necessary to use some technique such as the elliptic solver of Section 4.3.2 to smooth out the internal mesh points. Otherwise, instabilities and sawtooth solution modes may arise from the numerical smoothing or from the numerical method itself.

Another important consideration is the degree of grid resolution in various regions of the mesh. Since the code includes viscous no-slip wall boundary conditions, additional points must be clustered near the walls in order to resolve the fluid boundary layers present there. The Reynolds number based on internal diameter,

$$Re_D = \frac{\rho u_z D}{\mu_g} = \frac{\dot{m} D}{\mu_g A}, \tag{F.1}$$

varies from 100-5000 for most of the arcjet cases modeled, while the Reynolds number based on length can be on the order of 10,000. Another important boundary layer is the diffusion boundary layer formed by electrons and ions diffusing to the electrode walls. Assuming a charged particle balance exists between particles being created through ionization events and particles diffusing to the walls by ambipolar diffusion, the characteristic diffusion length for this process is

$$\delta_D \sim \sqrt{D_a \tau_{ion}}, \tag{F.2}$$

where τ_{ion} is the effective ionization time, given by

$$\tau_{ion} = \frac{1}{R S n_n}. \tag{F.3}$$

For typical near wall electrothermal arcjet flow parameters, this diffusion length δ_D is on the order of 10^{-4} to 10^{-5} meters. In order to physically capture these boundary layers in the computational sense, at a minimum the regions should be spanned by at least a few grid points in the direction normal to the walls.

The degree of grid resolution is also influenced by the steep gradients often found in physically complex numerical simulations such as this one. Gradients in flow variables near the cathode tip, at the edge of the arc, and near the constrictor exit where the current attaches all require that extra grid points be positioned in these regions. Additional grid resolution beyond the scale of the flow grid is necessary to accurately resolve the electric potential distribution, especially near the electrodes and in the main arc region.

F.3 Variable Limiters

Upper or lower limiters on the value of a flow variable were found to be necessary in some cases in order to achieve convergence. These were especially necessary when a solution to the baseline arcjet case was first being sought from an initial guess at the steady-state flowfield. Since the starting conditions were so far from steady-state, initial rapid fluctuations in both time and space occurred for some variables, and without limiters these fluctuations could have driven the code unstable. Once a baseline solution was obtained, this solution was used as the starting point for all other cases run, and the initial fluctuation problem was minimized.

Even in steady state, however, some limiters were required. The very strong current concentration at the cathode tip always caused electron temperatures to rise to unreasonably high values, so an upper limit of $40,000^{o}K$ was placed on T_e. In addition, in order for the electron difference equations to be solved, a lower limit had to be placed on the ionization fraction. This reflected the fact that a nonzero inlet ionization fraction had to be prescribed because the model could not create ions from an entirely neutral flow and also that the electron equations could become unstable for very low electron number densities. A minimum ionization fraction of 1×10^{-6} was typical. Finally, upper and lower limiters for species mass fractions were required. A minimum x_H was required to avoid computational problems in the atomic hydrogen continuity equation. Other mass fraction limiters were necessary in order to maintain consistency in the calculation of transport coefficients.

Appendix G

Arcjet Thruster Experimental and Numerical Data

Table G.1: Stuttgart TT1 Radiatively-Cooled H_2 Arcjet Experimental Data

$\dot{m}$(g/s)	I(A)	Voltage(V)	Power(kW)	Sp. Power(MJ/kg)	Isp(s)	Thrust(N)	Eff.
0.05	80	81	6.48	130	990	0.49	0.364
0.05	100	78	7.80	155	1070	0.52	0.352
0.05	120	77	9.24	185	1130	0.55	0.332
0.05	135	74	9.99	200	1160	0.57	0.322
0.10	60	117	7.02	70	810	0.79	0.448
0.10	80	113	9.04	90	885	0.87	0.416
0.10	100	112	11.2	110	960	0.94	0.394
0.10	120	111	13.4	135	1030	1.01	0.382
0.10	140	110	15.4	155	1090	1.07	0.372
0.10	150	110	16.5	165	1120	1.10	0.366
0.15	60	127	7.62	50	715	1.05	0.482
0.15	80	121	9.68	65	755	1.11	0.424
0.15	100	119	11.9	80	805	1.18	0.392
0.15	120	118	14.2	95	855	1.26	0.374
0.15	140	117	16.4	110	905	1.33	0.360
0.15	150	116	17.4	115	925	1.36	0.354
0.15	175	115	20.1	135	965	1.42	0.334

Table G.2: Stuttgart TT1 Water-Cooled H_2 Arcjet Experimental Data

$\dot{m}$(g/s)	I(A)	Voltage(V)	Power(kW)	Sp. Power(MJ/kg)	Isp(s)	Thrust(N)	Eff.
0.10	60	160	9.60	95	640	0.63	0.204
0.10	80	153	12.2	120	695	0.68	0.188
0.10	105	148	15.5	155	735	0.72	0.166
0.10	135	144	19.4	195	805	0.79	0.160
0.10	150	142	21.3	215	850	0.83	0.162
0.20	50	201	10.1	50	450	0.88	0.192
0.20	65	194	12.6	65	480	0.94	0.174
0.20	80	188	15.0	75	505	0.99	0.162
0.20	90	184	16.6	85	525	1.03	0.158
0.20	105	180	18.9	95	545	1.07	0.150
0.20	120	178	21.4	105	570	1.12	0.146
0.20	130	175	22.8	115	590	1.16	0.146
0.20	140	173	24.2	120	605	1.19	0.146
0.30	50	234	11.7	40	390	1.16	0.190
0.30	60	224	13.4	50	410	1.21	0.182
0.30	75	215	16.1	55	435	1.28	0.168
0.30	95	207	19.7	65	455	1.33	0.150
0.30	105	203	21.3	70	465	1.37	0.146
0.30	120	201	24.1	80	480	1.41	0.136

Table G.3: Stuttgart TT1 Radiatively-Cooled H_2 Arcjet Numerical Data

$\dot{m}$(g/s)	I(A)	Voltage(V)	Power(kW)	Sp. Power(MJ/kg)	Isp(s)	Thrust(N)	Eff.
0.05	70	89	6.23	125	1040	0.51	0.417
0.05	100	85	8.50	170	1150	0.56	0.374
0.05	120	83	9.96	200	1200	0.59	0.347
0.10	60	118	7.08	70	900	0.88	0.546
0.10	100	115	11.5	115	1030	1.01	0.442
0.10	130	113	14.7	145	1120	1.09	0.410
0.15	60	140	8.40	55	810	1.18	0.561
0.15	95	138	13.1	85	920	1.34	0.465
0.15	130	137	17.8	120	1010	1.48	0.410

Table G.4: Stuttgart TT1 Radiatively-Cooled H_2 Arcjet Numerical Data, with Coupled Temperatures from Anode Thermal Model

$\dot{m}$(g/s)	I(A)	Voltage(V)	Power(kW)	Sp. Power(MJ/kg)	Isp(s)	Thrust(N)	Eff.
0.10	60	115	6.90	70	870	0.85	0.527
0.10	100	111	11.1	110	1050	1.03	0.477
0.10	130	110	14.3	140	1170	1.14	0.456

Appendix H

Tungsten and Molybdenum Thermal Conductivity

Table H.1: Thermal Conductivity of Tungsten (Low Temperature)

$T(°K)$	$\kappa_W(W/cm/°K)$
0	0.0
10	82.4
20	32.6
30	13.1
40	6.50
50	4.17
60	3.18
70	2.76
80	2.56
90	2.44
100	2.35
200	1.97
300	1.78
400	1.62
500	1.49
600	1.39
700	1.33
800	1.28
900	1.24
1000	1.21

Table H.2: Thermal Conductivity of Tungsten (High Temperature)

$T(°K)$	$\kappa_W(W/cm/°K)$
1100	1.18
1200	1.15
1300	1.13
1400	1.11
1500	1.09
1600	1.07
1700	1.05
1800	1.03
1900	1.02
2000	1.00
2100	0.98
2200	0.96
2300	0.94
2400	0.925
2500	0.915
2600	0.905
2700	0.900
2800	0.895

Table H.3: Thermal Conductivity of Molybdenum

$T(^{o}K)$	$\kappa_M(W/cm/^{o}K)$
300	1.375
400	1.325
500	1.280
600	1.235
700	1.200
800	1.160
900	1.120
1000	1.080
1100	1.050
1200	1.025
1300	1.000
1400	0.980
1500	0.960
1600	0.950
1700	0.940
1800	0.930
1900	0.925
2000	0.920
2100	0.915
2200	0.910
2300	0.910
2400	0.910